

Elettra Highlights 2022–2023





Elettra Sincrotrone Trieste

**Browse the digital collection
of Elettra Highlights here:**



ELETTRA HIGHLIGHTS 2022 | 2023

Editorial committee

Laura Badano

Federica Bondino

Iulia Cojocariu

Silvia Di Fonzo

Giovanni Di Santo

Raghurama Hegde

Elena Longo

Alessandro Mariani

Emanuele Pedersoli

Robert Richter

Nadia Sambaello

Print

Riccigraf S.a.s. – Trieste

This publication reporting our activities for 2022-2023 includes contributions from work performed at the Elettra third generation synchrotron radiation source and at the FERMI free-electron laser (FEL) facility collected in the same thematic sections. For clarity, we identify each article with the "Elettra" or "FERMI" acronym on the topmost right corner, followed by the name of the beamline or laboratory where the experiments have been performed. Scientific articles published in the last year stemming from work performed at the two facilities reached a total of 588, in line with that of the previous year, and included many high-impact publications. The major challenge to this high level of scientific productivity is represented by the current increase in energy cost.

To maintain Elettra and FERMI in operation we use each year about 32 GWh of electric energy from the national grid and about 5.5 million standard cubic meters of methane gas for our two high-efficiency trigeneration plants. In the first three quarters of 2022 the availability of a fixed-priced contract for electric energy allowed us to mitigate the impact of the increase in the cost of energy worldwide. We were able to maintain the normal user beamtime schedule, although we had to use all of our financial reserves to cover energy costs in the last quarter of the year. In 2023 no fixed-price contracts for energy and gas were available and we were forced to reduce the number of operating hours of Elettra and FERMI by 40%. This yielded a reduction of about 34% in the number of scheduled user experiments at Elettra and FERMI relative to 2022. In view of the typical 1-2 year time interval between experiment and publication of experimental results, we expect this to have a major impact on the scientific productivity of our facilities in 2024-2025.

The reduction in the number of operating hours of Elettra and FERMI is especially unfortunate at a moment when the efficiency and reliability of Elettra and FERMI are at their peak values. In 2022 Elettra supplied 5026 hours of beamtime to 28 beamlines with an overall 97.4% operating efficiency, while FERMI provided 5388 hours of user beamtime with an overall 95.5% operating efficiency. We hope that the initiatives that are taking place at the European level, for example the launch of the REPowerEU program, will provide a route to the implementation of new mitigation strategies, as well as long-term solutions to the energy problem.

For the 28 operating beamlines at Elettra selective upgrade programs have had as a common denominator the implementation of preparatory interventions for the transition towards the new Elettra 2.0 light source, such as to guarantee a positive short-term impact on users, but also long-term usability. Important instrumental acquisitions were carried out last year for the Spectromicroscopy, XAFS, Xpress, XRD1 and MCX beamlines, as well as for the new Coherent Diffraction Imaging (CDI), SYRMEP-Life Science (SYRMEP-LS), HB-SAX, μ XRD and μ XRF beamlines.

The Elettra 2.0 source, belonging to the 4th generation DLSR class, will be housed in the existing tunnel and utilize the existing injection system, in order to minimize the required infrastructural changes, cost and installation time. Its design adopts a symmetric 6-bend achromat lattice that will allow us to achieve an horizontal bare emittance of 212 pm-rad at 2.4 GeV, i.e. 50 times lower than the present Elettra value, with a 60-fold increase in the coherence fraction at 1 keV. At the same time the energy consumption of the new source is expected to be *lower* than that of the existing source. A few upgraded machine systems such as the solid-state RF transmitters, enhanced feedbacks and controls have already been installed and tested on the current Elettra storage ring and will be transferred to the new machine. Procurement of all Elettra 2.0 machine components is in progress, and the switch between the old and the new machine is expected to occur between July 2025 and July 2026.

Upgrade programs of existing beamlines carried out last year were performed to achieve a positive impact on current users, but also guarantee full exploitation on Elettra 2.0. For example, the XAFS beamline has been equipped with two new fluorescence detectors, namely a 7-element SDD and a 36-element Ge detector. The two detectors increase the efficiency of the experimental station with regards to experiments in fluorescence geometry in the entire operating energy range of the beamline. For the Xpress beamline, three new diamond cells, a



Alfonso Franciosi

President and Chief Executive
Elettra-Sincrotrone Trieste S.C.p.A.

cryostat and an optical microscope for loading were acquired, significantly reducing the dead times between one measurement and the next. The Spectromicroscopy beamline is being equipped with a new electron analyzer with high energy resolution and high angular acceptance for high transmission ARPES measurements. An integrated system for the analysis of the spin of the photoelectrons and the subsequent 3D determination of the spin configuration will be available to Spectromicroscopy users.

Three new beamlines currently under constructions will use in-vacuum undulator sources on Elettra 2.0 capable of producing high energy bright X-ray beams. HB-SAXS is designed for small-angle X-ray scattering experiments and other techniques with very bright and highly coherent beams even in the hard-X-ray range. μ XRD, will be the reference beamline at Elettra for diffraction experiments of proteins and small molecules. μ XRF will be the new beamline for fluorescence imaging and absorption spectroscopy with micrometer spatial resolution.

A new development project entitled Pathogen Readiness Platform for CERIC-ERIC Upgrade (PRP@CERIC) is being implemented in collaboration with Area Science Park and the Consiglio Nazionale delle Ricerche (CNR) as part of the Italian National Recovery and Resilience Plan. The project will enhance our capabilities in the area of structural biology, hyperspectral cytology and histology, as well as for dynamic studies of biomolecules and integrate our X-ray structural determination techniques with a new cryo-electron microscopy user facility established at Elettra in collaboration with CNR.

The support obtained through the project will be used also to strengthen the structural biology laboratory as a user facility, improve the expression and purification capabilities for recombinated proteins, and implement a high-efficiency crystallization facility. Additional equipment will be installed on the SISSI-Bio and IUVS beamlines for cytology experiments and hyperspectral histology. In the NanoInnovatiLab a new high-speed, high-spatial-resolution AFM instrument will be added for dynamic studies of hydrated biosystems.

All of the above actions are consistent with the evolution foreseen for the XRD2 and SAXS beamlines at Elettra, which will evolve into the μ XRD, HB-SAXS and HF-SAXS beamlines at Elettra 2.0, and enhance also the low and very low energy beamlines, in order to keep them active during the July 2025-July 2026 dark period and strengthen their complementarity with other imaging and microfluorescence techniques.

The scientific programs at FERMI, the only FEL user facility in the world currently exploiting external seeding to offer unparalleled intensity, wavelength and linewidth stability, were able to exploit the experimental stations for Diffraction and Projection Imaging (DiProl), Elastic and Inelastic Scattering – TIMEX (EIS-TIMEX), Low Density Matter (LDM), Elastic and Inelastic Scattering – TIMER (EIS-TIMER), Magnetic Dynamics (MagneDyn) and THz spectroscopy (TeraFERMI).

Among the most important scientific results obtained last year we mention the use of optical beams with angular momentum to study the magnetic response of macroscopic systems at DiProl and of nanometric systems at LDM. At EIS-TIMER the use of the non-linear response of a magnetic multilayer system highlighted the possibility of implementing all-optical switching at the nanoscale.

Experiments carried out at EIS-TIMEX exploiting the interaction of the high intensity radiation produced by FERMI with matter highlighted the competition between two non-linear effects, i.e., two-photon absorption and induced transparency. MagneDyn was used to inject and detect spin-polarized currents in silicon. This result is a first step towards the development of technologies that will allow magnetic storage to be combined with electronic readout in a single semiconductor device.

The future evolution of FERMI has been summarized in the the Conceptual Design Report (CDR) of FERMI 2.0, and include the primary goals of extending the photon energy range to the N (410 eV) and O (543 eV) K-edges and possibly beyond, and reduce pulse duration below 10 fs in selected spectral ranges.

FERMI higher-order harmonic emission has been successfully used already to perform experiments at the iron L edge, albeit with approximately 10^3 times fewer photons than expected as a result of the proposed FERMI 2.0 upgrade. The planned upgrades include increasing the electron beam energy up to 2 GeV while reducing wakefields and improving beam quality.

On the two FEL-1 and FEL-2 laser lines of FERMI, we will exploit the solid experience gained over the years of operation and the encouraging results of the Echo-Enabled Harmonic Generation (EEHG) experiments and super-radiance. Implementing the EEHG configuration on FEL-1 will increase beam quality and reliability and double the maximum achievable photon energy. As for FEL-2, we propose to use of an EEHG configuration in the first stage coupled with a high-gain harmonic generation (HG) type conversion section with fresh-bunch, similar to the one currently in use, in the second stage. The combination of these two techniques is the one that provides the greatest extension in energy for the seeded FEL according to the calculations and the simulations.

An early upgrade of the LINAC has been completed, introducing two new high-gradient, low wakefield accelerating sections and increasing the electron beam energy to 1.7 eV. Conversion of FEL-1 to the EEHG operating mode will be completed by the end of 2023 and the new and improved FEL-1 source will be ready for users at the beginning of 2024. This will open a second phase in which the new configuration will be exploited to improve performance and control of the light from FEL-1, study new modes of operation, and build a solid experience and scientific confidence for the next step, namely converting the first stage of FEL-2 to the EEHG configuration.

In the Fall of 2023 we will be celebrating thirty years of operation of the Elettra synchrotron radiation source. Six thematic workshops have been organized for our users and staff. On September 11-12 a first workshop entitled " μ -XRF@elettra2.0: Challenges and Opportunities" has been organized in collaboration with the International Atomic Energy Agency. On September 12-13 the "PhotonMEADOWE23" workshop focused on X-ray optics design and metrology. On November 8-9 the "26th European Synchrotron Radiation Light Sources Radio Frequency Workshop" will examine issues ranging from beam dynamics to RF hardware development. On November 14-15 the "Permanent Magnets for Low Emittance Rings" workshop will attempt to facilitate the sharing of know-how in this area among the many facilities that are upgrading or planning to upgrade to 4-th generation generation storage rings.

On November 29-30 the "BatSynch: The Battery Challenge at Synchrotrons" workshop will bring to Trieste the top scientists working on battery innovation and developments and highlight the most recent achievements obtained with synchrotron-based approaches. On November 30 and December 1, the "NTP:Nanoscale Transport Phenomena" workshop will examine the impact that the application of time-resolved experiments by means of free-electron lasers will have on the understanding of dynamic processes related to phonon, charge and spin transport at the nanoscale. After two years when the COVID-19 crisis prevented us from having in-person gatherings of this type, organizing such workshops seemed to us the best way to celebrate together with our users the thirty-year anniversary of Elettra.

We take this opportunity to thank all of our employees and collaborators, our Partners and our users for their continuing support of our activities during the COVID-19 pandemics and during the current energy-related crisis, as well as for their enthusiasm and dedication over the years.

Alfonso Franciosi

President and Chief Executive
Elettra-Sincrotrone Trieste S.C.p.A.

Table of contents

Functional Materials

Unveiling the H ₂ production mechanism in methanol decomposition on Ni ₃ Sn ₄ surfaces	12
Unveiling the Potential of Cobalt Ditelluride Topological Dirac Semimetal in Terahertz Photodetection.	14
Winding of electrons in the quantum world	16
Unveiling the Potential of Gallium Telluride in Electrochemistry, Photochemistry, and Gas Sensing	18
Creating high-resolution fluorescent micropatterns of 3D-oriented porous films	20
Solid electrolyte interphase composition and distribution in “zero excess” lithium-metal batteries . . .	22
Unlocking the potential of carbon atomic wires by synchrotron-based UV resonance Raman spectroscopy	24
Insight into the structural evolution of Co-Poor Lithium Rich Oxides for Lithium Ion Battery	26
Exploring the complexity of functionalized nanoparticles through a combination of machine-learning and experiments.	28
Direct observation of phase separation and evolution in Li _x CoO ₂ particles	30
Ordered 3D quantum dot superlattices with excellent transport properties.	32
Infrared Plasmons in Ultrahigh Conductive PdCoO ₂ Metallic Oxide	34
Loading H atoms in porous nickel covered by monolayer graphene	36
Cavitation in silica-filled styrene-butadiene rubber nanocomposite upon cyclic tension resolved by in-situ synchrotron radiation tomography	38
Role of defects in colored TiO ₂ hollow spheres for photocatalytic applications.	40
Tuning thermal expansion properties in materials by insertion of guest molecules.	42
Confused-Prism[5]arene: a conformationally adaptive host with stereoselective guest inclusion	44

Life Sciences, Environmental Science and Cultural Heritage

A deep look at two Stradivari’s violins from micro to nanoscale	48
Variabilities in DNA methylation and intracellular proteins structure establish spectroscopic landscapes among subtypes of pancreatic cancer	50
High resolution propagation-based lung imaging at clinically relevant X-ray dose levels	52
Iron and toxic environmental elements in human endometriosis: a combined role?	54
Engineered neurotransmitter transporter provides insights into GABA uptake inhibition	56
Triple negative breast cancer-derived small extracellular vesicles: modulators of cells biomechanics . .	58
Optical manipulation of charge delocalization in a bulk heterojunction material	60
New method reconstructs 3D landscape in XRF microscopy: breakthrough enhances imaging accuracy	62
X-ray Imaging and spectroscopy Reveals Ovarian Structures in bovine model	64
A first time in jellyfish science: 3D X-ray computed μ CT of the gastrovascular system of <i>Rhizostoma pulmo</i>	66

Low Density and Soft Matter

Photo-processing of nitrogenated aromatics in space: dissociative photoionisation of quinoline as a test case	70
The importance of gas phase photoelectron spectroscopy in science and its relationship to molecular orbital theory.	72
Driving Rabi oscillations with extreme-ultraviolet light pulses	74
Filming molecular chiral dynamics from the inside with free electron laser	76
Real-time motion of molecules unveiled	78
Non-linear Terahertz spectroscopy reveals temperature-independent behavior in the response of liquid water	80

Structure and Dynamics

The struggle of dipeptides for Life	84
Shedding light on PTG/PP1 holoenzyme structure – a promising target for Lafora disease	86
Targeting 3CL ^{pro} for pan-CoVs antiviral drug candidate: medicinal chemistry and X-ray studies.	88
Unfolding the mysteries of the fascinating interplay of magnetism and electricity in Ni ₃ TeO ₆	90
Vacancy influence on manganese hexacyanoferrate Na-ion batteries: structural perspective	92
Depth selective local structure in CoFeB thin film interfaced with W: A standing wave XAFS study	94
All-optical switching of magnetization on a nanometer spatial scale	96
Extreme ultraviolet transient gratings: a tool for nanoscale photoacoustics	98
Revealing all-optical spin injection in silicon in the femtosecond time scale at FERMI.	100
Layer-by-layer control of the electron dynamics in magnetic topological insulators	102
Visualizing excitons in the twodimensional semiconductor ReSe ₂	104

Surfaces and Interfaces

Orbital symmetry regulates charge transport across a phthalocyanine-graphene interface.	108
Playing with reaction conditions on surfaces	110
Effects of visible light illumination on Photostrictive/Magnetostrictive PMN-PT/Ni Heterostructure	112
Uncovering the evolution of h-BN-Graphene Heterostructure in oxygen-rich environment	114
Moving the Dirac cones of BaNiS ₂ by Surface Charge Doping	116
2D ferrimagnetism in quasifreestanding graphene.	118
Understanding carbide evolution and surface chemistry during deep cryogenic treatment in high-alloyed ferrous alloy.	120
Identifying charge distribution and support effects in Au catalysts under reaction conditions	122
Single-active site character in a bottom-up constructed π -conjugated nickel-porphyrin network	124
Epitaxially-aligned and rotated graphene on cobalt: exploring spin-polarized hybrid states	126
Stripy domain of striped electronic phase.	128
Time-resolved x-ray spectroscopy reveals atomic and electronic dynamics in adsorbates	130
Unique adsorption configuration of M(II)-tetraphenylporphyrins on the r-TiO ₂ (110) surface	132
The oxidation of sub-nanometer graphene-supported Fe clusters.	134

Photon Sources and Instrumentation

Elettra Status	138
Elettra 2.0	140
Polarizers for solar physics at key spectral lines	142
Synchrotron radiation study of GaAs avalanche photodiodes for hard x-ray	144
FERMI Status Report	146
Free electron laser stochastic spectroscopy revealing silicon bond softening dynamics	148
Polarization shaping of ultrashort extreme-ultraviolet light pulses	150
MagneDyn: a tool for the study of ultrafast magnetic phenomena in solids	152

Fact & Figures / Events

Elettra and FERMI lightsources	156
Shareholders	157
Partnerships and Alliances	157
Organization	158
Staff	159
Budget allocation 2023	159
Projects and International Initiatives	160
Ongoing research contracts	162
Novel technological ICT developments for Elettra 2.0	164
CERIC-ERIC	166
Our beamlines, laboratories and services	168
Proposal Review Panels	169
Users at Elettra	170
Users at FERMI	171
Industrial Liaison Office News	172
Revolutionizing Insertion Device Design and Manufacturing at Kyma S.p.A.: A Cutting-Edge Approach	173
Institutional Visits and Events	174
Conferences	176
Workshops, Meetings and Schools	177
Public Engagement Events	180
Other News	182
Elettra Fellows	184



Functional Materials



Unveiling the H₂ production mechanism in methanol decomposition on Ni₃Sn₄ surfaces

Elettra | APE-HE

Hydrogen production from direct methanol decomposition reaction ($\text{CH}_3\text{OH} \rightleftharpoons 2\text{H}_2 + \text{CO}$) is a valuable alternative to the steam reforming of methane, commonly exploited at an industrial level. Given the urgent need to find viable alternatives to the use of fossil fuels for economic and environmental issues, methanol owns the great advantage of being one of the most important chemical feedstocks obtained from several sources, including biomass. Because of the high H content, methanol is regarded as a viable solution to the problems related to H₂ transport. The methanol decomposition reaction brings about the production of the so-called "syngas mixture" (H₂ + CO), which can be used for a wide range of applications, including the use of H₂ as a fuel. Among the state-of-the-art catalysts for methanol decomposition reaction, Ni-based catalysts combine stability, efficient catalytic activity, and low cost of raw materials, thus representing ideal candidates for industrial scaleup. One of the major challenges when using Ni-based catalysts regards the optimization of the catalytic activity and selectivity with respect to undesired secondary reactions that can occur in parallel with the methanol decomposition, with the consequent production of CO₂, CH₄, CH₂O, H₂O and C. These secondary products can poison the catalyst surface, with a consequent quick deactivation. In this context, Ni-Sn intermetallic compounds deserve particular attention, considering that the incorporation of Sn atoms can be beneficial for hydrogen selectivity and makes CO adsorption energetically unfavorable, thus preventing the poisoning of the catalyst. In this study, we investigated the methanol decomposition mechanism of Ni₃Sn₄ at temperatures between 250 and 300 °C. This hitherto unexplored temperature range, in addition to being extremely advantageous for

the industrial implementation of methanol decomposition, would also allow for the recovery of waste heat in methanol-fueled vehicles. To this aim, we combined *operando* ambient-pressure NEXAFS (Near-Edge X-ray Absorption Fine Structure) with synchrotron-based *in situ* XPS (x-ray Photoemission Spectroscopy), both performed at the APE-HE beamline of Elettra, complemented by HR-TEM (High Resolution Transmission Electron Microscopy) and DFT (Density Functional Theory) calculations. The use of *operando* and *in situ* spectroscopic techniques using synchrotron radiation proved to be particularly appropriate to monitor the status of the catalyst surface during the reaction. The *in situ* XPS technique allowed us to detect a selective oxidation of Sn (Fig. 1 (a)) atoms when the Ni₃Sn₄ surface is exposed to an oxidizing atmosphere. This result indicated the presence of a Sn-rich surface oxide skin emerging from the natural interaction of the catalyst surface with the ambient atmosphere, also imaged by HR-TEM (Fig. 1 (b)). The electronic structure modifications of Ni atoms were monitored by means of *operando* NEXAFS upon realistic reaction conditions, i.e., exposing the sample to methanol at 250 °C and 300 °C at the total pressure of 1 bar, with a continuous detection of the reaction products by means of micro gas chromatography. The CH₃OH decomposition reaction was followed by monitoring the Ni L₃ absorption edges (Fig. 1 (c)). When exposing Ni₃Sn₄ to CH₃OH at 250 °C, regardless of the surface pretreatment, the Ni L₃ edge spectral shape remained unchanged during and after the reaction (left panel of Fig. 1 (c), first and third rows). Thus, for the pre-oxidized sample, Ni maintained a prevailing +2 oxidation state, while, for the pre-reduced sample, Ni kept its metallic character. However, a rigid spectral shift to higher photon energies by +0.2 eV was found, thus

suggesting that CH₃OH weakly perturbs the local chemical environment of Ni atoms. Such a reversible energy shift could arise from a charge transfer associated with the methanol-tin oxide interaction.

Correspondingly, H₂ was detected with the online micro gas chromatography, proving the effective decomposition of methanol to syngas. Upon CH₃OH interaction at 300 °C (left panel of Fig. 1 (c), second and fourth rows), the Ni L₃ edge was unchanged in the pre-oxidized sample, while NiO was formed in the case of the pre-reduced sample. Correspondingly, side-reaction gas products, such as H₂O or CO₂, were detected. To evaluate the optimal Sn content in the Ni-Sn alloy, we repeated the *operando* NEXAFS experiments for the case of Ni₃Sn₂ (right panel of Fig. 1 (c)), although acquired spectra indicated an easier catalyst deactivation. The results we obtained indicate that the Sn-rich oxide skin plays a pivotal role in the catalytic mechanisms. Indeed, by the comparison with the Ni₃Sn₂ compound, we understood that Sn surface content helps preserve the underlying Ni atoms from irreversible electronic structure modifications due to the poisoning by secondary products adsorption (Fig. 1 (c)). This was confirmed by a semi-quantitative analysis of the gas products detected with the online micro gas chromatograph, finding an important increase in H₂ selectivity in pre-oxidized Ni₃Sn₄ (Fig. 1 (d)) with respect to pre-oxidized Ni₃Sn₂. Similar experiments performed with pre-reduced samples (Fig. 1 (c-d)) confirm the important role of the Sn-rich oxide skin naturally formed on the Ni_xSn_y surfaces in oxidizing conditions, paving the way for further catalyst optimization. The DFT calculations confirmed the experimental results, indicating that H₂ and CO desorption are favored on the surface of the pre-oxidized Ni₃Sn₄ compound, thus preventing the catalyst surface deactivation.

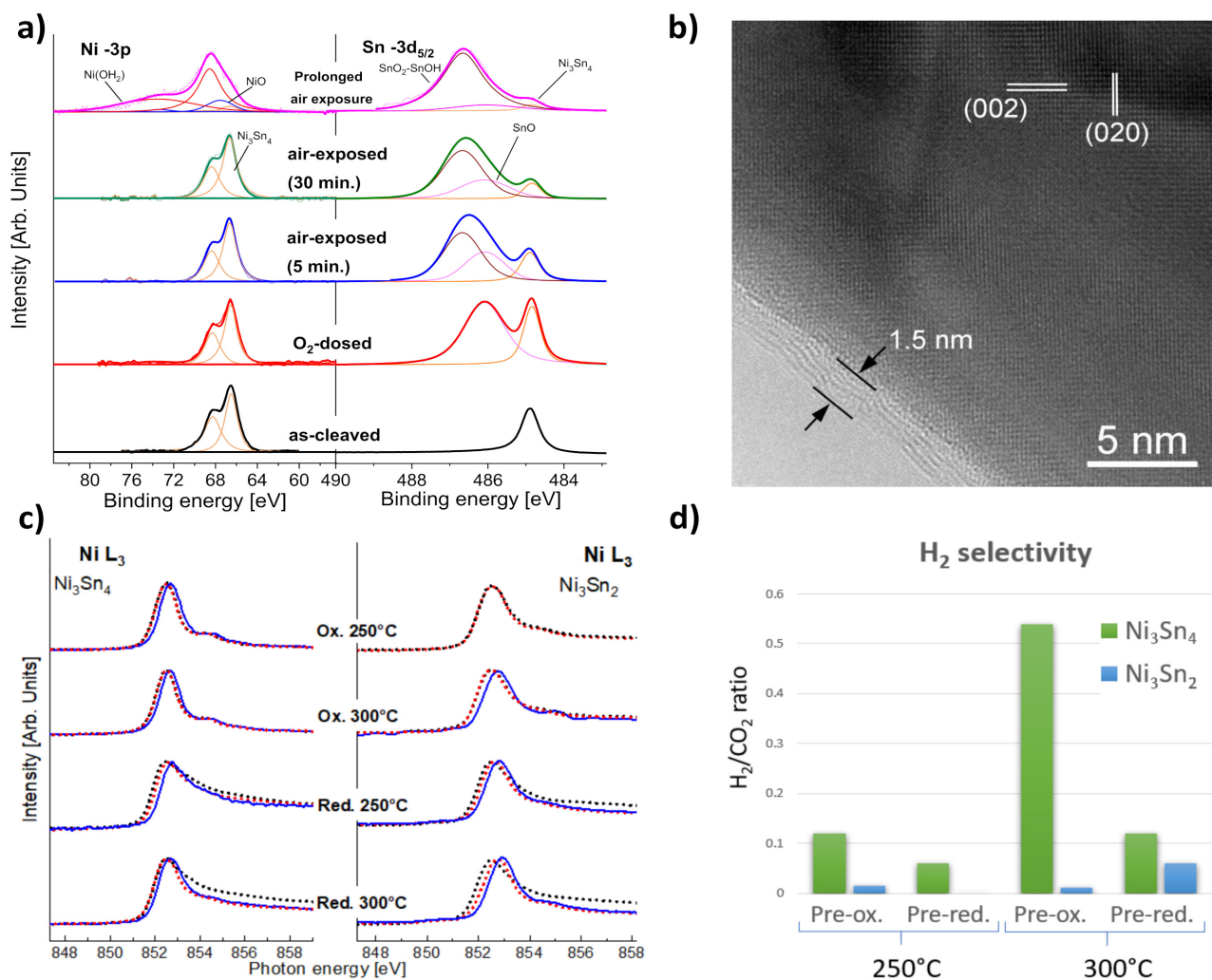


Figure 1. (a) Ni 3p and Sn 3d XPS spectra for Ni₃Sn₄ in different oxidizing environments. (b) HR-TEM micrograph of a Ni₃Sn₄ grain. An oxide skin with an average thickness of ~ 1.5 nm is indicated by the two arrows. (c) Operando NEXAFS spectra of Ni L₃ edge acquired during the exposition to CH₃OH. Black dotted, red dotted, and blue spectra denote spectra acquired before introducing the CH₃OH in the NEXAFS reaction cell, after having removed CH₃OH from the reaction cell, and during the exposition to CH₃OH, respectively. (d) Online micro gas chromatography results obtained by detecting the gas products of the CH₃OH decomposition catalyzed by Ni₃Sn₄ and Ni₃Sn₂, after sample pre-oxidation and pre-reduction, at 250 and 300°C. Adapted with permission from S. Mauri et al., *J. Phys. Chem. Lett.* **14**, 1334 (2023). Copyright 2023 American Chemical Society.

Acknowledgments

This work has been performed in the framework of the Nanoscience Foundry and Fine Analysis (NFFA-MUR Italy Progetti Internazionali) facility (<https://www.trieste.nffa.eu/>).

C.G. and M.C.I. acknowledge funding through POC No. 332/390008/29.12.2020-SMIS 109522.

Original paper

S. Mauri et al., *J. Phys. Chem. Lett.* **14**, 1334 (2023); DOI:10.1021/acs.jpcclett.2c03471.

S. Mauri^{1,2}, G. D'Olimpio³, C. Ghica⁴, L. Braglia¹, C.N. Kuo^{5,6}, M.C. Istrate⁴, C.S. Lue^{5,6}, L. Ottaviano³, T. Klimczuk⁷, D. W. Boukhvalov⁸, A. Politano³, P. Torelli¹

¹ TASC Laboratory, IOM-CNR, Trieste, Italy

² Physics Department, University of Trieste, Trieste, Italy

³ Department of Physical and Chemical Sciences, University of L'Aquila, L'Aquila, Italy

⁴ National Institute of Materials Physics, Magurele, Romania

⁵ Department of Physics, National Cheng Kung University, Taiwan

⁶ Taiwan Consortium of Emergent Crystalline Materials, Ministry of Science and Technology, Taipei, Taiwan

⁷ Department of Solid-State Physics, Gdansk University of Technology, Poland

⁸ College of Science, Institute of Materials Physics and Chemistry, Nanjing Forestry University, P. R. China

e-mail: mauri@iom.cnr.it; antonio.politano@univaq.it; piero.torelli@elettra.eu

Unveiling the Potential of Cobalt Ditelluride Topological Dirac Semimetal in Terahertz Photodetection

Elettra | APE-LE

THz (Terahertz) radiation has unique properties such as no radiation damage to human tissues, penetrability to most dielectric materials, and fingerprint identification of innumerable molecules through their characteristic spectroscopic peaks. As a result, THz radiation has shown great potential in a wide variety of applications such as homeland security and imaging, materials diagnostics, biology and medical sciences, information and communication technology. However, due to the lack of reliable THz sources and detectors working at room temperature, the THz region is the most elusive in the electromagnetic wave spectrum, known as the “THz gap”. Therefore, the development of new materials for THz photodetectors is an active area of research with many challenges remaining. Quantum materials represent a viable solution for next-generation THz photodetection. In the rapidly evolving world of quantum materials, the discovery and exploration of topological semimetals have opened a new realm of possibilities. These materials, which host a variety of quasiparticles such as Dirac, Weyl, and other exotic fermions, have been the focus of intense research due to their unique electronic and optical properties. One such material that has recently caught the attention of researchers is CoTe₂ (cobalt ditelluride), a type-II Dirac semimetal. CoTe₂ is particularly interesting, due to its strong spin-orbit coupling and broken inversion symmetry, which give rise to unique properties that can be harnessed for practical applications. An international team involving researchers from Italy, China, Spain, India, and Taiwan has delved into the study of CoTe₂ topological Dirac semimetal with spin-ARPES experiments at the APE-LE beamline and its potential in the field of THz photodetection, by exploiting the NLHE (Non-Linear Hall effect) in CoTe₂ topological Dirac semimetal. The NLHE refers to the second-order transverse current induced by an applied alternating electric field,

which is indicative of the topological properties of inversion-symmetry-breaking crystals. The observation of second-order NLHE in CoTe₂ under time-reversal symmetry implies significant implications for the development of room-temperature THz rectification devices. In practical terms, this means that CoTe₂ could be used to create THz photodetectors that operate without the need for semiconductor junctions or bias voltage.

A SHG (Second-Harmonic Generation) experiment was used to study the second-order response at microwave and THz frequencies and determine the symmetry of the material. SHG measurements were performed using femtosecond laser pumping technology, as shown in Fig. 1 (a). A comparative measurement of the SHG from CoTe₂ and the mica substrate was conducted under 860 nm illumination, as depicted in Fig. 1 (b). The observation of an SHG signal indicates symmetry breaking at the surface. The polarization-dependent second-harmonic signal indicates strong anisotropy due to inversion symmetry breaking. The presence of type-II Dirac fermions in bulk CoTe₂ was inferred from the presence of topologically protected surface states with time-reversal symmetry in spin-ARPES, as shown in Fig. 1 (g-j). The orbital-resolved band structure along the Γ -A direction in Fig. 1 (d) indicates that the Dirac band crossing is ascribed to Te-5p orbitals.

Importantly, room-temperature THz rectification was observed without the need for semiconductor junctions or bias voltage, demonstrating the potential of CoTe₂ for nonlinear photodetection applications. The fabricated CoTe₂-based detectors showed a photoresponsivity over 0.1 A W⁻¹, a response time of approximately 710 ns, and a mean noise equivalent power of 1 pW Hz^{-1/2} at room temperature. The superb performance of the THz nonlinear Hall rectifier in terms of speed, sensitivity, and bandwidth could have practical applications in various fields. These results open a new pathway

for high-efficiency photodetection using materials with strong spin-orbit coupling and inversion symmetry breaking, with potential applications in communication, sensing, and infrared/THz photonics. The generation of a nonlinear THz photoresponse based on a second-order nonlinear Hall rectifier without the need for semiconductor junctions could provide a new approach to overcoming the limitations of infrared/THz photonics. Finally, considering the need of ambient stability for THz photodetectors, the team assessed by NAP-XPS (Near Ambient Pressure X-ray Photoelectron Spectroscopy) the effect of air exposure on CoTe₂, observing that even a short exposure to air could induce the formation of a new component in the Co-2p spectra. This new component, recorded at a Binding Energy (BE) of 780.5 eV, was attributed to the formation of Co-O. The study also revealed that the oxide layer formed due to air exposure acted as a surface passivation layer, preserving the transport properties of the bulk crystal over time. In conclusion, the results of this study represent an exciting development in the field of topological physics and infrared/THz photonics. Further research is needed to fully understand the potential implications and applications of these findings. The exploration of the NLHE in newly emerging topological quantum materials could lead to even more exciting discoveries in the future.

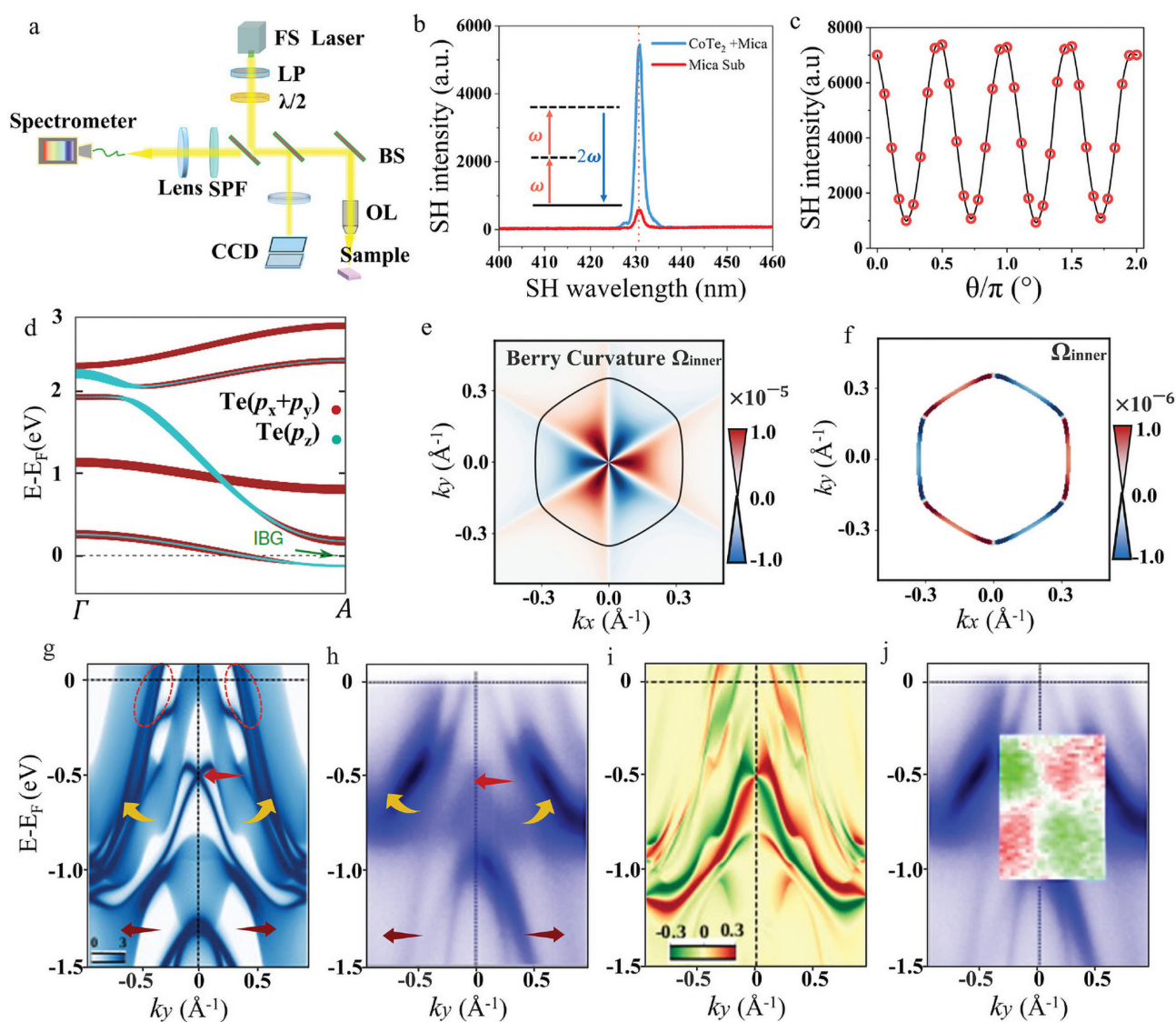


Figure 1. (a) The SHG measurement setup. (b) Measured spectra of the SHG from CoTe₂ and the mica substrate. (c) Dependence of SHG emission on the polarization of the pumping laser. (d) Orbital resolved bulk band dispersion of CoTe₂ along the Γ -A direction. (e) Schematic of the calculated Berry curvature distribution of the topological surface states on the whole Brillouin zone. (f) The calculated Berry curvature distribution over the Fermi surface. (g) Density functional theory-calculated momentum-resolved spectral function plots along the direction. (h) Experimental ARPES spectra. (i, j) The calculated and experimental spin texture of the surface bands.

Original paper

Z. Hu et al., *Adv. Mater.* **35**, 209557 (2023);
DOI:10.1002/adma.202209557

Z. Hu^{1,2}, L. Zhang^{1,3}, A. Chakraborty⁴, G. D'Olimpio⁵, J. Fujii⁶, A. Ge^{1,2}, Y. Zhou^{1,2},
C. Liu³, A. Agarwal⁴, I. Vobornik⁶, D. Farias^{7,8}, S.-W. Wang^{1,2}, W. Hu^{1,2}, X. Chen^{1,2},
W. Lu^{1,2}, L. Wang^{1,2}

¹ State Key Laboratory of Infrared Physics, Shanghai Institute of Technical Physics, Chinese Academy of Sciences, Shanghai, China

² University of Chinese Academy of Sciences, Beijing, China

³ College of Physics and Optoelectronic Engineering, Hangzhou Institute for Advanced Study, University of Chinese Academy of Sciences, Hangzhou, China

⁴ Department of Physics, Indian Institute of Technology Kanpur, Kanpur, India

⁵ Department of Physical and Chemical Sciences, University of L'Aquila, L'Aquila, Italy

⁶ TASC Laboratory, IOM-CNR, Trieste, Italy

⁷ Department of Condensed Matter Physics and "Nicolás Cabrera" Institute, Universidad Autónoma de Madrid, Madrid, Spain

⁸ IFIMAC, Universidad Autónoma de Madrid, Madrid, Spain

e-mail: antonio.politano@univaq.it

Winding of electrons in the quantum world

Elettra | APE-LE

What makes an orange different from a coffee mug?

Let's take two objects and let's transform one into another without making or removing holes. If such transformation is possible, those objects share the same "topology". Therefore, topologically-speaking, a donut is identical to a coffee mug (1 hole), but it is different from a tangerine or a tennis ball (zero holes). This geometrical concept has been used also by physicists to describe the electronic structures of solid state systems: A metal is a material where the electrons of the valence and conduction bands overlap without discontinuities (no gaps/holes). Instead, a semiconductor or an insulator will have an energy gap, separating the valence from the conducting band.

However, there are systems, so-called topologically non-trivial, which falls in between the standard classification of metals and insulators. These systems have properties where both electrons and spins are strongly entangled, and give rise to the appearance of novel phenomena, highly desired for spintronics applications. The discovery of topological materials marks one of the biggest milestones in condensed matter physics because they can be tailored to host currents which are robust against disorder and various external conditions. Such currents, so-called spin-currents, thus enable non-volatile processes to take place with high efficiency and without dissipation.

One of the main parameters related to topology and which describes 'how the electrons wind' around the space where they live is called Berry-curvature and could deepen our understanding on topological quantum matter drastically. A group of scientists has measured for the first time this quantum parameter, opening a potential pathway to understanding, studying, and potentially controlling the topology of quantum materials. This research is now published in Nature Physics.

In order to perform this research, the beamline APE-LE at the Elettra

synchrotron was used, thanks to the availability of circularly polarized synchrotron radiation and the electron spin-detector present at the end station. By shining the light on the sample with circular polarization we are able to couple directly to the angular- and orbital-momentum of the electrons, while by filtering the photoemitted electrons according to their spins we can probe how the spins are oriented. Effectively, this methodology can be used to track what is known as "spin-Berry curvature".

In Fig.1, the main finding of the study is reported. DFT (Density Functional Theory) calculations (Fig.1 a-b) can be used, first of all, to explain the phenomenology that was experimentally discovered: As shown in the simplified version of Fig. 1a, the kagome system used has a Dirac cone similar to the one reported for graphene. Together with this cone, a flat band is also present. These two features are a peculiarity in common to all kagome metals. The minimum of the Dirac cone (at the point called 'I') is separated from the flat band by an energy gap. The latter is predicted to be topological. The same scenario is shown in Fig. 1b in a realistic picture. The experiment will be therefore aimed at demonstrating the topological nature of that gap.

This was done in the present research: by reversing the polarization chirality of the light, the spin character is flipped too (Fig.1 c-d) and this results in a circular dichroism (Fig.1 e) with nearly 100% signal. The latter is the ultimate proof of the topological nature of the states which form the gap.

The researchers, as a proof of principle, have placed the incoming synchrotron light within a mirror plane of the crystal and measured in the centre of the Brillouin zone, where the matrix elements are zero. This experimental geometry is crucial to the present experiment: by doing this in fact it was possible to remove the contribution given by the geometrical matrix elements, to access directly a 'pure'

signal from the Berry curvature, for the first time.

The researchers have performed this study on other members of the kagome family and they have shown that the topological character is ubiquitous to all of them, as it was previously suggested by the theoretical calculations. It is important to stress that this study has implications for understanding the relationship between curvature and topology. The importance of the Berry-curvature in the description of topology is a concept dear to the cold atoms community. The idea of this branch of physics is to 'freeze' a few atoms down to very low temperatures (from which the name cold-atoms) to build artificial lattices that mimic clean and simple versions of particular structures, i.e. honeycomb, hexagonal, kagome, Lieb. Cold-atoms experiments have shown an immense potential: They demonstrated how to measure the Berry curvature by detecting with circularly polarized light the "*winding of the eigenstates across the Brillouin zone*". However, the detection of the Berry-curvature in real materials is more challenging than in optical lattices: for a multi-orbital system, where very often electronic bands are fully or partially spin-degenerate, observing the spin-projection is required to get a signal different from zero.

The study performed at Elettra is the first on a real material.

This work, in summary, sheds light on one of the experimentally most elusive quantities tightly connected to the concept of topology in quantum matter.

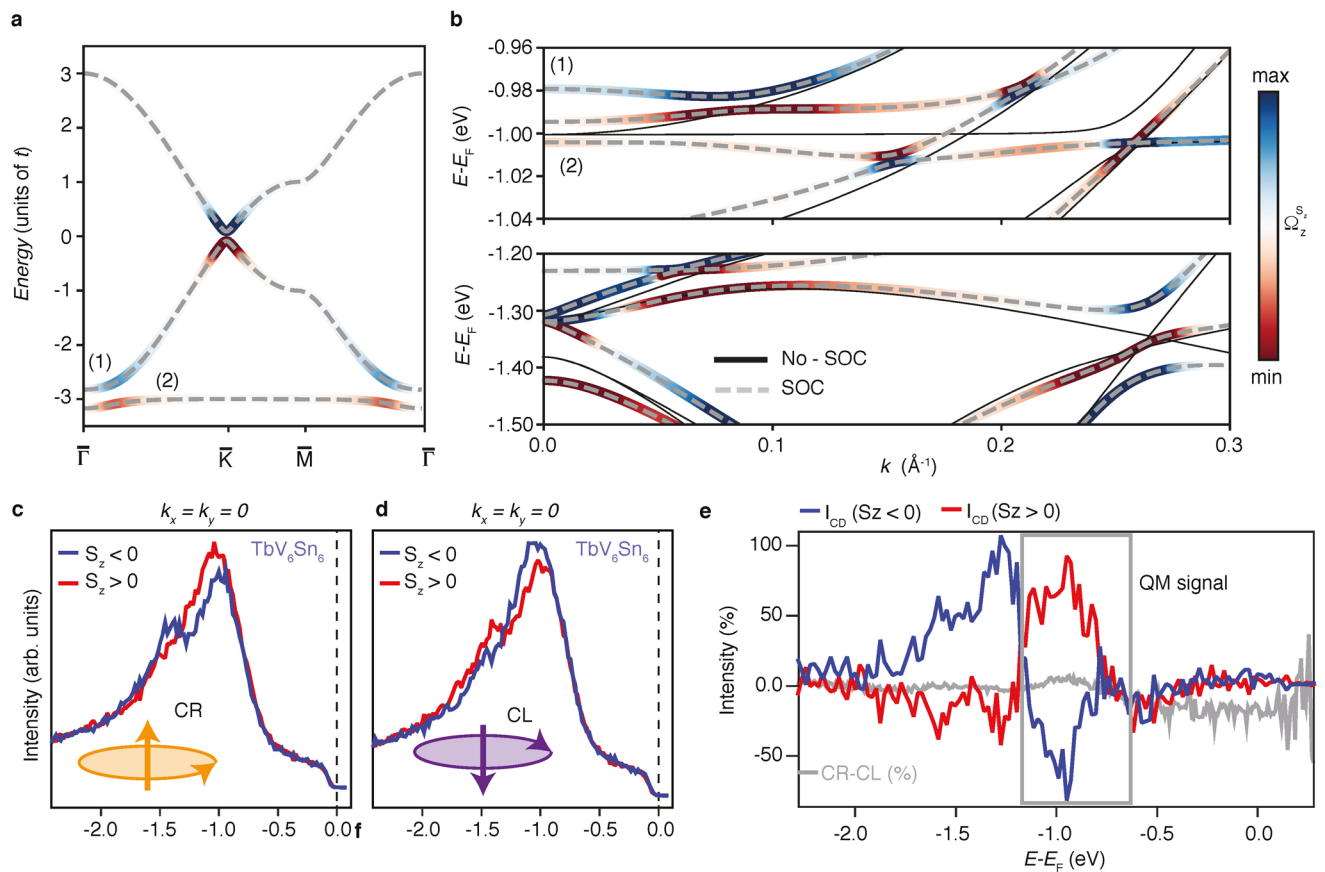


Figure 1. (a) Calculations of the spin-Berry curvature for a simplistic kagome lattice performed by using density functional theory (DFT). The blue and red colours represent the minimum and maximum value of the spin-Berry curvature. (b) Same as (a) performed for the real material TbV_6Sn_6 . (c) Real measurements performed for spin up (red) and spin down (blue) species with circular left and (b) circular right light. As a result of the measurements, the (e) circular dichroism resolved in spin is plotted (for both species) along with the integrated value (gray line), which is significantly smaller.

Original paper

D. Di Sante *et al.* *Nat. Phys.* **19**, 1135 (2023).
DOI:10.1038/s41567-023-02053-z

D. Di Sante¹⁻², C. Bigi³, P. Eck⁴, S. Enzner⁴, A. Consiglio⁴, G. Pokharel⁵, P. Carrara⁶⁻⁷, P. Orgiani⁸, V. Polewczyk⁸, J. Fujii⁷, P.D.C. King³, I. Vobornik⁷, G. Rossi⁶⁻⁷, I. Zeljkovic⁹, S.D. Wilson⁵, R. Thomale⁴, G. Sangiovanni⁴, G. Panaccione⁷, F. Mazzola⁷⁻¹⁰

¹ Department of Physics and Astronomy, University of Bologna, Bologna, Italy

² Center for Computational Quantum Physics, Flatiron Institute, New York, NY, USA

³ School of Physics and Astronomy, University of St Andrews, St Andrews, UK

⁴ Institut für Theoretische Physik und Astrophysik und Würzburg-Dresden Cluster of Excellence ct.qmat, Universität Würzburg, Würzburg, Germany

⁵ Materials Department, University of California Santa Barbara, Santa Barbara, CA, USA

⁶ Dipartimento di Fisica, Università degli Studi di Milano, Milano, Italy

⁷ Istituto Officina dei Materiali, Consiglio Nazionale delle Ricerche, Trieste, Italy

⁸ TASC Laboratory, IOM-CNR, Trieste, Italy

⁹ Department of Physics, Boston College, Chestnut Hill, MA, USA

¹⁰ Department of Molecular Sciences and Nanosystems, Ca' Foscari University of Venice, Venice, Italy

e-mail: domenico.disante@unibo.it ; sangiovanni@physik.uni-wuerzburg.de
panaccione@iom.cnr.it ; federico.mazzola@unive.it

Unveiling the Potential of Gallium Telluride in Electrochemistry, Photochemistry, and Gas Sensing

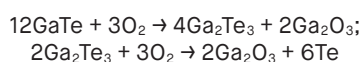
Elettra | BACH, Nanospectroscopy

Among the atlas of 2D materials, vdW (van der Waals) semiconductors deserve particular attention due to their unique characteristics and their complementarity with respect to the forefather of 2D materials, i.e., graphene, lacking a band gap.

One of such materials which has been garnering attention in the realm of vdW semiconductors is Gallium Telluride (GaTe). GaTe exhibits great potential for utilization in photonic and optoelectronic devices.

As a matter of fact, a vdW semiconductor showing a direct band gap already in the bulk would be highly desirable.

GaTe crystallizes in a monoclinic structure (space group B2/m) with Te-Ga-Ga-Te stacking. When exposed to oxidative environments, bulk GaTe is transformed into a Ga₂O₃ skin, upon the following reaction pathway:



Its rapid degradation in ambient atmosphere has been seen as a drawback for its application in devices. But what if this inevitable degradation could be turned into an advantage?

An international multidisciplinary team at the Elettra Synchrotron has found that when GaTe is exposed to oxidative environments, it transforms into a Ga₂O₃ skin. This transformation, which was once seen as a disadvantage, is now being viewed as a potential catalyst for new applications.

The team used XPS (X-ray Photoemission Spectroscopy) and XPEEM (X-ray Photoemission Electron Microscopy) to assess the oxidation of the material. They found that while the stoichiometric GaTe sample remained chemically inert towards oxygen and water, defective GaTe surfaces displayed gallium-oxide and Ga₂Te₃ components. This is evident in Figure 1 LEFT panels, which shows the Ga-3d and Te-3d core levels for as-cleaved GaTe crystal surface and its

aging upon exposure to air for 1 min, 10 min, 2h, 21 h, 7 days.

Considering the potential beneficial effect of increasing the surface-to-volume ratio in nanosheets compared to the bulk crystals for applications in catalysis and gas sensing, the stability of exfoliated GaTe nanosheets was assessed by synchrotron-based XPEEM, which enables the acquisition of XPS spectra with nanoscale spatial resolution. GaTe nanosheets can be easily noticed as dark areas in the substrate Si-2p signal in the XPEEM image in Figure 1 RIGHT. The flakes appear bright in the Te-4d (Figure 1 RIGHT panel b) and Ga-3d XPEEM images. The analysis of μ -XPS spectra, collected with low-energy photons to improve surface sensitivity, indicated that GaTe nanosheets are mostly oxidized, with gallium-oxide components dominating the Ga-3d spectra.

The formed gallium-oxide skin is amorphous, as inferred by the absence of Ga₂O₃ diffraction rings in the SAED (Selected area diffraction) patterns. This conclusion is supported by the HR-TEM (High-Resolution Transmission Electron Microscopy) micrograph recorded in the proximity of the nanosheet border. Definitely, the nanosheet was enveloped by an amorphous shell with a thickness of ≈ 3.5 nm, while its central part consisted of a mixture of crystalline Te nanograins and amorphous material. Similar results were obtained on the TEM specimen freshly prepared from the same liquid suspension after 3 months. Considering the presence of the amorphous Ga₂O₃ skin on the surface of GaTe (both bulk and nanosheets), the catalytic activity of GaTe-based systems on the HER (Hydrogen Evolution Reaction) was evaluated. Whereas the pristine defect-free bulk GaTe is unsuitable for HER, due to an energy cost, which even increases in the monolayer regime, defective GaTe_{0.97} is instead competitive with state-of-the-art catalysts Pt. Considering the reduction of cost of raw materials by 160 times compared to Pt-based electrocatalysts,

the self-assembled Ga₂O₃/GaTe heterostructure represents a suitable catalyst for HER in acidic media. But the potential of GaTe doesn't stop there. The wide-band-gap oxide skin formed over narrow-band-gap GaTe upon air exposure makes the self-assembled gallium-oxide/gallium-telluride heterostructure suitable for light harvesting. This opens up the possibility of GaTe-based photocatalytic devices. As the magnitude of endothermic steps of HER over Ga₂O_{3-x} is manifestly smaller (more than 0.5 eV) than over GaTe_x substrates, the Ga₂O_{3-x} skin could be proposed as the chemically active part of GaTe-based photocatalytic devices. Photocatalysis on Ga₂O₃/GaTe interface can be modelled as a two-steps process. In the first step, a photo-induced transition of electrons occurs from valence to conduction bands of the GaTe_x substrate. In the second step, photo-generated electrons migrate from conduction bands of the GaTe_x substrate to the states with lower energies in the conduction band of the Ga₂O_x skin, where these electrons participate in electrochemical reactions on chemically active sites on the surface. Finally, the Ga₂O₃/GaTe interface can be also considered as a perspective material for gas sensing. The sensing properties of GaTe are enhanced by surface oxidation, which induces an increase of the area of charge redistribution after adsorption of analytes, such as water, ammonia, and nitrogen dioxide. Remarkably, Ga₂O₃/GaTe enables high-temperature gas sensing at operational temperature as high as 600°C, so as to enable its use for detection of gaseous species in combustion processes. All these findings pave the way for a novel generation of (photo-) electrocatalysts and gas sensors, based on self-assembled heterostructures produced by exploiting the natural interaction of van der Waals semiconductors with air.

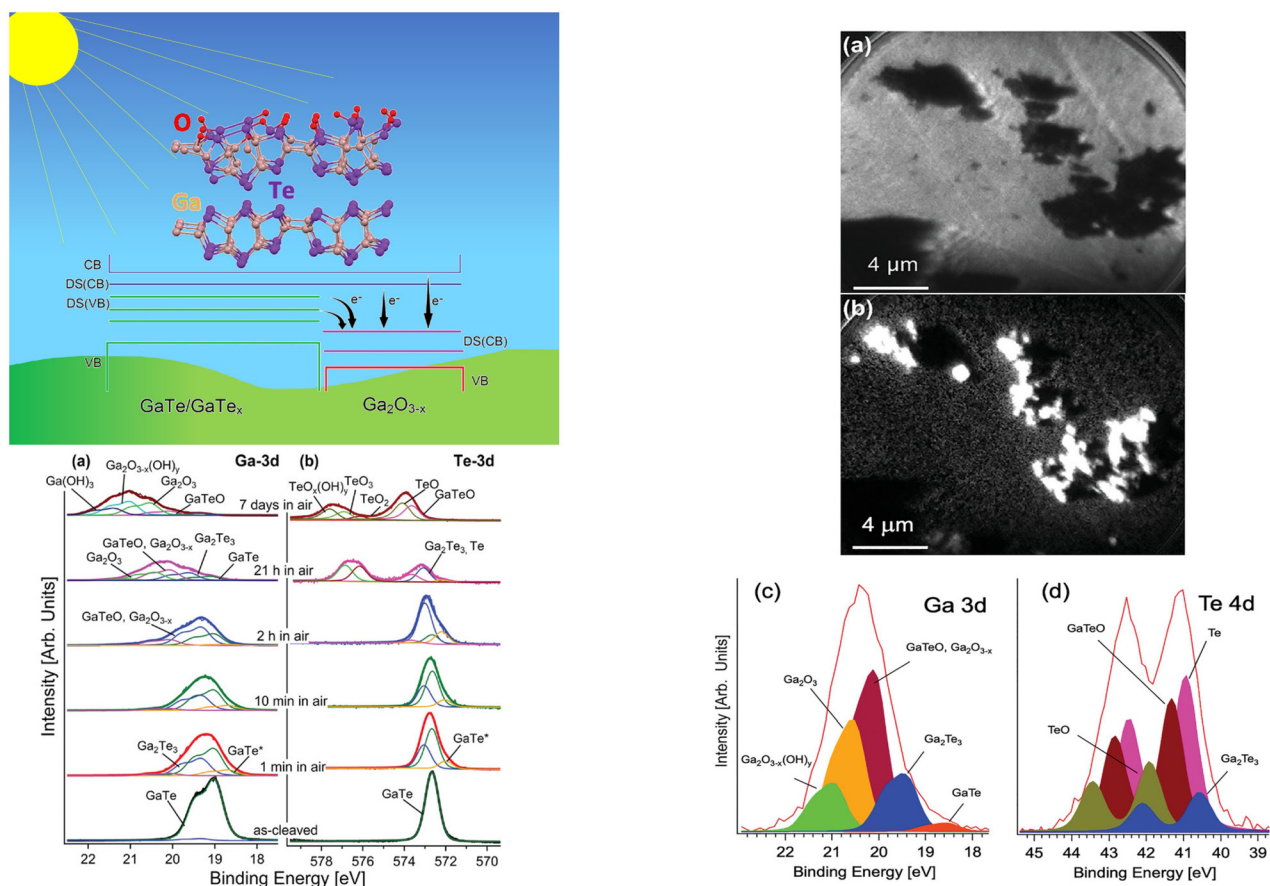


Figure 1. Figure LEFT panels: Scheme of the possible use of the self-assembled gallium-oxide/gallium-telluride heterostructure for light harvesting in photocatalytic devices (a) Ga-3d and (b) Te-3d core levels (XPS) for as-cleaved GaTe crystal surface and its aging upon exposure to air for 1 min, 10 min, 2h, 21 h, 7 days. RIGHT panels: (a, b) XPEEM images of exfoliated GaTe nanosheets at the (a) Si-2p, (b) Te-4d core levels. (c, d) XPS spectra in the region of (c) Ga 3d and (d) Te 4d core levels. Reproduced with permission under a Creative Commons Attribution-NonCommercial 4.0 International Public License CC BY-NC 4.0 © 2022 The Authors. *Advanced Materials Interfaces* published by Wiley-VCH GmbH.

Acknowledgments

CG and MCI acknowledge funding through the contract POC 332/390008/29.12.2020-SMIS 109522 AP thanks CERIC-ERIC for granting access to the facilities in Trieste, Prague, and Magurele. FB and SN acknowledge support from MUR (EuroFEL project). Open Access Funding provided by Università degli Studi dell'Aquila within the CRUI-CARE Agreement.

Original paper

F. Bondino *et al.*, *Adv. Funct. Mater.* **32**, 2205923 (2022). DOI: 10.1002/adfm.202205923

F. Bondino¹, S. Duman², S. Nappini¹, G. D'Olimpio³, C. Ghica⁴, T.O. Mentes⁵, F. Mazzola¹, M.C. Istrate⁴, M. Jugovac⁵, M. Vorokhta⁶, S. Santoro⁷, B. Gürbulak⁸, A. Locatelli⁵, D.W. Boukhvalov⁹, A. Politano³

¹ IOM-CNR, Trieste, Italy

² Basic Sciences Department, Faculty of Sciences, Erzurum Technical University, Erzurum, Turkey

³ Department of Physical and Chemical Sciences, University of L'Aquila, L'Aquila (AQ), Italy

⁴ National Institute of Materials Physics, Atomistilor, Magurele, Romania

⁵ Elettra - Sincrotrone Trieste S.C.p.A., Trieste, Italy

⁶ Charles University, Prague, Czech Republic

⁷ Department of Environmental Engineering (DIAM), University of Calabria, Rende, Italy

⁸ Department of Physics, Atatürk University, Erzurum, Turkey

⁹ College of Science, Institute of Materials Physics and Chemistry, Nanjing Forestry University, Nanjing, P. R. China

e-mail: antonio.politano@univaq.it ; bondino@iom.cnr.it

Creating high-resolution fluorescent micropatterns of 3D-oriented porous films

Elettra | DXRL

MOFs (Metal-Organic Frameworks) are a family of extended microporous crystalline materials, composed of metal ions connected by organic ligands. This building block approach used for their construction offers high flexibility for the design of MOFs with different chemical and physical properties, such as chemical stability, pore volume, accessible surface area, electrical conductivity, refractive index, and fluorescence. This precise control over their chemical functionality and network structure makes MOFs attractive materials for device fabrication including chemical sensors, microelectronic components, and photonic devices. To become compatible with the current fabrication technology, a two-step approach is desirable: the deposition of supported MOF films and the subsequent spatial control of the MOF crystals on the substrate (positioning) with micrometer precision (micropatterning). A recent advance in MOF film research showed that oriented polycrystalline MOF films can be prepared at commercially relevant scales. These films were synthesized from pre-aligned metal hydroxide nanostructures ($\text{Cu}(\text{OH})_2$ NBs (nanobelts)) where the ceramic material simultaneously acts as a metal source and directs the epitaxial growth of the aligned MOF crystals. In this way, it is possible to obtain films of fully "3D-oriented" MOF crystals grown on aligned ceramic substrates (Fig. 1a). However, the fabrication of micropatterns composed of 3D-oriented crystals had not been shown. Remarkably, the combination of anisotropic properties originated from the 3D-orientation with precise micropatterning protocols would be highly desirable in porous material-based technologies where directional properties are needed. In this work, we applied the DXRL (Deep X-Ray Lithography) technique to obtain oriented MOF polycrystalline micropatterns (Fig. 1a). Previous works also performed at the DXRL beamline

of Elettra Synchrotron (Trieste) by R. Ameloot and co-workers showed that this technique could be used for the patterning of halogen-functionalized MOF crystals. Inspired by this seminal work, we employed a Br-functionalized linker, 2,5-dibromoterephthalic acid (Br_2BDC), in combination with BDC (1,4-benzenedicarboxylic acid) and DABCO (1,4-diazabicyclo[2.2.2]octane) to obtain 3D-oriented MOF crystals that were sensitive to the x-ray radiation. Specifically, highly aligned $\text{Cu}(\text{OH})_2$ nanobelt films were used as a sacrificial template to induce the heteroepitaxial growth of $\text{Cu}_2\text{L}_2\text{DABCO}$, where $\text{L} = \text{Br}_2\text{BDC}$ and/or BDC, with in-plane orientation (Fig. 1a). Previous works showed that MOFs containing C-Cl bonds would experience a hard x-ray-induced cleavage after exposure, which allowed the resist-free patterning of MOF crystals. In our case, Br_2BDC was selected because bromine will result in a large number of x-ray photons absorbed and a lower C-Br dissociation energy compared to chlorine (C-Cl). We utilized a mixed-linker ($\text{Br}_2\text{BDC} + \text{BDC}$) strategy to ensure that the resulting MOF films had in-plane orientation and homogeneity, as the fully brominated MOF did not afford a uniform continuous MOF film. A mixture of 94% Br_2BDC and 6% BDC (in molar ratio) was successfully applied to obtain radiation sensitive MOF crystals forming a continuous and oriented film (Fig. 1a and c). In order to achieve the right patterning conditions, a dose matrix was performed (i.e. exposure of the MOF films to increasing x-ray doses). On these test samples, we evaluated the chemical and structural changes in the exposed areas by infrared spectroscopy and x-ray diffraction. After finding the proper surface dose, we explored different etching protocols until the conditions were found to produce clearly defined patterns. The finally chosen conditions were 1748 J cm^{-2} and an etching solution composed of a mixture of MeOH, H_2O and acetic acid. In these conditions,

the oriented MOF films were exposed to hard x-rays through a lithography mask (DXRL), and then the MOF patterns were developed by selective dissolution of the irradiated area in the etching solution (Fig. 1a). We were able to achieve well-defined MOF patterns of different shapes and sizes, from tens to hundreds of micrometers (Fig. 1 b). A close inspection by SEM (Scanning Electron Microscopy), performed at CNR-IOM, shows that the morphology of the MOF crystals in the unexposed areas remains intact, while the etched areas show the presence of residual $\text{Cu}(\text{OH})_2$ NBs on the substrate (Fig. 1 c).

The quality of our MOF patterns can be further demonstrated by illuminating the samples with a laser: the patterns can function as diffraction gratings, showing the optical quality of our samples (Fig. 1d). To showcase the anisotropy-derived properties of these patterns, we explored the incorporation of a fluorescent molecule (4,4-difluoro-4-bora-3a,4a-diaza-s-indacene, BODIPY) within the oriented pores of the MOF framework (Fig. 1a). We employed two different strategies for the incorporation of BODIPY to the framework: i) *in situ* encapsulation during synthesis and subsequent patterning, and ii) post-infiltration of already patterned samples. Both strategies were successful to obtain fluorescent micropatterns, as revealed by Confocal Laser Scanning Microscopy (CLSM) (Fig. 1b). Since the pores are oriented, these infiltrated MOF patterns show anisotropic fluorescence properties. The angular dependence of the fluorescent patterns was investigated with a fluorescence microscope equipped with a polarizer (Fig.1d). This anisotropic optical property could be used in switchable photonic devices. The combination of microporosity, preferential orientation, and positioning of the MOF crystals makes this a new class of promising nanomaterials for the development of new sensing and optoelectronic devices.

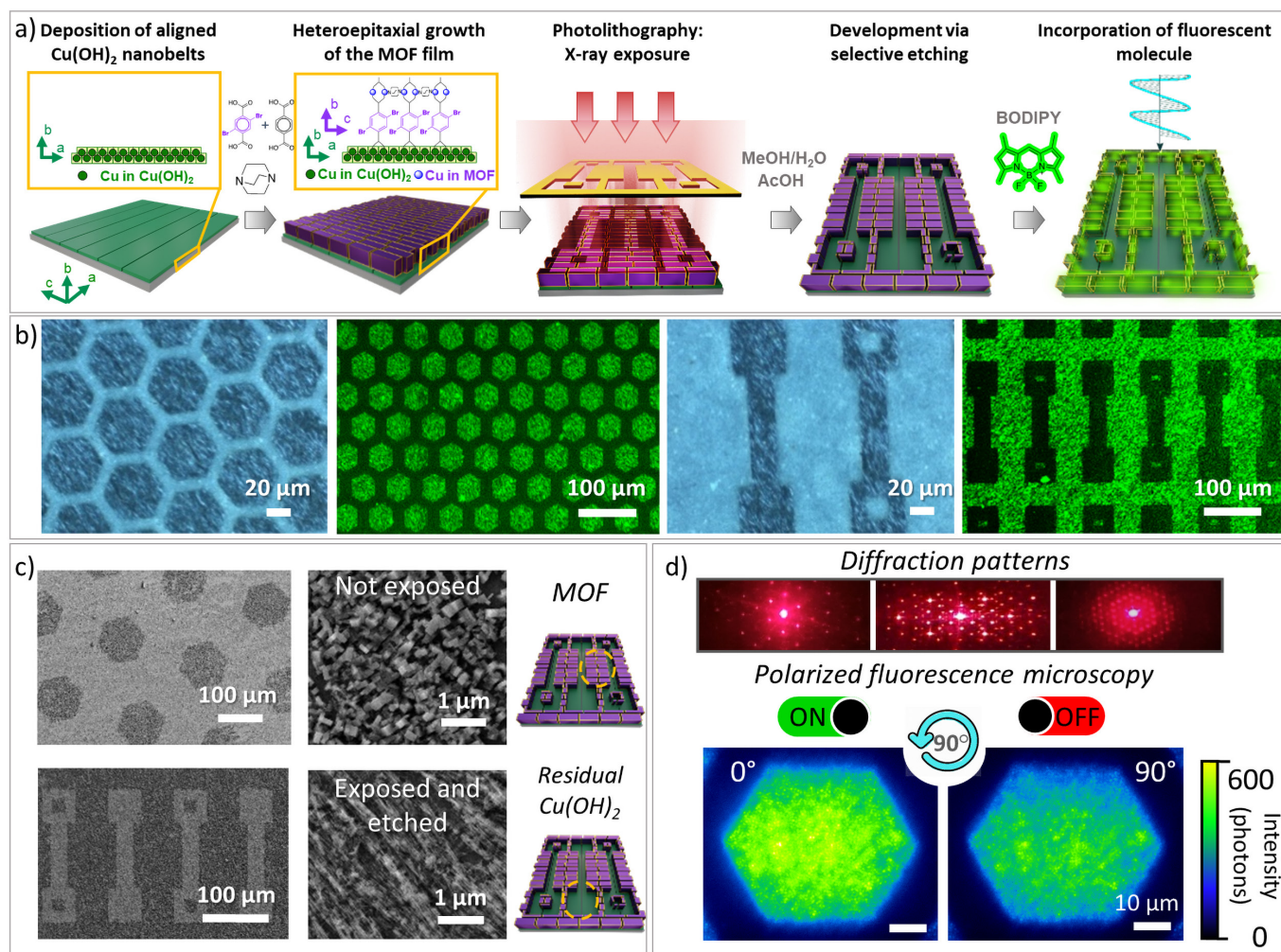


Figure 1. (a) Schematic of the different fabrication steps to obtain 3D-oriented MOF patterns by DXRL; (b) Polarized optical microscopy and CLSM images of MOF patterns with different shapes and sizes; (c) SEM images of the MOF patterns and of the exposed and unexposed areas; (d) Diffraction patterns obtained by illuminating the MOF patterns on transparent substrates with a red laser (top); anisotropic response obtained by rotating 90° the polarization in fluorescence microscopy (bottom). Figures were adapted with permission from M.de J. Velásquez-Hernández, M. Linares-Moreau, *et al.*, *Adv. Mater.* **35**, 25 (2023).

Acknowledgments

M. de J.V-H and M.L-M contributed equally to this work. This work has received funding from the European Research Council under the European Union's Horizon 2020 Programme (FP/2014-2020)/ERC Grant Agreement No. 771834—POPCRYSTAL and TU Graz Lead Project (LP-03). The authors acknowledge CERIC-ERIC for access to the DXRL beamline experimental facilities at Elettra Sincrotrone and financial support.

Original paper

Velásquez-Hernández, M. de J., Linares-Moreau, M., *et al.*, *Adv. Mater.* **35**, 25 (2023); DOI:10.1002/adma.202211478

M.d.J. Velásquez-Hernández¹, M. Linares-Moreau¹, L.A. Brandner¹, B. Marmiroli², M. Barella³, G.P. Acuna³, S.D. Zilio⁴, M.F.K. Verstreken⁵, D.E. Kravchenko⁵, O.M. Linder-Patton⁶, J.D. Evans⁶, H. Wiltsche⁷, F. Carraro¹, H. Wolinski⁸, R. Ameloot⁵, C. Doonan⁶, P. Falcaro¹

¹Institute of Physical and Theoretical Chemistry, Graz University of Technology, Graz, Austria

²Institute of Inorganic Chemistry, Graz University of Technology, Graz, Austria

³Department of Physics, University of Fribourg, Fribourg, Switzerland

⁴IOM-CNR, Trieste, Italy

⁵Centre for Membrane Separations, Adsorption, Catalysis, and Spectroscopy for Sustainable Solutions (cMACS), KU Leuven, Leuven, Belgium

⁶Department of Chemistry, The University of Adelaide, Adelaide, South Australia, Australia

⁷Institute of Analytical Chemistry and Food Chemistry, Graz University of Technology, Graz, Austria

⁸Institute of Molecular Biosciences, Field of Excellence BioHealth, University of Graz, Graz, Austria

e-mail: paolo.falcaro@tugraz.at ; mlinaresmoreau@tugraz.at

Solid electrolyte interphase composition and distribution in “zero excess” lithium-metal batteries

Elettra | ESCA Microscopy, BEAR

In 2019, John B. Goodenough, M. Stanley Whittingham and Akira Yoshino were awarded the Nobel Prize for the development of the LIBs (Lithium-Ion Batteries) – a secondary battery with very high energy density. One of the key features towards the tremendous success of this battery technology is its high cell voltage of about 4 V. This high cell voltage, however, required the transition from the so far used water-based electrolytes to electrolyte systems based on organic solvents that are characterized by a substantially wider electrochemical stability window. Nonetheless, even these electrolytes are not thermodynamically stable towards the low potential at which the lithium cations are intercalated into the graphite-based negative electrode. The reversible intercalation of lithium cations into graphite has become possible only thanks to the introduction of ethylene carbonate, which initially decomposes when the battery is charged, forming a protective surface layer on the negative electrode that suppresses further electrolyte decomposition – in other words kinetically stabilizes the interface between the negative graphite electrode and the electrolyte. This protective – or passivating – surface layer is commonly referred to as SEI (solid electrolyte interphase).

During the last decades, the LIB was continuously improved, and the energy density increased. However, to meet the enormous energy density requirements of, e.g., electric vehicles and other advanced applications, new cell concepts are required. One possibility is to replace the graphite negative electrode by lithium metal. In combination with common electrode materials for the positive electrode such as $\text{Li}(\text{Ni}_{1-x-y}\text{Mn}_x\text{Co}_y)\text{O}_2$ or LiFePO_4 , though, this means an excess of (costly) lithium in the system, as these electrode materials comprise lithium as well. Accordingly, it has been suggested to achieve further enhanced energy densities by plating the lithium from the positive electrode as metallic lithium

directly on the current collector of the negative electrode, i.e., without providing any “host matrix” like graphite. This concept is also known as “zero excess” LIBs (Lithium-Metal Batteries). However, lithium metal does not deposit homogeneously in a flat layer by default. Instead, tip shapes are growing, which poses a safety risk once they reach the other electrode, resulting in a short circuit. Additionally, such “zero excess” LMBs suffer from parasitic side reactions at the (continuously evolving) electrode | electrolyte interface. These unwanted side reactions with the electrolyte lead to low reversibility, which severely limits the cycle life of the battery cell.

To address these issues, we introduced a thin crosslinked polymer electrolyte interlayer between the copper current collector and the electrolyte with the objectives to (i) homogenize the lithium deposition on the negative electrode current collector and (ii) stabilize the electrode | electrolyte interface by hampering the direct contact between the lithium metal deposited underneath the polymer interlayer and the liquid electrolyte – comparable to the SEI on graphite.

And, indeed, the introduction of the polymer interlayer enabled a greater reversibility of the lithium metal deposition and thus longer cycle life. To understand the origin of this improvement, we performed a detailed *ex situ* analysis of the negative electrode. In addition to the investigation *via* scanning electron microscopy, which showed that the polymer helps to achieve a more homogeneous lithium deposition, the comprehensive *ex situ* analysis encompassed inter alia SPEM (Scanning X-ray Photoelectron Microscopy), i.e. XPS mapping at the ESCAMicroscopy Beamline), and soft XAS (X-ray Absorption Spectroscopy) at the BEAR beamline). By means of SPEM, in other words by collecting XPS spectra at many different points of the sample, the chemical composition and its homogeneity of the topmost layer of the interphase formed on the

copper current collector was studied. Complementarily to this, soft-XAS allowed the identification of the chemical composition of the interphase formed at greater probing depths, thereby providing valuable information across the thickness of the interphase – in other words adding the third dimension to the 2D analysis *via* SPEM, especially when conducting the experiments in total electron and total fluorescence yield mode.

Fig. 1 (a) displays selected XPS detail spectra, acquired at the ESCA Microscopy beamline, of the SEI that formed in the “zero excess” lithium-metal battery without and with the polymer interlayer. For the sample without the interlayer, inhomogeneously distributed lithium carbonate and lithium oxide were detected by SPEM, providing an explanation for the rather poor reversibility and extensive electrolyte decomposition at the electrode | electrolyte interface. The polymer interlayer suppressed the extensive lithium carbonate and lithium oxide formation (the latter is illustrated in Fig. 1 (a)). This observation agrees very well with the soft-XAS data presented in Fig. 1 (b). Whereas the SEI formed without the polymer interlayer shows strong absorption signals from lithium carbonate and/or lithium oxide, the respective absorption signals were negligible in the case of the sample with the polymer interlayer. Instead, a very homogeneous, fluorine-rich SEI formed underneath the polymer (compare Fig. 1 (a,b), which is known to stabilize the electrode | electrolyte interface. These findings imply that adverse side reactions with the electrolyte can be greatly reduced when introducing such polymer interlayer and, thus, enhancing the reversibility of the lithium metal deposition on the negative electrode current collector. Therefore, such a polymer layer is an effective and practical strategy to improve the performance and lifetime of “zero excess” LMBs.

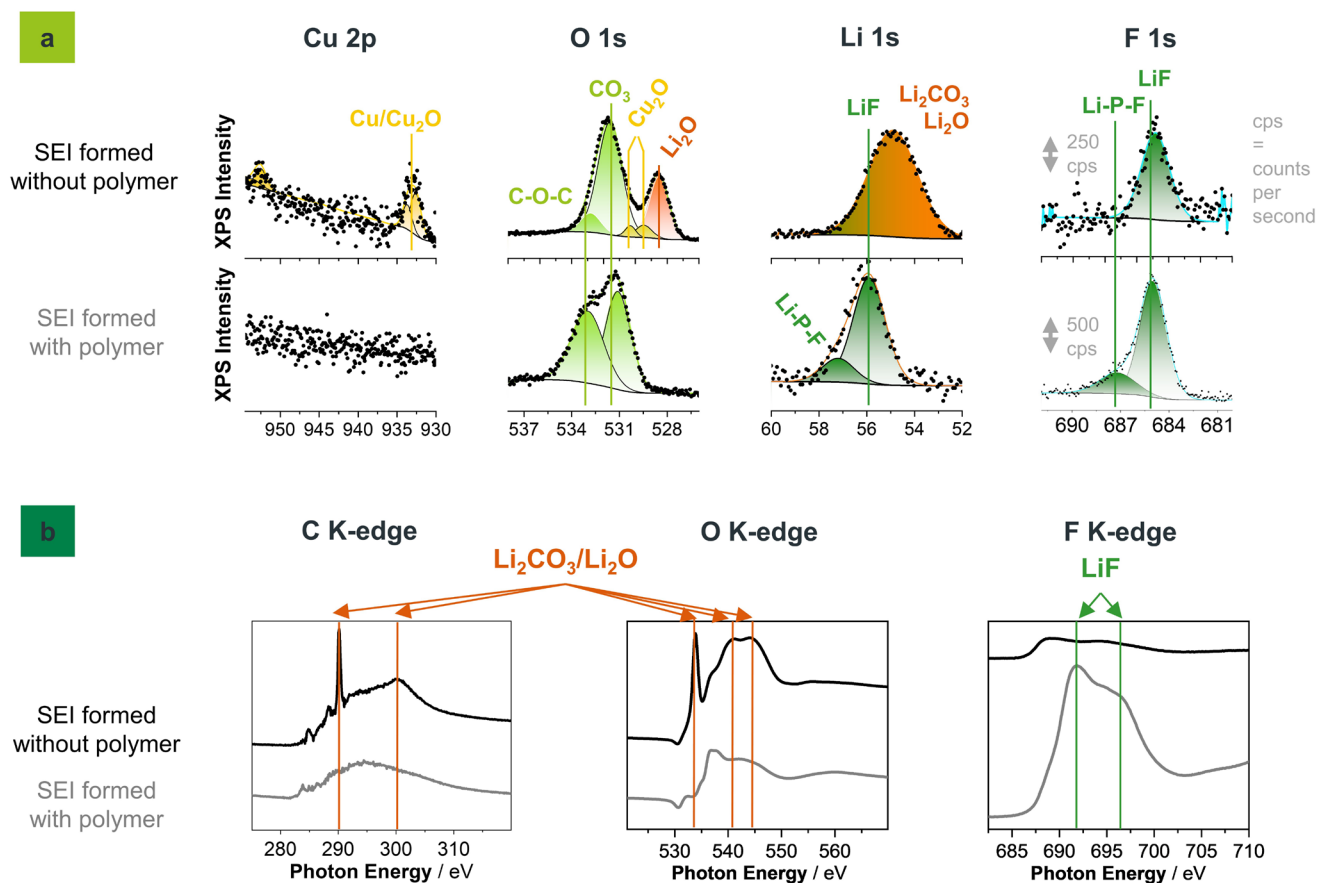


Figure 1. (a) XPS detail spectra from the SPEM experiment of the SEI formed without and with an artificial polymer layer in “zero excess” lithium metal batteries; (b) soft-XAS spectra of the same samples. Figures adapted from K. Geng et al., *J. Electrochem. Soc.* **169** (110521).

Acknowledgments

The authors would like to acknowledge financial support from the Federal Ministry of Education and Research (BMBF) within the HighSafe-II project (03XP0306C) and from the Helmholtz Association. We acknowledge Elettra Sincrotrone Trieste for providing access to its synchrotron radiation facilities, particularly the ESCA Microscopy and BEAR beamline.

Original paper

K. Geng *et al.*, *J. Electrochem. Soc.* **169** (110521) (2022); DOI:10.1149/1945-7111/ac9f74

K. Geng^{1,2}, T. Eisenmann^{1,2}, R. Parmar³, J. Rezvani^{4,5}, R. Gunnella⁶, M. Amati³, L. Gregoratti³, D. Stepien^{1,2}, T. Diemant^{1,2}, D. Bresser^{1,2}

¹ Helmholtz Institute Ulm (HIU), Ulm, Germany

² Karlsruhe Institute of Technology (KIT), Karlsruhe, Germany

³ Elettra - Sincrotrone Trieste S.C.p.A., Trieste, Italy

⁴ Frascati National Laboratory, INFN, Frascati, Italy

⁵ TASC Laboratory, IOM-CNR, Trieste, Italy

⁶ Physics department, University of Camerino, Camerino, Italy

e-mail: dominic.bresser@kit.edu

Unlocking the potential of carbon atomic wires by synchrotron-based UV resonance Raman spectroscopy

Elettra | IUVS

CAWs (carbon atomic wires) have attracted significant attention in the scientific community due to their remarkable mechanical, thermal, and optoelectronic properties, making them highly relevant and versatile compounds for a wide range of applications in various fields. Composed of one-dimensional linear chains of carbon atoms, CAWs offer a structurally simple yet valuable model system for studying fundamental properties of matter, showcasing a practical example of the one-dimensional chain concept commonly found in physics textbooks. One of the exceptional features of CAWs is their high optical absorption capacity, surpassing 105 L/mol/cm, along with sharp and well-resolved electronic transitions in the UV region, strictly dependent on the wire length and terminations. CAWs possess a characteristic collective vibration (or phonon) that involves all the carbon-carbon bonds within the chain. This vibrational feature is closely linked to the other properties of CAWs, due to their strong π -electron conjugation. Raman spectroscopy emerges as a powerful technique to investigate this captivating and fundamental aspect. However, the study of CAWs' vibrational properties presents significant challenges due to their limited stability, often limiting the observation of low-concentrated solutions. Understanding the vibrational and electronic properties of CAWs is crucial for unraveling their unique behavior and exploring their potential applications. By employing advanced characterization techniques and overcoming stability hurdles, researchers aim to unlock the full potential of these intriguing carbon-based nanostructures.

In this study, we analyzed the vibrations of the simplest class of CAWs, called hydrogen-capped polyynes. These chains represent the fundamental model for understanding the behavior of similar structures. To explore their vibrational properties, we employed resonance Raman spectroscopy, a technique

that exploits the strong and selective absorption of UV light by these chains, as highlighted in Fig. 1 (a). Working at the resonance with the excitation wavelength enhances the signal related to the collective vibrations of these chains by several orders of magnitude. While a limited number of laboratory-based laser lines can cover the whole UV range of interest, they lack the precise tunability needed to excite all the UV absorption peaks of CAWs accurately. On the contrary, the remarkable brightness and tunability offered by the IUVS beamline enabled us to collect the complete resonance Raman spectra of these atomic chains.

Fig. 1 (b) displays the resonance Raman spectra of an example of a hydrogen-capped wire with eight carbon atoms (HC_8H). By matching the resonance conditions with different electronic transitions, we were able to detect the fundamental Raman modes (α and β) even from low-concentrated CAWs samples. Additionally, we observed high-order vibrational processes, known as overtones (2α , 3α , 4α , and 5α in Fig. 1 (b)). Analyzing the energy of these overtones allowed us to reconstruct the vibrational structure of the ground electronic state of these compounds with the highest precision so far reached.

In each compound, we have identified the selective enhancement of overtones at specific electronic transitions in each compound – i.e., by tuning the synchrotron-based Raman probe to the different absorption peaks in Fig. 1 (a) – reported in Fig. 2 (a). These findings are crucial for validating one of the fundamental theories in resonance Raman spectroscopy, known as Albrecht's theory. Indeed, by employing this analytical model, we could nicely predict the enhancement of the second- and higher-order peaks, as depicted in Fig. 2 (b), along with the other spectral features.

Moreover, we combined the results coming from UV resonance Raman spectra with UV-Vis absorption data

to estimate the Huang-Rhys factor, as illustrated in Fig. 2(c). This factor quantifies the strength of electron-phonon coupling in crystals. Our analysis revealed that the electron-phonon coupling in CAWS is comparable to that of other carbon nanostructure and organic molecules, employed in nonlinear optical applications and for optical sensors. Furthermore, we found a strong correlation between the magnitude of the electron-phonon coupling and the chain length, representing the short limit of what has been observed in long linear carbon chains (confined carbyne).

In summary, the study of carbon atomic wires offers a unique platform for understating the vibrational properties of conjugated systems and uncovering electron-phonon coupling in one-dimensional materials. Ongoing investigations into phonon anharmonicity aim to refine theoretical models and improve predictions in the future. The research conducted at the IUVS beamline on carbon atomic wires could promise further advancements in developing nonlinear optical and optical sensing devices based on carbon atomic wires, along with carbon-based nanoelectronics. Importantly, the insights gained from our findings may contribute to the development of more accurate models that can describe a wide range of materials beyond carbon atomic wires, including other conjugated systems and one-dimensional structures.

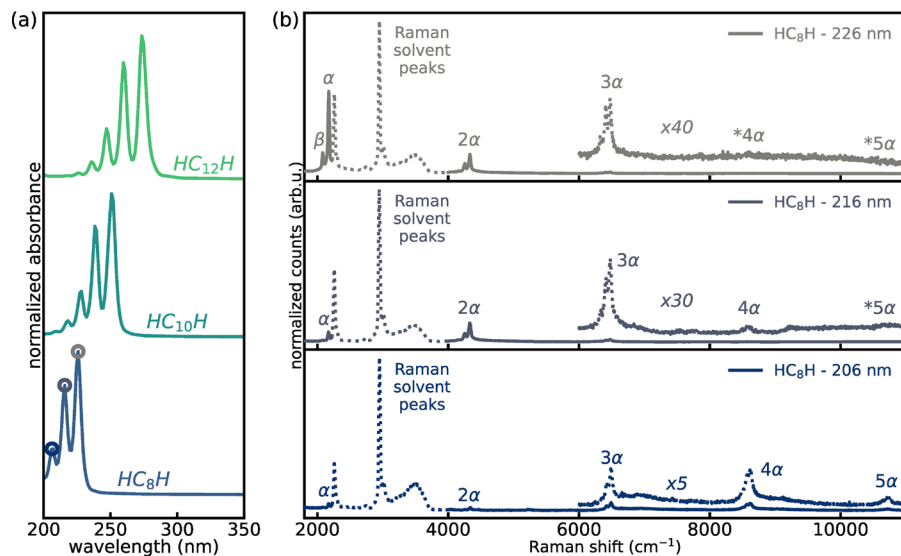


Figure 1. (a) UV-Vis absorption spectrum of hydrogen-capped polyynes with 8 (HC₈H), 10 (HC₁₀H), and 12 (HC₁₂H) carbon atoms. (b) UV resonance Raman spectra of HC₈H at 3 different excitation wavelengths: 226, 216, and 206 nm corresponding to the most intense peaks in its UV-Vis absorption spectrum (colored circles in panel a).

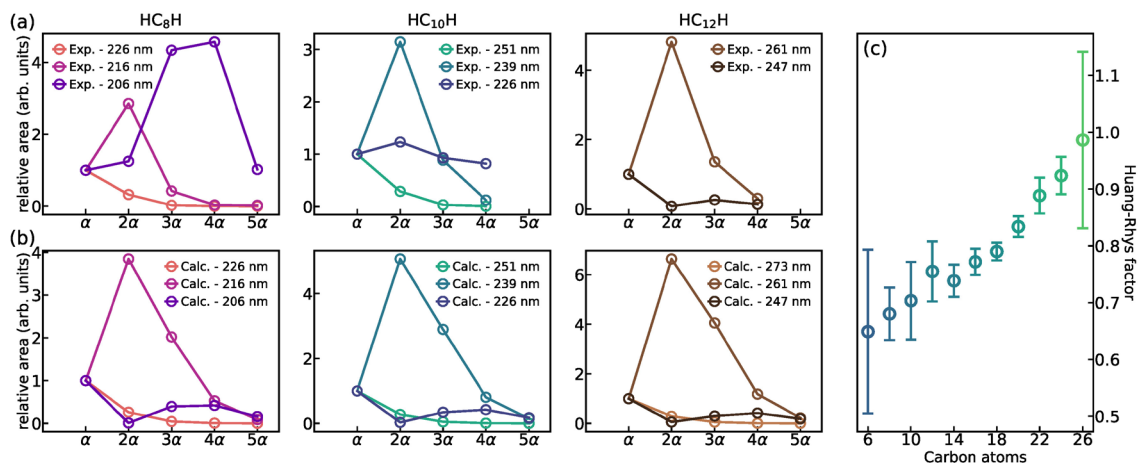


Figure 2. (a) Experimental trend of the area of the overtones of the α mode compared to the first order for the 3 hydrogen-capped polyynes. (b) Calculated trend of panel a with Albrecht's theory. (c) Electron-phonon coupling (quantified by the Huang-Rhys factor) of hydrogen-capped polyynes from 6 to 26 carbon atoms.

Acknowledgments

P.M., M.T., C.C., P.S., S.P., A.L.B., V.R., and C.S.C. acknowledge funding from the European Research Council (ERC) under the European Union's Horizon 2020 research and innovation program ERC Consolidator Grant (ERC CoG2016 EspLORE grant agreement no. 724610, website: www.esplora.polimi.it). We acknowledge Elettra Sincrotrone Trieste for providing access to its synchrotron radiation facilities and for financial support.

Original paper

P. Marabotti *et al.*, *Nat. Comm.* **13**, 5052 (2022); DOI: 10.1038/s41467-022-32801-3

P. Marabotti¹, M. Tommasini², C. Castiglioni², P. Serafini¹, S. Peggiani¹, M. Tortora³, B. Rossi³, A. Li Bassi¹, V. Russo¹, C.S. Casari¹

¹ Department of Energy, Politecnico di Milano, Milano, Italy

² Department of Chemistry, Materials and Chem. Eng. 'G. Natta', Politecnico di Milano, Milano, Italy

³ Elettra - Sincrotrone Trieste S.C.p.A., Trieste, Italy

e-mail: carlo.casari@polimi.it

Insight into the structural evolution of Co-Poor Lithium Rich Oxides for Lithium Ion Battery

Elettra | MCX

LIBs (Lithium-Ion Batteries) are part in everyday life in all mobile applications as well as in hybrid/electric mobility. The extraordinary market success of this technology is forcing hard the need of LIBs with improved energy density, environmental compatibility, and safety, thus making necessary to push this technology beyond the current state of the art. In this framework, Co-poor LRLOs (Lithium Rich Layered Oxides) are the most strategic alternative to current Co-rich layered oxides for their use as positive electrodes. LRLOs combine the outstanding large specific capacity ($>250 \text{ mAhg}^{-1}$) with high energy density (up to 900 WhKg^{-1}), small costs and improved environmental benignity. The excellent performance of LRLOs derives from the combination of redox processes originated from the transition metals and the oxygen anions sublattice. Cationic and anionic redox activity helps to achieve high energy density but the potential profile of LRLOs dramatically changes after the first charge due to the partly irreversibility of oxygen redox. The consequence is a voltage decay upon cycling and structural changes.

In this work, we synthesized a new family of LRLOs, using Sol-Gel route, with general formula $\text{Li}_{1.2+x}\text{Mn}_{0.54}\text{Ni}_{0.13}\text{Co}_{0.13-x-y}\text{Al}_{0.03}\text{O}_2$ ($0.03 \leq x \leq 0.08$ and $0.03 \leq y \leq 0.05$), obtained from the replacement of cobalt with lithium and aluminum and we highlighted how the balancing of the metal blend can lead to improvements in battery performance. Relevant enhancements compared to Co-rich LRLO have been obtained in terms of Coulombic efficiency, capacity retention and voltage decay.

Fig 1a shows the Synchrotron x-ray Diffraction patterns obtained at MCX beamline for the 4 samples under study. The high-quality patterns allowed to confirm the phase identity despite the introduction of aluminum and lithium instead of cobalt into the structure. No nucleation or segregation of other

phases can be detected, and Rietveld refinements show the alteration of lattice parameters, thus confirming the success of the doping. The electrochemical behavior has been investigated by galvanostatic tests (Fig 1b-1c). Voltage profiles show the very large specific capacity exchanged in the first cycle by all cathode materials and relevant improvements in the Coulombic efficiency according to the reduction of cobalt amount into the samples. This is a direct clue of an improved reversibility of the redox process. Moreover, the calendar performance demonstrates a very constant specific capacities delivered for hundreds of cycles and a remarkable reduction of voltage decay (figure 1c). Overall, the Co-poorest sample shows the best battery performance among all materials.

To shed light on the complex crystal-chemistry of this class of LRLOs we studied the sample $\text{Li}_{0.08}\text{Al}_{0.03}$, the Co-poorest member of this homologue material series, namely $\text{Li}_{1.28}\text{Mn}_{0.54}\text{Ni}_{0.13}\text{Co}_{0.02}\text{Al}_{0.03}\text{O}_2$, to prove the structural evolution occurring upon charge/discharge in lithium cell. According to the figure 1d, electrodes have been recovered at different state of charge/discharge during the first and the second cycles and after ten cycles of galvanostatic tests by de-assembling lithium cells into an Ar-filled glove box. These *postmortem* materials have been sealed in borosilicate capillary tubes and studied *ex situ* by x-ray diffraction at the MCX beamline.

Fig. 1d (upper panel) shows the potential profiles upon de-insertion/insertion of Li^+ ions in galvanostatic conditions for the first two cycles and highlights the points, marked with A, B, C etc., where the test has been stopped, and the materials has been collected for *ex situ* analysis. According to the diffraction data (Fig. 1d bottom panel), structural alterations of $\text{Li}_{1.28}\text{Mn}_{0.54}\text{Ni}_{0.13}\text{Co}_{0.02}\text{Al}_{0.03}\text{O}_2$ start with a fast broadening and a shift of the peaks suggesting a smooth lattice

modification. When the cell reaches 4.8V vs Li^+ , a second phase can be identified. In the discharge process opposite structural transformations occur.

These high-resolution patterns have been analysed by Rietveld refinement, assuming a rhombohedral unit cell, to disclose quantitative information of the lattice parameters and their changes. The changes in the a and c parameters of the rhombohedral unit cell are highly correlated with the redox processes. The shrinking of the a parameter is related to the oxidation of Ni^{2+} and Co^{3+} to Ni^{4+} and Co^{4+} , respectively. Overall, the oxidation of transition metals leads to more compact crystal packing thank to the decrease of ionic radii and the increase of the net charges. These phenomena result in the shortening of the M-O bond length and in the shrinking of the MO_6 octahedra. While, the c parameter increases due to loosening of the staking among the O-Li-O-M layers due to the removal of lithium ions and the consequent increase of the electrostatic repulsions between vicinal oxygen layers. An opposite trend is found during the discharge mode. Remarkably, Rietveld refinement analysis confirms the segregation of a second phase at the end of the first charge. This new phase is isostructural to the parent pristine material and, once formed, does not disappear upon cycling. Both phases participate in the reversible electrochemical reactions.

The development of novel materials for next generation batteries requires to carefully balance performance improvements, enhanced environmental benignity and cost sustainability along the entire life cycle, from synthesis to recycling. This study exploits the use of a synchrotron-based technique to characterize the working mechanism of LRLOs in batteries: this is a crucial step to promote a knowledge-based design of innovative materials for high-capacity positive electrodes.

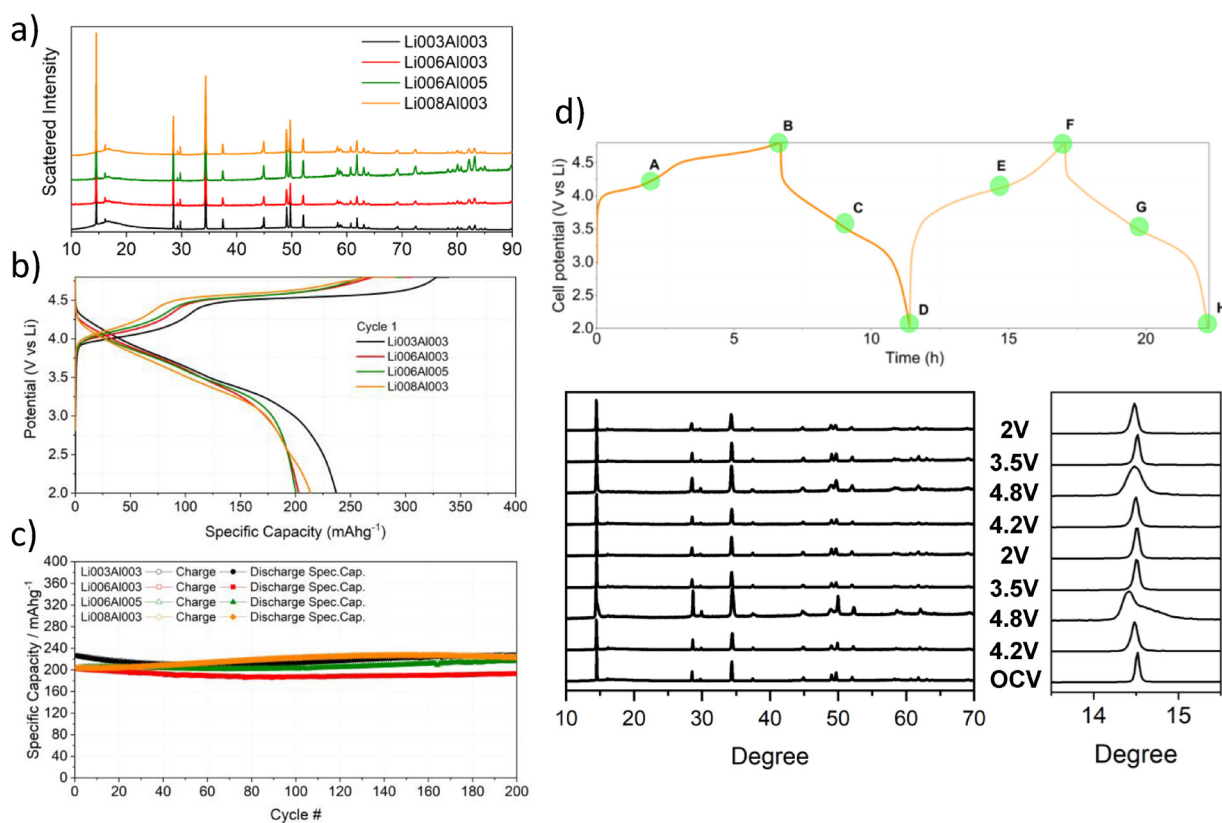


Figure 1. (a) Synchrotron XRD patterns, (b) first charge/discharge voltage profiles and (c) calendar electrochemical performance at C/10 (1C=377 mA g^{-1}) of $Li_{1.2-x}Mn_{0.54}Ni_{0.13}Co_{0.02}Al_{0.03}O_2$ series. (d) Voltage profiles during first and second cycle of $Li_{1.28}Mn_{0.54}Ni_{0.13}Co_{0.02}Al_{0.03}O_2$ and evolution of XRD pattern during lithiation/de-lithiation.

Acknowledgments

We acknowledge Elettra Sincrotrone Trieste for providing access to its synchrotron radiation facilities and we thank Jasper Plaisier for assistance in using beamline MCX.

Original paper

A. Celeste *et al.*, *Electrochimica Acta* **428**, 140737 (2022); DOI: 10.1016/j.electacta.2022.140737

A. Celeste^{1,2}, F. Girardi³, L. Gigli⁴, V. Pellegrini^{1,5}, L. Silvestri⁶ and S. Brutti⁷

¹ Italian Institute of Technology, Genoa, Italy

² Department of Chemistry and Industrial Chemistry, University of Genoa, Genoa, Italy

³ Fusion and Technology for Nuclear Safety and Security Department, C.R. Casaccia, Rome, Italy

⁴ Elettra - Sincrotrone Trieste S.C.p.A., Trieste, Italy

⁵ BeDimensional Spa, Genoa, Italy

⁶ Department of Energy Technologies and Renewable Sources, ENEA C.R. Casaccia, Rome, Italy

⁷ Department of Chemistry, "Sapienza" University of Rome, Rome, Italy

e-mail: sergio.brutti@uniroma1.it

Exploring the complexity of functionalized nanoparticles through a combination of machine-learning and experiments

Elettra | Materials Science Beamline

Over the last years, the research on gold NPs (nanoparticles) passivated by organic coatings consisting of ligands has flourished, demonstrating the far-reaching range of uses for these nanomaterials in fields such as biomolecule sensing, catalysis, therapy, diagnosis, plasmonic materials. In addition to applications, parallel investigations have been carrying out aiming at the advancing of structural and mechanistic characterization, which is a complex but crucial step toward fully understanding the properties and the reactivity of these hybrid organic-inorganic nanosystems.

As for proteins the study of the tertiary and/or quaternary structure enables to determine, among other properties, the accessibility to or the solvation of catalytic pockets, in case of SAM (self assembled monolayer) protected gold NPs, unveiling the local structure, dynamics and solvation of SAM at atomic and nanoscale affords the potential to explain existing as well undiscovered phenomena. This information might be directly assessed experimentally by using techniques such as NMR (Nuclear Magnetic Resonance), SANS (Small-Angle Neutron Scattering), MS (Mass Spectrometry), ESR (Electron Spin Resonance); yet, these techniques suffer of some limitations, as the monolayer needs to be designed ad hoc for the specific technique to be used.

In this work we described a novel general approach to identify local environments and their features within SAM protected gold NPs. It is based on a computational workflow capable of detecting first and then comparing local (supra)molecular environments, without the need for predefined information and with minimal user intervention. The method combines AA-MD (All Atom - Molecular Dynamics) calculations of SAM-NPs and Smooth Overlap of Atomic Position (SOAP) descriptors for machine learning-driven analysis (Fig. 1a). The local patterns thus recovered are then described and rationalized by MD calculations (Figure 1b). As final step, they are compared

and ranked, helping in the identification of those molecular factors that define nature and properties of a specific environment inside the monolayer. An example is illustrated in Fig.1b; the SOAP analysis of the MD trajectories has identified two distinct environments in NP4 nanoparticles: the first one corresponds to most hydrophobic states where the molecular probe is close to the gold core, (orange points, state 1), the second one instead outlines sites of lower hydrophobicity explored by the radical probe during the simulation time (blue points, state 2).

The computational methodology was tested and validated against a set of NPs having enough chemical diversity (Fig. 1c). NPs were synthesized and characterized by a plethora of techniques, among the XPS (X-ray Photoelectron Spectroscopy) measurements carried out at the Material Science beamline of Elettra. Synchrotron-based XPS measurements allowed here to estimate the thickness of the organic shell around the NP. The NPs were dispersed in aqueous solution and then drop-casted on a n-doped Si wafer, capped with a layer of native oxide. After drying the samples for 24 h in a protected environment at atmospheric pressure, they were inserted in the experimental UHV (Ultra High Vacuum) chamber of the beamline and promptly measured.

As an example, the data shown in Fig. 1d were acquired on the NP sample containing ligand 2 (NP2). The Au 4f and C 1s core level were acquired with a photon energy of $h\nu = 410$ eV, while the S 2p was acquired with a photon energy of 360 eV. The BE (binding energy) scale was aligned with the main component of the C 1s, which is the tabled C=C bond of the thiols (BE = 284.9). The Au 4f_{7/2} component was found at BE = 83.9 eV, a value which is compatible with the presence of metallic gold. Similarly, the S 2p shows a spin-orbit doublet located at BE=162.2 eV for S 2p_{3/2}, as already shown in thiolate molecules adsorbed on gold. The determination of

the organic layer thickness was carried out by evaluating the intensity of the photoemission signal of C 1s and Au 4f spectra, an approach that allowed the determination of the organic shell for nanoparticles with known core radius. ESR (Electron Spin Resonance) - a spectroscopic technique highly sensitive to the polarity of the local environment perceived by a radical probe - was then used to provide experimental evidence of the environments detected by the computational predictions.

The local environments identified in our SAMs differ for accessibility, local solvation, and hydrophobicity, which are imparted by specific ligand length, nature of ligand end-group, and monolayer 3D structure.

Our investigation demonstrated that local (supra)molecular environments created by ligands self-assembling on the surface of gold NPs can be precisely detected and exploited. This is feasible with a computational approach, validated with experimental data, which enables automated identification and comparison of such environments driven from the data and without previous knowledge. This work suggests that in the future, the design of SAM gold NPs may be guided by machine-learning algorithms of local motifs with pre-defined properties. This approach opens to a new way to afford the experimental synthetic preparation of NPs with a saving of chemicals, characterization experiments and time.

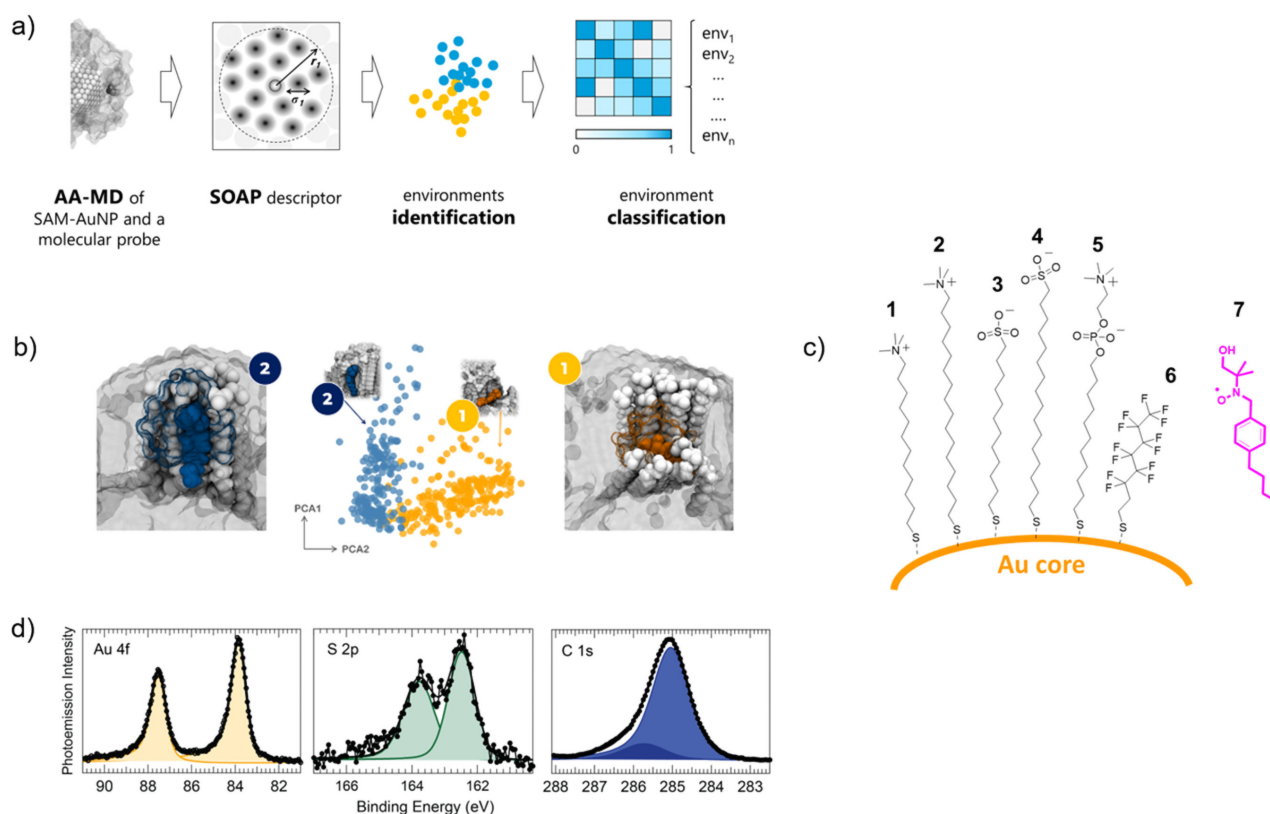


Figure 1. (a) Conceptual diagram of the workflow used for the detection and comparison of local molecular environments within SAMs using the SOAP-based structural analysis. (b) Example of two molecular environments (labeled as 1 and 2) perceived by a molecular probe as spotted out by the workflow shown in Fig.1a. (c) Functionalized gold NPs investigated and the radical probe in pink. (d) Background-subtracted Au4f, S 2p and C 1s core level spectra acquired for the NP2 sample. The black dots are the experimental data, the black continuous line is the best fit to the spectrum obtained using the spectral components (indicated in color).

Acknowledgments

This work received support from the Italian Ministry of University Research through the projects "Structure and function at the nanoparticle biointerface" (RBSI14PBC6 to P. P.), PRIN2017 NiFTY (2017MYBTXC to L. P.), PRIN2017 "BacHounds: Supramolecular nanostructures for bacteria detection" (2017E44A9P to M. L.) and "Nemo" (20173L7W8K to P. F.). P. P. and C. G. are particularly grateful to the University of Trieste for scholarship support and acknowledge the CINECA award under the ISCRA initiative, for the availability of high-performance computing resources. CERIC-ERIC consortium is acknowledged for the access to the Materials Science beamline at the Elettra synchrotron radiation facility (proposal number 20192081). The staff of the Materials Science beamline is kindly acknowledged for technical support. Z. P. acknowledges the assistance provided by the Technology Agency of the Czech Republic, under the project Metamorph, project No. TO01000329.

Original paper

C. Gabellini *et al.* ACS Nano, **16**, 20902 (2022); DOI: 10.1021/acsnano.2c08467

C. Gabellini¹, M. Sologan², E. Pellizzoni², D. Marson¹, M. Daka², P. Franchi³, L. Bignardi⁴, Z. Posel⁵, A. Baraldi⁴, P. Pengo², M. Lucarini³, L. Pasquato², P. Posocco¹

¹ Department of Engineering and Architecture, University of Trieste, Trieste, Italy

² Department of Chemical and Pharmaceutical Sciences and INSTM Trieste Research Unit, University of Trieste, Trieste, Italy

³ Department of Chemistry "G. Ciamician", University of Bologna, Bologna, Italy

⁴ Department of Physics, University of Trieste, Trieste, Italy

⁵ Department of Informatics, Jan Evangelista Purkyně University, Ústí nad Labem, Czech Republic

e-mail: lpasquato@units.it; paola.posocco@dia.units.it; marco.lucarini@unibo.it

Direct observation of phase separation and evolution in Li_xCoO_2 particles

Elettra | Nanospectroscopy

LCO (LiCoO_2) is widely used in Li-ion batteries, which are a key power source in portable electronic devices, electric vehicles, and renewable energy storage, but it is also used in diverse applications including electrocatalysis or ECRAM (ElectroChemical Random-Access Memory) devices, based on electronic resistance switching controlled by Li-ion intercalation. The LCO structure can accommodate a wide-ranging Li concentration thanks to both the high mobility of the Li atoms and the ability of the lattice to stabilize different Li molar fractions. During charge–discharge cycles, LCO exhibits phase transformations that are significantly complicated by electron correlation. Phases with drastically different electronic and ionic transport properties will charge at different rates, leading to reduced overall capacity. Understanding these effects is essential to modeling battery performance and for predicting the scalability and performance of electrocatalysts and ECRAM. LiCoO_2 is a band insulator (α phase), but Li_xCoO_2 is metallic for $0.5 < x < 0.75$ (β phase, with a structure close to the α phase). For $0.75 < x < 0.94$ Li_xCoO_2 is also metallic, but the α and β phases coexist. This range coincides with the Li content most used when LCO acts as a battery cathode. While the bulk phase diagram for an ensemble of battery particles has been studied extensively, it remains unclear how these phases scale to nanometer dimensions and the effects of strain and diffusional anisotropy at the single-particle scale. By using a combination of experimental techniques, we have gained invaluable insight into the complexities associated with the appearance and evolution of phase transformations in LCO single particles. These studies are more challenging due to the strong orientation dependence of diffusion in LCO and the nanoscopic nature of the phase domains. C-AFM (Conductive - Atomic Force Microscopy) was used to characterize the spatial distribution of conducting and insulating phases on individual

islands before and after electrochemical cycling. This technique allows us to see the distribution after electrochemical cycling for both (001) and (104) oriented particles. The differences observed between the two cases are due to the different orientation of the Li intercalation planes in each case. We observed that Li diffusion is highly anisotropic, producing Li rich and Li poor regions corresponding to insulating α and metallic β phases, respectively. Since Li diffusion is favorable within certain crystalline planes intercalation proceeds from the island edge. While c-AFM provides insight into a few particles, it is desirable to acquire information across a larger number of particles. The stoichiometry of each particle and the distribution over large areas were studied with a combination of PEEM (Photoelectron Emission Microscopy) and LEEM (Low Energy Electron Microscopy), performed at the Nanospectroscopy beamline of the Elettra synchrotron as shown in Figure 1. A charge shift is observed in the XPS-PEEM spectrum, related to the metallic or insulating nature of the LCO islands. It was also used to determine the conductivity of the islands. The LCO islands were delithiated in situ using a sputter/anneal delithiation process. There is preference for certain islands to become delithiated, with some islands having a more metallic character and a lower Li to Co ratio. Li deficient islands make up around 50% for small field of view ($1 \mu\text{m}^2$) regions. This is consistent with the β -phase segregated to the very top surface. The study of individual islands suggests that no border effects or inhomogeneity within individual islands is found using PEEM, as we observed following electrochemical delithiation. The results of the sputter/anneal delithiation process provide an interesting comparison to the electrochemically delithiated samples. The lack of preferential delithiation from the edge is consistent with the sputter/anneal process as opposed to

intercalation from the planes. The anneal process raises the temperature such that the surface has enough thermal energy to evolve towards thermodynamic equilibrium, rather than having any kinetic metastability. Therefore, the fact that the system evolves to having certain particles in a more delithiated state suggests that there is a preference toward such an equilibrium thermodynamically. Our research highlights the importance of nanoscale effects, which cannot be reliably predicted from bulk phase diagrams alone, in understanding and exploiting optimal device performance. The complex interplay between diffusion, strain, and electron correlation results in unpredictable phase morphologies as a function of dimensionality and charging rates. Implications of our results for batteries, electrocatalysis, and ECRAM include the effects of particle orientation and morphology on the possibility of forming a kinetically arrested state with surface phase segregation, as well as the creation of a conductivity difference at island boundaries, which can determine device properties where the macroscopic conductance depends on the behavior of the regions near contact electrodes. Finally, we note that imaging of electrochemically delithiated samples using PEEM/LEEM is a promising approach for future work for comparing larger scale statistics to the nanoscale features observed with c-AFM.

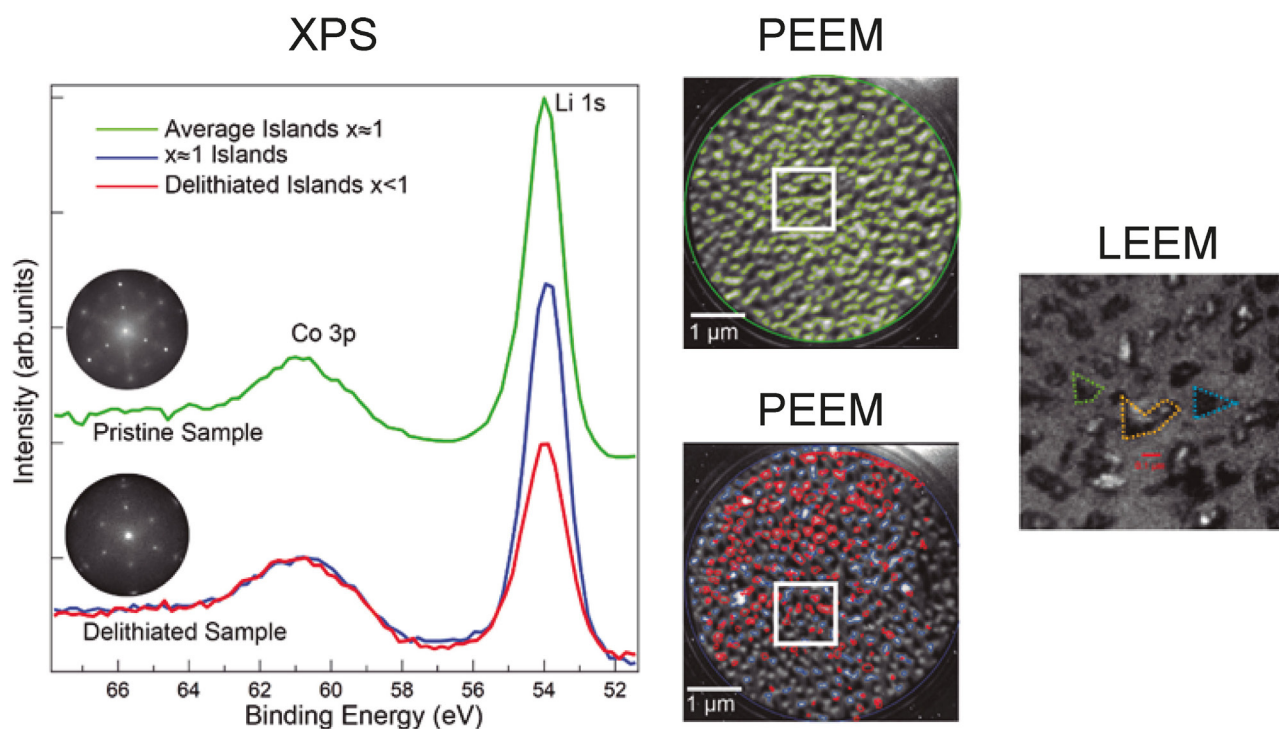


Figure 1. PEEM/LEEM data of LCO (001) islands. Left: Integrated XPS of Co 3p and Li 1s peaks for the pristine case (green) and delithiated case (blue) and over selected islands that showed strong delithiation (red). LEED insets of the pristine and sputtered samples are also shown. Center: Subsequent PEEM image at a photon energy of 150 eV for the pristine (top) and after a delithiation process (bottom). Green shading in the PEEM was obtained by imaging over Li 1s to identify regions with high Li content corresponding to the LCO α phase. Right: Example of a LEEM image to highlight the topography. Dashed contours are a guide to the view.

Acknowledgments

E.J.F. and A.A.T. were supported by the Sandia Laboratory Directed Research and Development (LDRD) Program. B.B., Y.S., and P.A. were supported by the U.S. Department of Energy, Office of Science, Office of Basic Energy Sciences, under Award Number DE-SC0021070. This work was supported by projects/grants PRX19/00486, PID2020-117024GB-C43, FIS2017-82415-R, UEM-ERA.NET 2018, PCI2019-103604 and PCI2019-103594 and CALIPSOplus. We acknowledge Elettra Sincrotrone Trieste for providing access to its synchrotron radiation facilities and for financial support.

Original paper

E.J. Fuller *et al.*, ACS Nano **16** (10), 16363, (2020); DOI: 10.1021/acsnano.2c05594

E.J. Fuller¹, D.S. Ashby¹, C. Polop^{2,3}, E. Salagre², B. Bhargava⁴, Y. Song⁴, E. Vasco⁵, J.D. Sugar¹, P. Albertus⁴, T.O. Menteş⁶, A. Locatelli⁶, P. Segovia^{2,3}, M.A. Gonzalez-Barrio⁷, A. Mascaraque⁷, E.G. Michel^{2,3}, A.A. Talin¹

¹ Sandia National Laboratories, Livermore, USA

² Departamento de Física de la Materia Condensada and Instituto Universitario de Ciencia de Materiales Nicolás Cabrera (INC), Universidad Autónoma de Madrid, Madrid, Spain

³ IFIMAC (Condensed Matter Physics Center), Universidad Autónoma de Madrid, Madrid, Spain

⁴ Department of Chemical and Biomolecular Engineering, University of Maryland, USA

⁵ Instituto de Ciencia de Materiales de Madrid, CSIC, Madrid, Spain

⁶ Elettra - Sincrotrone Trieste S.C.p.A., Trieste, Italy

⁷ Departamento de Física de Materiales, Universidad Complutense de Madrid, Madrid, Spain

e-mail: a.mascaraque@ucm.es

Ordered 3D quantum dot superlattices with excellent transport properties

Elettra | SAXS

In the short-wavelength infrared range, there is poor or no availability of cheap and optically tunable bulk semiconductors for optoelectronic applications like telecommunications and sensing in automated transport. Semiconducting CQDs (colloidal quantum dots) like lead chalcogenides instead, display bandgap tunability (800-3000 nm) with size and are cheaply synthesized in solution. Unfortunately, due to their deposition techniques, thin films of such materials are often disordered and therefore display poor transport properties. Self-assembled arrays of colloidal quantum dots, the so-called SL (superlattices), are expected to provide coherent transport through minibands thus approaching the electronic properties of the bulk counterparts. However, up to now, the poor control on ordering, electronic coupling and surface trap passivation has led to the observation of disappointing charge transport properties.

To obtain ordered 3D PbSe CQDs superlattices, we have optimized a solution based bottom-up approach, consisting of a sequential self-assembly process followed by a surface modification procedure (Fig. 1i-iv). First, an ordered multilayered film is assembled at the air-liquid interface. By drop casting at the center of a teflon bath filled with ethylene glycol (EG) controlled amounts of 5.2 ± 0.3 nm diameter PbSe CQDs covered with oleic acid (OA) and dispersed in octane (Fig 1i), solid films of different thickness are formed after solvent evaporation (Fig 1ii). In order to assess the structural order within such a film, GISAXS (grazing incidence small-angle x-ray scattering) measurements were performed on samples transferred on Si substrates at the SAXS beamline in Elettra. Fig. 1A shows the GISAXS pattern for a multilayered film of CQDs. The pattern consists of several well-defined diffraction spots, suggesting a high degree of ordering for the packed CQDs covered by the organic layer. Peak assignment reveals a BCC

(body centered cubic) structure with a lattice parameter of 9 nm and with the 110 planes highly oriented parallel to the substrate. The BCC structure and the high degree of long range order is confirmed by TEM (Transmission Electron Microscopy) (Fig. 1D). The calculated wall-to-wall distance between neighbouring CQDs is 4 nm which, considering their size, implies the presence of two OA molecules. Despite its nice ordered structure, the OA-SLs are not useful for optoelectronic applications since the insulating organic layers do not allow for electrical transport. Thus, the second step of our process is the removal of the organic ligands covering the CQDs surface by injection of EDA (EthyleneDiAmine) in the EG bath. This process of ligand exchange (LE) (Fig. 1iii) is known to strip out the loosely bound OA ligands from the {100} facets of the CQDs and cause them to epitaxially connect. Analysis of the GISAXS pattern taken for the deposited film (Fig. 1B) shows how the LE induces a change in the CQDs packing to a rhombohedral (Rh) structure with lattice parameter of 6.1 nm, meaning that CQDs are now much closer and eventually touching along the {100} facets. Most importantly, the GISAXS patterns for the LE samples still reveal the presence of well-defined diffraction spots, suggesting that the long-range ordering of the OA-SL is largely maintained during the LE and structural transition from BCC to Rh. The high resolution GISAXS patterns acquired at the SAXS beamline in Elettra allows us to quantify the extent of the structural order. Indeed, the width of the diffraction spots along the horizontal q_x and vertical q_z direction allows us to calculate the so-called coherent length of the ordered domains in the plane (IP, OP coherent length = $\frac{2\pi}{\Delta q_{\text{IP}}}$) and vertically out of the plane. The GISAXS data summarised in Fig. 1C provided us with few striking findings. Firstly, the OP coherent length measured for a 8 layer film is 43 nm, meaning that the SL is a mono domain in the vertical direction. Secondly, the IP coherent length for the

LE-SLs is about 90 nm, very close to the 100 nm measured for the OA-SLs. The IP coherent length must be intended as the minimum size of the ordered domains without any structural defects. From TEM the macroscopic domain size of the LE-SLs seems much larger, approaching 1 μm , yet containing some local defects (Fig. 1E). Another nice feature of these LE-SLs is that the CQDs are also epitaxially aligned among themselves, as assessed by GIWAXS data presented in our manuscript.

The remarkable level of structural order achieved here and quantitatively assessed by GISAXS has a direct implication on the optoelectronic properties of the LE-SLs. Using the described approach above we have been able to produce high quality IGFET (Ionic-gel Gated Field-Effect Transistors) with channel length between 1 and 12 μm (Fig. 1G), thus probing the transport across about 10-100 LE-SL grains. The transfer curve of the best performing device displays a very high 'on' current and modulation with n-type dominated transport, which is expected from the non-stoichiometric composition of the CQDs (Fig. 1H). Most importantly, we measured for these ordered 3D superlattices a record electron linear mobility of $278 \text{ cm}^2 \text{ V}^{-1} \text{ s}^{-1}$, approaching the value for bulk PbSe.

In summary, the use of high resolution GISAXS is fundamental to assess in a quantitative manner the structural transitions and the order both in the plane and out of the plane of these self-assembled optoelectronic structures, providing a unique statistical tool to build a clear structure-property relationship in such systems. Moreover, from a technological point of view, the process adopted here holds great promise as it is simple, scalable and provides dimensional control over the film thickness, enabling in the future technological applications of CQDs active in the SWIR (Short-Wave Infrared) range.

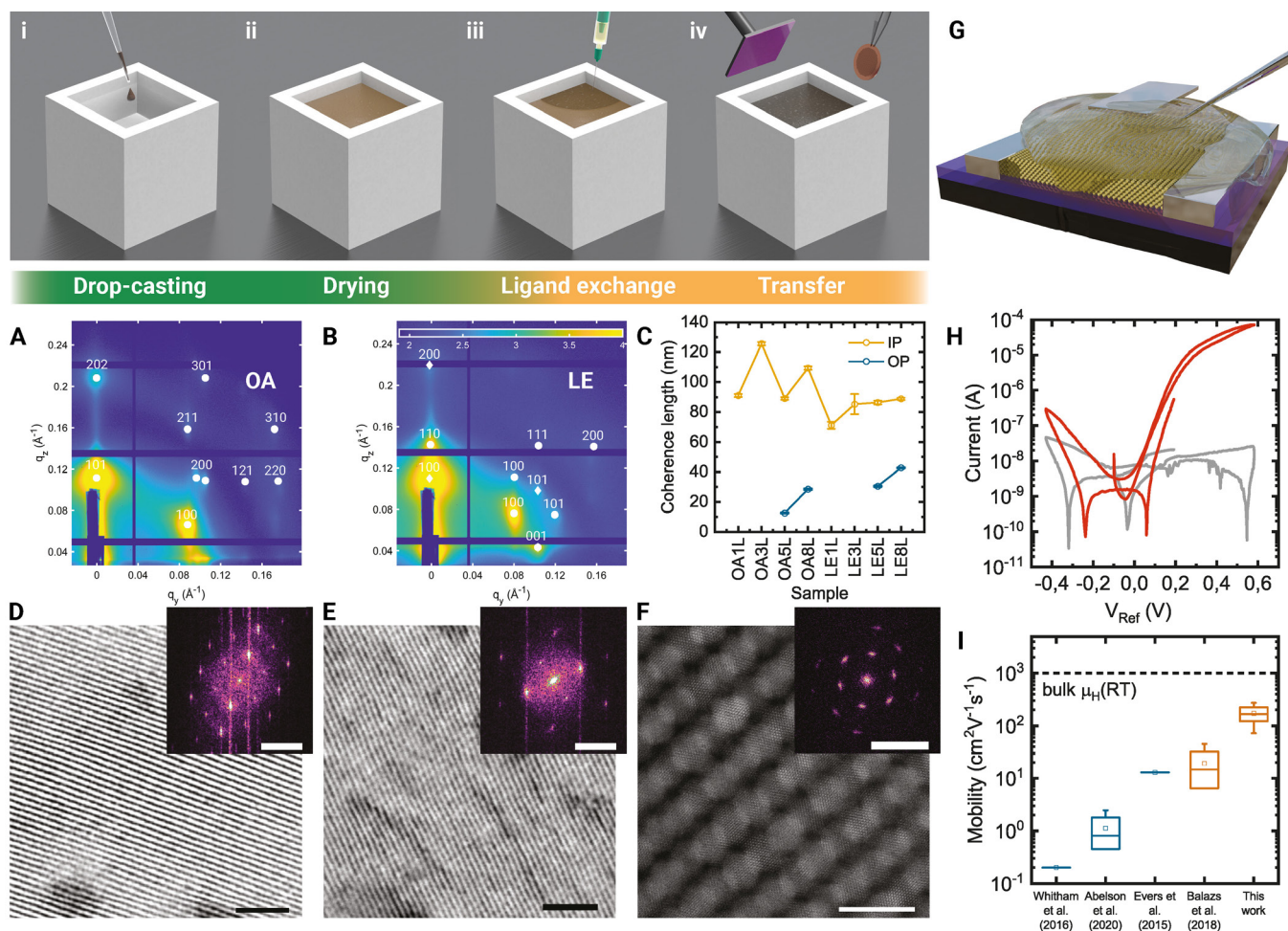


Figure 1. (i-iv) The concentrated CQD solution is dropped on EG at the center of a teflon well (i) and it slowly dries (ii) to allow for the self-assembly; the new ligands are injected in the subphase (iii); after a given time, the film is deposited on the desired substrate via Langmuir-Schaefer method. (A) GISAXS pattern for the thickest oleic acid sample with indexing for a {110} BCC superlattice and (B) for the correspondent LE sample indexed with both a {110} (circles) and {100} (diamonds) Rhombohedral unit cell. (C) Measured in-plane (IP) and out-of-plane (OP) coherence lengths for the systematic series of samples. (D,E) Scanning-TEM micrographs with respective FFTs for the same samples as in (A,B) showing ordered superlattices with the same structures (scale bars: 50 nm, 0.2 nm⁻¹). (F) Atomic-resolution STEM micrograph of the eight-layers LE sample showing collective alignment of the CQD (scale bars: 10 nm, 10 nm⁻¹). (G) Schematic model of an ionic-gel gated transistor. (H) Transfer curve of the best performing device (red) altogether with the gate leakage (gray). (I) Comparison of electron mobilities in PbSe CQD superlattices in this work and previous reports.

Acknowledgments

This research work is funded via the project Metamaterials for Optoelectronics (MeMOE) (with project number 17896 of the research programme Materialen NL: Challenges 2018 which is (partly) financed by the Dutch Research Council (NWO). The research leading to these results has benefitted to the use of the SAXS beamline at Elettra and has been supported by the project CALIPSOplus under Grant Agreement 730872 from the EU Framework Programme for Research and Innovation HORIZON 2020. Dr. Sigrid Bernstorff is acknowledged for the great assistance in using the beamline.

Original paper

J. Pinna, et al. *Advanced Materials* **35.8**, 2207364 (2023); DOI:10.1002/adma.202207364

J. Pinna, R. M. Koushki, D.S. Gavhane, M. Ahmadi, S. Mutalik, M. Zohaib, L. Protesescu, B. J. Kooi, M.A. Loi, G. Portale

Zernike Institute for Advanced Materials, University of Groningen, Groningen, The Netherlands

e-mail: g.portale@rug.nl

Infrared Plasmons in Ultrahigh Conductive PdCoO₂ Metallic Oxide

Elettra | SISSI Mat

Surface plasmons, the collective oscillations of electrons in metals and doped semiconductors, show outstanding EM (electromagnetic) properties spanning from a reduced wavelength in comparison to that of an exciting electromagnetic field, an extreme local electric field enhancement several orders of magnitude larger than the incident EM field, to several nonlinear effects like harmonic generation and optical rectification. Those properties are at the basis of nano-infrared and surface-enhanced Raman spectroscopies, currently applied in many biosensing techniques. Although conventional metals, like gold and silver, are usually used in plasmonics, nonconventional conductors like graphene, transparent oxides, high-T_c superconductors, strongly-correlated oxides, and topological materials are now on the scientific edge, providing additional properties like plasmon tunability due to their extreme sensitivity, to external parameters like doping, temperature, and electric and magnetic fields. Among metallic oxides, PdCoO₂ layered delafossite is the most conductive, having a room temperature resistivity of nearly $2\mu\Omega\text{cm}$, corresponding to a mean free path of about 600\AA . These values are comparable to those of the best 3D (three-dimensional) metallic conductors such as Al, Au, Cu and Ag, although the charge density of PdCoO₂ is $\sim 30\%$ the copper one. PdCoO₂ has a nearly 2D (two-dimensional) layered structure composed by Pd triangular layers and CoO₂ slabs. Theories and experiment show that the electronic density of states at the Fermi level is dominated by Palladium indicating that the electronic states are nearly 2D. Its single-particle electrodynamics has been measured on single crystals and it is dominated at IR (infrared) and THz (Terahertz) frequencies by intraband excitations, well described by the Drude model, while interband transitions appear above 8000cm^{-1} (1 eV). Although the very long mean free

path at room temperature, and the nearly perfect separation between intra and interband electronic transitions provide an ideal framework for investigating the collective electronic excitations (surface plasmons) of PdCoO₂ layered delafossite, these modes have never been measured to our knowledge.

In this work we reported the experimental evidence of surface plasmonic excitations in thin films of PdCoO₂ on sapphire substrates. In particular, we have fabricated parallel ribbons array structures of PdCoO₂ and investigated their optical properties from THz to Visible (VIS) for light polarization parallel and perpendicular to the ribbons. When the polarization is perpendicular to the ribbon array, one excites plasmon modes at the surface of the PdCoO₂ film. Through the measurements of several ribbon arrays, we have sampled the plasmon frequency vs. wavevector, being able to experimentally determine the energy/momentum dispersion of surface plasmons in PdCoO₂. Five 100 nm films of palladium-cobalt delafossite were grown by molecular beam epitaxy (MBE) on $500\mu\text{m}$ thick Al₂O₃ substrates. The reflectance $R(\omega)$ of an as grown film was measured across the THz to UV (ultraviolet) spectral range. Micro-ribbon arrays of different widths W and periods $2W$ have been fabricated through electron lithography, to select suitable values of the plasmon wavevector q , so that a series of discrete values of $q = \pi/W$ were obtained. Then, plasmon excitations have been studied by measuring the reflectance of patterned samples for light polarization perpendicular to the ribbons. Plasmon excitations appear as a dip in the reflectance measured for light polarization perpendicular to the ribbons. In order to better understand these plasmonic excitations we performed electromagnetic simulations and used an analytical model that allowed us to assign the low-frequency dips to plasmons living at the PdCoO₂-sapphire and at the PdCoO₂-air interface. By extracting the experimental plasmon

frequency ω_{SPP} from reflectance measurements, we were able to estimate the plasmon dispersion ω_{SPP} vs. the wavevector q . Electromagnetic simulation and a thin-film analytical model reproduce very well this dispersion. Near the ribbon edges at the PdCoO₂-sapphire interface, we calculated a strong field enhancement due to plasmonic confinement, suggesting the use of PdCoO₂-based plasmonic structures for sensing and non-linear spectroscopy applications in the mid-infrared and terahertz spectral regions.

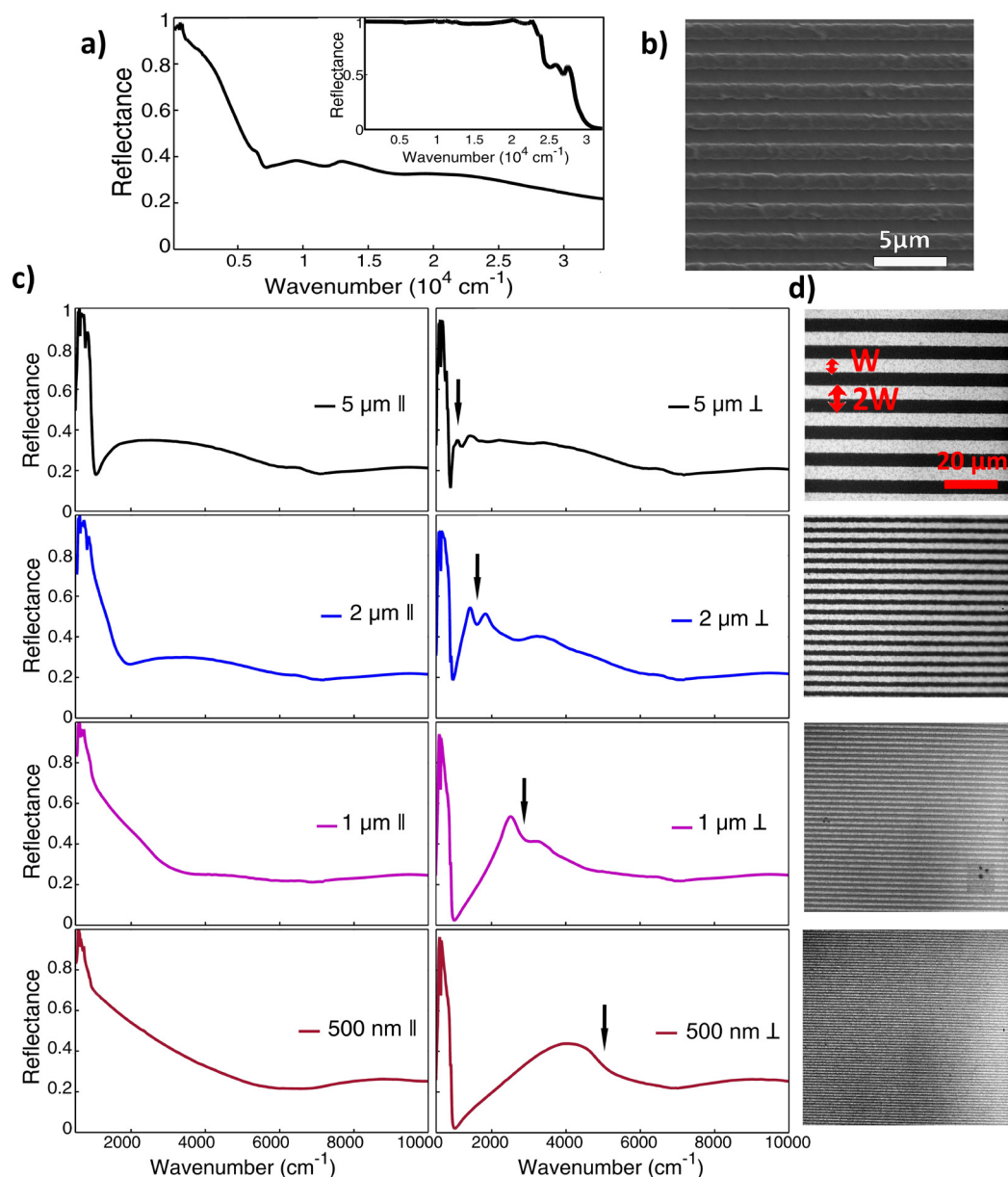


Figure 1. Reflectance of unpatterned and patterned PdCoO₂ thin-films on sapphire. a) Reflectance of the as-grown, unpatterned film of PdCoO₂. The inset in the right upper side shows the bare reflectance of PdCoO₂ extracted through RefFit program. b) SEM (Scanning Electron Microscopy) image of the W=1 μm patterned film. The bar-size is 5 μm. c) Reflectance of the four patterned films, with the radiation electric field parallel to the ribbons (left column) and perpendicular to the ribbons (right column). Arrows indicate approximately the frequency location of surface plasmon excitations. d) Optical microscope images of the four patterned films with different widths W and periods 2W. All the images have the same dimensions. Brighter parts are related to the oxide film, while darker regions are associated to the sapphire substrate.

Acknowledgments

This work has received the financial support of the Bilateral Cooperation Agreement between Italy and China of the Italian Ministry of Foreign Affairs and of the International Cooperation (MAECI) and the National Natural Science Foundation of China (NSFC), in the framework of the project of major relevance 3-Dimensional Graphene: Applications in Catalysis, Photoacoustics and Plasmonics. Work at Rutgers University is supported by supported by National Science Foundation (NSF) Grant No. DMR2004125 and Army Research Oce (ARO) Grant No. W911NF2010108.

Original paper

S. Macis, et al. Communications Physics 5, 145 (2022); DOI: 10.1038/s42005-022-00924-0

S. Macis^{1,2}, L. Tomarchio^{1,3}, S. Tofani⁴, F. Piccirilli⁵, M. Zacchigna⁶, V. Aglieri⁷, A. Toma⁷, G. Rimal⁸, S. Oh⁸ and S. Lupi^{1,6}

¹ Department of Physics, Sapienza University, Rome, Italy

² Frascati National Laboratory, INFN, Frascati, Italy

³ INFN, Rome, Italy

⁴ Astrophysical and Space Planetology Institute, INAF, Rome, Italy

⁵ Elettra - Sincrotrone Trieste S.C.p.A., Trieste, Italy

⁶ CNR-IOM, Trieste, Italy.

⁷ Italian Institute of Technology, Genova, Italy

⁸ Department of Physics and Astronomy, Rutgers, The State University of New Jersey, Piscataway (NJ), USA

e-mail: stefano.lupi@roma1.infn.it

Loading H atoms in porous nickel covered by monolayer graphene

Elettra | SuperESCA

Hybrid composites where Gr (graphene) and other 2D materials replicates the meso- and micro-structure of 3D porous substrates have shown innovative functionalities in catalysis and in energy-related fields. Concerning hydrogen storage, the high surface-to-volume ratio exhibited by both 2D and 3D components of the hybrid material is expected to increase the efficiency of surface chemisorption and bulk absorption of hydrogen in comparison to the flat counterparts. To explore this possibility, we have grown single layer Gr on porous nickel foams and have investigated the interaction with H atoms as a function of the temperature by using XPS (x-ray Photoelectron Spectroscopy) and TPD (Thermal Programmed Desorption) at the SuperESCA beamline of Elettra.

Figure 1 (a) displays the SEM (Scanning Electron Microscopy) image of the bare Ni foam which show the three-dimensionally structured skeleton, made of interconnected struts that create small and large open pores. The growth of Gr on the Ni foam was obtained by exposing the sample at 773 K to ethylene. Selected C1s spectra taken at increasing growth time are shown in Fig. 1 (b). When the ethylene flux is switched on, the carbide phases (N_{1-N_4} components) present in the as-received sample progressively disappear, while the Gr components C_0 and C_1 rise in intensity and finally saturate together. C_0 can be related to Gr_S regions grown on the (111) foam grains, where the interaction with the support is as strong as that existing between Gr and the ordered Ni(111) crystal, and the C_1 component to Gr_W regions rotated with respect to (111) grains or grown on grains exposing different orientations, and therefore, interacting weakly with the support.

Figure 1 (c) shows the C1s spectra measured on the Gr/foam exposed to a flux of H atoms at dosing temperatures T_H between 78 and 298 K. Starting from $T_H=98$ K the C1s line shapes appear

broadened on the high BE (binding energy) side due to the appearance of the component A (285.0 eV), and on the low BE side, where the components B (284.1 eV) arises. A and B are due in order to C atoms directly bonded to H atoms and to their first neighbors, and therefore indicate the occurrence of H chemisorption on Gr. From $T_H=198$ K, some intensity is transferred from C_0 to C_1 because at this temperature the H atoms start to intercalate below Gr_S , which gets progressively detached from the substrate. The intercalation under the nearly free-standing Gr_W remains undetected because here the penetration of H underneath does not cause any measurable extra-shift of the C_1 component.

Figure 1 (d) shows the H_2 TPD curves measured while heating the Gr/foam hydrogenated at increasing T_H . The desorption of H atoms chemisorbed on Gr originates solely the weak peak G at ~ 650 K. Hence, all other TPD features correspond to the desorption of H atoms intercalated below Gr and residing at the Ni foam surface or even diffused into the Ni bulk. Hence, differently from Gr_S , where H atoms intercalate only for $T_H=198$ K, below Gr_W intercalation occurs at much lower temperatures. The TPD curves up to $T_H=173$ K are dominated by the D peak, due to the desorption of H atoms penetrated in metastable subsurface sites of the Ni foam. The H_2 release at higher temperatures is related to the slower desorption of bulk H atoms and to the release of H atoms chemisorbed on the Ni surface. After having examined the processes which in the Gr/foam sample drive storage and release of hydrogen, it is dutiful to establish the effective role of graphene and also evaluate the amount of accumulated H. The first important consideration based on the comparison with the TPD results obtained for the bare Ni foam (not shown here) is that the presence of the Gr cover does not reduce the effectiveness of H loading. We have also noticed that the Gr_W

regions tend to stabilize the H coverage at the foam surface and to keep it up to a few tens K above the temperature at which it desorbs from the bare foam, but do not seem to be effective in holding, more than the bare foam, the hydrogen diffused in the bulk.

As for the evaluation of the hydrogen stored in the samples, the TPD curves measured without and with graphene make evident that the bulk of the foam can be loaded only below RT and that the presence of the Gr coating in some cases affects the distribution of H atoms at the interface, but in general does not increase significantly the amount of stored hydrogen. The highest quantity of loaded hydrogen for Gr/foam is detected at $T_H=113$ K, whereas for the sample dosed at 298 K, the total quantity of released H_2 decreases by 3 times. What can be extracted from our measurements is a rough evaluation of the maximal amount of stored H_2 in the conditions adopted in this experiment, which is of the order of 5 times the quantity desorbed from the Ni(111) surface of equivalent macroscopic lateral dimension, saturated with chemisorbed H. However, it must be considered that the foam has pores distributed in the bulk and often interconnected between them, from where hydrogen can desorb in all directions and might be missed by our detector optimized for flat samples. It must be pointed out, however, that the invaluable advantage anyway provided by the presence of Gr is the protection of the foam surface from the adsorption of contaminants, which might limit H chemisorption and consequently subsurface diffusion and loading in the bulk.

Although the fundamental aspects of Gr/foam hydrogenation were here investigated in a regime far below the saturation of the bulk absorption, these measurements can be the starting point for further investigations aimed at establishing the ultimate storage capability of these hybrid nanostructured tanks.

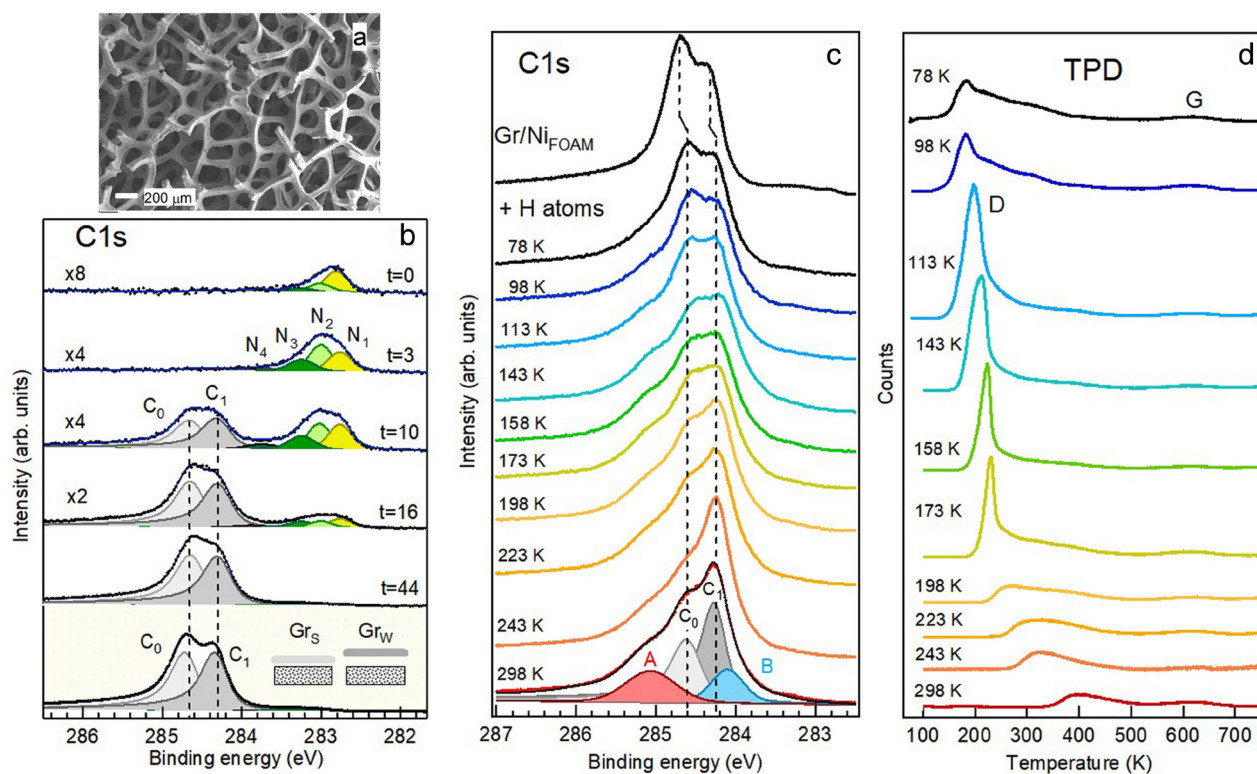


Figure 1. (a) SEM images of the Ni foam; (b) C1s spectra measured during the growth of the graphene layer after 0, 3, 10, 16 and 44 minutes of exposure of the foam substrate to ethylene at 773 K and (bottom) measured at RT after the growth; (c) C1s spectra acquired on the Gr/foam sample hydrogenated with the same H dose at the temperatures T_H indicated on the left; (d) TPD curves measured during the thermal annealing of the Gr/foam sample hydrogenated at the temperatures T_H reported on the left side.

Acknowledgments

We acknowledge Elettra Sincrotrone Trieste for providing access to its synchrotron radiation facilities and for financial support. GP, FZ, RF and RL acknowledge support from grant HPRIDE ("Production and storage of hydrogen in nanostructured graphene/nickel systems"; Grant No. 85-2017-15316), funded by LazioInnova/ Regione Lazio in the frame "Progetti di Gruppi di Ricerca" (L.R. Lazio 13/08).

Original paper

G. Petrone *et al.*, Carbon **199**, 357 (2022)

G. Petrone^{1,a}, F. Zarotti^{1,b}, P. Lacovig², D. Lizzit^{2,c}, E. Tosi^{2,d}, R. Felici³, S. Lizzit², R. Larciprete¹

¹ CNR-ISC, Roma, Italy

² Elettra - Sincrotrone Trieste S.C.p.A., Trieste, Italy

³ CNR-SPIN, Roma, Italy

Present affiliations:

^a CNR-IMM, Roma, Italy

^b Department of Electronic Engineering, University "Tor Vergata", Roma, Italy

^c Polytechnic Department of Engineering and Architecture, University of Udine, Udine, Italy.

^d ICMM-CSIC, Madrid, Spain

e-mail: rosanna.larciprete@isc.cnr.it

Cavitation in silica-filled styrene-butadiene rubber nanocomposite upon cyclic tension resolved by in-situ synchrotron radiation tomography

Eletra | SYRMEP

Silica-filled rubber nanocomposites are widely used in automotive, sealing and damping applications because of their ability to withstand repeated strains. However, the mechanical durability of these materials is drastically influenced by the formation of strain-induced cracks during the material use. These cracks are characterized by the development of cavities that grow and propagate through the rubber matrix upon mechanical cycling, engendering the failure of the component. In the present works, SR μ CT (Synchrotron Radiation micro-Computed Tomography) has been used to study cavitation phenomena in silica-filled styrene-butadiene rubber nanocomposite cured at different temperatures (150°C and 170°C) upon cyclic tensile loading, prior to and after a thermal exposure (120°C for 48 h in air). Different curing temperatures are selected to potentially vary the filler-matrix interactions, whereas the thermal exposure is conducted to mimic, in an accelerated way, any potential structural changes occurring during the material utilization. The samples are pre-fatigued in our laboratory and scanned at the SYRMEP beamline. To this end, pre-fatigued dumbbell samples are mounted in a Deben CT5000 miniature tensile/compressive machine and are investigated using the propagation-based phase contrast imaging mode with a sample-to-detector distance set to 120 mm. The observations of the samples are performed after applying an extension of 10 mm with the Deben machine to re-open any potential cavities induced by the pre-applied tensile cycles. The average energy of the polychromatic beam is set to 20 keV, using a silicon filter with a thickness of 1.5 mm. The materials are imaged with a water-cooled 16-bit scientific sCMOS microscope camera whose effective pixel size is set at 0.9 $\mu\text{m} \times 0.9 \mu\text{m}$, yielding a maximum field of view of about 19 mm \times 19 mm. The detector system is equipped with a motorized system hosting four scintillator screens. A 17- μm -thick GGG:Eu scintillator screen

(ESRF, Grenoble, France) is selected for this experiment. For each imaging, 1800 radiographs are recorded during continuous rotation over a total scan angle of 180°. The exposure time/projection is set to 150 ms. A comparison with our laboratory μ CT measurements has been first conducted to highlight the benefit of SR μ CT. The results show that the minimum detectable objects are 3 μm with the SR μ CT instead of 20 μm with the μ CT, and that the observable volume fraction is 2% instead of 0.4%. Thus, SR μ CT provides around 5-6 times more resolution for the filler's detection when scanning under in-situ conditions (with a miniature testing machine) compared to our laboratory μ CT. The strain at break of the nanocomposites, measured in our laboratory by monotonic tensile testing, increases in the following material order: cured at 150°C followed by thermal exposure (229% \pm 11%) < cured at 170°C followed by thermal exposure (246% \pm 10%) < cured at 150°C (309% \pm 14%) < cured at 170°C (337% \pm 9%). Accordingly, the thermal exposure decreases the strain at break of the rubber nanocomposites. Based on these observations, samples have been subjected to fatigue tensile loading applying a maximum strain of approximately 70% of their strain at break for different numbers of cycle. The cavities are carefully inspected to identify the phenomena responsible for their formation. To this end, an inspection of several agglomerate-cavity pairs is conducted in the case of the sample cured at 170°C and cycled 33 times at 70% of elongation at break. Three types of cavitation phenomenon have been identified: (a) debonding at the agglomerate poles, (b) internal agglomerate fracture and (c) combination of debonding at the poles and internal agglomerate fracture. These phenomena are represented in Figs. 1 (a-c), respectively, showing a typical 3D rendering of a cavity-filler pair with the filler represented in yellow and the cavity

represented in red. The quantification of the cavity characteristics in terms of equivalent diameter and volume fraction is extracted from SR μ CT data at different numbers of tensile cycle (Figs. 1 (d-e)). When comparing the samples cured at 150°C and 170°C, the latter exhibits smaller but more cavities in the studied range of cycles. The volume fraction of the cavities is more important in the sample cured at 170°C above 33 cycles, demonstrating a lower fatigue life. The growth in the number of cavities and their decrease in size prove that fatigue (around 1000 cycles) is mainly governed by the initiation of small cavities. Moreover, changes in the structural parameters occur between the 1st cycle and 33rd cycle, whereas changes are less marked when approaching 1000 cycles. Cavitation in the rubber composite cured at 150°C is dominated by debonding at the agglomerate's poles, whereas cavitation in the rubber composite cured at 170°C is evenly dominated among the three categories. The curing temperature is probably dictating the filler-matrix interaction and hence filler-matrix debonding at the origin of cavitation. Thermal exposure induces fewer cavities in the material, but their size is larger than in the sample that have not been submitted to thermal exposure. Our study has revealed the benefit of SR μ CT compared to laboratory μ CT to reveal cavitation phenomena in term of resolution. The gathered data in terms of cavitation aspects will enable to improve material formulation and processing conditions, the final aim being the extension of material durability. Another important aspect to investigate is the interfacial region structure between the filler and the polymer matrix, requiring the use of micro-/nano-probe techniques.

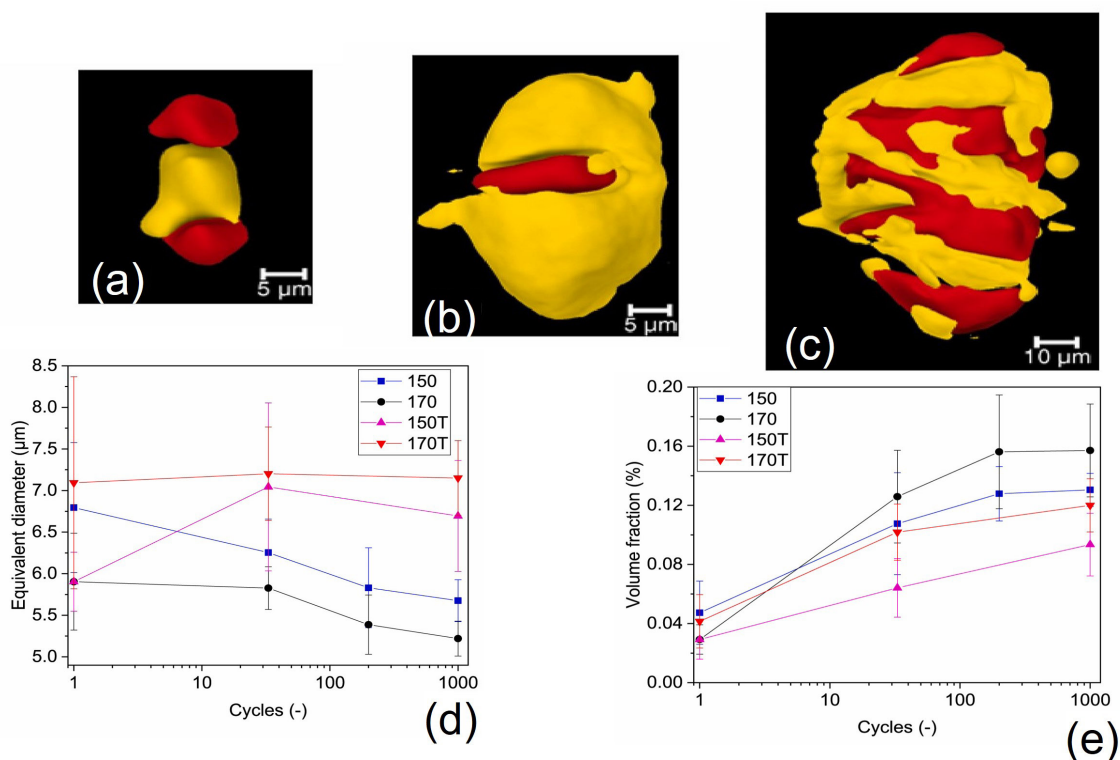


Figure 1. 3D rendering of the three phenomena of cavitation identified in this work in the case of the sample cured at 170°C and cycled 33 times at 70% of elongation at break: (a) debonding at the poles; (b) agglomerate fracture; and (c) combination of debonding at the poles and agglomerate fracture (filler in yellow, cavity in red); and evolution of (d) equivalent diameter; and (e) volume fraction as a function of the number of cycles for the samples cured at 150°C (150), cured at 170°C (170), cured at 150°C followed by thermal exposure (150T), and cured at 170°C followed by thermal exposure (170T).

Acknowledgments

This research was conducted within the framework of the IBPG program supported by the Luxembourg National Research Fund (FNR), Project reference IPBG16/11514551/TireMat-Tech. The authors are grateful to Sébastien Gergen (LIST) for conducting the mechanical testing. The authors acknowledge the SYRMEP specialists, Giuliana Tromba, Adriano Contillo, Konstantinos Giannoukos and Giulia Saccomano, for all their support during the testing at the Synchrotron Elettra.

Original paper

C.E. Federico et al., *Compos. B: Eng.* **247**, 110337 (2022); DOI:10.1016/j.compositesb.2022.110337

License Number 5585390056533 to reuse contents of the original paper.

C.E. Federico¹, Y. Fleming¹, O. Kotecky², R. Rommel², A.-M. Philippe¹, S. Westermann¹, F. Addiego¹

¹ Materials Research and Technology Department, Luxembourg Institute of Science and Technology, Esch-sur-Alzette, Luxembourg
² Goodyear Innovation Center Luxembourg, Colmar-Berg, Luxembourg

e-mail: frederic.addiego@list.lu

Role of defects in colored TiO₂ hollow spheres for photocatalytic applications

Elettra | VUV-Photoemission

AOPs (Photocatalytic Advanced Oxidation Processes), such as heterogeneous catalysis, can accelerate oxidation and degradation of a wide range of organic pollutants, like dyes and drugs, in wastewater. Semiconductors are often used in AOPs applications as their interaction with light gives origin to excitons, whose dissociation induces the formation of electron-hole pairs (e^-h^+) and radicals that can degrade and completely mineralize pollutant molecules. As a rule of thumb, enhancing the creation of photogenerated e^-h^+ and slowing their charge recombination are necessary to ensure high photocatalytic activity of semiconductor materials. In this context, TiO₂ (titania) is one of the most attractive photoactive semiconductors, in consideration of its non-toxicity, photostability and high versatility. However, the fast charge carriers' recombination and wide bandgap of stoichiometric TiO₂ (in the range of 3.0-3.2 eV) limit its efficiency and the exploitation of solar light as a source of energy for heterogeneous photocatalysis. Here, we report on the optical and electronic properties of colored THSs (TiO₂ hollow spheres) that show efficient photodegradation of a targeted antibiotic (Ciprofloxacin, CIP) in water under sunlight irradiation. Fig. 1a summarizes the synthesis procedure of the THSs: a sacrificial core of PMMA (PolyMethylMethAcrylate) is covered with a shell of amorphous TiO₂ nanoparticles (step 1,2); after removal of the PMMA core by calcination at 500 °C, hollow spheres of 350 nm diameter and composed of white TiO₂ (anatase phase) are formed (step 3); hydrogenation by CVD (Chemical Vapor Deposition) gives rise to increasingly darker gray THSs (step 4-6). Catalytic tests demonstrate that THSs display a superior degradation rate of Ciprofloxacin under simulated solar light with respect to reference TiO₂ (CIP degradation only at 61% with a kinetic constant of $7.2 \cdot 10^{-3} \text{ min}^{-1}$). The best performance is seen for gray and dark gray THSs (G_THS and DG_THS, respectively).

In detail, G_THS can degrade 82% of CIP in 6 hours with a kinetic constant of $11.9 \cdot 10^{-3} \text{ min}^{-1}$. Remarkably, the high hydrogenation content of DG_THS80 is accompanied by reduced photocatalytic activity among the colored samples. This behavior can be attributed to the synergistic effect of several factors. The hierarchically structured THSs are expected to combine high surface area and strong light confinement within a small volume, thus increasing the light absorption probability of TiO₂. Sub-stoichiometric (TiO_{2-x}) colored titania is considered one of the best sunlight harvesters, as it can absorb light from the UV (ultraviolet) to the IR (infrared) region. Finally, defects, such as Ti³⁺ sites and oxygen OV (oxygen vacancies), display enhanced photoactivity in several oxidation reactions under visible light compared to stoichiometric TiO₂. In our work we explore the relation between defects and the enhanced photocatalytic behavior of colored THSs. Optical measurements (Fig. 1b) reveal the presence of a broad absorption feature in the low-energy spectral region (onset at about 500 nm wavelength) only for colored THSs. Its intensity increases for increasingly darker gray THSs, thus making a link between the optical and catalytic behavior of the THSs. The origin of the new absorption feature could be associated to the presence of defect-induced states within the TiO₂ bandgap below the CB (conduction band) minimum. In order to directly access the properties of these states we combined synchrotron-based XPS (X-ray Photoemission Spectroscopy), performed at the VUV Photoemission beamline of Elettra, and Electron Paramagnetic Resonance (EPR). XPS data (Fig. 1c) are representative of the near surface region of the THSs. For all THSs the O²⁻/Ti⁴⁺ stoichiometric ratio (P1/D1) is close to 2. Differences in the high binding energy side of the O1s spectra (P2-P4) are attributed to the adsorption of OH, C-O, C-OH and H₂O. In particular, the increasing H₂O signal (P4/P1) for darker gray THSs is an indirect signature

of higher surface density of OV, with which H₂O molecules tend to bind. A little and constant amount of Ti³⁺ defects is seen in the Ti2p core levels of all THSs (D2). EPR data (Fig. 1d) provide a picture of the bulk electronic structure of the THSs. The sharp peak at about 345 mT is attributed to bulk OV, which form upon thermal treatment at 500 °C and remain stable for CVD processes occurring at lower temperature (step 4). Instead, the broad peak at higher magnetic field emerges only after hydrogenation. This feature is associated with the presence of bulk Ti³⁺ defects (color centers) and explains the optical properties of the THSs. The XPS valence band analysis (Fig. 1c) uses resonant conditions (photon energy 469 eV) in order to probe the defect states within the bandgap of TiO₂ with highest sensitivity. Strong O2p-related states between ≈ 3 and 10 eV (V1) and low-intensity defect states at ≈ 1 eV (V2, better visualized in the inset) are detected for all THSs. The V2/V1 ratio can be used to estimate the concentration of the defects in the near-surface region of the samples. As V2/V1 increases for darker gray THSs and the Ti³⁺ concentration remains stable at the surface, the concentration of surface OV increases with the CVD treatments. This allows us to conclude that the enhanced photocatalytic activity in colored THSs is directly related to the presence of OV on the catalyst's surface. In conclusion, the use of two complementary techniques provides a complete picture of the role of surface and bulk defects in the optical and catalytic properties of colored THSs.

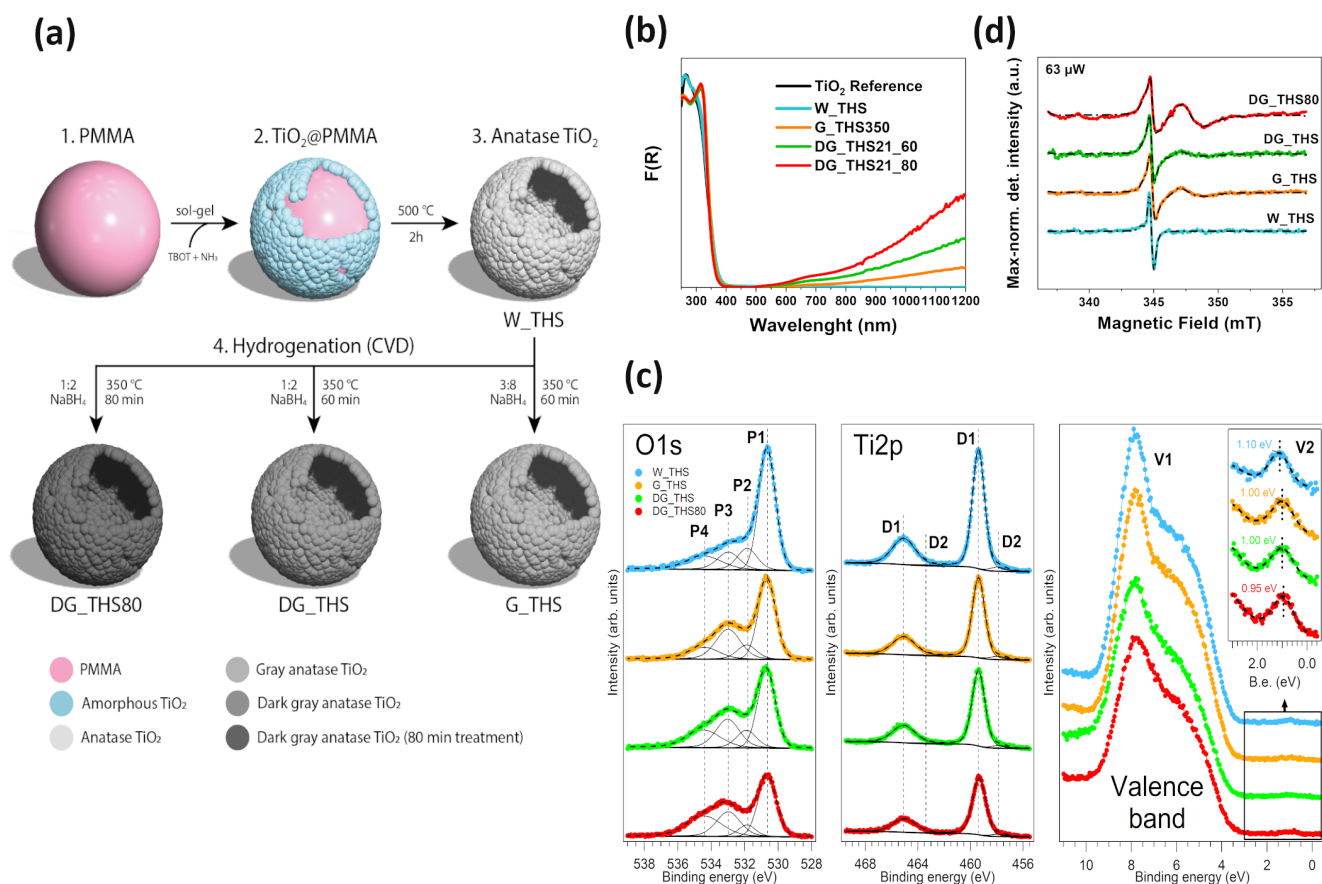


Figure 1. (a) Synthesis scheme of THSs; (b) F(R) spectra calculated through Kubelka–Munk functions showing the optical properties for all the THSs including TiO₂ reference; (c) O1s, Ti2p (photon energy 750 eV) and valence band (photon energy 469 eV) XPS spectra of the THSs. (d) Stacked EPR spectra of the THSs.

Acknowledgments

This work was carried out within the agreement “Convenzione operativa per collaborazione scientifica tra CNR ISM e Dipartimento di Scienze Molecolari e Nanosistemi Università Ca’ Foscari Venezia (Prot.n. 709, 14/04/2021)”. Partial support through the project EUROFEL-ROADMAP ESFRI was gratefully acknowledged. The Kempe Foundation and the Knut och Alice Wallenberg Foundation were acknowledged for financial support. Elettra Sincrotrone Trieste was acknowledged for providing access to its synchrotron radiation facilities and for financial support under the SUI international project.

Original paper

L. Liccardo *et al.*, *Adv. Funct. Mater.* **33**, 2212486 (2023); DOI: 10.1002/adfm.202212486

L. Liccardo¹, M. Bordin¹, P. M. Sheverdyayeva², M. Belli³, P. Moras², A. Vomiero^{1,4}, E. Moretti¹

¹ Department of Molecular Sciences and Nanosystems, Ca’ Foscari University of Venice, Venezia Mestre, Italy

² ISM-CNR, Trieste, Italy

³ IMM-CNR, Agrate Brianza, Italy

⁴ Department of Engineering Sciences and Mathematics, Division of Materials Science, Luleå University of Technology, Luleå, Sweden

e-mail: alberto.vomiero@unive.it; elisa.moretti@unive.it

Tuning thermal expansion properties in materials by insertion of guest molecules

Elettra | Xpress

Materials are expected to expand with increasing temperature due to the anharmonicity of chemical bonds. Surprisingly, a few of them show an opposite trend, principally due to the flexibility of their crystal structure networks or to magnetic or electronic properties. Materials with NTE (negative thermal expansion) properties have been attracting great technological interest due to their potential use in mechanical, electronic and optical applications. These include mirror supports and solar panels for spatial applications, thermoelectric modules, microchips, precision manufacturing and even dental fillings. Typically, materials with negative thermal expansion are combined with those with positive thermal expansion in order to engineer composites with very low or zero thermal expansion. This strategy is not always viable as the differences in thermal expansion can give rise to cracking or other types of failure at the interfaces between the components of the composite and thus other approaches are needed. In this study by x-ray diffraction as a function of pressure and temperature at the Xpress beamline of Elettra, we show how a material could have its NTE properties tuned by insertion of guest molecules in its structure.

The porous aluminophosphate $\text{AlPO}_4\text{-17}$, with a hexagonal structure of the same type as the zeolite mineral erionite, is the oxide, which exhibits the highest coefficient of negative thermal expansion. This zeolite-type material is built up of 4-, 6-, 8- and 12-membered rings of alternating AlO_4 and PO_4 tetrahedra forming large erionite cages, with a diameter of 6.556 Å, and columns of smaller cancrinite cages linked to double six-membered rings of tetrahedra. The NTE mechanism in this material corresponds to a structural contraction around the empty pores and cages due to thermally-excited transverse motions of oxygen atoms bridging the AlO_4 and PO_4 tetrahedra, which bring the Al and P atoms closer

together. The insertion of small molecules into the empty cages of $\text{AlPO}_4\text{-17}$ offers a means to modify its thermal expansion properties by reducing this structural contraction. Atoms or molecules with a maximum kinetic diameter of about 3.4 Å can diffuse into the porosity of the $\text{AlPO}_4\text{-17}$ structure via the 8-membered rings of the structural framework. In the present study, high quality, single-crystal and powder XRD (X-Ray Diffraction) measurements were used to monitor the NTE in $\text{AlPO}_4\text{-17}$. The insertion of oxygen molecules with a kinetic diameter of 3.46 Å at high pressure into the empty cages of $\text{AlPO}_4\text{-17}$ was found to tune its very strong NTE. The experiments were performed at the Xpress beamline, using a high-pressure DAC (diamond anvil cell) in a closed-cycle helium cryostat with very precise control of the pressure and temperature.

Under atmospheric conditions, $\text{AlPO}_4\text{-17}$ contains water molecules in the cages and pores of its structure and thus this hydrated $\text{AlPO}_4\text{-17}$ was first dehydrated under vacuum at 110°C before the experiment. The dehydrated form (with empty pores) was loaded with liquid oxygen cryogenically and, then, compressed by using a DAC to promote the insertion of molecular oxygen in the pores of the structure. Ruby, samarium-doped, strontium borate and gold were included in the DAC along with the sample to monitor in situ the pressure and the temperature of the sample by luminescence for the first two and by XRD for the latter (P-T calibrants). The temperature was also checked using a thermocouple placed on one of the diamond anvils of the DAC. The structure of the oxygen-filled material was determined in situ at high-pressure by single-crystal XRD (see Fig. 1). Nine O_2 molecules were found to be located in the large erionite cages of the structure increasing their diameter from 6.556 Å at ambient pressure in the empty form to 6.633 Å in the oxygen-filled material. This insertion of oxygen also results in

an expansion of the structure in the xy plane. Powder XRD with a much larger sample to detector distance providing greater precision of the unit-cell parameters allowed us to determine the thermal expansion coefficient upon cooling at a pressure of 0.38 GPa, by using a closed-cycle He-cryostat. The pressure was carefully controlled after each change in temperature. Whereas the volumetric thermal expansion only exhibits a small change with respect to $\text{AlPO}_4\text{-17}$ (with empty pores) at ambient pressure, the thermal expansion coefficients for the oxygen-filled material along the two main crystallographic directions are surprisingly different. While the thermal expansion along the equivalent hexagonal *a* and *b* directions decreases almost to zero upon molecular insertion, the negative expansion along *c* becomes 7 times (!) larger, see Fig. 1. Such highly anisotropic thermal expansion properties are of great interest for mechanical and optical applications.

Molecular guest insertion is thus a very powerful tool for tuning the thermal expansion properties of porous materials opening a way to design materials with zero thermal expansion. High-pressure, variable temperature XRD is the technique of choice to determine the effect of guest content on the thermal expansion properties of these porous materials. As the insertion of the oxygen molecules is reversible on pressure release, the insertion of non-volatile guest species or the polymerization of guest molecules under pressure could be used as a strategy to design composites for potential applications, in particular in highly stable supports for electronic and optical devices.

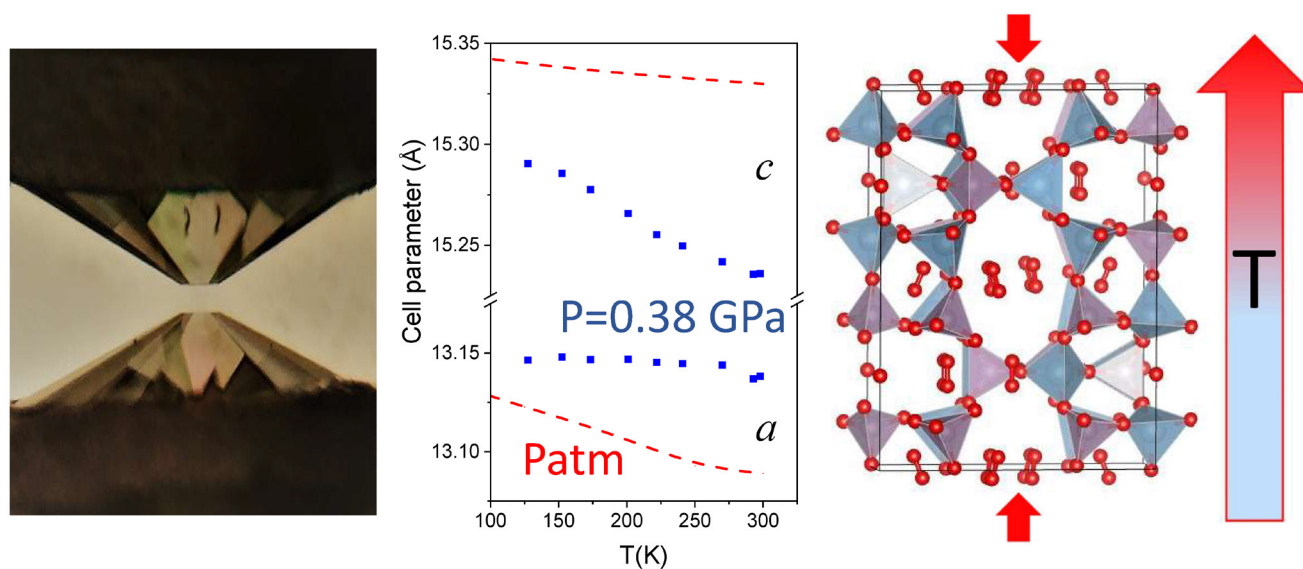


Figure 1. (left) View of the diamond anvil cell, (center) Unit cell parameters (blue square symbols) of oxygen-filled AlPO₄-17 powder at 0.38 GPa as a function of temperature. Data (red dashed line) for empty AlPO₄-17 at ambient pressure are from Attfield and Sleight (1998). (right) Crystal structure of O₂-filled AlPO₄-17 at 0.5 GPa obtained from single-crystal. Reprinted (Adapted or Reprinted in part) with permission from F.G. Alabarse *et al.*, *J. Phys. Chem. Lett.* **13**, 9390 (2022). Copyright 2022 American Chemical Society.

Acknowledgments

The research leading to this result has been supported by the project CALIPSOplus under Grant Agreement 730872 from the EU Framework Programme for Research and Innovation HORIZON 2020. We acknowledge Elettra Sincrotrone Trieste for providing access to its synchrotron radiation facilities and we thank R. Borghes, V. Chenda and I. Cudin for assistance in using beamline Xpress.

Original paper

F.G. Alabarse *et al.*, *J. Phys. Chem. Lett.* **13**, 9390 (2022); DOI:10.1021/acs.jpcclett.2c02718

F.G. Alabarse¹, B. Baptiste², B. Joseph¹, J. Haines³

¹ Elettra - Sincrotrone Trieste S.C.p.A., Trieste, Italy

² Institute of Mineralogy, Physics of Materials, and Astrochemistry (IMPMC), CNRS Sorbonne University, Paris, France

³ ICGM, CNRS, University of Montpellier, ENSCM, Montpellier, France

e-mail: Julien.Haines@umontpellier.fr

Confused-Prism[5]arene: a conformationally adaptive host with stereoselective guest inclusion

Elettra | XRD1

Synthetic macrocycles have found applications in fields such as molecular recognition, catalysis, and as building blocks in self-assembled architectures. Taking inspiration from natural receptors, synthetic macrocyclic hosts are designed to incorporate a biomimetic internal cavity which can host complementary guests. Recently, much effort has been devoted to synthesise deep-cavity macrocycles based on naphthol monomers, such as naphthotubes, calixnaphtharene, oxatubarene and saucerarenes. A characteristic of such systems is that they exhibit both high conformational mobility and adaptive behaviour in the presence of complementary guests. Similar conformational adaptive processes are diffuse in biological systems. For example, protein–substrate binding often involves conformational changes of the protein, which can occur either prior to the ligand binding event (“conformational selection”), or as a consequence of the ligand binding event (“induced fit”).

In 2020, we reported the first examples of a new class of macrocycles named prismarenes, composed of methylene-bridged 2,6-dialkoxynaphthalene monomeric units. Prismarenes show a deep π -electron rich aromatic cavity which exhibits a high affinity for ammonium guests. The solid-state structures of two types of prismarenes were described in the first report: symmetric pentameric (PrS[5]^{Me}, Figure 1a, left) and hexameric (PrS[6]^{Me}, Figure 1a, right) prismarenes. A third, asymmetric pentameric variant called confused-prism[5]arene (c-PrS[5]^{Me}, Figure 1a, middle) was also observed in solution. Prismarenes exhibit planar chirality and each stereogenic naphthalene unit can be described with pR and pS descriptors. Thus, c-PrS[5]^{Me} can adopt 32 conformations of different planar chiralities (Figure 1b), which can interconvert by rotation of the naphthalene units around the methylene bridges.

In the symmetric prism[n]arenes, all the naphthol rings are linked at their 1,5-positions and the misalignment of the C–C bridging bonds at positions 1 and 5 partially hinders the mutual rotation of the naphthalene moieties. However, c-PrS[5]^{Me} contains one naphthalene group with a 1,4-bridging arrangement. In this case, the alignment of the two C–C bridging single bonds on positions 1 and 4 means that the naphthalene moiety can rotate more freely. This makes it as an ideal candidate to study conformational adaptive processes in the presence of suitable guests.

X-ray diffraction data were obtained at XRD1 beamline of Elettra for free c-PrS[5]^{Me} and host-guest complexes of c-PrS[5]^{Me} with both 1²⁺ and 2⁺ as guests (Figure 1c). The atomic-scale resolution of the data obtained allowed all the relevant intramolecular and intermolecular (host/guest) interactions to be identified in the various structures. For free c-PrS[5]^{Me}, the conformation of the 1,4-bridged naphthalene flap is opposite to those of the four 1,5-bridged naphthalene moieties (racemic mixture of pS(pR)₄/pR(pS)₄ enantiomers). Our previously reported PrS[5]^{Me} analogues showed racemic mixtures of all-pR / all-pS conformations of the 1,5-naphthalene moieties.

Structural analysis of the pseudorotaxane 1²⁺@c-PrS[5]^{Me} shows that the crystals are composed of a racemic mixture of homochiral all-pS / all-pR conformations. The central bicyclic unit of 1²⁺ is inserted symmetrically in the host, with the two N⁺ atoms of 1²⁺ equidistant from the mean plane of the 5 methylene CH₂ bridges of c-PrS[5]^{Me} (Figure 1d). Upon threading of the 1,4-dihexyl-DABCO (1²⁺) axle, the 1,4-bridged naphthalene ring of the complexed host c-PrS[5]^{Me} opens up to become a nearly regular pentagonal prism. The conformation of the pentagonal prism is stabilized by a network of nine intramolecular H-bonds formed by the methoxy groups

and aromatic H atoms of adjacent naphthalene moieties. Two of these stabilizing H bonding interactions would be lost in the heterochiral orientations of the naphthalene flap, in addition to the presence of a destabilizing repulsive interaction between two OMe groups.

With regard to 2⁺, the x-ray investigation confirmed the stereoselective formation of the homochiral 2⁺@c-PrS[5]^{Me} complex (Figures 1d). However, due to its lower bulk, the 1,4-bridged ring rotation is significantly lower than that observed for 1²⁺@c-PrS[5]^{Me}. The intramolecular H-bond network involving adjacent naphthalene groups is also observed for this complex. However, the H-bond interactions involving the 1,4-linked naphthalene show a much less significant direction characteristic due to the smaller flap rotation. Upon complexation with the asymmetric guest 2⁺, the potential stereochemistry of the complexes is more complicated as 2⁺ may adopt one of two non-equivalent orientations in the macrocycle (up/down). The X-ray structure shows that the directional stereochemistry of the racemic complex is predominantly up (U)-2⁺@(pR)₅-c-PrS[5]^{Me} / (U)-2⁺@(pS)₅-c-PrS[5]^{Me}. However, about 30% of the complexes are present in the inverted down orientation. In the down orientation, stabilizing host-guest ammonium interactions observed in the up conformation are largely absent.

In conclusion, c-PrS[5]^{Me} shows conformationally adaptive stereoselective behaviour. After inclusion of the ammonium axle, a homochiral conformation of the host that inverts the planar chirality of the 1,4-naphthalene flap in free c-PrS[5]^{Me} is observed. The homochiral complexes are stabilized by favourable intramolecular and intermolecular interactions. In addition, directional threading is observed in the presence of asymmetric axles.

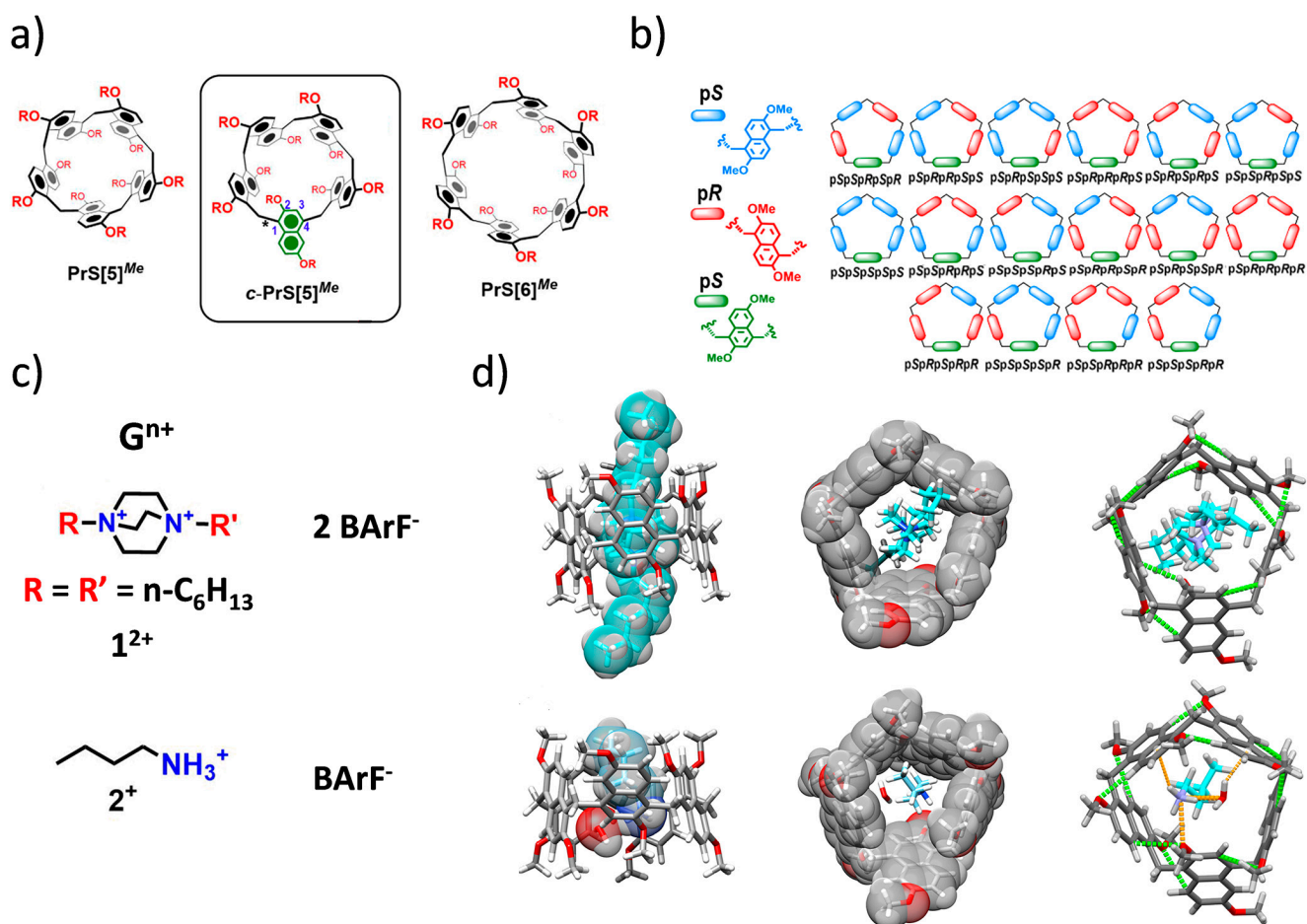


Figure 1. (a) Prismatic macrocycles based on methylene-bridged 2,6-dimethoxynaphthalene monomeric units: Left – pentameric PrS[5]^{Me}; Center – center-confused pentameric c-PrS[5]^{Me}; Right – hexameric PrS[6]^{Me}; (b) Schematic representation of 16 diastereoisomers c-PrS[5]^{Me} in which the 1,4 naphthalene shows pS chirality. A further 16 have the 1,4 flap with pR chirality; (c) Guests (Gn⁺) in the host/guest complexes of c-PrS[5]^{Me}: 1²⁺ = 1,4-dihexyl DABCO (1,4-diaxabicyclo[2.2.2]octane), 2⁺ = n-butylammonium, BARF⁻ = tetrakis[3,5-bis(trifluoromethyl)phenyl]borate. (d) X-ray structural models of the host/guest complexes: 1²⁺@(pR)₅-c-PrS[5]^{Me}, (U)-2⁺@(pR)₅-c-PrS[5]^{Me}. Left: side views of the complexes with the guest molecules as vdW spheres. Center: top views of the complexes with the host molecules as vdW spheres. Right: bottom views of the complexes with the stabilizing intramolecular C-H...OMe H-bonds as dashed green lines and the host-guest interactions as dashed orange lines.

Original paper

P. Della Sala et al., Chem. Eur. J. **29**, e202203030 (2023); DOI: 10.1002/chem.202203030

P. Della Sala¹, R. del Regno¹, A. Capobianco¹, V. Iuliano¹, C. Talotta¹, S. Geremia², N. Hickey², P. Neri¹, C. Gaeta¹

¹ Department of Chemistry and Biology "A. Zambelli", University of Salerno, Salerno, Italy

² Department of Chemical and Pharmaceutical Sciences, University of Trieste, Trieste, Italy

e-mail: sgeremia@units.it; cgaeta@unisa.it; acapobianco@unisa.it



Life Sciences, Environmental Science and Cultural Heritage



A deep look at two Stradivari's violins from micro to nanoscale

Elettra | SISSI-Bio

Antonio Stradivari is considered one of the best luthiers of all the times. The incredible aesthetic and acoustic qualities of his masterpieces are due to the meticulous choice of wood, but also to the manufacturing processes. In the last years, several scientific studies have been focused on the characterisation of the varnish coating system applied, which provides protection against moisture, damage and biological growth. However, less attention has been devoted to the other treatments. The use by Antonio Stradivari of a ground coat (also defined as preparation layer), directly spread on the wood surface before the varnish layers, represents a long-debated question among the experts of his work. Some studies revealed the presence of protein layer on the wood surface through chemical staining and GC-MS (Gas Chromatography-Mass Spectrometry) analysis, while some others detected only a layer of drying oil at the interface between the varnish and the wood. Recently, our group provided additional evidences of the presence of proteinaceous materials applied beneath the varnish of Stradivari's instruments using non-invasive FTIR (Fourier Transform Infrared) spectroscopy. However, the low spectral quality achievable by portable instruments, associated with the complexity of the coating system showed by some Stradivari's instruments at the microscopic level, required the application of more sophisticated methods for characterising the chemical nature of the preparation layer. This was the case of two cross-sectioned micro-samples collected from the top plates of two Stradivari violins, the Toscano 1690 and the San Lorenzo 1718 (Fig. 1) that have been studied at the SISSI-Bio beamline of Elettra Sincrotrone Trieste. Preliminary observation of the UV-light images in Fig. 1 (a,b) showed

coating systems possibly composed by few thin layers (indicated by V - varnish layer; P - preparation layer; and W - wood substrate), difficult to differentiate from each other. FTIR microscopy measurements in reflection mode, exploiting the advantages of the high brilliance of synchrotron radiation, were performed in two regions at the interface between the first row of the wood cells and the varnish layers, where the presence of a proteinaceous material was expected. Chemical maps generated by integrating the Amide I spectral range suggested the potential distribution of proteins within the ground layer, deeply penetrated into the first rows of wood cells. However, deviations in the shape and proportions of the Amide I and Amide II bands, challenged the definitive assignment to proteinaceous materials, especially in the case of the Toscano violin (Fig. 1(a-d)). With the aim of obtaining further robust evidence regarding the materials used by Stradivari in the construction of his violins, also the infrared s-SNOM (scattering-type Scanning Near-field Optical Microscopy) was employed. This technique combines an AFM (Atomic Force Microscope) with an Infrared spectrometer enabling the simultaneous collection of sample topography and the chemical information of the material composing the sample, reaching lateral resolutions of a few tens of nanometres. For these measurements, four areas labelled as SL-A, SL-B and Tos-A, Tos-B were analysed for the San Lorenzo and Toscano violins, respectively (Fig. 1 (box e,f)). The areas scanned with infrared s-SNOM showed morphological details, such as scratches, depressions, holes and dispersed particles, possibly reflecting the effects of manual polishing procedures. From the chemical point of view, the nano-resolved spectra collected on the San Lorenzo sample (Fig.1 (e)) showed the Amide I and

II bands, unequivocally confirming the presence of proteins within the preparation layer, in close proximity to the first row of wood cells. Since some proteinaceous hotspots have been also detected in the V and P layers, a possible displacement of some protein particles across the cross-section have been associated to the polishing treatments. Compared with the San Lorenzo sample, the s-SNOM spectra collected from areas Tos-A and Tos-B (Fig.1 (f)) of the Toscano violin exhibited more complex profiles revealing signals of Amide I and II bands accompanied by some overlapping features. In the Toscano sample, the proteins composing the ground coat are probably strongly diluted into the wooden matrix, partially degraded or affected by the formation of additional degradation products such as carboxylates. Summarizing, the analysis conducted on the two valuable violins Toscano 1690 and San Lorenzo 1718 demonstrates the complexity of the layering structure and the materials used, which may have undergone degradation over time. The nanometric-scale resolution offered by infrared s-SNOM is the key to resolve such fine chemical details, offering new insights for addressing the long-debated question regarding Stradivari's use of proteinaceous materials. Even if the analysis of only two samples is insufficient to allow for a generalization of the Stradivari's manufacturing process during his long career, the data presented provide unprecedented chemical details of the Toscano and San Lorenzo violins. These results undoubtedly encourage further application of the nano-FTIR microscopy, employed for the first time in cultural heritage field, and in particular on priceless musical instruments, for deeper investigations of challenging samples.

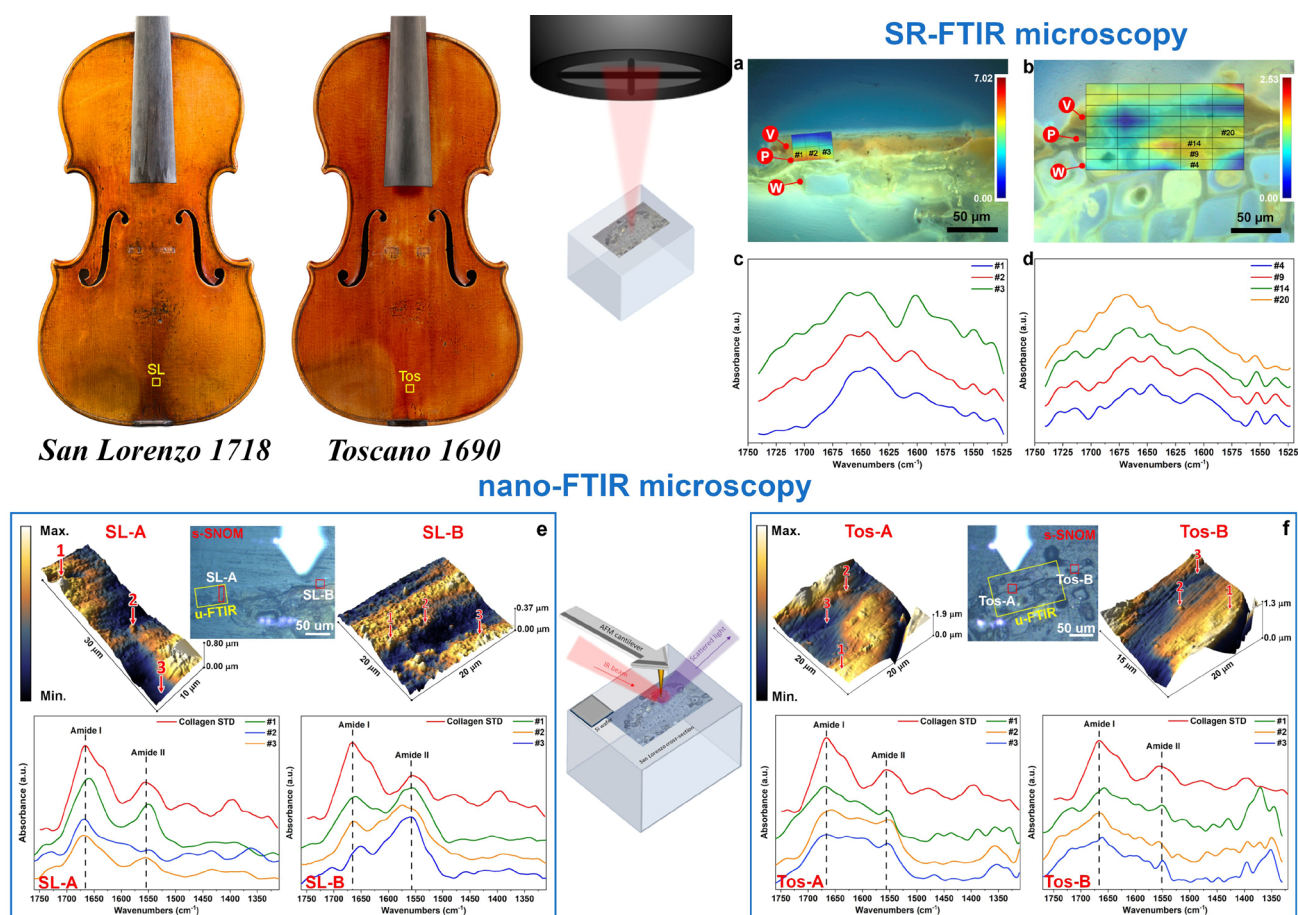


Figure 1. The two Stradivari's violins: San Lorenzo 1718 and Toscano 1690. (a,b) UV light images of the San Lorenzo and the Toscano cross-sectional samples, respectively. False-color infrared maps, obtained by integrating the Amide I spectral range, are superimposed. (c,d) SR-FTIR microspectra extracted from false-color maps of San Lorenzo and Toscano violins respectively. (e,f) s-SNOM measurements for San Lorenzo and Toscano violins respectively: the boxes report the optical images of the two cross-sections where the measured areas are highlighted by red frames and labeled as SL-A, SL-B (e) and Tos-A, Tos-B (f); the 3D AFM topography images and nano-IR spectra collected by s-SNOM on the areas SL-A and SL-B of the San Lorenzo violin and on the areas Tos-A and Tos-B of the Toscano one, respectively. Min and Max values of the scale bars of AFM images correspond to the z-axis values. The collected spectra are compared with the reference spectrum of standard type I collagen (red trace). The spatial resolution is around 20 nm. Adapted with permission from "C. Stani et al., *Anal. Chem.* 2022, **94** (43), 14815-14819, DOI: 10.1021/acs.analchem.2c02965. Copyright 2023 American Chemical Society.

Acknowledgments

The authors acknowledge Elettra Sincrotrone Trieste for providing access to the SISSI-Bio and CERIC-ERIC Consortium for access to experimental facilities and financial support (proposal no. 20182129 and 20195306).

Original paper

C. Stani *et al.*, *Anal. Chem.*, **94** 14815 (2022), DOI: 10.1021/acs.analchem.2c02965

C. Stani¹, C. Invernizzi², G. Birarda³, P. Davit⁴, L. Vaccari^{3*}, M. Malagodi^{2,5*}, M. Gulmini⁴, G. Fiocco^{2,5}

¹ CERIC-ERIC, Trieste, Italy

² Laboratorio Arvedi di Diagnostica non Invasiva (CISRIC), Università degli Studi di Pavia, Cremona, Italy

³ Elettra - Sincrotrone Trieste S.C.p.A., Trieste, Italy

⁴ Dipartimento di Chimica, Università degli Studi di Torino, Torino, Italy

⁵ Dipartimento di Musicologia e Beni Culturali, Università degli Studi di Pavia, Cremona, Italy

e-mail: lisa.vaccari@elettra.eu; marco.malagodi@unipv.it

Variabilities in DNA methylation and intracellular proteins structure establish spectroscopic landscapes among subtypes of pancreatic cancer

Elettra | SISSI-Bio

PC (Pancreatic cancer) is the fourth most lethal neoplasm in the USA and seventh in the world. The 5-year survival rates are still below 10%. One of the reasons for this poor prognosis is the lack of specific and sensitive early diagnostic methods, which leads to late-stage disease at the time of diagnosis. New molecular detection and differentiation methods must be introduced to increase PC patient survival.

RHM (Raman hyperspectral mapping) is a molecular imaging technique that involves Raman spectroscopy measurements of adjacent parts of the studied sample, resulting in a tissue map image. Our study showed the RHM-based distinction among the three main types of pancreatic malignancies. Specifically, we investigated cPDAC (conventional pancreatic ductal adenocarcinoma), IPMC (intraductal papillary mucinous carcinoma), and AVAC (ampulla of Vater adenocarcinoma). These tumors are treated similarly in terms of clinical management, but recent reports suggest that they differ in prognostic factors occurrences, resulting in variations in PC patient survival.

To initiate the overview of insights into the PC biology that molecular spectroscopy might provide, we utilized FTIR (Fourier Transform Infrared) microspectroscopic imaging of PC samples. Knowledge of the spatial distribution of cancerous and noncancerous components of studied samples permitted the cognitive collection of RHM maps. Subsequently, we employed advanced statistical tools to extract PC spectral markers and explore their spectral differences. Furthermore, as a proof of concept of utilizing VS (vibrational spectroscopy)-based methods in the development of early PC diagnostic and subtyping technology, which requires automation, we studied the potential of deep networking, specifically CNNs (conventional neural networks), to distinguish AVAC, IPMC, and cPDAC from raw spectra selected from RHM maps. This approach allowed automatic

spectral classification without the need for human-dependent preprocessing or manual re-evaluation. First, however, the investigations in this project addressed the biomolecular context of PC. We aimed to introduce the epigenetically complex reality of PC and its influence on protein modifications. The goal was to extend beyond "single-gene" genetics and transcriptomics with their (not unsubstantial) hope to decipher the still-elusive "language" of these most malignant neoplasms and to find common and specific differences in their observable biomolecular signatures. VS might be an excellent tool supporting such an approach.

The results of our studies showed significant differences among cancer tissues of the studied PC groups. The main findings are the varying content of β -sheet-rich proteins within the PC cells and alterations in the relative DNA methylation level. Our CNN model efficiently differentiated PC groups with 94% accuracy. The usage of CNN in the classification task did not require Raman spectral data preprocessing and eliminated the need for extensive knowledge of statistical methodologies. The use of Raman imaging for PC subtyping was not described before, except in a recent preliminary report from our lab. This time our study started with FTIR microspectroscopy, to allow viewing the distribution of tissue components on a larger scale, recognizing their spatial heterogeneity. FTIR permitted analysis of the tumor stroma compartment and selection of the areas of interest for subsequent Raman measurements. RHM allowed spectral analyses of nuclear and cytoplasmic regions of PC cells separately. This was not possible with FTIR only, because of its relatively lower (in comparison to Raman) spatial resolution. Our combined approach facilitated the analysis of DNA methylation patterns and the secondary structure of intracellular proteins thus revealing the differences among the studied PC types. Our findings confirm the global hypomethylation status

of DNA in all PC types and are in line with the results described by other authors that cPDAC is associated with global hypomethylation. However, it was found that the DNA of IPMN (the benign precursor of IPMC) was not hypomethylated. Our results indicate that even though cancer arising from IPMN is slightly hypomethylated compared to benign pancreatic duct tissue, the DNA methylation ratio is highest among the other two PC types (IPMC and cPDAC). This might confirm that the DNA hypomethylation process is the domain of malignancy. Furthermore, the status of DNA methylation significantly differed between the studied PC groups. We were the first to compare the global DNA methylation levels among PC subtypes. Recognizing protein secondary structure by FTIR at Elettra was a subject of the classification of human glial tumors, however, no studies have investigated spectral differences in protein composition among PC subtypes. In our study, the analysis of NMF components associated with proteins of RHM spectra allowed us to determine the secondary structure of proteins in PC groups. We recognized the overall protein β -sheet richness. Their contents varied among the studied PC types and were particularly high in AVAC. Molecular spectroscopy combined with CNN technology is a powerful PC detection and subtyping tool. The molecular fingerprint of DNA methylation and β -sheet cytoplasmic proteins established by our results is different for the main PC groups and allowed the subtyping of pancreatic tumors, which can improve patient management and increase their survival. Our observations are of key importance in understanding the variability of PC and allow translation of the methodology into clinical practice by utilizing liquid biopsy testing.

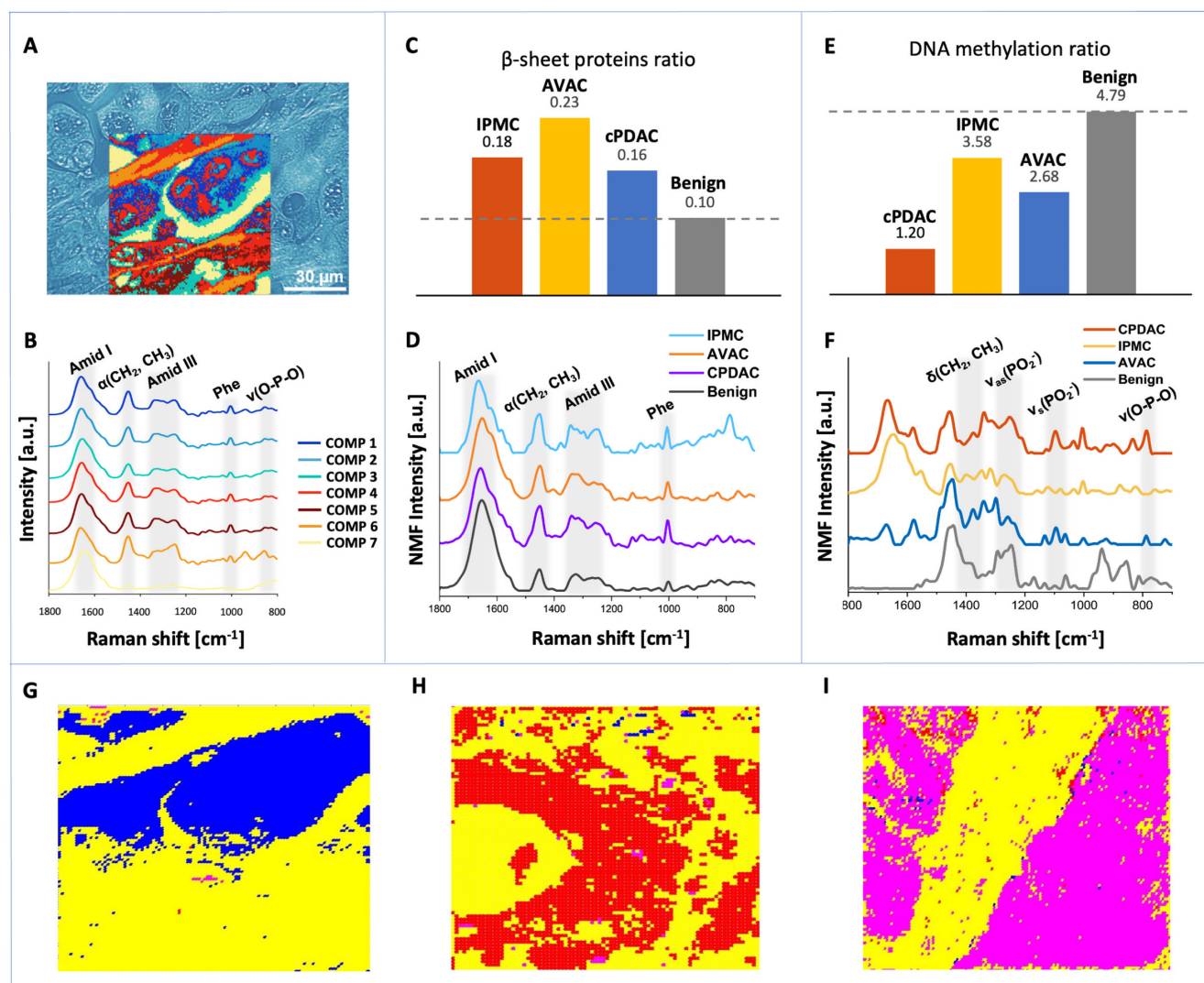


Figure 1. (A–B) Raman molecular imaging of AVAC tissue. (A) The optical unstained tissue image with superimposed HCA map, and (B) the corresponding Raman spectra from the HCA (the color of each corresponds to the color of the cluster in the HCA map); (C–D) Spectral marker bands of proteins in NMF components of studied PC types and benign pancreatic duct tissue. (C) The relation between Raman bands characteristic for proteins' β -sheet secondary structure (1690–1668 cm^{-1} , β -sheet amide I to 1750–1514 cm^{-1} , total amide I), and (D) a comparison plot of NMF components; (E–F) Spectral marker bands of DNA methylation in NMF components corresponding to nucleic acids. (E) The relation between Raman bands characteristic for DNA methylation in mean NMF components of each of the studied PC types and the control benign pancreatic duct tissue (1360–1420 cm^{-1} , $\delta(\text{CH}_2, \text{CH}_3)$ to 1050–1150 cm^{-1} , $\nu_s(\text{PO}_2^-)$), and (F) a comparison plot of NMF components calculated for nucleic acids of PC types and a benign pancreatic duct tissue; (G–I) Prediction map images as generated by the CNN, which classified each PC tumor with pixel colors - (G) the blue color for AVAC, (H) red for cPDAC, and (I) magenta for IPMC.

Acknowledgments

This work is supported by the National Science Centre, Poland under the "OPUS 19" project (Reg. No. UMO-2020/37/B/ST4/02990).

The research leading to this result has been supported by the project CALIPSOplus under Grant Agreement 730872 from the EU Framework Programme for Research and Innovation HORIZON 2020 (proposal number 20205239).

Original paper

K. Szymoński *et al.*, *Eur. J. Nucl. Med. Mol. Imaging* **50**, 1792 (2023); DOI: 10.1007/s00259-023-06121-7

K. Szymoński^{1,2}, E. Lipiec³, K. Sofińska³, K. Skirlińska-Nosek³, M. Czaja³, S. Seweryn³, N. Wilkosz³, G. Birarda⁴, F. Piccirilli⁴, L. Vaccari⁴, Ł. Chmura^{1,2}, J. Szpor², D. Adamek¹, M. Szymoński³

¹ Department of Pathomorphology, Jagiellonian University Medical College, Cracow, Poland

² Department of Pathomorphology, University Hospital, Cracow, Poland

³ M. Smoluchowski Institute of Physics, Jagiellonian University, Cracow, Poland

⁴ Elettra-Sincrotrone Trieste S.C.p. A, Trieste, Italy

e-mail: krzysztof.szymanski@uj.edu.pl

High resolution propagation-based lung imaging at clinically relevant X-ray dose levels

Elettra | SYRMEP

Lung diseases continue to present a major burden to public health as recently evidenced by the COVID pandemic. Due to the high air content virtually only CT (Computed Tomography) can be used to depict fine anatomical alterations within the lung. However, CT uses ionizing radiation causing side effects such as elevated cancer risk. Therefore, CT is not used to its full technical potential in clinical routine in order to keep the applied x-ray dose at a reasonably low level. In turn, clinical lung CT lacks the spatial resolution for a comprehensive analysis of, for instance, lung cancer nodules or metastases. Thus, often an additional, more detailed analysis based on lung biopsies is needed. Taking lung biopsies is associated with health risks such as internal bleeding or pneumothorax.

PBI (Propagation Based Imaging) is a phase sensitive x-ray imaging technique, which has proven to greatly enhance soft-tissue contrast at very low x-ray dose levels. PBI is especially suited for lung imaging, but requires at least a partially coherent x-ray source, sufficient sample-to-detector distance and detectors with small pixel sizes to capture the interference effects. Thus, its application is limited to high resolution imaging in small specimens or small animal models at synchrotron sources. However, PBI holds the potential to perform high resolution low dose lung CT in patients and would therefore be of great interest to diagnose and fight lung diseases.

Here we present the current status of our project to establish PBI lung imaging in patients at the Italian synchrotron Elettra. To evaluate the potential of PBI for patient lung imaging we used the antropomorphic human chest phantom ARTIChest (Figure 1a and b). The phantom was equipped with fresh pig lungs. The trachea of the pig lung is connected via a plastic tube to the outside, while the phantom is sealed. By applying a negative pressure to the artificial chest cavity, the pig lung gets passively inflated. To achieve a direct

comparison the phantom was studied with the same lung in a state-of-the-art clinical CT using a high resolution (HR) protocol with the resolution of $0.45 \times 0.45 \times 0.9 \text{ mm}^3$ (Fig. 1 (a)) and at the SYRMEP beamline of the Italian synchrotron – the resolution of $0.067 \times 0.067 \times 0.067 \text{ mm}^3$ (Fig. 1 (b)). Please note that due to the fact that the x-ray beam at the synchrotron has a fixed orientation, the phantom needed to be mounted up-right and was rotated. In contrast, in the clinical scanner the phantom was positioned horizontally while the detector and x-ray tube performed a combined rotation. Since the energy of the x-rays (spectra in the clinical scanner and monochromatic x-rays of 40 keV at the synchrotron) are different, TLD (thermoluminescence dosimeters) were placed in the phantom to enable reliable x-ray dose measurements in both devices. The dramatically higher resolution (Fig. 1 (c)) was achieved at the same x-ray dose level (~13 mGy) used in the clinical HRCT (High-Resolution Computed Tomography) protocol. Fig. 1 (c) demonstrates that this approach allows to study minuscule structural details within the lung as illustrated by the comparison with a penny. These results were possible by combining a novel direct conversion x-ray detector with a pixel size of $0.1 \times 0.1 \text{ mm}^2$ with a sample-to-detector distance of 10.7 m. Fig. 1 (d) shows a clinical lung CT of a patient. The red arrow points to a lung nodule which is further shown in the detailed view. Clearly, the structure can be identified as a potential pathological alteration of the lung and was later confirmed to be a solid lung cancer nodule. However, the limited resolution of clinical CT does not allow to depict the surface of the nodule in detail, which typically provides evidence, if the nodule is indeed benign or cancerous. Figure 1e shows the clinical HRCT results of a pig lung inside the aforementioned ARTIChest phantom. A solid nodule was mimicked by injection of agarose gel mixed with iodine. The appearance has

clear similarities to the example patient CT data set in Fig. 1 (d). Fig. 1 (f) shows the PBI results obtained at the SYRMEP beamline for the exact same region and at the same x-ray dose level. The surface of the artificial nodule (red arrow) can be seen in detail. Moreover, the diffusely increased density in the region labeled with § in Fig. 1 (e) can now clearly be attributed to alveoli filled with the same iodine agarose mix (Fig. 1 (f) §). As demonstrated, the strongly increased spatial resolution of our PBI setup allows for a more comprehensive characterization of lung pathologies such as solid and sub-solid nodules and also features of acute alveolar damage, at comparable radiation doses to clinical CT. Therefore, we believe that especially in patients at high risk of complications from invasive biopsies, e.g. in suspected IPF (idiopathic pulmonary fibrosis), PBI could offer a non-invasive alternative to a classical lung biopsy, delivering the necessary microstructural insight for a confident diagnostic decision making. We also expect that the completely new level of imaging details in-vivo will majorly improve radiomics approaches and help to refine or generate new imaging biomarkers for different lung diseases. However, further experiments are needed before the first patients can be scanned at the planned SYRMEP life science beamline. In this regard a major step will be scanning lungs from pig lung disease models and validating the findings by histology. In addition a new experimental station to handle large and bulky specimen and a refined lung phantom are now in place.

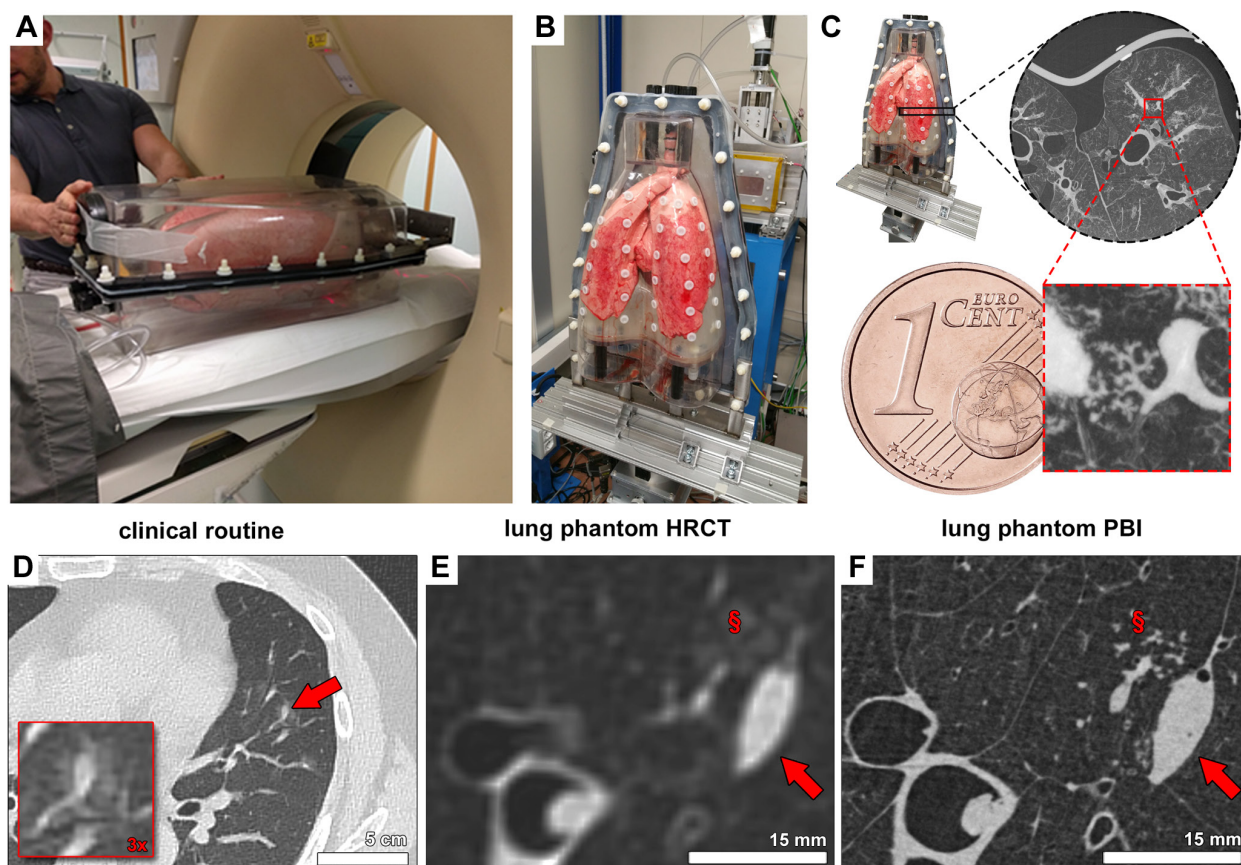


Figure 1. a) positioning the ARTIChest lung phantom with an inflated pig horizontally in a clinical CT scanner, b) positioning of the same phantom in up-right position at the SYRMEP beamline, c) a scan depicts the lung at a resolution of ~ 0.067 mm. Details much smaller than a penny can clearly be visualized inside the entire lung. d) shows the limits in state-of-the-art clinical CT. A nodule can clearly be seen within the lung (red arrow), however its surface and structure cannot be resolved. e) artificially generated lung nodules within the pig lung can be seen by clinical HRCT but the surface of the nodule (red arrow) as well as the unspecific increase in density § cannot be visualized in detail. f) the same lung at the same location was scanned with PBI at the SYRMEP beamline with the same x-ray dose of ~ 13 mGy. Clearly even small structures like the obstructed alveoli (§) can be resolved in detail.

Acknowledgments

The here presented experiments were realized using the infrastructure provided by the EUROBioImaging initiative. The study presents a collaboration between the University Medical Center Goettingen, The German Lung Research Center Heidelberg, Elettra - Sincrotrone Trieste, the University Hospital Cattinara Trieste and the University Trieste. We like to thank all people that in various ways have contributed to the success of the experiments. This paper includes data from the thesis of Willi L. Wagner submitted to University Clinic Göttingen under the title "Lokale Phasenkontrast-Computertomographie eine neue Strategie für die Lungenbildgebung im Menschen".

Original paper

Albers, J. Albers *et al.*, Scientific Reports **13**, 4788 (2023); DOI: <https://doi.org/10.1038/s41598-023-30870-y>.

Jonas Albers^{1,2}, Willi L. Wagner^{3,4}, Mascha O. Fiedler^{4,5}, Anne Rothermel^{3,4}, Felix Wünnemann^{3,4}, Francesca Di Lillo⁶, Diego Dreossi⁶, Nicola Sodini⁶, Elisa Baratello⁷, Marco Confalonieri⁸, Fulvia Arfelli⁹, Armin Kalenka^{4,10,11}, Joachim Lotz¹, Jürgen Biederer^{3,4,12,13}, Mark O. Wielpütz^{3,4}, Hans-Ulrich Kauczor^{3,4}, Frauke Alves^{1,14,15}, Giuliana Tromba⁶, Christian Dullin^{1,3,4,15}

- ¹ Department for Diagnostic and Interventional Radiology, University Medical Center Goettingen, Goettingen, Germany
- ² Biological X-ray imaging, European Molecular Biology Laboratory, Hamburg Unit c/o DESY, Hamburg, Germany
- ³ Diagnostic and Interventional Radiology, University Hospital Heidelberg, Heidelberg, Germany
- ⁴ Translational Lung Research Center (TLRC), German Center for Lung Research (DZL), University Heidelberg, Heidelberg, Germany
- ⁵ Department of Anaesthesiology, Heidelberg University Hospital, Heidelberg, Germany
- ⁶ Elettra-Sincrotrone Trieste S.C.p.A., Trieste, Italy
- ⁷ Department of Medicine, Surgery and Health Sciences, University of Trieste, Trieste, Italy
- ⁸ Pulmonary Unit, University Hospital of Cattinara, Trieste, Italy
- ⁹ Department of Physics, University of Trieste and INFN, Trieste, Italy
- ¹⁰ Department of Anaesthesiology and Intensive Care Medicine, District Hospital Bergstrasse, Heppenheim, Germany
- ¹¹ Faculty of Medicine, University of Heidelberg, Heidelberg, Germany
- ¹² Faculty of Medicine, Christian-Albrechts-Universität zu Kiel, Kiel, Germany
- ¹³ Faculty of Medicine, University of Latvia, Riga, Latvia
- ¹⁴ Department for Haematology and Medical Oncology, University Medical Center Goettingen, Goettingen, Germany
- ¹⁵ Translational Molecular Imaging, Max-Planck-Institute for Multidisciplinary Sciences, Goettingen, Germany

e-mail: christian.dullin@med.uni-goettingen.de

Iron and toxic environmental elements in human endometriosis: a combined role?

Elettra | TwinMic

Around 10-15% of women worldwide in reproductive age suffer of endometriosis, an inflammatory disease cause by the abnormal growth of endometrial tissue (similar to that of the uterus) outside the womb, particularly in the ovaries and fallopian tubes. This causes pain and, in many cases, infertility. Even if women have always been affected by endometriosis, it is only since recently that the scientific community has started looking into it. Although the disease etiology has not yet been clarified, it is believed that several factors contribute to the pathogenesis, including environmental factors and a genetic predisposition, and that most manifestations originate from an oxidative stress state sustaining the inflammatory condition. Retrograde menstruation has become the most widely accepted theory for the initial development. However, since retrograde menstruation is quite common among women and not all of them suffer from endometriosis, other concurrent conditions must promote the adhesion and the proliferation of endometrial tissue in very distant organs such as lungs and brain. Recently, increasing studies started to focus on the role of altered iron metabolism revealing features of iron overloads in the peritoneal cavity of endometriosis patients. Iron accumulation is related to the periodic bleeding in the ectopic endometriotic lesions that causes the formation of hemosiderin conglomerates, similar to those usually associated with toxic pathological states in humans. Additionally, even if most manifestations may be originated from an oxidative stress state sustaining the inflammatory condition, it is generally believed that several factors contribute to the pathogenesis, including environmental factors and a genetic predisposition. Thus, there is an increasing interest to explore the potential role of the exposure to environmental endocrine disruptors in the pathogenesis of this frequent and distressing disease.

A recent international study arising from the collaboration of Burlo Garofolo hospital and Elettra Sincrotrone Trieste highlights the existence of a possible link between endometriosis pathology and exposure to environmental pollutants, specifically metals. In order to investigate the iron overloads as well as the possible role or appearance of other metals in the endometrial lesions of women affected by endometriosis, low energy XRF (X-Ray Fluorescence) mapping, combined with soft x-ray microscopy at sub-micrometric spatial resolution, was carried out at the TwinMic of Elettra, and were complemented by hard XRF mapping at ID21 beamline of ESRF (Grenoble, France). This allowed to cover a wide energy range and thus investigate the presence of several chemical elements, comparing healthy and diseased tissues. Endometriosis and control patients undergoing conservative laparoscopy were enrolled at the Department of Obstetrics and Gynecology of the Institute and the study was approved by the regional (FVG) Ethics Committee (CEUR-2021-Os-168). The endometriosis patients (12 cases) aged 18 to 40 years, with regular menstrual cycle, and carrying uni- or bi-lateral symptomatic ovarian endometriomas ≥ 3 cm in diameter. Healthy endometrium used as control was obtained from seven patients of similar ages undergoing surgery for benign gynecologic pathologies. Histological sections of these formalin-fixed, paraffin-embedded tissue samples were used. Although the XRF technique is not able to distinguish the chemical state of the iron present in the tissue, it offers a label- and bias-free method with an outstanding sensitivity that cannot be reached by common histochemical analysis. The iron mapping by XRF of the samples revealed that there was an excess iron in many epithelial regions in contact with endometrial cysts, also spreading towards the stroma and also reaching the fibrotic tissue underneath. Quantitative XRF analysis

permitted to reveal large amounts of iron in the analyzed tissues, reaching a concentration of 10-20% p/p in multiple iron microspots-like deposits. Similar levels of excess iron have been reported in other pathological conditions such as hepatic siderosis and asbestosis. It is clear that such iron overload could represent a dangerous condition, leading tissues to have a higher risk of oxidative stress and of developing/worsening flogosis. The study revealed also that there is a co-localisation of iron and some environmental metals, such as Al, Si, Br, Ti, Mn, Cr, Pb and Rb, in the endometriotic lesions of affected women, thus suggesting a role of them in the pathogenesis of endometriosis. The light elements distribution revealed at TwinMic is shown in Fig 1. As shown, iron appears as microaggregates with important concentrations and in the same areas XRF reveals the presence of exogenous and possibly toxic metals. Recent studies demonstrated that some of these metals such as Cd, Hg, Pb, Ni and Al are functionally similar to estrogens, and for these characteristics they are called "metalloestrogens". This fact may explain why these metals accumulate in reproductive tissues. It is not clear why those metals accumulate in endometriotic lesions and further studies are suggested focusing on the relation between environmental metals and iron dysmetabolism, as well as investigations confirming the involvement of environmental pollution. This research was performed in the frame of a three year project of Burlo Garofolo, funded by the Italian Ministry of Health, which aims at discovering the causes of this pathology, by involving an interdisciplinary team of geneticists, gynecologists, microbiologists and immunologists.

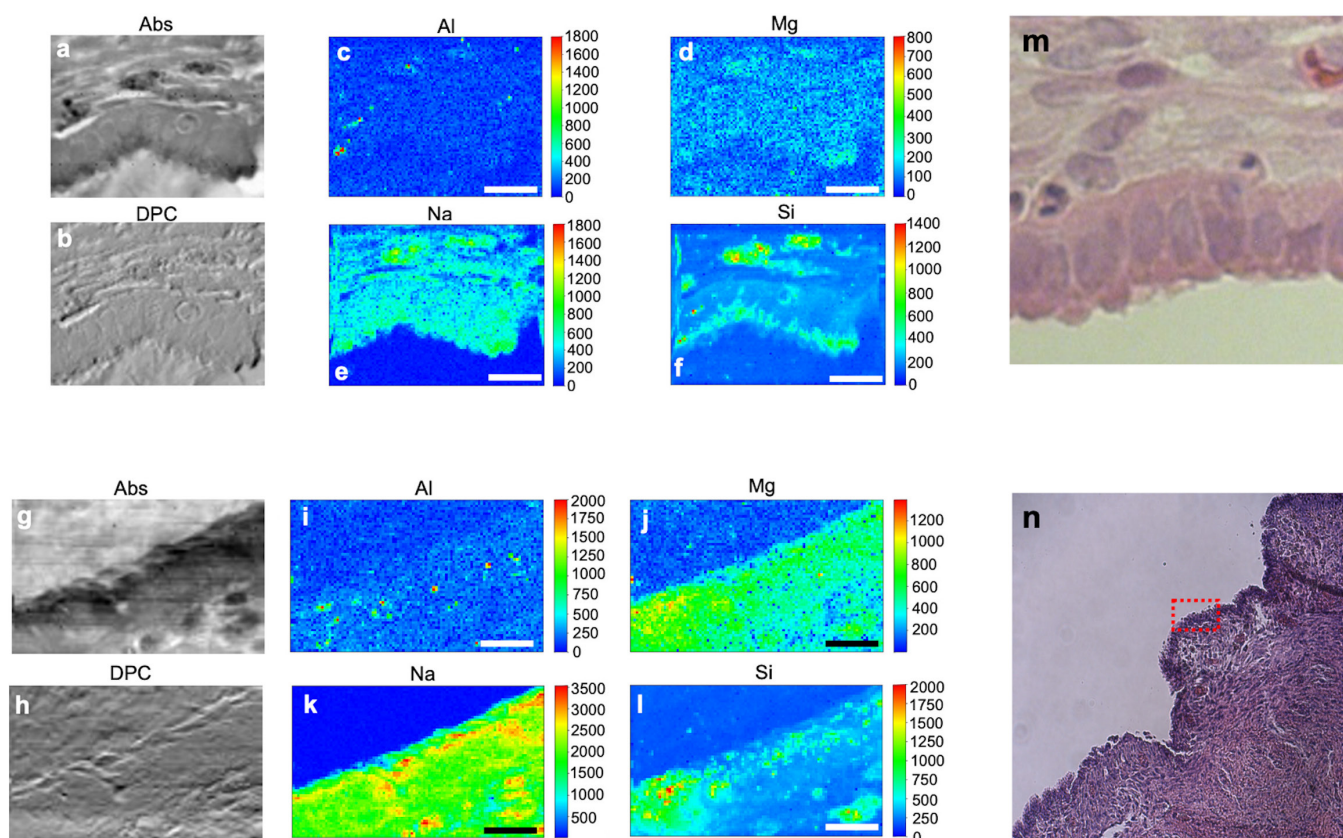


Figure 1. X-ray microscopy absorption (a,g) and phase contrast (b,h) images and the corresponding Al (c, i panels), Mg (d, j panels), Na (e, k panels), Si (f, l panels) XRF intensity maps of an endometrial tissue of a patient collected at TwinMic (scale bar 20 μm). Corresponding histological images are shown in panels m and n.

Acknowledgments

We acknowledge Elettra Sincrotrone Trieste for providing access to its synchrotron radiation facilities and for financial support under the SUI internal project

Original paper

L. Pascolo *et al.*, *Science of The Total Environment* **110**, 161028 (2022); DOI: 10.1016/j.scitotenv.2022.161028

L. Pascolo¹, M. Pachetti¹, A. Camillo², A. Cernogoraz³, C. Rizzardi⁴, K. Vogel Mikus^{5,6}, F. Zanconati⁴, M. Salomé⁷, V. Tardillo Suárez⁷, F. Romano¹, G. Zito¹, A. Gianoncelli⁸ and G. Ricci^{1,4}

¹ Institute for Maternal and Child Health, IRCCS Burlo Garofolo, Trieste, Italy.

² Department of Obstetrics and Gynecology, AOUI Verona, Verona, Italy.

³ Department of Gynecology and Obstetrics, F. Del Ponte Hospital, Varese, Italy

⁴ Department of Medical, Surgical, and Health Sciences, University of Trieste, Trieste, Italy.

⁵ Jožef Stefan Institute, Ljubljana, Slovenia

⁶ Slovenia Biotechnical Faculty, University of Ljubljana, Ljubljana, Slovenia.

⁷ European Synchrotron Radiation Facility, Grenoble, France

⁸ Elettra, Sincrotrone Trieste, Trieste, Italy

e-mail: lorella.pascolo@burlo.trieste.it

Engineered neurotransmitter transporter provides insights into GABA uptake inhibition

Elettra | XRD2

The role of neurotransmitters is to mediate communication between neurons across the synaptic space. The role is performed by numerous small molecule neurotransmitters that are derived from amino acids that are loaded in synaptic vesicles that release neurotransmitters into synaptic space upon activation by the action potential. Neurotransmitters can both excite or inhibit nerve cells and, in the process, strike a balance between excitatory and inhibitory inputs. GABA (γ -aminobutyric acid) is the major inhibitory neurotransmitter that is biochemically derived from glutamate which is an excitatory neurotransmitter. GABA released from interneurons activates both ionotropic and metabotropic receptors in the postsynaptic neurons to inhibit neural activation. GABA levels in the synaptic space are controlled by sodium and chloride coupled GABA transporters that are involved in reuptake of release GABA into neurons and glial cells. GAT activity enforces spatiotemporal control of GABA levels in the synaptic space and therefore is a high-value target to alter GABA levels in neurological disorders. GATs (GABA transporter isoforms) therefore play vital roles in affecting inhibitory neurotransmission and are a target for some antiepileptic drugs to treat partial seizures that result from an imbalance of excitatory and inhibitory neurotransmission. Other conditions like anxiety and schizophrenia are also observed as a consequence of defective GABA regulation. In order to understand the ability for some of the blockers of GAT1 we decided to engineer an available neurotransmitter transporter that could be structurally studied which is the dDAT (Drosophila dopamine transporter). The dDAT was engineered in the binding pocket by modifying ten residues to resemble the GAT1 and further used thermostabilizing mutants to tolerate these substitutions. This yielded a designed transporter with a dDAT structure but a binding site resembling GAT1, referred to as dDAT_{GAT}. This design

process allowed inhibitors specific to GAT1 to bind to the modified transporter and allowed co-crystallization of dDAT_{GAT} inhibitor complexes. This yielded x-ray structures of the transporter complexed with NO711 and SKF89976a that specifically block GAT1. We observed electron density for both the inhibitors in the primary binding site of modified dDAT (dDAT_{GAT}). Incidentally, the disordered linker connecting TM6a with TM6b undergoes a subtle shift in position to create a new subsite surrounded by the linker to accommodate the bound inhibitor. The residues substituted in the binding pocket also minimize the volume of subsite B and alter the binding site architecture from a trilobed binding site with subsites A, B and C to a bean shaped binding pocket with subsites A and C' (Fig. 1). These changes were observed for both NO711 and SKF89976a bound structures accommodating the carboxylate group of the drug in subsite A and the diaryl aromatic groups in the subsite C'. These results provided a basis to understand the highly specific and non-overlapping nature of inhibitor interactions between catecholamine and GABA transporters. We collected high quality x-ray diffraction data for SKF89976a bound neurotransmitter transporter at XRD2 and observed the drug to be bound into two distinct sites within the vestibule of the transporters. In addition to the inhibitor bound to the substrate-binding site, we observed a unique allosteric binding site for SKF89976a in the vestibule of the transporter that allowed us to understand how this inhibitor facilitates both competitive and non-competitive inhibition modes. We performed biochemical assays of GABA uptake and its inhibition by SKF89976a at varying concentrations in comparison to NO711(a competitive inhibitor) to observe both a competitive and non-competitive mode of transport inhibition. We further identified a previously uncharacterized residue in extracellular loop 4 that interacts indirectly with the allosterically

bound SKF89976a. Substitution of this residue to resemble an acidic residue in dDAT compromises GABA uptake. The reversal of this substitution to resemble GAT1 residue in dDAT severely effects dopamine uptake in the case of dDAT. This suggests the role of EL4 motif as a selectivity filter to allow entry of neurotransmitters into the vestibule besides having substrate selective residues with the primary binding pocket. Overall, the study provides insights into inhibitory mechanisms of well-known GAT1 blockers and explores the basis of drug binding specificities among GABA and other neurotransmitter transporters. The results have implications for structure guided inhibitor discovery of GAT blockers.

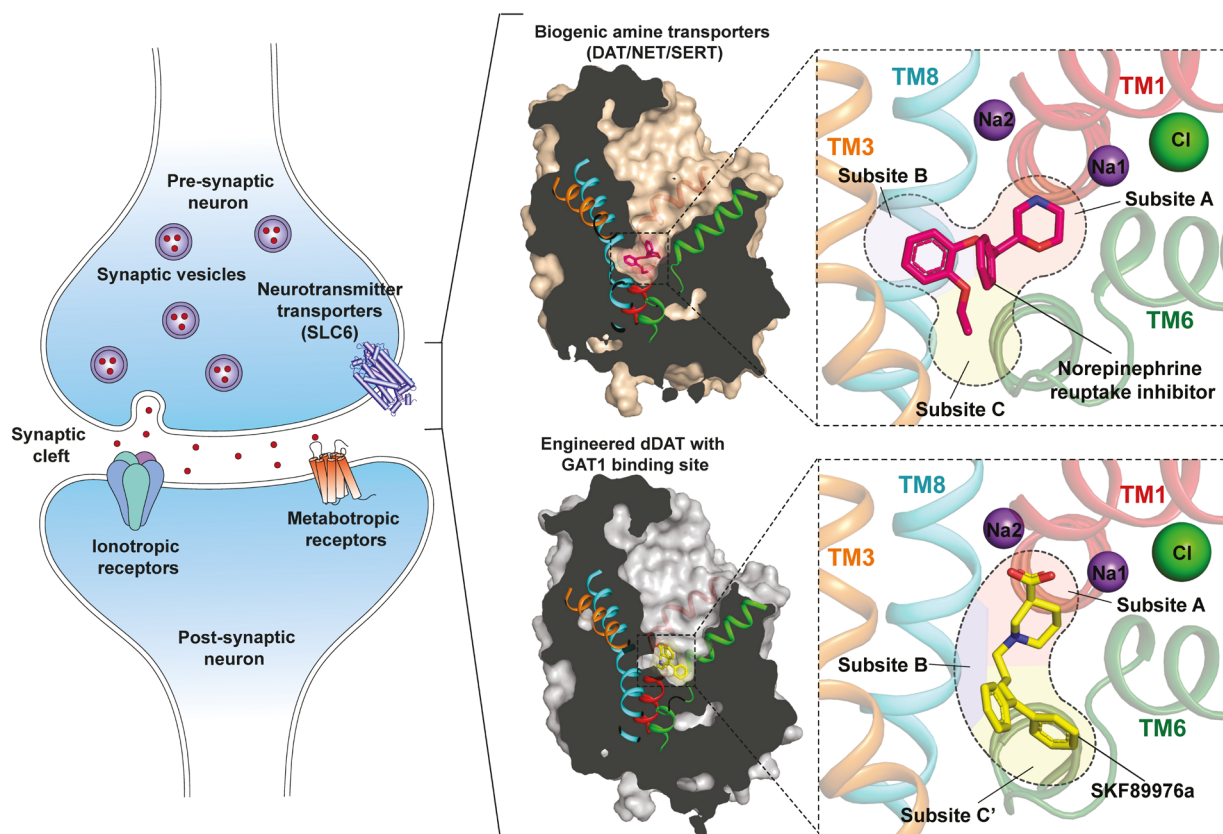


Figure 1. Comparison of binding site reorganization between inhibitors of catecholamine transport with GABA uptake blockers. The latter bind to a bean-shaped binding pocket due to altered binding site architecture within the transporter.

Acknowledgments

Access to the XRD2 beamline at Elettra synchrotron, Trieste was made possible through grant-in-aid from the Department of Science and Technology, India, vide grant number DSTO-1668. We thank Raghurama Hegde and Annie Heroux for support with the beamline operations during data collection.

Original paper

D. Joseph *et al.*, *EMBO J.* **41**, e110735 (2022), DOI: 10.15252/embj.2022110735

Deepthi Joseph¹, Smruti Ranjan Nayak¹ and Aravind Penmatsa¹

¹ Molecular Biophysics Unit, Indian Institute of Science, Bangalore, India

email: penmatsa@iisc.ac.in

Triple negative breast cancer-derived small extracellular vesicles: modulators of cells biomechanics

NanoInnovation Lab
Elettra | SISSI bio

EV (Extracellular vesicles) play a pivotal role in cell-cell communication, in maintaining cell homeostasis as well as in disease spreading, through the release of cell-specific biologically active content (proteins, mRNA, metabolites, etc.). In particular, small, nano-sized (30–200 nm in diameter) extracellular vesicles (sEV) have recently been highlighted for their contribution in the development of cancer metastasis, by promoting tumor-induced immune suppression, metastasis and angiogenesis. However, molecular details on how such nano-vesicles influence the recipient cells and their extracellular environment are scarce, given the challenge of correlating molecular and functional information with typical (small) sEV size. In the present work, we focused on TNBC (triple negative breast cancer), characterized by high aggressiveness and non-responsivity to classical therapies. We developed a protocol to isolate and purify sEV from TNBC cell lines, and followed their effect on non-metastatic BC cells. In particular, we focused on the mechanism of modulation of cell mechanics induced by sEV from the TNBC context. It is known in fact that the mechanical properties of cells and their environment are strongly correlated to their function, including cell shape, adhesion, motility and gene expression, which in turn determine the metastatic potency of cancer cells and their capacity to sustain the malignant process. By AFM (Atomic Force Microscopy) based spectroscopy in physiological environment combined with FM (Fluorescence Microscopy), we correlated biomechanical and phenotypic changes in non-metastatic breast cancer cells (from the MCF7 cell line) upon exposure to sEV isolated from TNBC cells (from the MDA-MB-231 cell line). By fitting force-indentation curves with suitable mechanical models we derived the cells Young modulus, i.e. the parametric representation of cell

compliance. MDA-MB-231 turned out significantly softer than MCF7 cells, in line with their metastatic profile (Figure 1a). Upon treatment with TNBC-derived sEV (231_sEV), the MCF7 cells acquired a compliance similar to the sEV's cells of origin, pointing to a direct modulation effect exerted by this nanovesicles (Figure 1a). Stiffness changes were accompanied by changes in cell morphology, as observed by immunofluorescence measurements: more elongated morphology, with increase number of cellular protrusion, i.e. actin-rich structures beneath the plasma membrane; an increase in the number and density of FA (focal adhesion) points, and FA augmented activity (increased activation of phosphorylated focal-adhesion kinase, pFAK); a reduction of nuclear size and circularity; an increase of actin filaments. Direct correlation between metastatic potential of cancer cells and the increased number of smaller FA with high activity have been reported also in previous works, together with the nuclear accumulation of YAP (Yes-associated protein), and important oncoprotein, modulator of cell biomechanics, observed also in our 231_sEV-treated MCF7 cells. Interestingly, we observed an increase of actin polymerization, which points towards stiffening rather than softening of the cells, as was expected for higher metastatic power. To shed light on the subcellular elements involved in sEV-cell interaction and in the induced biomechanical changes, we performed more detailed AFM measurements. Instead of using a micro-sized bead to probe the entire cell compliance, in correspondence of the nucleus, we carried out force-indentation measurements using a nano-sized pyramidal tip, to be sensitive to different cellular and subcellular compartments. In the area of the nucleus, we were able to distinguish two indentation regions, with different slopes: a first one, in

correspondence to cell membrane; a second, stiffer one, dominated by intracellular organization. Interestingly, the membrane-dominated Young modulus of 231-sEV treated MCF7 did not change with respect to the untreated MCF7 cells (was softer for the MDA-MB-231 cells); the other was instead significantly lower than for the MCF7 cells (Figure 1b). Therefore, the major change induced by sEV on MCF7 cells is at the level of nuclear rigidity. FTIR (Fourier transformed infrared) spectroscopy measurements performed at SISSI confirmed this results. By following the model developed by Morrish and coworkers, we considered three main spectral regions: lipid C-H stretching ($3000\text{--}2800\text{ cm}^{-1}$); the protein region (Amide I and II at $1718\text{--}1588$ and $1588\text{--}1482\text{ cm}^{-1}$, respectively); the nucleic acid PO_2 -symmetric stretching region ($1135\text{--}998\text{ cm}^{-1}$); and their relative ratios. We found a significant increase of protein/lipid ratio for the 231-sEV treated MCF7 cells, compared to both MCF7 and MDA-MB-231; no change in the sDNA/lipid ratio; lower sDNA/lipid ratio for metastatic MDA-MB-231 cells compared to both treated-untreated MCF7 cells (Figure 1c). In line with the findings of Morrish, our data can be explained with a change in the MCF7 cells chromatin architecture, specifically a relaxation/decondensation induced by the 231-sEV. In conclusion we showed that sEV derived from TNBC cells induce a metastatic transformation of non-metastatic, MCF7 cells. The softening of the cellular body, measured by AFM and confirmed by morphological data as well as oncogene YAP expression, seems to occur, at least at the initial stage, at the level of chromatin architecture rather than actin polymerization, as highlighted by FTIR spectroscopy data. This work contributes to disclose molecular details of TNBC spreading mechanism, and to find novel targets for anti-cancer therapies.

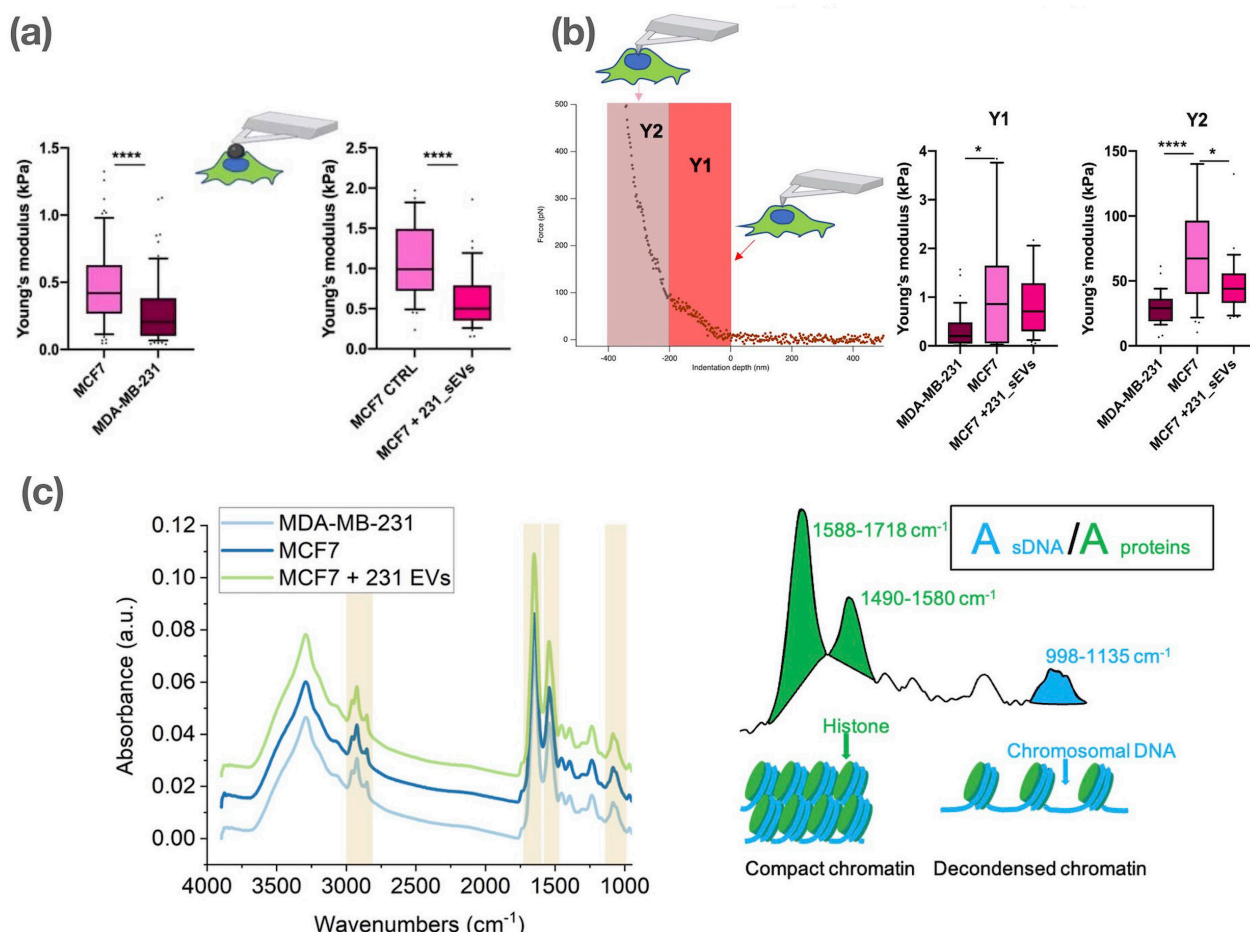


Figure 1. (a) Young's moduli obtained through AFM force spectroscopy of MDA-MB-231, MCF7, and 231_sEVs-treated MCF7 cells. Boxplots showing elastic moduli of cells by using a 20 μm -sized silica sphere (positioned on the nucleus) to obtain whole contribution of the cells and by using the Hertz model to fit the force curves FTIR spectroscopy of MDA-MB-231, MCF7, and 231_sEV-treated MCF7 cells. (b) Young's moduli obtained through AFM force spectroscopy of MDA-MB-231, MCF7, and 231_sEV-treated MCF7 cells and representative AFM force-indentation curve and boxplots showing the elastic moduli Y1 (external layer) and Y2 (cell body) of the cells. (c) FTIR spectra of the average absorbance used for the calculation of different peak ratios. The DNA-to-protein peak ratio is associated with the chromatin state at the single-cell level and a cartoon representing the compact or decondensed chromatin state.

Acknowledgments

The authors wish to thank the Structural Biology Laboratory of Elettra-Sincrotrone Trieste for the instrumentation and the continuous support. The work was supported by European Regional Development Fund and Interreg V-A Italia – Austria 2014-2020 (EXOTHERA- ITAT1036 to P.P., L.C.), AIRC (IG 21803 to L.Co.) and by Regione Friuli Venezia Giulia (legge regionale 17/2004, BioMec project to M.L., L.C.).

Original paper

B.Senigagliesi *et al.*, *Nanomedicine: Nanotechnology, Biology, and Medicine* **44**, 102582 (2022) DOI: 10.1016/j.nano.2022.102582

B.Senigagliesi *et al.*, *Biomolecular Concepts* **13**, 322 (2022) DOI: 10.1515/bmc-2022-0024

B. Senigagliesi^{1,2,3}, M. Apollonio¹, D. E. Bedolla³, G. Birarda³, M. Zanetti⁴, M. Lazzarino⁴, L. Vaccari³, L. Collavin¹, P. Parisse^{3,4*}, L. Casalis^{3*}

¹ Università degli Studi di Trieste, Trieste, Italy

² Scuola Superiore di Studi Avanzati (SISSA), Trieste, Italy

³ Elettra Sincrotrone Trieste, Trieste, Italy

⁴ Istituto Officina dei Materiali Consiglio Nazionale delle Ricerche, CNR-IOM, Trieste, Italy

email: parisse@iom.cnr.it; loredana.casalis@elettra.eu

Optical manipulation of charge delocalization in a bulk heterojunction material

Q4Q Laboratory

Blends of conjugated polymers and fullerene derivatives are among the most promising candidates to realize organic solar cells with high conversion efficiencies. In these systems, the generation of free carriers is achieved via the charge transfer from a light-absorbing electron donor (the polymer) to an electron acceptor (the fullerene C₆₀). The efficiency of the photoconversion process strongly relies on the states formed at the donor/acceptor interface, which are known as CTXs (charge transfer excitons) and consist of an interfacial electron-hole bound state with typically large binding energies (>500 meV). The mystery of how CTXs in a low dielectric environment overcome the Coulomb barrier to generate free carriers has bred a wealth of discussion on the microscopic mechanism leading to photoconversion in heterojunction materials.

Previous experiments using pump-push-probe techniques produced evidence that a "hot" delocalized CTX state may provide the excess energy needed to decrease the Coulomb binding and thus facilitate the barrier crossing to charge dissociation. However, the use of push pulses with photon energies higher than the exciton binding energy has complicated so far the interpretation of these experiments, raising the doubt that charge separation could be aided by the direct dissociation of charge transfer excitons rather than their degree of delocalization.

In this work, we use push pulses with photon energy in the range 0.12–0.25 eV and study their effects on the transient charge transfer species at the interface of the fullerene-based blend of the conjugated polymer F8BT. The uniqueness of the work compared to prior studies lies in the use of a lower energy mid-infrared push pulse below the exciton dissociation energy, which allows us to disentangle the effects of direct exciton dissociation and exciton delocalization on the dynamics of charge separation. By combining steady-state absorption, PP (pump-probe) and PPP (pump-push-

probe) measurements, we identified three types of CTXs, according to their degree of delocalization across the interface: delocalized, localized, and trapped. As depicted in the energy diagram in Fig. 1 (a), the state lying at higher energy is the delocalized CTX, where the excitation resides over multiple polymer chains and the electron-hole distance is large, eventually leading to a charge-separated state; the excitation is instead restricted to a single chain (albeit maintaining a degree of intrachain delocalization) in localized CTXs and then completely localized in trapped CTXs, that lie at lower energies.

Our time-domain experiments provided details on the nature and lifetimes of these interfacial states. We compare in the top panel of Fig. 1 (b) the PP decay associated spectra at early times in both the pristine polymer film (F8BT) and the blend film with fullerene (F8BT:C₆₀). The difference between the two curves (DCTX, purple area) reveals the presence of a peak only in F8BT:C₆₀ that is compatible with the blue-shifted delocalized CTX state, that rapidly localizes within 180 fs and consequently redshifts in later spectra (CTX, red area in the bottom panel).

The addition of a mid-infrared push pulse resonant with the charge transfer band (CT, yellow in the upper sketch in Fig. 1 (b)) has different effects in the pristine and the blend film. When the pump and the push simultaneously excite the F8BT film, changes in the pump-probe signal ($\Delta\Delta A = \Delta A^{(\text{push}|\text{ON})} - \Delta A^{(\text{push}|\text{OFF})}$) are persistently negative in all push-probe delays (see legend in the top panel of Fig. 1 (c)) which indicates that the population of the excited-state species decreases with the push pulse. Conversely, in the blend film (bottom panel of Fig. 1 (c)) the $\Delta\Delta A$ signal, initially negative and peaked at the localized CTX, turns into positive after 400 fs and blueshifts to the energies of the delocalized CTX. This means that the push initially depletes the localized CTX states, but its effect on the long

run is to enhance the population of the delocalized CTX states.

Interestingly, as soon as the push is delayed in time with respect to the pump (>1 ps), the $\Delta\Delta A$ signal in F8BT:C₆₀ displays only negative spectra, and the sign does not change throughout the push-probe time window. This implies that localized CTXs populated at later times do not respond to the push pulse; these states do not display intra- or interchain delocalization and are therefore trapped CTXs.

Our results demonstrate that the photoexcitation of localized CTXs with push pulses resonant to the mid-infrared charge transfer absorption can promote delocalization and, in turn, contribute to the formation of long-lived charge separated states. Conversely, as soon as delocalized states become trapped over time (~180 fs), the system is irresponsive to the push pulse and its excess energy is wasted. Furthermore, by tuning the photon energy of the mid-infrared push in resonance with strong infrared absorption from the C≡C stretching mode, we observed a depletion of delocalized states, confirming that delocalization is uniquely favored by the electronic CT absorption and not by the vibrational excitation.

These findings emphasize the importance of engineering both the energy offset between the singlet exciton and charge transfer states and local polymer morphology to optimize high-yield charge separation. They also show the strength of the pump-push-probe technique that we have used in shedding light beyond what is readily available in pump-probe experiments into the physical nature and dynamics of the states involved in the ultrafast photophysics of polymer:fullerene blends.

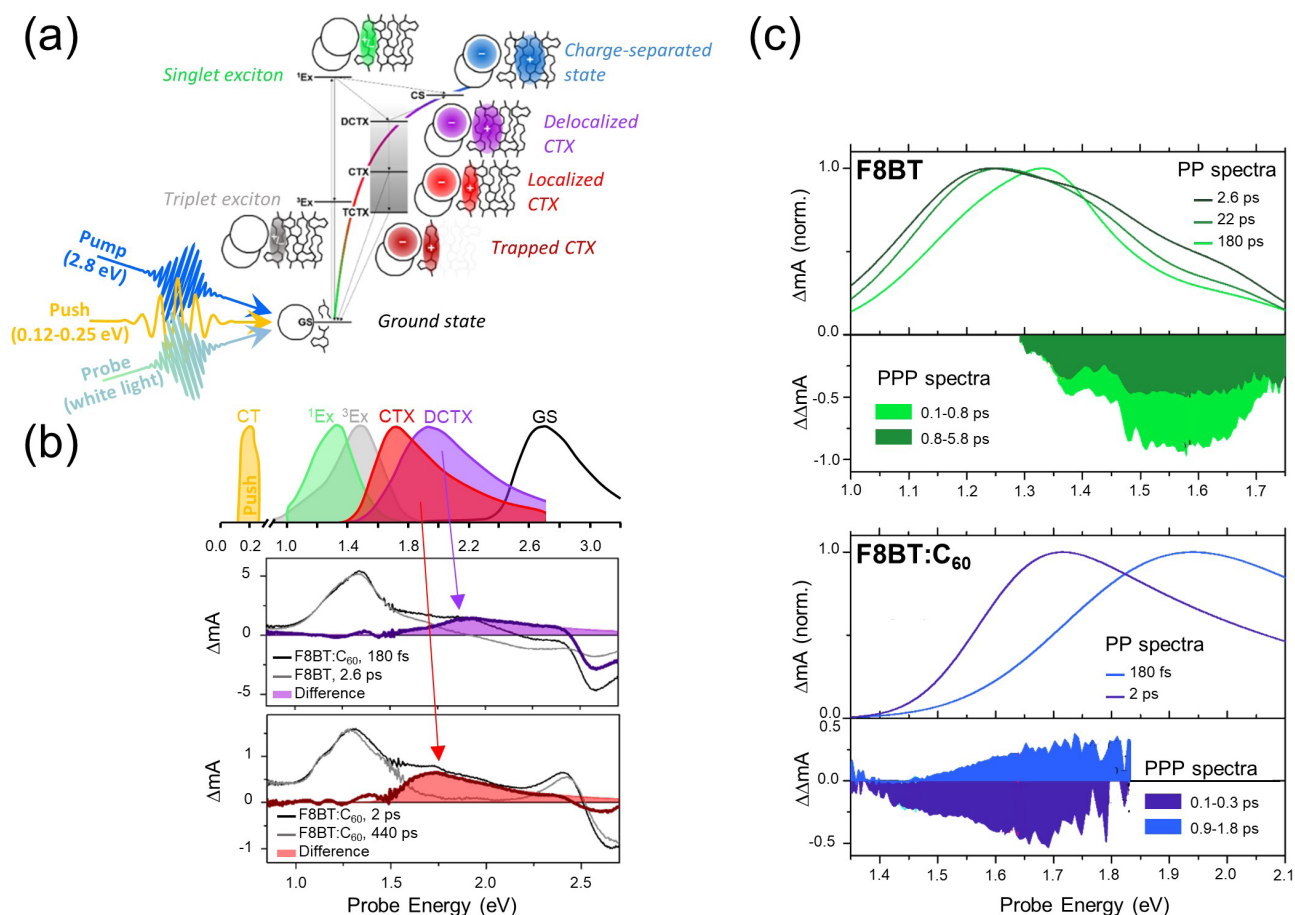


Figure 1. (a) Energy diagram and spatial distribution of all excited states identified using pump-probe and pump-push-probe experiments; (b) Pump-probe experiments allow to dynamically isolate the excited states in the heterojunction. Top: blue-shifted delocalized CTX state observable only in the blend (DCTX in purple). Bottom: the CTX redshifts as it localizes on a single-chain within 180 fs (CTX in red). (c) The color-filled spectra are the results of the PPP experiments in the pristine sample (top) and in the blend film (bottom).

The normalized PP spectra of the excited species are plotted in the upper panels for comparison. The pump and the push overlap in time, while the PPP spectra are integrated over the push-probe delay indicated in the legend. Importantly, only in the presence of the fullerene acceptor the effect of the push pulse is to deplete localized CTX states (negative purple spectrum) and favor instead delocalized DCTX states (positive blue spectrum).

Acknowledgments

Financial support was provided by the Division of Chemical Sciences, Geosciences and Biosciences, Office of Basic Energy Sciences, of the US Department of Energy through grant no. DE-SC0015429. F.F. acknowledges financial support from the European Union's H2020 Marie Skłodowska-Curie actions (grant agreement no. 799408). D.F. was supported by the European Commission through the European Research Council (Project INCEPT, Grant 677488).

Original paper

A. Montanaro *et al.*, *J. Phys. Chem. C* 127, 28, 13712 (2023); DOI: 10.1021/acs.jpcc.3c02938

A. Montanaro^{1,2,3}, K.H. Park⁴, F. Fassioli^{3,4,5}, F. Giusti^{1,2}, D. Fausti^{1,2,3}, G.D. Scholes⁴

¹ Physics Department, University of Trieste, Trieste, Italy

² Elettra - Sincrotrone Trieste S.c.p.A., Trieste, Italy

³ Physics Department, University of Erlangen-Nürnberg, Erlangen, Germany

⁴ Chemistry Department, Princeton University, Princeton, US

⁵ SISSA - Scuola Internazionale Superiore di Studi Avanzati, Trieste, Italy

e-mail: daniele.fausti@elettra.eu; gscholes@princeton.edu

New method reconstructs 3D landscape in XRF microscopy: breakthrough enhances imaging accuracy

SciComp
Elettra | TwinMic

XRF (X-Ray Fluorescence) spectroscopy is widely used for detecting and quantifying elements in various samples. However, accurately determining elemental concentration is challenging due to self-absorption of the XRF signal emitted by the sample, especially when micrometric or nanometric beam size are involved and the sample surface cannot be considered completely flat. This study introduces a new approach using multiple silicon drift detectors and ray-tracing to reconstruct a 3D sample with correct topography based on 2D XRF count rate maps. The reconstructed sample is then used to calculate self-absorption effects on X-ray fluorescence radiation, enabling quantitative correction. The proposed methodology is tested on a simulated sample and a web application implementing the method is provided.

Previous attempts have been made to address the self-absorption effect in XRF analysis, including the use of Monte Carlo algorithms and the FP (Fundamental Parameter) Method. However, these methods have limitations, such as focusing primarily on the surface of the object or requiring multiple imaging techniques that may be impractical to implement. Recent advancements have aimed to achieve a 3D (three-dimensional) characterization and correction of the self-absorption problem. One approach involved a multimodal method combining XRF microscopy, STXM (Scanning Transmission X-ray Microscopy), and AFM (Atomic Force Microscopy) along with the FP method. This approach calculated the absorption of both the incident beam and XRF radiation for each pixel in the 2D XRF maps, considering the sample's thickness obtained from AFM and the density map from STXM. While successful in retrieving quantitative maps of molar concentration, this approach required complex data acquisition and registration. Building upon previous research, the current study presents a novel and superior ray-tracing-based method for

inverse reconstruction of a 3D sample with its topographical landscape using 2D XRF maps acquired from multi-detector systems. Additional information, such as an absorption image (STXM map), average density value, and maximum thickness value of the sample, may also be taken into account. By reconstructing the 3D sample structure and comparing it with the actual simulated structure, the research demonstrated the possibility of numerically calculating self-absorption effects at a 3D level and achieving quantitative correction. This enables a more comprehensive understanding of the sample's structure and composition. In brief and as illustrated in Fig.1, the sample used in the study consists of three different sized hemispheres that simulate cells. The composition of the sample is based on the composition of human colon carcinoma cells. Magnesium is introduced into the sample in small regions. The original manuscript describes the quantitative evaluation process, which involves calculating XRF photons in each voxel source to determine the mass of each element in the sample. There it is also presented the reconstruction of the 3D sample structure and the statistical analysis carried out to compare the reconstructed data with the true data. The results show that the reconstructed sample structure closely resembles the actual sample, and the corrected data shows a good level of similarity with the simulated data further suggesting the efficiency of the IR algorithm and its robustness against inexact mass fractions. The study demonstrates then the feasibility of using the reconstructed 3D sample to quantitatively correct for the self-absorption effects on XRF radiation. By considering the sample's topography in the calculations, a more accurate assessment of elemental concentration can be achieved. This advancement has the potential to enhance the reliability and precision of XRF analysis in various fields, including biology, cultural heritage, geology, and archeology. In

general, in fields beyond XRF, the actual morphology is of scientific significance (eg. cell morphology, electrodeposition, paint structure, mineral formation etc.). The presented methodology offers a promising solution to overcome the limitations of previous approaches and provides a pathway for 3D characterization and correction of self-absorption artifacts. The development of a web application further facilitates the implementation and accessibility of this methodology for researchers and practitioners in the field. Overall, the study contributes to the advancement of XRF analysis by introducing an innovative approach to reconstruct 3D samples and correct for self-absorption effects. It opens up new possibilities for more accurate elemental quantification and deeper insights into the composition and structure of analyzed samples. It is evident that the advancements in reconstructing 3D samples and correcting self-absorption effects in XRF analysis are crucial for scientific progress. They enhance accuracy, provide detailed information about elemental distributions, and enable deeper insights into sample composition. Future and on-going research is towards better XRF fitting and quantification using the revealed/reconstructed topography.

In summary, this research contributed a novel methodology using ray-tracing and multi-detector systems to retrieve a 3D representation of a sample with resolved topographical landscape from XRF data. The reconstructed sample can be utilized to quantify and correct the self-absorption artifact at the 3D level. This approach offers potential advancements in XRF analysis, enabling more accurate and detailed elemental concentration measurements in various fields of research and application.

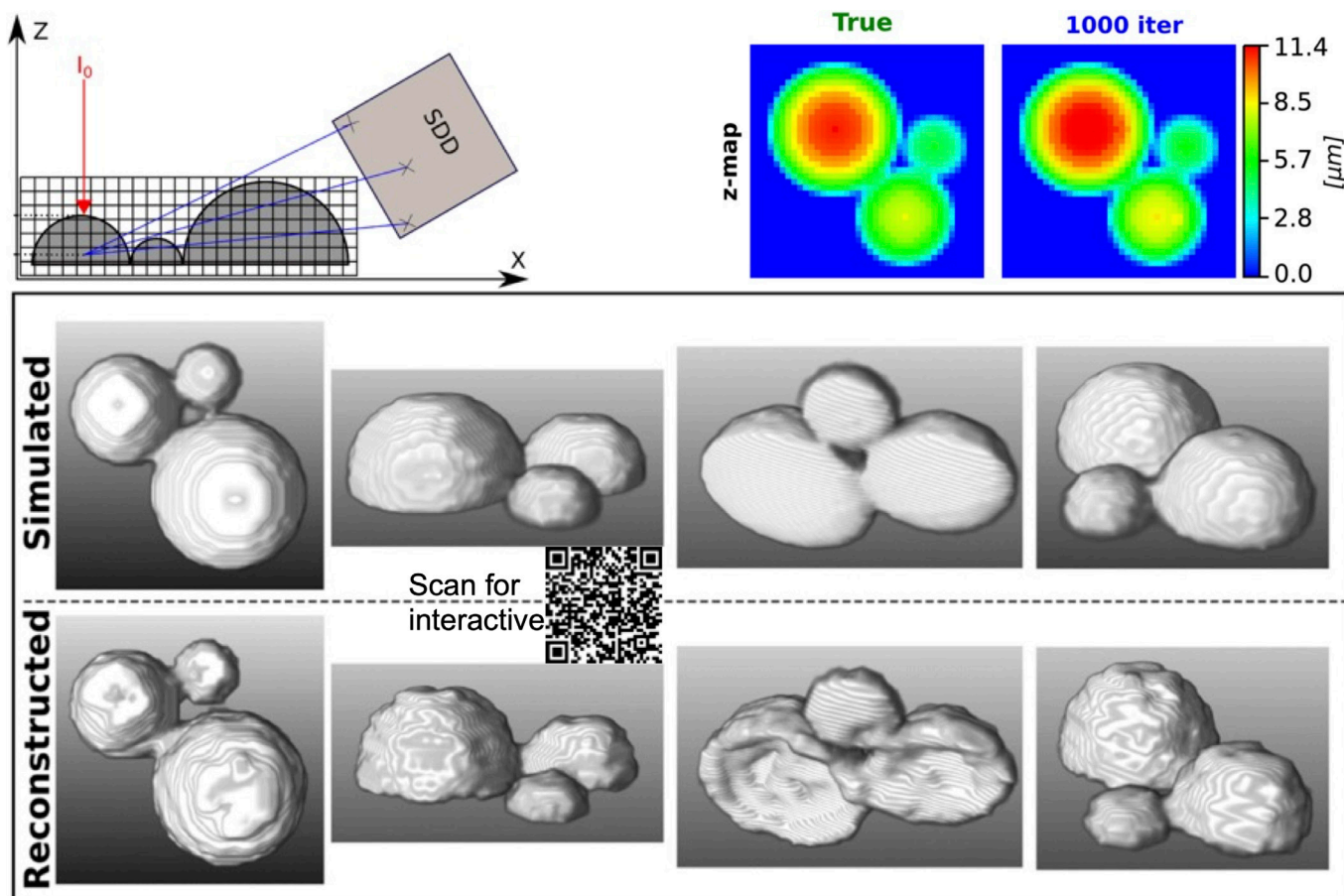


Figure 1. 1D, 2D and 3D simulations and reconstructions of topography derived from XRF. Hemispherical samples resembling human colon carcinoma cells.

Original paper

M. Ippoliti *et al.*, Scientific Reports **12**, 20145 (2022); DOI: 10.1038/s41598-022-24059-y

M. Ippoliti¹, F. Billè¹, A.G. Karydas², A. Gianoncelli¹, G. Kourousias¹

¹Elettra - Sincrotrone Trieste S.C.p.A., Trieste, Italy

²Demokritos, Institute of Nuclear and Particle Physics, Athens, Greece

email: george.kourousias@elettra.eu

X-ray Imaging and spectroscopy Reveals Ovarian Structures in bovine model

SciComp
Elettra | TwinMic, SYRMEP

MicroCT (Microtomography) is one of the most attractive synchrotron techniques for the medical community, since it allows three-dimensional visualization of organs and portions of them, with resolutions up to single cell level and below.

Microtomography analysis in in-vitro studies of ovary is fairly recent and our group has already demonstrated the feasibility and utility of microCT measurements on human ovarian tissues. The development of effective protocols to study these samples is fundamental for visualising the features of interest as best as possible and to take full advantage of the three-dimensional imaging mode offered by microCT.

The high coherence beam provided by most of the third and fourth generation synchrotron facilities permits the use of in-line propagation phase-contrast microtomography, a technique that helps to enhance the contrast in low-density tissues. Nevertheless, since these samples present similar densities among different tissues or structures, simple in-line phase-contrast technique may not be able to provide images with enough contrast to distinguish the different structures. Thus, the use of a correct staining protocol can be an alternative solution as it can dramatically improve the image quality. Several protocols have been developed and investigated in the recent years on different types of tissues, highlighting advantages and disadvantages of the different staining procedures.

In the present work four different staining protocols were considered in order to specifically study in-vitro ovary tissue morphology using synchrotron radiation propagation phase-contrast microtomography. For ethical reasons and for easier accessibility to the samples, the study was performed on bovine tissues, but the results can be easily extended to human ones and may have important repercussions. For instance a suitable procedure to investigate in a three-dimensional way,

the quality and state of cryopreserved human ovary tissues could provide important useful information on the efficacy of such preservation techniques. A better knowledge of the three-dimensional structure of human ovarian tissue could also favour the setting of the artificial ovary, which is the most challenging and risky perspective in the reproductive medicine field.

The four staining protocols investigated in this study, that is Lugol's solution, PTA (phosphotungstic acid) and Iodine solutions at different incubation times, were chosen because of the simplicity of the sample preparation and their safer nature compared to other ones, such as Osmium.

The microCT imaging was performed at two synchrotron facilities, each exploiting its peculiar capabilities. At ID19 beamline of ESRF the incident energy was chosen accordingly to the staining protocol; for Iodine protocol the measurements were carried out at 33 keV while for PTA one at 69keV, in order to take advantage of the absorption edges of Iodine and Tungsten respectively. A 2.2 micron pixel size was chosen as best compromise at the applied energies to preserve the integrity of the specimens and to allow a bigger field of view for scanning the whole sample. The ID19 experimental set up seemed to favor PTA staining, allowing to easily identify theca and granulosa cells, and also follicle at early development stage, probably due to an increase penetration of the contrast agent in the samples. In particular PTA allowed well identifying large structures in the tissue, while Iodine ones better highlights smaller features, especially when acquiring the images above the K-edge energy of the specific metal. At SYRMEP beamline a fixed energy well below the K-edge energy of both metals was employed, with a higher resolution of 0.9 micron pixel size, with a set-up optimised for phase contrast imaging. The obtained reconstructions showed very good contrast with all staining, allowing to highlight internal

structures, such as follicular and intrafollicular structures at different maturation stages, independently of the staining protocol and in a better way than what we previously obtained with osmium staining. (Fig. 1 a, d) shows a reconstructed slice from a PTA stained tissue and a zoom of a follicle region where both follicle and stromal cells are easily visible.

The microCT results were further complemented by XRF (X-Ray Fluorescence), a multi-elemental technique which allows identifying the presence, and under certain conditions, the concentrations of the excited chemical elements. When combined with scanning systems, it allows determining also the distribution of those chemical elements on the whole analysed area. The XRF measurements here reported (Fig. 1 b,c) were performed at two incident energies (1.5 and 7.3 keV, at TwinMic beamline in Elettra Sincrotrone Trieste and at ID21 beamline at ESRF synchrotron, in Grenoble, France, respectively) on histological slices obtained from the previously analysed samples. The XRF outcomes further support the benefit of using PTA, presenting an increased contrast efficiency because of its higher penetration in the tissues, as shown in Fig. 1 (c-d) that depicts the distribution of several chemical elements, obtained at TwinMic and ID21 beamlines for a slice of PTA stained ovarian tissue. Indeed tungsten is present in high levels in the whole tissue slice, highlighting also its morphology.

Interestingly, microCT imaging demonstrated to preserve the condition of the specimen, as no visible radiation damage was detected, enabling further analyses with other methods, such as for instance XRF.

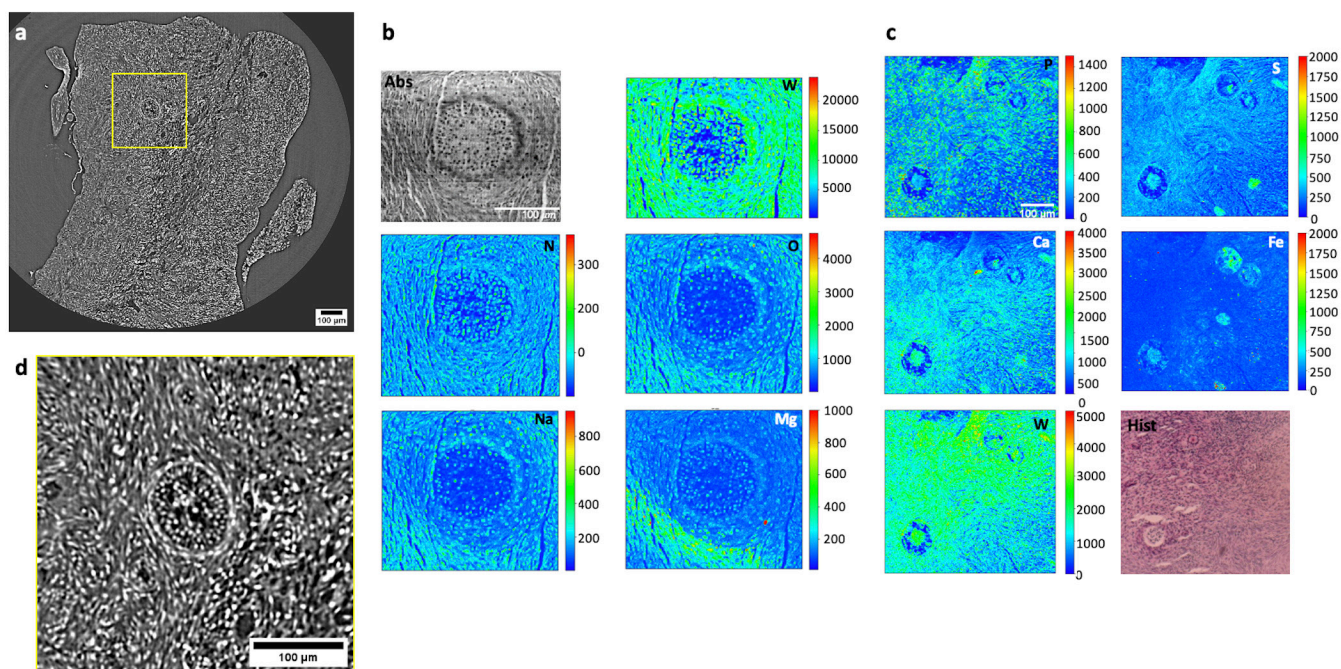


Figure 1. (a) Slice extracted from the microtomography reconstruction, measured at 27 keV at SYRMEP beamline with 0.9 µm spatial resolution, from the PTA stained tissue. (d) zoom of the follicle region. In all panels the scale bar is 100 µm. (c-d) µXRF and X-ray microscopy of PTA stained bovine ovarian tissue. The absorption (Abs) image was acquired at the TwinMic beamline (b) with 1.5 keV photon energy and 1 µm spatial resolution, together the corresponding Na, Mg, N, O, (300 µm × 220 µm) showing the distribution of different elements XRF maps, while W map was collected at 2 keV. The right panels (c) show the P, S, Ca, Fe, W XRF maps 200 µm × 190 µm acquired at ID21 beamline at 7.3 keV and 1 µm spatial resolution, together with the histological image (Hist) of the oocyte from an adjacent slice stained with eosin and hematoxylin dye. Adapted from A. Gianoncelli et al., *nt. J. Mol. Sci.* 24, 3545 (2023); DOI:10.3390/ijms24043545.

Original paper

A. Gianoncelli et al., *Int. J. Mol. Sci.* 24, 3545 (2023); DOI:10.3390/ijms24043545

A. Gianoncelli¹, G. Sena Souza², G. Kourousias¹, E. Pascotto³, P. Tafforeau⁴, E. Longo¹, R. Cely Barroso⁵, M. Salomé⁴, M. Stebel⁶, F. Zingaro^{7,1}, C. Calligaro⁸, G. Ricci^{9,10}, L. Pascolo⁹

- ¹ Elettra - Sincrotrone Trieste S.C.p.A., Trieste, Italy
- ² Chemistry Institute, Federal University of Rio de Janeiro, Rio de Janeiro, Brazil
- ³ ULSS n.2 Marca Trevigiana. Dipartimento di Prevenzione - Servizi Veterinari di Asolo, Treviso, Italy
- ⁴ European Synchrotron Radiation Facility, Grenoble, France
- ⁵ Physics Institute, State University of Rio de Janeiro, Rio de Janeiro, Brazil
- ⁶ Life Sciences Department, University of Trieste, Trieste, Italy
- ⁷ Physics Department, University of Trieste, Trieste, Italy
- ⁸ Servizio Diagnostica Veterinaria, University of Udine, Udine, Italy
- ⁹ Institute for Maternal and Child Health, IRCCS Burlo Garofolo, Trieste, Italy
- ¹⁰ Department of Medical, Surgical, and Health Sciences, University of Trieste, Trieste, Italy

email: alessandra.gianoncelli@elettra.eu

A first time in jellyfish science: 3D X-ray computed μ CT of the gastrovascular system of *Rhizostoma pulmo*

TomoLab

Cnidaria phylum include 10,000 species, of which 4,000 are jellyfish. Up to the present day, jellyfish are growing in importance and they are more and more attracting the interest of the scientific community. If in the past jellyfish were considered secondary characters in our Oceans, now it is evident how much these organisms are fundamental actors in the ecosystems as they can structure trophic webs, they can interfere with human activities (both economical and recreational), they may alter the provision of ecosystem goods and services. Their role may also increase in importance in the near future, if we consider the noticeable increase of blooms in the last decades. For these reasons, a complete knowledge on these organisms could help to understand jellyfish blooms dynamics, presence, impacts and to mitigate potential issues related to them.

In this context, understanding physiological aspects like the shape and function of the gastrovascular system of jellyfish is a key aspect to address, since few data are available. Historically, jellyfish gastrovascular systems have been studied with "old and traditional" techniques like stain injections, dissections, and external observations. These analyses have several limitations and criticalities, for example stain injections can highlight the path of superficial canals but can't provide information about their structure and volume. Plus, large jellyfish may have thick and opaque tissues, reducing the accuracy of observations. This led, at least for the order Rhizostomeae, a lack of descriptions and tridimensional data. In our work, made in collaboration between Elettra Sincrotrone Trieste, University of Trieste and Stazione Zoologica Anton Dohrn of Naples, we set a new protocol made by the combination of resin endocast and laboratory-based x-ray μ CT (computed microtomography). This innovative technique allowed the analysis in a complete and quantitative way.

Resin endocast is cheap, easy to produce and provides tridimensional representation of the whole gastrovascular system, hidden and deep areas included. The second step, the x-ray microtomography, can extract measure of interest such as volume, length, thickness and connectivity of canals (Fig. 1). Furthermore, the 3D render analysis (with masking and cropping) makes feasible the observation of inaccessible parts and, similarly, the quantification of smaller but numerous body parts, such as the count of branching and terminal openings of the canals. From a scientific communication perspective, once a tomographic render is done, it is easy to be shared and analyzed all over the world, compared to jellyfish sample delivery which is one of the most limiting factors in this field.

This analysis allowed us to measure, first of all, the total volume of the gastrovascular system and the single body parts (umbrella, scapulae, central canal and oral arms) of a specimen of *Rhizostoma pulmo* (14.6 cm diameter), accounting for 26.050 cm³, 11.591 cm³, 5.955 cm³, 0.193 cm³ and 8.312 cm³, respectively.

Second, considering both the endocast and the μ CT, we noticed a two hemi-canal structure of canals, never described before in jellyfish. In successive in vivo trials with vital stains, we confirmed that the hemi-canal structure function is to keep centrifugal circulation (running in the distal hemi-canals and expelled by outer openings on jellyfish arms) completely physically separated from the centripetal one (running in the medial hemi-canals and uptaken by medial openings on jellyfish arms).

The analysis on the single oral arm on canals thickness and openings number highlighted a slightly higher thickness of canals in the medial part of the jellyfish (the ones assigned to uptake water) compared to the canals of the external part of oral arms (assigned to excretion). The number of openings in the internal and external part of oral arms portion

accounted for 234 (internal), 257 (external), respectively. Considering the whole organism (8 oral arms), we estimated a total of 1953 intake openings while the external ones should account for about 2048. These numbers support the observations and theory of a double flux circulation, where uptake canals are fewer but thicker compared to centrifugal ones.

From a broader and evolutionary perspective, since cnidarians are described to possess a single pore blind gut, our results show a different structure resulting from a potential adaptive convergence in this species that is more similar to a bilaterian through gut, thus debating the parading of the single oral pore structure common in all cnidarians.

Concluding, this work proves another time that the concept of evolution is not a simple single-axis time-line but it is made by many different facets that need to be addressed all to have the best complete picture.

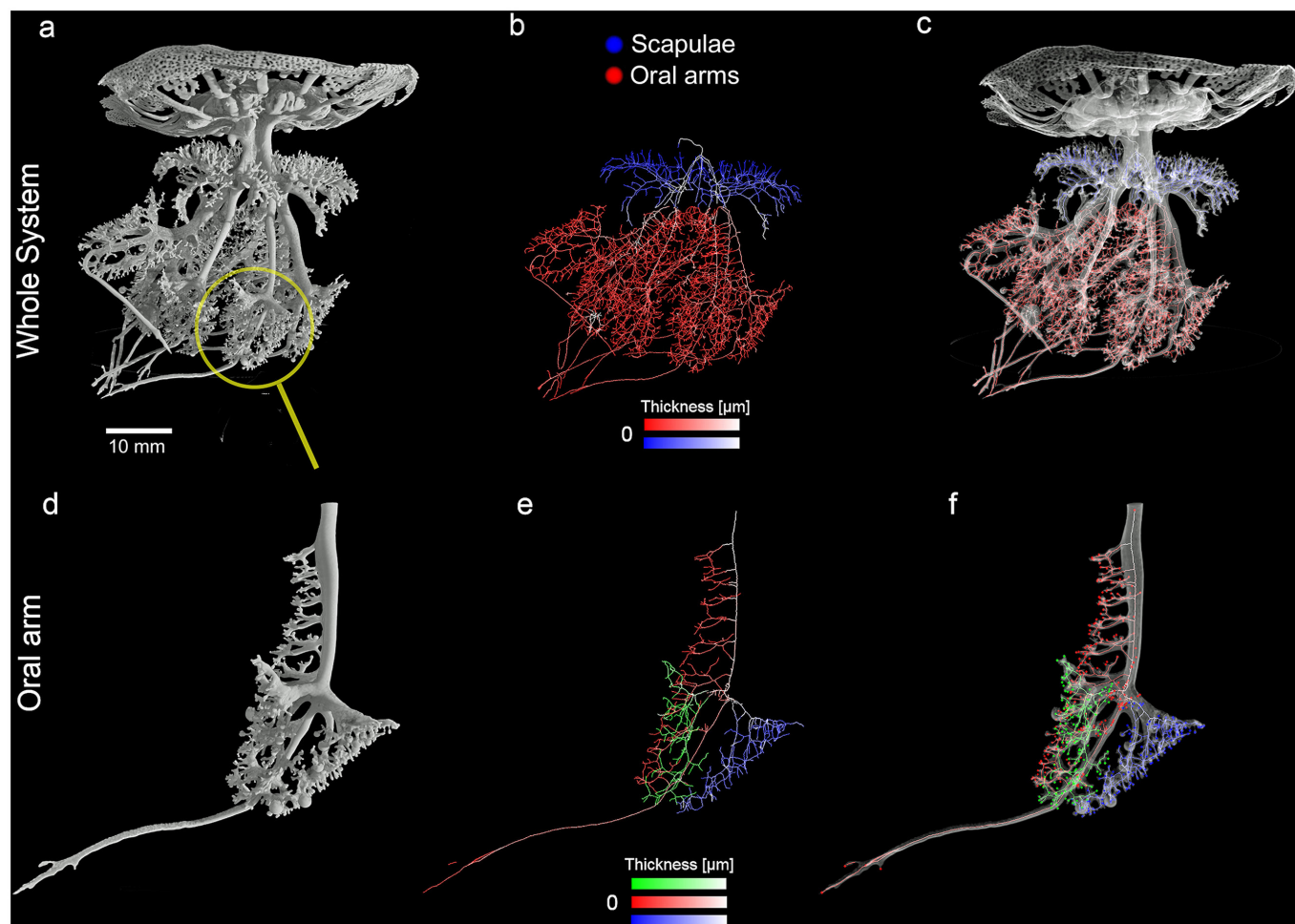


Figure 1. Graphical summary of the results of the quantitative analysis on the gastrovascular system.

(a) 3D rendering of the whole cast of the gastrovascular system measured via X-ray μ CT. (b) Isosurface rendering showing the segmented gastrovascular system of the whole manubrium; false colors refer to the two different structures analyzed (blue = scapulae, red = oral arms). Color intensity is proportional to the local thickness values in the medial axis at that specific voxel. (c) Volume rendering of the cast; medial axes analysis, high intensity colors indicate the smaller canals. (d) Volume rendering of a single oral arm. (e) Thickness-labeled skeleton of the three-winged portions, each characterized by a specific hue (red, green, and blue). (f) Openings of the three different wings labeled with the three different colors as in (e). CT reconstruction performed with an isotropic voxel size of 62.0 μ m. Reproduced from Avian M. et al., PLoS One. 17, e0272023 (2022); DOI:10.1371/journal.pone.0272023

Acknowledgments

We acknowledge Elettra Sincrotrone Trieste for providing access to its laboratories and we thank the staff for assistance in using the FAITH instrument.

Original paper

Avian M. et al., PLoS One. 17, e0272023 (2022); DOI:10.1371/journal.pone.0272023

M. Avian¹, L. Mancini^{2,7}, M. Voltolini^{2,8}, D. Bonnet³, D. Dreossi², V. Macaluso¹, N. Pillepich¹, L. Prieto⁴, A. Ramsak⁵, A. Terlizzi^{1,6}, G. Motta^{1,6}

¹ Department of Life Science, University of Trieste, Trieste, Italy

² Elettra-Sincrotrone Trieste S.C.p.A., Basovizza, Trieste, Italy

³ MARBEC, Université de Montpellier, CNRS, Ifremer, IRD, Montpellier, France

⁴ Group Ecosystem Oceanography, Department of Ecology and Coastal Management, Instituto de Ciencias Marinas de Andalucía (CSIC), Ca' diz, Spain

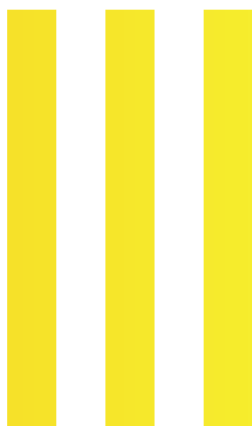
⁵ National Institute of Biology, Marine Biology Station, Piran, Slovenia

⁶ Department of Integrative Marine Ecology (EMI), Stazione Zoologica Anton Dohrn, Napoli, Italy

⁷ Slovenian National Building and Civil Engineering Institute, Ljubljana, Slovenia

⁸ Current address: Department of Earth Science Arditò Desio, University of Milano, Milano, Italy

e-mail: avian@units.it



Low Density and Soft Matter



Photo-processing of nitrogenated aromatics in space: dissociative photoionisation of quinoline as a test case

Elettra | GasPhase, CiPo

How life came about is a long-standing mystery to humans. For well over a century, humans believed that life originated in a complex primordial soup driven by complex chemistry in oceans, volcanos, etc. on Earth. Essentially a complex blend of chemicals in a dense, energetic environment driven by several chemical processes and assisted by liquid water. The famous Urey-Miller experiment reinforced this view in modern times. In the last few decades, this perception has changed radically thanks to the astronomical observations within and beyond our solar system, as well as several interplanetary missions. The chemical mainstay of life is a class of complex and large molecules woven with the help of a carbon-based backbone studded with other primary atoms like hydrogen, nitrogen, oxygen, sulfur, phosphorous, etc. These large molecules are often built brick by brick with smaller subunits like amino acids and nucleobases. Such small molecules are expected to be very fragile against high energy radiation in open space and were not expected to live long unless a planet like Earth provides a protected environment. To our surprise a large number of organics, especially aromatic organics (molecules with rings, generally hexagonal rings) have been detected in abundance in and around young stars, and nebulae in the last three decades. These molecules are not only present, but they are also the dominant molecular species in certain cases. Moreover, recent studies with asteroid samples retrieved from outer space have shown that the first set of biologically important organic molecules formed in our solar system well before the process of planet formation was completed. Thus it has become evident that complex photo processing of small aromatic organic substances is essential for the formation of molecules of life in a cold rarified environment in a protoplanetary stage of a solar system. And this can possibly be an alternative way of seeding life on earth by bringing such active molecular inventory to Earth via precipitation of

asteroid or cometary fragments. Polycyclic aromatic heterocycles (PAHs) and their nitrogenated derivatives are an important class of compounds that are detected in situ, or expected to exist in, a diverse range of environments outside Earth, such as the interstellar medium, protoplanetary discs, in the atmospheres of planets and moons, also in samples of meteorites, asteroids, and comets, etc. It is understood that these molecules play a major role in the organic chemical evolution of a solar system when irradiated with high-energy solar radiation. Therefore, their formation and subsequent photochemistry in such environments are of particular interest and an area of widespread research. The task becomes quite convenient for small, representative molecules such as naphthalene, azulene, indole, quinoline, and iso-quinoline. Such investigations will help us to identify common dissociative mechanisms spanning across the whole class of compounds. Such a unifying feature will radically simplify our efforts to model chemistry in interplanetary and interstellar environments. The photo-driven elimination of species such as HCN, HNC, C₂H₂, HCNH, and HC_nN from quinoline and other PANHs may solve the long-standing mystery of the origin of such species in and around astronomical bodies such as Titan's (moon of Saturn) atmosphere and cometary comae, etc. and aid in understanding the recent discoveries of a broad range of biomolecules in such bodies.

With this motivation, a series of PEPICO investigations are being conducted at the GasPhase and CiPo beamlines at Elettra. EUV photons ranging from 15 eV to up to 90 eV were used to cause dissociative photoionisation of quinoline and iso-quinoline molecular targets. Photoelectron spectra and breakdown curves are measured and carefully interpreted. These results were compared with the suitable quantum structure and kinematics calculations, which has resulted in

a few startling findings. It is found that the resilience of PAHs and PANHs against direct VUV photodamage allows great scope for molecular rearrangements, isomerization, and statistical decay. The present study demonstrates the unequivocal similarity between dissociative photoionization of naphthalene, azulene, quinoline, and iso-quinoline. We could identify and demonstrate the prevalence of certain pre-dissociation isomerization mechanisms which could essentially bring the photoprocessing of a large family of aromatic organics in a unified single highway of decay progression. A careful comparison of breakdown curves of various fragments identifies the dissociation sequence of the primary channels as well. Interestingly, every primary and secondary fragment produced in the studied photon energy range has been known to be present in significant quantities in the ionosphere of Titan, asteroids, and cometary comae. Finally, we highlight two fundamental questions arising from the results obtained here that form the basis of much wider and more diverse investigations in PANHs. First, considering the underlying similarity in naphthalene and quinoline photodissociation processes, is it plausible to identify and quantify photodissociative properties that are common to most, if not all PANHs? Second, is the commonality of the dissociative photoproducts of quinoline and the upper atmospheric composition of Titan of any significance? All the decay products observed in the present study are found abundantly in Titan's atmosphere. Considering the astronomical importance of quinoline and in situ confirmation of the presence of large-sized nitrogenated hydrocarbons in Titan's atmosphere, our observations indicate the possible role of PANHs in the equilibrium composition of Titan's atmosphere, asteroids, and even cometary surroundings, which warrants further investigation.

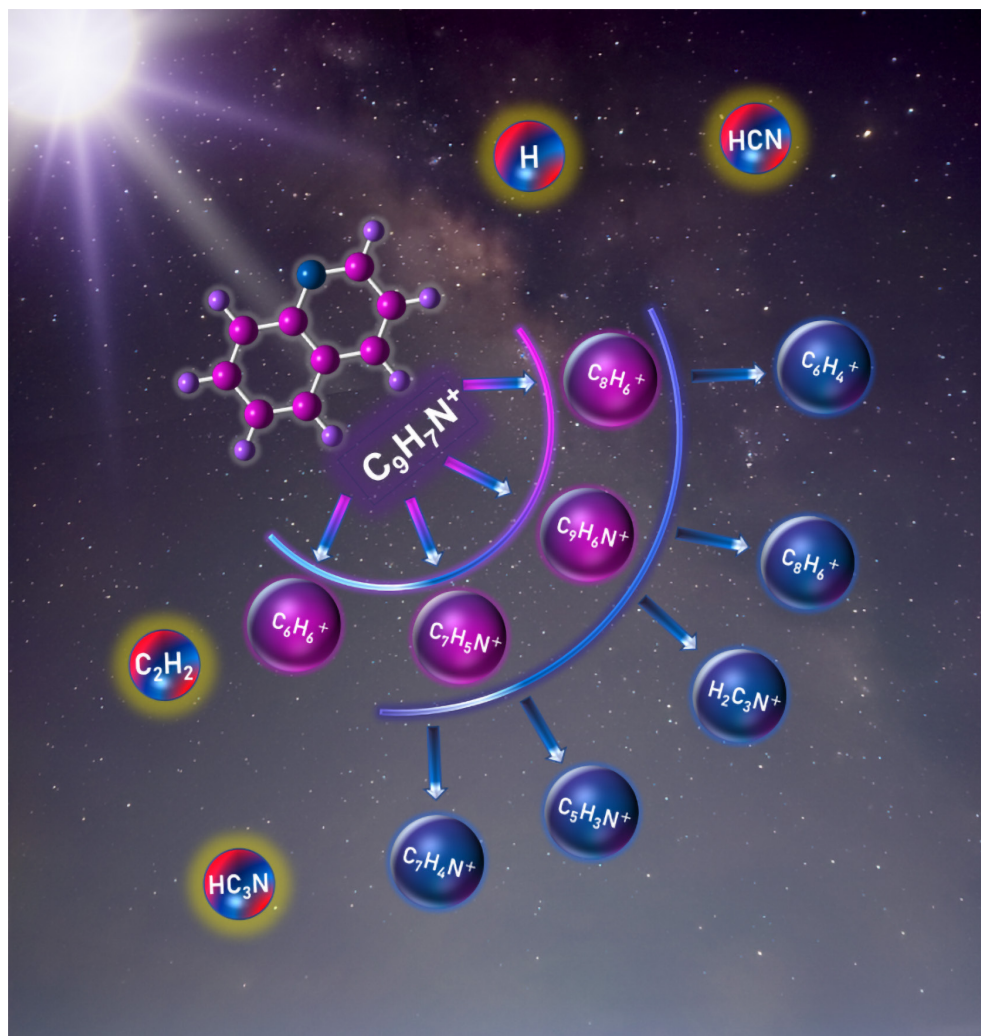


Figure 1. Primary and Secondary decay channels of Quinoline. Each of the fragment is of astronomical significance. The larger fragments are found to have more than one isomeric structure.

Acknowledgments

The authors acknowledge the support provided by the 2022-024 Indo-Italian program for exchange of researchers "Genesis of organic molecules in the extra-terrestrial environment: role of energetic radiation." This work was supported, in part, by NASA's Solar System Exploration Research Virtual Institute (SSERVI): Institute for Modeling Plasma, Atmosphere, and Cosmic Dust (IMPACT).

Original paper

(1) Umesh R. Kadhane *et al.*, *J. Chem. Phys.* **156**, 244304 (2022) DOI: 10.1063/5.0092158

(2) Karthick Ramanathan *et al.*, *J. Chem. Phys.* **157**, 064303 (2022) DOI: 10.1063/5.0092161

1) U.R. Kadhane¹, M.V. Vinitha¹, K. Ramanathan¹, S.Arun¹, J. Bouwman^{2,3,4}, L. Avaldi⁵, P. Bolognesi⁵, R. Richter⁶

2) K. Ramanathan S. Arun, J. Bouwman, L. Avaldi, M. V. Vinitha, P. Bolognesi, R. Richter, U. R. Kadhane

¹ Indian Institute of Space Science and Technology, Kerala, India

² Laboratory for Atmospheric and Space Physics, University of Colorado, Boulder, Colorado, USA

³ Department of Chemistry, University of Colorado, Boulder, Colorado, USA

⁴ Institute for Modeling Plasma, Atmospheres and Cosmic Dust (IMPACT), NASA/SSERVI, Boulder, Colorado, USA

⁵ Institute of Structure of Matter-CNR (ISM-CNR), Monterotondo, Italy

⁶ Elettra - Sincrotrone Trieste S.C.p.A., Trieste, Italy

e-mail: umeshk@iist.ac.in

The importance of gas phase photoelectron spectroscopy in science and its relationship to molecular orbital theory

Elettra | GasPhase

Up to circa 1960, the solutions to the SE (Schrödinger Equation), which had been developed in the early 20th century, were primitive for Chemistry. The HMO (Hückel molecular orbital) theory developed in the 1930's was an important development for Chemistry in particular, but took the cavalier attitude, that if it was difficult or impossible to evaluate some of the required integrals for solution of the SE, then just declare them zero. This was known to be false from the start, but it enabled forward movement from the completely empirical RT (Resonance Theory) which had been developed earlier. The arrival of HMO extended the concept of doubly occupied molecular orbitals to new challenges. This did not happen with acclamation, the RT supporters attacked supporters of MO theory personally, as well as attempting to stop their publications in Journals controlled by the scientific societies. The development of commercial journals, i.e. ones outside the control of the scientific societies, was one necessary solution for the MO community. However, there was little experimental support for MO theory at the time. The invention of PES (photoelectron spectroscopy) in the 1960s changed all that. The quality of the theoretical (i.e. computational) analysis has been dramatic. The advent of parallel and vector processors around 1980, especially the Cray super-computers, introduced hardware stability and speed of processing almost exponentially. This in turn allowed the full range of theoretical methods, including configuration interaction and coupled cluster (CI and CC) methods, to be exploited for molecules containing 20 or so atoms, to very high accuracy, and very much larger molecules to be studied to unprecedented levels. The corrections necessary to the HMO theory were largely solved by the use of Gaussian functions, rather than Slater (exponential) ones. These allowed all terms in the SE to be evaluated, except interelectron correlation; that is achieved

by CI and CC methods. The methods had been known but the application was almost impossible. All of this required high resolution spectra, as are measured on the Gas Phase port extremely important, to check that theory and experiment agree. Our joint Project is a good example of this interdependence. When a sample absorbs UV (ultraviolet) light, then (generally) one electron is 'excited' from its resting orbital into an excited one, forming an 'excited state'. If the energy ($h\nu$) of this light is sufficiently high, then the excited electron is detached from the molecule. If we measure the kinetic energy of this electron, then we can determine the energy that it had in the molecule, from the difference in energy from the ionizing light. This is widely called photoelectron spectroscopy, the procedure is photoionization, and the gas phase port of Elettra performs this.

Originally, PES used the He(I) resonance line, 584 Å (21.21 eV); in practice, the low count rate made ionization energies higher than about 18 eV, so weak, as to be very unreliable. But, this enabled the ionization (or binding) energies (IE) of the outer valence shell electrons to be measured systematically, compared with theoretical calculations, and proceeded from 1963 to the present; this had not been possible previously. The resolution of the early instruments was ~12 meV, with most being supplied by Perkin-Elmer and subsequently Helectros. Later, the use of singly ionized helium, (He(II) at 304 Å, 40.81 eV) extended the IE range, but the very low light intensity made this of limited value. Synchrotron radiation, as in the gas phase port of Elettra performs this, with high cross-section, and use of this type of radiation has almost completely replaced the use of He(I and II). However, the quality of the analyser is also crucial. The VG-Scienta SES-200 photoelectron analyser is an important part of the Gas Phase port on Elettra.

As an example of our research project, our subject is γ -pyrone, systematically named as 4H-pyran-4-one, and shown in

Figure 1(1) as structures 1a and 1b. The individual bands of the PES can often have complex vibrational patterns, and an example is in Figure 1(4). As well as the spectral analysis, our configuration interaction (CI) basis theoretical profile can be obtained. We use the CAM-B3LYP functional in the time dependent density functional theoretical (TDDFT) method. The onset of the photoelectron spectrum of γ -pyrone, is shown Figure 1(4). The overlap of the Franck-Condon profiles for the 1^2B_2 (in blue) and 1^2B_1 (in red) ionic states. The inset peaks have Half-Widths at Half-Maximum (HWHM) of 10 and 70 cm^{-1} (narrow and wide lines respectively). This band, is complex and cannot be rationalized solely in terms of the predicted vibrational structure for the lowest ionic state, 1^2B_2 , at the FC (Franck-Condon) level. However, if the observed band is accepted as the resultant profile from both 1^2B_2 and 1^2B_1 , then we arrive at the combined profile shown. All the observed principal peaks are accounted for. The calculated separation of the two states given above is relatively close to the calculated separation of the 0-0 bands for the two states. These 0-0 bands are by far the most intense for either state. It is unusual for two different IE with overlapping vibrational structure to both show relatively sharp bands. Normally the higher energy member is degraded by the interference of the lower band wave-train.

The data collection and present analysis is believed to be at 'The state of the Art.' This arises from the high-quality analyser used in the experiment, together with the high-level computational approach.

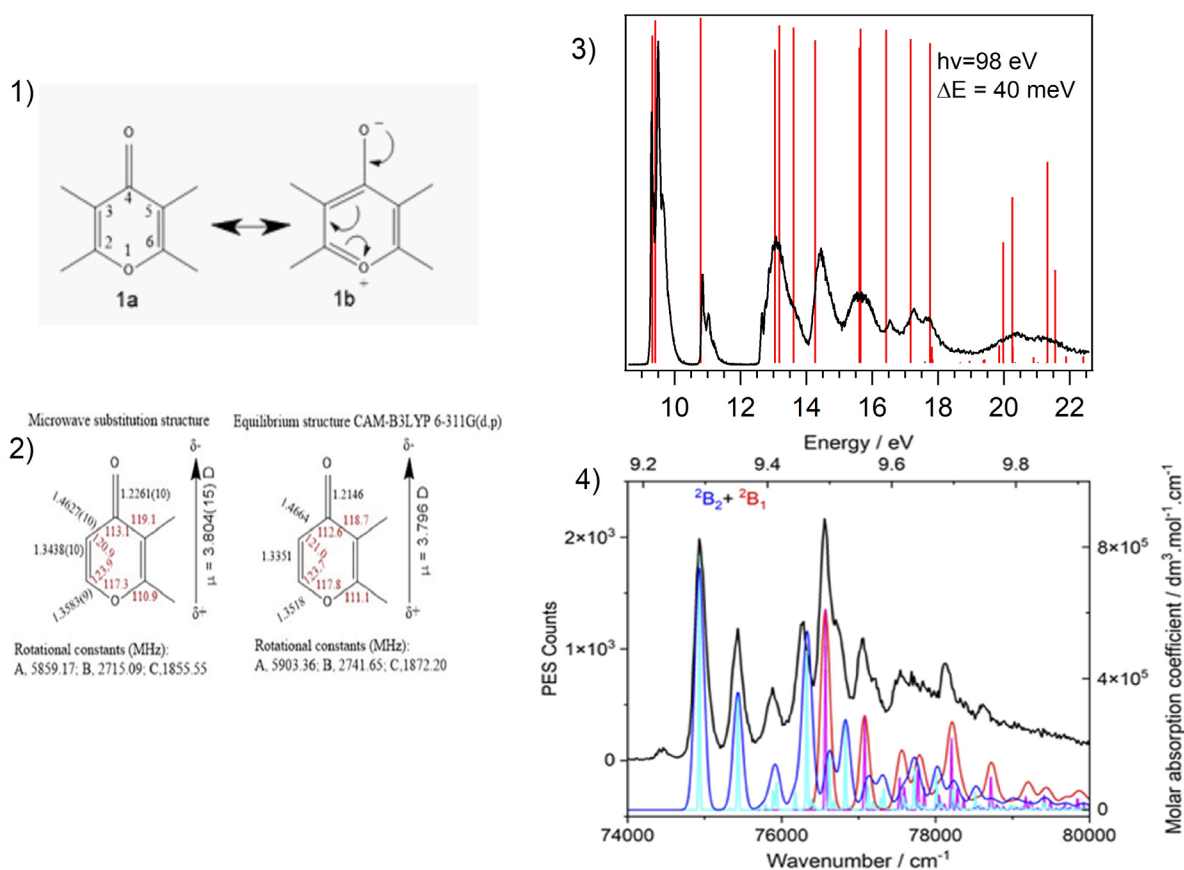


Figure 1. The polar structure of γ -pyrone (1) The molecule is planar, with 2 planes of symmetry, denoted as C_{2v} . It has bond lengths close to 1a, but the molecule has a large dipole moment, which is represented by 1b; classically called a resonance hybrid (1) its microwave spectral and equilibrium structures (2). The wide scan photoelectron spectrum for γ -pyrone was acquired at $h\nu=98$ eV, for the range 8 to 27 eV; the energy resolution, ~ 40 meV, is shown in Figure 1(3). The vertical bars are the pole strengths (intensities) from calculations of the ionic state energies using the Tamm-Dancoff approximation (TDA). This method gives a good approximation to the observed PES band energies, as well as the symmetries and orbital compositions of each band (3) and onset (4) showing the assignment as two overlapping states.

Acknowledgments

We thank (a) the Elettra Synchrotron facility for the grant of beamtime and C. Puglia (Uppsala University, Sweden) and the Carl Tryggers Foundation for making available the VG-Scienta SES-200 photoelectron analyser; (b) the University of Edinburgh (Eddie3) and Edinburgh Parallel Computing Centre's (Cirrus) super-computing facilities for support.

We thank the Journal of Chemical Physics and AIP for permission to re-use the published data.

Original paper

J. Chem. Phys. **158**, 014304 (2023)
<https://doi.org/10.1063/5.0128764>

M. H. Palmer¹, M. Coreno², M. de Simone³, C. Grazioli³, N. C. Jones⁴, S. V. Hoffmann⁴, R. A. Aitken⁵, D. K. Sonecha⁵

¹ School of Chemistry, University of Edinburgh, Edinburgh, Scotland, UK

² ISM-CNR, Istituto di Struttura della Materia, Trieste, Italy

³ IOM-CNR, Istituto Officina dei Materiali, Basovizza, Trieste, Italy

⁴ ISA, Department of Physics and Astronomy, Aarhus University, Aarhus, Denmark

⁵ School of Chemistry, University of St Andrews, North Haugh, St Andrews, Scotland, UK

e-mail: m.h.palmer@ed.ac.uk; marcello.coreno@elettra.eu; desimone@iom.cnr.it; grazioli@iom.cnr.it; vronning@phys.au.dk; nykj@phys.au.dk; raa@st-andrews.ac.uk; dks1@st-andrews.ac.uk

Driving Rabi oscillations with extreme-ultraviolet light pulses

FERMI | LDM

Let us consider an electromagnetic field interacting with a 2-level quantum system. In the presence of the field, the population can be transferred periodically from one level to the other if the natural lifetime of the excited state is larger than the duration of the external field. The periodic exchange of population between the ground and excited states are known as Rabi oscillations, a ubiquitous phenomenon in physics. The coherent electromagnetic field driving the oscillations usually have long wavelengths ranging from infrared to ultraviolet. Over the last two decades, light pulses with shorter wavelength in the extreme ultraviolet, or, XUV (λ : 12 - 120 nm) domain have started to become readily available. These include high-order harmonic generation (HHG) based tabletop sources as well as seeded free-electron lasers (FELs) dependent on linear electron accelerators. HHG sources can provide pulses down to few attoseconds (1 as = 10^{-18} s), making the bandwidth of the pulses more than few tens of electron volts. Pulses from FELs can be of few tens of femtoseconds (1 fs = 10^{-15} s), but with a bandwidth of only a few tens of milli-electron volts. The narrow bandwidth combined with high temporal and spectral coherence make the pulses from seeded FELs, such as FERMI, an ideal tool to study Rabi oscillations between two quantum levels in the XUV domain.

Here, we study the Rabi oscillations between the two levels, $1s^2$ and $1s4p$ in neutral helium atoms using femtosecond intense XUV pulses (photon energy: around 23.4 eV) from FERMI. One photon from an XUV pulse couples these two levels, while a second photon from the same pulse ionizes the helium atom, acting as an *in-situ* probe of the Rabi dynamics. The physical picture behind our experiment is described in Fig. 1. At time $t = 0$, the system is at the ground state, $|a\rangle = 1s^2$, from which it takes two photons to ionize the atom. At time $t = \pi/\Omega$, where Ω is the Rabi frequency, the systems is at the excited state, $|b\rangle = 1s4p$, from where it takes one

photon to ionize. At the resonance, the amplitude of the two levels (under rotating wave approximation) can be expressed as: $a(t) = \cos(\Omega t/2)$ and $b(t) = -i \sin(\Omega t/2)$. Clearly, $a(t)$ changes sign after $1/2$ Rabi period, whereas $b(t)$ changes sign after 1 Rabi period. Quantum mechanically, changing sign implies that the photoelectron wave-packet picked up an additional phase of π (note that $e^{i\pi} = -1$). The destructive interference between the two photoelectron wave-packets emitted at $t = 0$ and $2\pi/\Omega$ with amplitude $a(t)$, or, at $t = \pi/\Omega$ and $3\pi/\Omega$ with amplitude $b(t)$ leads to a splitting in the measured photoelectron spectra, identified as the Autler-Townes (AT) doublet. In other words, the Rabi oscillations in the temporal domain manifests itself as the AT doublet in the spectral domain. In our experiment, the AT splitting was measured to be around 80 ± 2 meV, which implies a Rabi period of 52 fs and an effective intensity of the XUV-FEL pulse of about 2×10^{13} W/cm². However, we noticed that the measured photoelectron spectra were highly asymmetric as a function of the photon energy of the driving pulse (see Fig. 2(a)). In addition, the symmetric AT doublet was found to be at the photon energy of 23.753 eV, which is blue-shifted by almost 11 meV from the exact $1s^2 \rightarrow 1s4p$ transition energy of $\hbar\omega_0 = 23.742$ eV in helium (see Fig. 2(b)). The observed avoided crossing can easily be explained by the 'photon+atom' dressed-state picture developed by C. Cohen-Tannoudji. To explain the observed asymmetry as well as the blue shift, we used an analytical model based on perturbation theory on top of the Rabi model. The Rabi model implies that the frequency components of the amplitude $a(t)$ would be asymmetric: $1 \pm (\Delta\omega/W)$, where, $\Delta\omega$ is the photon energy detuning from ω_0 and $W = \sqrt{(\Delta\omega)^2 + \Omega^2}$ is the generalized Rabi frequency. On the other hand, for the amplitude $b(t)$, the frequency components are symmetric: $\pm\Omega/W$. Therefore, the observed asymmetry in the experimental photoelectron spectra

would imply a significant contribution from the two-photon non-resonant ionization pathways from the ground state. This surprising finding can be understood as follows: the resonant ionization pathway from the excited state is a one-photon process, therefore describable by the first order time dependent perturbation theory. The non-resonant ionization pathway from the ground state is a two-photon process and thus, can only be described by a second order time dependent perturbation theory. At such a high effective intensity of the driving XUV-FEL pulse, the contributions from all the dipole-allowed states, below and above the continuum, can interfere constructively to give rise to a giant wave for the two-photon pathway, making it comparable to the one-photon pathway. One may wonder whether these pathways, having similar transition probabilities can interfere with each other. To test it, we used the analytical model to add both the pathways coherently allowing them to interfere. It turned out that for $\Delta\omega = 0$, the resulting AT doublet is highly asymmetric (see Fig. 2(c)). The AT doublet becomes symmetric only when $\Delta\omega > 0$. Thus, the observed blue shift of the symmetric AT doublet in the measured photoelectron spectra is a direct manifestation of the quantum interference between the one-photon and two-photon ionization pathways. In addition to the experimental demonstration of Rabi oscillations and light-dressed states at short wavelengths, our results shows that the high intensities at seeded FELs can initiate quantum interferences between different ionization pathways. This opens up new avenues to manipulate the relative phase between these pathways to control the outcome of the coherent light-matter interaction in complex systems.

Low Density and Soft Matter

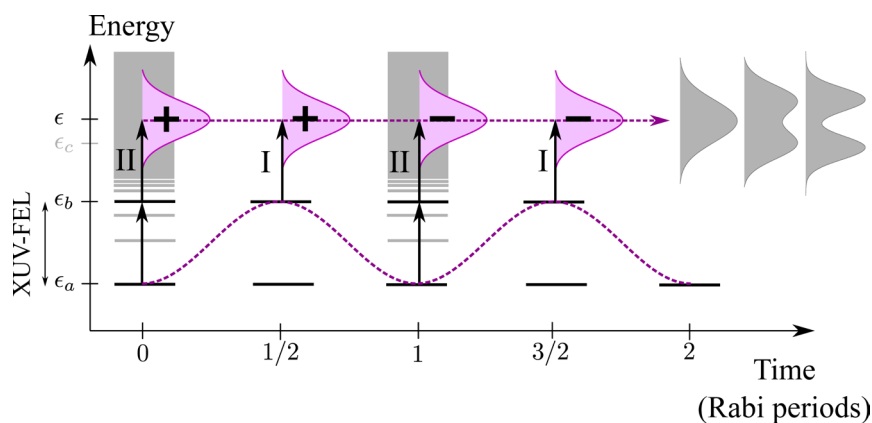


Figure 1. The time dependent development of the Autler-Townes splitting. The amplitude $a(t)$ changes sign after $\frac{1}{2}$ Rabi period, whereas the amplitude $b(t)$ changes sign after 1 Rabi period. The destructive interference between the two photoelectron wave-packets with amplitude $a(t)$ or $b(t)$, having a phase difference of π leads to the doublet structure in the frequency domain. Adapted from S. Nandi et al., *Nature* **608**, 488 (2022), published under a Creative Commons Attribution 4.0 International License.

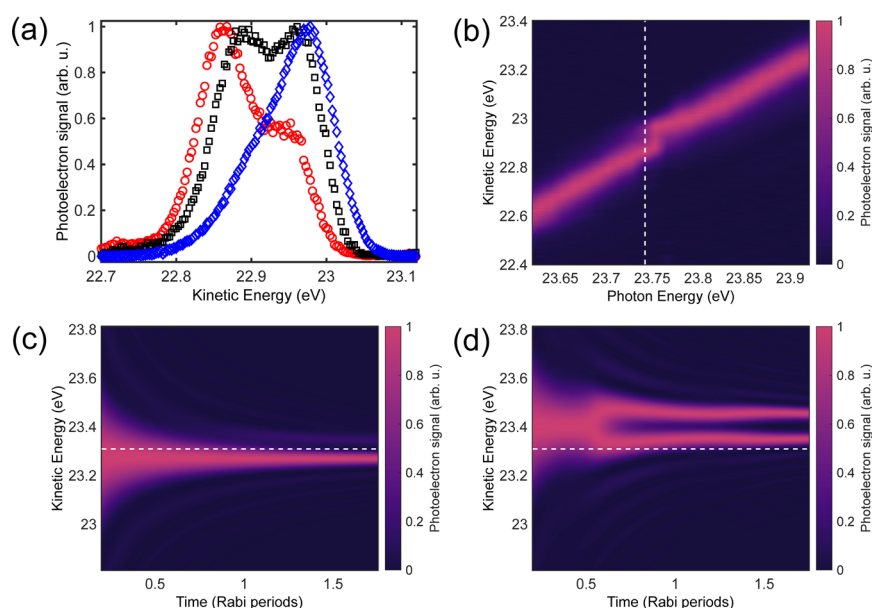


Figure 2. (a) Experimental photoelectron spectra at 23.753 eV (black squares) and at ± 13 meV detuning (blue diamonds and red circles respectively); (b) Experimental avoided crossing at XUV wavelength. The dashed line represents the photon energy for $1s^2 \rightarrow 1s4p$ transition in helium, obtained from the NIST database; (c) Theoretical photoelectron spectra obtained from the analytical model as a function of Rabi periods at the resonance, $\Delta\omega = 0$; (d) Same as (c), but at $\Delta\omega = 62$ meV. The dashed line in (c) and (d) represents the expected kinetic energy (23.3076 eV) of a photoelectron that has absorbed two resonant photons. Adapted from S. Nandi et al., *Nature* **608**, 488 (2022), published under a Creative Commons Attribution 4.0 International License.

Acknowledgments

We acknowledge networking grants from LASERLAB-EUROPE to attend the beamtime at FERMI. S.N. thanks Centre National de la Recherche Scientifique (CNRS) and Fédération de Recherche André Marie Ampère for financial support. J.M.D. acknowledges support from the Knut and Alice Wallenberg Foundation (2017.0104 and 2019.0154), the Swedish Research Council (2018-03845) and the Olle Engkvist's Foundation (194-0734). R.F. thanks the Swedish Research Council (2018-03731) and the Knut and Alice Wallenberg Foundation (2017.0104) for financial support. P.E.-J. acknowledges support from the Swedish Research Council (2017-04106) and the Swedish Foundation for Strategic Research (FFL12-0101).

Original paper

S. Nandi, et al., *Nature* **608**, 488 (2022);
DOI : 10.1038/s41586-022-04948-y

S. Nandi¹, Edvin Olofsson², M. Bertolino², S. Carlström², Felipe Zapata², D. Busto², C. Callegari³, M. Di Fraia³, P. Eng-Johnsson², R. Feifel⁴, G. Gallician⁵, M. Gisselbrecht², S. Maclot², L. Neoričić², J. Peschel², O. Plekan³, K. Prince³, R. Squibb⁴, S. Zhong², P. V. Demekhin⁶, M. Meyer⁷, C. Miron⁵, L. Badano³, M. Danailov³, L. Giannessi³, M. Manfredda³, F. Sottocorona³, M. Zangrando³, J. M. Dahlström²

¹ Université de Lyon, Université Claude Bernard Lyon 1, CNRS, Institut Lumière Matière, Villeurbanne, France

² Department of Physics, Lund University, Lund, Sweden

³ Elettra-Sincrotrone Trieste, Trieste, Italy

⁴ Department of Physics, University of Gothenburg, Gothenburg, Sweden

⁵ Université Paris-Saclay, CEA, CNRS, LIDYL, Gif-sur-Yvette, France

⁶ Institute of Physics and CINSaT, University of Kassel, Kassel, Germany

⁷ European XFEL, Schenefeld, Germany

e-mail: saikat.nandi@univ-lyon1.fr ; marcus.dahlstrom@matfys.lth.se

Filming molecular chiral dynamics from the inside with free electron laser

FERMI | LDM

Chiral molecules, with their unique properties and behaviour, significantly impact various scientific disciplines, including chemistry, biology, and physics. The concept of chirality refers to the property of a molecule that cannot be superimposed onto its mirror image. As such, chiral molecules can be found in nature in two specular forms, which are known as enantiomers. This structural difference often leads to distinct reactivity, biological activity, and pharmacological properties between the two opposite enantiomers. Consequently, understanding and manipulating the behaviour of chiral molecules is crucial for advancements in materials science, pharmaceutical development, and catalysis. Moreover, chirality is intricately linked to the origin of life itself. A remarkable example is homochirality, which refers to the emergence of a sole type of chirality in certain biomolecules that played a crucial role in the development of biological information storage and transfer systems, such as the formation of DNA and RNA.

Scientists in the fields of physics, biology, and chemistry have dedicated considerable efforts to studying chirality. However, much is still unknown about the ultrafast dynamics of chiral compounds. Recently, a promising technique called TR-PECD (Time-Resolved Photo-Electron Circular Dichroism) has emerged for investigating the time-dependent evolution of chiral systems. Within this approach, a molecule is first excited by an ultrashort visible or ultraviolet pulse, and the relaxation dynamics that follows this photoexcitation is probed by photoionizing the molecule with an ultrashort circularly polarized pulse. The photoionization by the circular pulse leads to an asymmetric emission of the electrons along the propagation direction of the pulse, which provides valuable information about the transient chirality of the medium. However, in this experiment, the observed photoelectron

asymmetry can arise from either the chirality of the initial orbital from which the electron is ionized or the chirality of the surrounding electronic potential through which the photo-electron scatters. Disentangling the role of these two contributions can be experimentally challenging.

In our investigation, we used the circularly polarized radiation generated by the free-electron laser Fermi to measure the chiral dynamics of photo-excited fenchone, an organic chiral molecule. The molecule was initially excited with an ultrashort visible pulse and subsequently probed by photoionization from the core-level carbon 1s states of the molecule. Compared to valence TR-PECD, in this case, the electron is ionized from an initial orbital which is *localized, achiral, and specific* to the molecule. It thus serves as an ideal in-situ probe for studying the chiral electronic potential through which the photoelectron scatters. Moreover, depending on the molecular structure and the chemical shifts of the electron binding energy, different sites of the molecule may be simultaneously probed with a single experiment.

The experiment was conducted at the Low-Density Matter (LDM) beamline of FERMI, a free-electron laser facility known for providing circularly polarized soft X-ray pulses with high temporal coherence and high polarization purity. The excitation scheme involved a two-photon absorption process using an ultrafast UV pump to excite the molecule to a diffuse 3s Rydberg state. The relaxation dynamics of the molecule were then probed by photoionizing the excited molecule with a circularly polarized FEL probe pulse of a few femtoseconds duration. The photoelectron angular distribution was collected with the VMI (velocity map imaging) spectrometer available at LDM, which allowed us to characterize the complete angular distribution of

the emitted photoelectrons and the degree of forward-backward asymmetry produced by the enantio-specific response of the molecule.

The experiment demonstrated that the pump excitation not only initiated relaxation dynamics from the excited Rydberg state but also caused transient changes in the binding energies of some of the carbon 1s sites of the molecules. These excited state chemical shifts (ESCS) allowed us to achieve an enhanced *site-specificity* of the technique, by making it possible to measure the local chirality of the electronic environment around specific carbon atoms that were not visible in the ground state. Indeed, in the ground state, these carbon atoms were mixed with contributions from other carbon 1s sites of the molecule. We demonstrated that the combination of a site-selective enantio-sensitive probe and the chemical shift induced by the excitation enabled their individual characterization in terms of energy shift and chiral response. This capability is particularly appealing for studying organic compounds at the Carbon K-edge, where it could be exploited for measuring the contribution of different carbon atoms through their different ESCS.

The ability to observe the chirality of a molecule from the perspective of individual atoms during ultrafast processes represents a significant advancement in the study of chiral molecules. It opens up possibilities for advanced TR-chiral-XPS (Time Resolved - *chiral* - X-ray Photoelectron Spectroscopy) approaches, which can provide novel insights into fundamental questions in photochemistry and biochemistry related to chirality. This includes examining the chiral dynamics of electron transfer processes, exploring the role of chirality in enzymatic reactions, and elucidating the mechanisms of chiral recognition in biological systems.

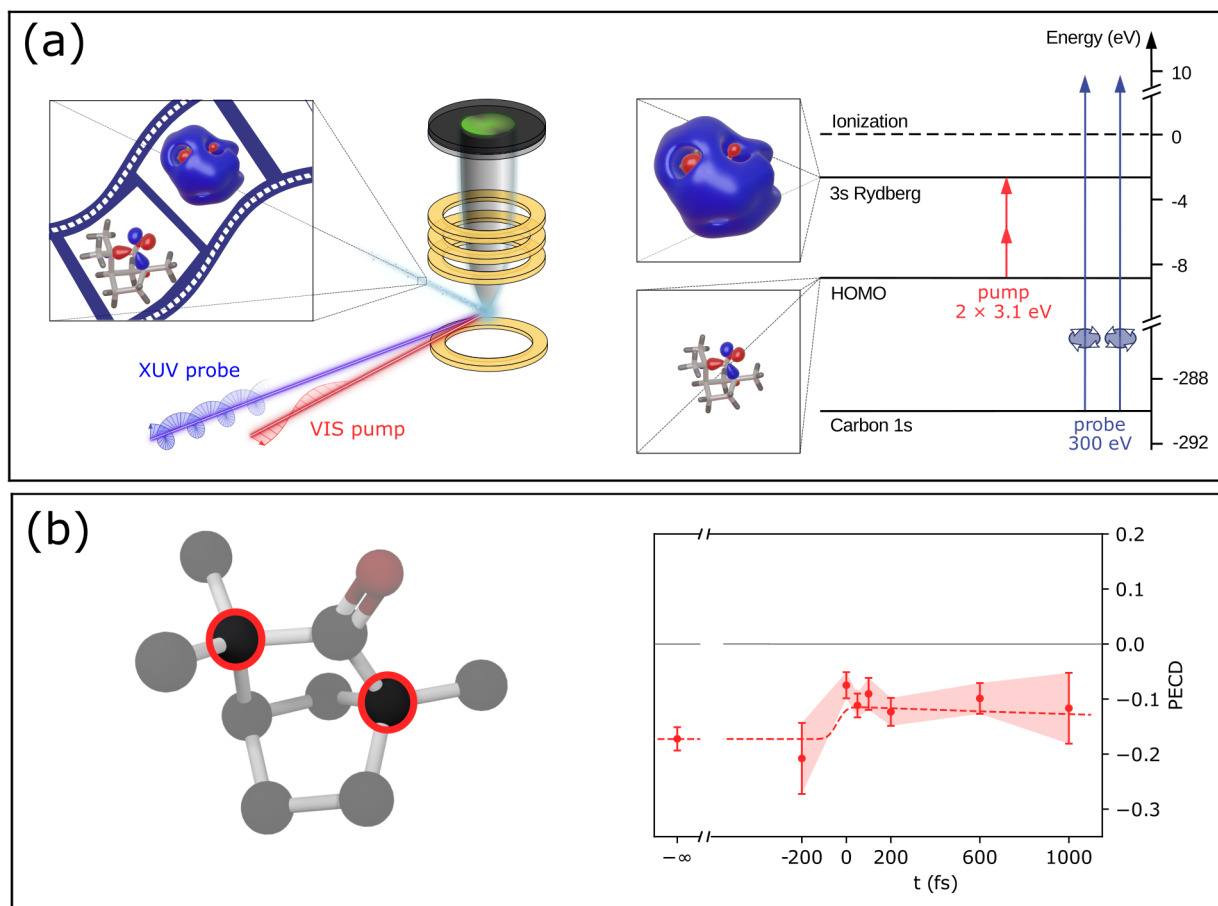


Figure 1. (a) experimental setup (left), excitation scheme (right); (b) the core-level PECD contribution from the carbon sites shown in red (left) is probed in a time-resolve way (right). Adapted from the original under the terms of the Creative Commons Attribution 4.0 International license.

Acknowledgments

This project has received funding from the European Union's Horizon 2020 research and innovation programme under Grant Agreement Nos. 674960 (ASPIRE), 860553 (SMART-X), 682978 (EXCITERS) and 654148 (LASERLAB-EUROPE), from the Italian Ministry of Research and Education with the projects ELI ESFRI Roadmap, from the Consiglio Nazionale delle Ricerche with the Joint Laboratory ATTOBIO. FC, MG and LC acknowledge support from the Deutsche Forschungsgemeinschaft (DFG, German Research Foundation) - SFB-925 - project 170620586 and the Cluster of Excellence Advanced Imaging of Matter (AIM).

Original paper

D. Faccialà *et al.*, Phys. Rev. X **13**, 011044 (2023); DOI:10.1103/PhysRevX.13.011044

D. Faccialà¹, M. Devetta¹, S. Beauvarlet², N. Besley³, F. Calegari^{4,5}, C. Callegari⁶, D. Catone⁷, E. Cinquanta¹, A. G. Ciriolo¹, L. Colaizzi⁴, M. Coreno^{6,7}, G. Crippa^{1,8}, G. De Ninno^{6,9}, M. Di Fraia⁶, M. Galli^{4,8}, G. A. Garcia¹⁰, Y. Mairesse², M. Negro¹, O. Plekan⁶, P. Prasanna Geetha^{1,8}, K. C. Prince⁶, A. Pusala^{1,8}, S. Stagira^{1,8}, S. Turchini⁷, K. Ueda¹¹, D. You¹¹, N. Zema⁷, V. Blanchet², L. Nahon¹⁰, I. Powis³ and C. Vozzi¹

¹ Istituto di Fotonica e Nanotecnologie-CNR (CNR-IFN), Milano, Italy

² Université de Bordeaux-CNRS-CEA, CELIA, Talence, France

³ School of Chemistry, University of Nottingham, Nottingham, United Kingdom

⁴ Center for Free-Electron Laser Science, DESY, Hamburg, Germany

⁵ Physics Department, Hamburg University, Hamburg, Germany

⁶ Elettra-Sincrotrone Trieste S.C.p.A, Trieste, Italy

⁷ Istituto di Struttura della Materia-CNR (ISM-CNR), Roma, Italy

⁸ Dipartimento di Fisica, Politecnico di Milano, Milano, Italy

⁹ Laboratory of Quantum Optics, University of Nova Gorica, Nova Gorica, Slovenia

¹⁰ Synchrotron Soleil, Gif sur Yvette, France

¹¹ Institute of Multidisciplinary Research for Advanced Materials, Tohoku University, Sendai, Japan

e-mail: davide.facciala@cnr.it ; michele.devetta@cnr.it; caterina.vozzi@cnr.it

Real-time motion of molecules unveiled

FERMI | EIS-TIMEX

The atomic structure of molecules is today well known and can be readily studied with both experimental and theoretical methods. However, scientists are aware that many properties of molecules do not depend solely on their stationary atomic structure but also, and critically, on how they move. Indeed, every molecule in nature is characterized by typical (ground-state) vibration modes that are always active at temperatures higher than zero degrees Kelvin. The dynamic properties of molecules reside in those modes whose amplitude dramatically increases with the temperature. At ambient temperature (about 300 degrees Kelvin) molecular vibrations definitely affect how molecules interact with the surrounding environment thus determining their functionality. For example, the functionality of a drug is that of stimulating a beneficial effect on a biological cellular environment. Other molecules can activate a charge transfer (primary step of the photosynthesis) when illuminated by the light of the sun or favor physical-chemical processes when in contact with other substances (molecular catalysts). Improving the functionality of molecular systems, requires accurate knowledge and control of their periodic movements.

Unfortunately, still today, it is extremely difficult to experimentally monitor those vibrations as the size of molecules can be extremely small, sometimes in the order of a thousandth of microns, and the oscillatory displacement of atoms that form the molecules is even smaller. Conventional techniques can barely reveal ground-state vibrations, and when it is possible, they can monitor them indirectly measuring the frequency of the vibration. This limited insight onto the dynamics of molecules definitely hinders improvement and comprehension of the molecular functionality.

A recent campaign of measurements carried out at the TIMEX beamline of FERMI has demonstrated that FEL (Free

Electron Laser) radiation can be fruitfully used to observe the motion of molecules recording how the soft x-ray absorption of selected molecules oscillates in time. Typical low frequency modes of molecules are in the THz (tera Hertz) frequency domain, therefore the period of those oscillations is in the picosecond (1 ps = 0.000001 microsecond) time scale.

The scientists of the TIMEX beamline succeeded in activating a coherent oscillation of ibuprofen molecules, a very common anti-inflammatory non-steroidal drug (Fig. 1(a)) made of a racemic mixture of left and right-handed enantiomers. Coherent molecular motion has been triggered by an ultrashort laser light pulse with a duration shorter than 0.1 ps acting as a gentle, sudden, optical pump. This technique is called "impulsive stimulated Raman scattering" (ISRS). The coherent dynamics initiated by ISRS drastically amplifies the experimental signal as the oscillation of the excited molecules results from a phased collective motion. By monitoring the soft x-ray transmission of oscillating ibuprofen molecules with ultrashort (< 0.1 ps) FEL pulses across to the carbon K-edge photon energy (284.2 eV), the experimental team has observed a periodic fluctuation of the transmission signal associated with the movement of specific carbon atoms present in the ibuprofen molecule. Fig. 1(b) shows an example of those vibration modes (30 cm⁻¹ ≈ 1 THz). The frequency of those vibrations is in agreement with numerical simulations. Importantly, exploiting the different kinds of polarization of the light emitted by FERMI, the method helps the researchers to distinguish not only which carbon atom is involved in the vibration, but also the enantiomer to which the atoms belong. By changing the polarization of the probe light from circular-right to circular-left, one can access the same atom, which however belongs to the mirror symmetric molecule. This can be extremely important as molecular reactivity is

enantiospecific, that means it depends on the orientation of a specific group in space. (see Fig. 1(a)).

Fig. 1(b) has been obtained measuring the absorption at different time delays between the fs-laser pump and the soft x-ray probe covering a delay interval of about 4 ps (between -1 ps and + 3 ps). This method, called "pump-probe", allows scientists to monitor ultrafast dynamics that are not accessible by conventional instrumentation. The pump-probe approach exploits the finite and universal speed of light that is about 300000 km/s in air. Therefore, by tuning the length of the probe pulse path one can precisely set the delay between the pump and probe pulses. This can be done using a "delay line", that is an accurate linear translation stage equipped with plane mirrors. By increasing the path length of the probe by 300 μm one increases the delay of the probe accordingly by 1 ps.

Notably, the experiment demonstrates that the properties of the FEL soft x-ray pulses emitted by FERMI (duration, circular polarization, spectral purity) can be used to discriminate between atoms of the same type associating a specific vibration mode with a well-defined carbon atom of a specific enantiomer. This chemical and positional sensitivity is a unique tool for the analysis of the dynamics of molecules, and it can be employed by researchers to study the functionality of many complex molecules.

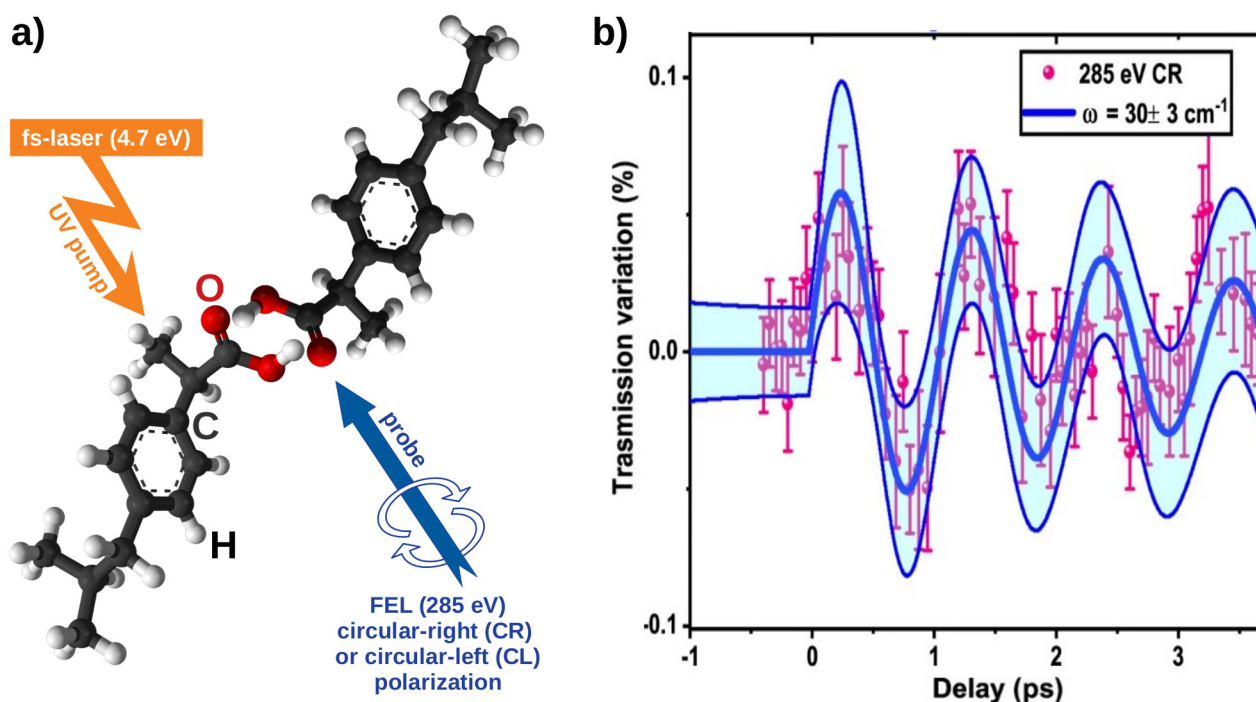


Figure 1. (a) Graphical representation of the ibuprofen dimer composed by a left-handed and a right-handed enantiomer ($C_{13}H_{18}O_2$). Gray atoms are carbon (C), white atoms are hydrogen (H), red atoms are oxygen (O). (b) Ultrafast fluctuation of the transmission of an ibuprofen molecular specimen activated by an ultrashort ultraviolet (UV) laser pulse and measured at the beamline TIMEX of FERMI. This fluctuation reflects a specific ground-state vibration mode of ibuprofen. Figure adapted from R. Mincigrucchi et al., *Nat. Comm.* **14**, 386 (2023).

Acknowledgments

R. M. feels that the society should be aware of the energy required to write the original paper. This quantity is about 136 MWh. M.C. acknowledges support by the Swiss NSF via the NCCR:MUST and by the European Research Council Advanced H2020 Grant ERCEA 695197 DYNAMOX. S.M gratefully acknowledges the support of National Science Foundation (Grant CHE-1953045) and computational support of the Department of Energy (DE-FG02-04ER15571). J.R.R. was supported by the LABEX MANUTECH-SISE (ANR-10-LABX-0075) of Université de Lyon and by the Fédération de Recherche André Marie Ampère (FRAMA). S.C. also thanks the research project "FSE-REACT EU" financed by National Social Fund–National Operative Research Program and Innovation 2014–2020 (D.M. 1062/2021), personal Grant number 23-G-15445-3. We acknowledge Prof. S. Lupi and CNR-IOM for the use of the FTIR interferometer. Thanks to A. Ajdarzadeh, K. Oberhofer, J. Hugues and R. Versteeg for their help with the deep-UV transient absorption measurements of the IBP powders.

Original paper

R. Mincigrucchi et al., *Nat. Comm.* **14**, 386 (2023); DOI:10.1038/s41467-023-36047-5

R. Mincigrucchi¹, J. R. Rouxel^{2,3}, B. Rossi^{1,4}, E. Principi¹, C. Bottari^{1,5}, S. Catalini^{6,7,8}, J. S. Pelli-Cresi¹, D. Fainozzi^{1,5}, L. Foglia¹, A. Simoncig¹, A. Matruglio⁹, G. Kurdi¹, F. Capotondi¹, E. Pedersoli¹, A. Perucchi¹, F. Piccirilli¹, A. Gessini¹, M. Giarola¹⁰, G. Mariotto¹¹, M. Oppermann^{2,12}, S. Mukamel¹³, F. Bencivenga¹, M. Chergui¹³, C. Masciovecchio¹

¹ Elettra-Sincrotrone Trieste S.C.p.A., Trieste, Italy

² Lausanne Centre for Ultrafast Spectroscopy (LACUS), École Polytechnique Fédérale de Lausanne, Lausanne, Switzerland

³ University of Lyon, UJM-Saint-Etienne, CNRS, Saint-Etienne, France

⁴ Department of Physics, University of Trento, Trento, Italy

⁵ Department of Physics, University of Trieste, Trieste, Italy

⁶ European Laboratory for Non-Linear Spectroscopy (LENS), Università di Firenze, Florence, Italy

⁷ Department of Physics and Geology, University of Perugia, Perugia, Italy

⁸ CNR-INO, Consiglio Nazionale Delle Ricerche, Istituto Nazionale di Ottica, Florence, Italy

⁹ CERIC-ERIC, Trieste, Italy

¹⁰ Centro Piattaforme Tecnologiche, University of Verona, Verona, Italy

¹¹ Department of Computer Science, University of Verona, Verona, Italy

¹² Department of Chemistry, University of Basel, Basel, Switzerland

¹³ Department of Chemistry and physics and astronomy, University of California Irvine, USA

e-mail: riccardo.mincigrucchi@elettra.eu, emiliano.principi@elettra.eu

Non-linear Terahertz spectroscopy reveals temperature-independent behavior in the response of liquid water

FERMI | TeraFERMI

Liquid water has been extensively studied, yet its enigmatic properties continue to challenge scientific understanding. At the microscopic level, water molecules in the liquid phase form intricate networks of hydrogen bonds, exhibiting dynamic fluctuations on the picosecond timescale. These fluctuations contribute to the rich behavior of water, yet the precise connection between macroscopic properties and underlying molecular interactions remains elusive. THz (Terahertz) radiation, spanning the frequency range of 0.01 to 20 THz, has emerged as a valuable spectroscopic tool for studying the collective dynamics of water molecules on the picosecond timescale.

Non-linear terahertz spectroscopy techniques, such as OTP (optical-pump THz-probe) and THz-Kerr experiments, have provided valuable insights into the behavior of liquid water. These methods enable the investigation of water's response to intense terahertz fields, shedding light on its non-linear optical properties. Experiments employing OTP have shed light on the coupling between solvating water and solutes, inhomogeneity in the bulk liquid, and proton quantum effects. Additionally, THz-Kerr experiments have been used to explore the anisotropic polarizability of hydrogen-bonded water molecules, the coupling between rotational and translational modes, and the influence of salts on water's structure. THz-pump THz-probe (TPTP) experiments are complementary to these approaches as they allow for both the pump and probe to interact resonantly with infrared-active modes. While these experiments have reported intriguing non-linear signals, the interpretation of the observed phenomena has been the subject of debate, and different theoretical models have been proposed. Various theoretical models have been put forth to explain the non-linear response of liquid water in the THz range. One such model suggests that resonant reorientation of hydrogen-bonded water

molecules plays a key role in describing the experimental observations. This resonant reorientation process involves the excitation of librational motions of water molecules by the THz field, leading to non-linear optical responses. Another proposed model posits that the non-linear refraction of water at approximately 1 THz originates from non-resonant contributions related to oscillations in the mid-infrared range, rather than intermolecular modes involving hydrogen-bonded water molecules. However, the non-resonant model implies a strong temperature dependence, which is inconsistent with our experimental findings.

In our study, we performed non-linear transmission measurements on liquid water at approximately 1 THz, comparing two temperatures, 21°C and 4°C. Experiments were conducted at the beamline TeraFermi with an experimental setup that allowed precise control of the sample temperature. The spot size of the terahertz field was maintained at 0.6 mm². At equilibrium, the linear absorption coefficient of water is strongly temperature-dependent. In Fig 1c we show the THz field transmitted by a static diamond sample cell filled with a thin layer of water at 21 and 4°C. When the water is cooled to 4°C, transmission increases compared to that at 21°C. With a high enough intensity of the input radiation, the absorption coefficient of liquid water can display a non-linear response. By varying the THz intensity while keeping the temperature constant, we observed no significant variation in the non-linear transmission of water (Fig. 1b). The non-linear transmission remained unchanged within the experimental uncertainty, indicating weak temperature dependence in the non-linear response of liquid water. Our experimental findings provide insights into the temperature-dependent behavior of the non-linear response in liquid water. The observed temperature independence suggests that the most appropriate microscopic models for describing the non-linear

response of water should exhibit weak dependence on temperature. The resonant reorientation of hydrogen-bonded water molecules emerges as a promising model that can explain the experimental observations consistently. Further investigations using advanced spectroscopic techniques, such as frequency-resolved measurements and complete fluence-dependent analyses, are warranted to better understand water's non-linear behavior in the THz range.

In conclusion, our study demonstrates that the non-linear transmission of intense terahertz radiation through liquid water remains unchanged at temperatures of 21°C and 4°C. These findings suggest weak temperature dependence in the non-linear response of water and provide support for theoretical models that incorporate the resonant reorientation of hydrogen-bonded water molecules. Our research contributes to the ongoing quest for a comprehensive understanding of water's unique properties and lays the foundation for future investigations into the intricate dynamics of this vital substance.

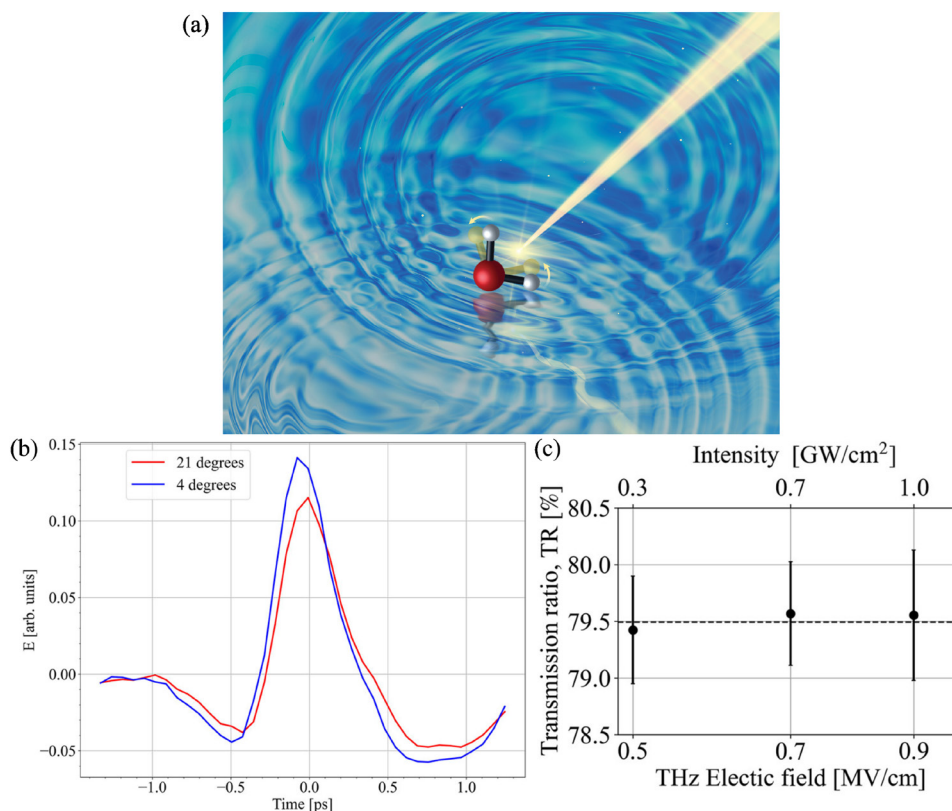


Figure 1. (a) Cartoon representation of a water molecule interrogated by THz radiation. (b) The terahertz field transmitted by a 100 μm thick layer of liquid water at two temperatures (21 and 4 $^{\circ}\text{C}$, in red and blue, respectively). (c) The transmission ratio (TR) was calculated from the THz peak fields transmitted by liquid water at 21 and 4 $^{\circ}\text{C}$. The TR is evaluated at three intensities ($I = 0.3, 0.7, \text{ and } 1.0 \text{ GW/cm}^2$; top axis) or, equivalently, for the maximum terahertz fields shown on the bottom axis (0.5, 0.7, and 0.9 MV/cm). The measured TR values are the same within the error bars, which are lower than about $\pm 0.5\%$. Thus, the water transmission at 21 and 4 $^{\circ}\text{C}$ is independent of the terahertz intensities probed here. The flat dashed line is a guide to the eye. The error bars are standard errors of the mean from 27 measurements. Part (a) of this figure is adapted with permission from the cover figure for Fabio Novelli, Martina Havenith *et al.* PCCP, **24**, 653 (2022), permission for reproduction is retained by the authors under RSC publishing agreement, (b) and (c) are adapted with permission from the original paper under the Creative Commons CC BY license.

Acknowledgments

We acknowledge financial support from the Cluster of Excellence RESOLV (Grant No. EXC 2033–390677874) funded by the Deutsche Forschungsgemeinschaft (DFG, German Research Foundation) and by the ERC Advanced Grant No. 695437 (THz Calorimetry). F.N. acknowledges funding by the DFG with Project No. 509442914. We acknowledge support by the Open Access Publication Funds of the Ruhr-Universität Bochum. These results are part of a project that has received funding from the European Research Council (ERC) under the European Union's Horizon 2020 research and innovation program (Grant Agreement No. 805202-Project Teraqua). This project received funding from the European Union's Horizon 2020 research and innovation program under the Marie Skłodowska-Curie Grant Agreement No. 801459-FP-RESOMUS. We thank CNR-IOM for the use of the MENLO C-Fiber780 laser. We are grateful to P. Di Pietro, A. Perucchi, and M. Havenith for support and discussions.

Original paper

C. Millon *et al.* AIP Advances **12**, 115319 (2022); DOI: 10.1063/5.0120417

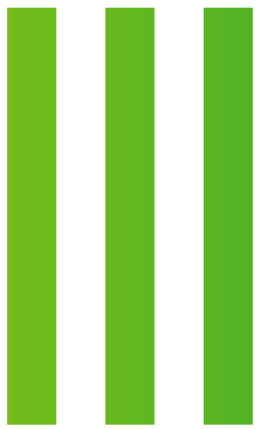
C. Millon¹, J. Schmidt², S. Ramos³, E.P. van Dam³, A. Buchmann³, C. Saraceno¹, F. Novelli³

¹ Photonics and Ultrafast Laser Science, Ruhr University Bochum, Bochum, Germany

² Elettra Sincrotrone Trieste S.C.p.A., Trieste, Italy

³ Department of Physical Chemistry II, Ruhr University Bochum, Bochum, Germany

e-mail: fabio.novelli@rub.de



Structure and Dynamics



The struggle of dipeptides for Life

Elettra | CiPo

The initial transition from inorganic to organic matter, the subsequent self-organization and growing of complexity into precursors of living organisms are among the main unsolved questions that challenge many branches of science. Numerous simple organic molecules, including amino acids and some dipeptides, have been found on meteorites while more than 240 organic compounds have been identified in several regions of space, from dense star-forming regions to protoplanetary disks, atmosphere and surface of minor planets, as well as on astronomical objects like comets and interplanetary dust.

The genesis of this material, its survival in the harsh conditions of space and/or primordial Earth and the mechanisms that guided the further evolution towards more complex biomolecular systems are the subject of an intense research activity which involves remote space observation, *in-situ* sampling and analysis with international space missions, laboratory experiments and theoretical modelling.

Dipeptides, the simplest peptides in nature, have been detected on meteorites. They are built by two amino acids joined via one (linear, l-dipeptide) or two (cyclic, c-dipeptide) peptide bonds. The l-dipeptides represent the first step in the growing complexity of biomolecules towards proteins and enzymes, made by hundreds or thousands of amino acids. However, c-peptides, despite the fact that are made by only few units, may have played a role in the evolution of life as intermediates for the survival of amino acids as well as supporting the synthesis of oligopeptides.

The common feature of any cyclic dipeptide is the 2,5-diketopiperazine (DKP) six member ring, where the functional groups from the two building block amino acids are bound, giving rise to a large variety of structural and bio-functional diversity. Besides being widespread in nature, with many applications in biological and pharmaceutical context and material

science applications, DKPs have also been studied for their possible role in the origin of life in space.

The experiments performed at the CIPO beamline of Elettra used the VG-TOF end-station, where electron and ions can be measured either independently of each other, for PES (photoemission spectroscopy) and mass spectrometry, respectively, or in time coincidence for PEPICO (Photo-Electron Photo-Ion Coincidence) measurements. The PES measurements provide information of the electronic structure of valence orbitals while the state – selected PEPICO allow to associate molecular fragmentation pathways to the specific molecular orbitals selected by the detected photoelectrons, or, in other words, to a specific amount of molecular internal energy. Data interpretation has been supported and guided by quantum chemical calculations and this work is the results of a well-established collaboration between CNR-ISM, Elettra, University Autonoma of Madrid and Stockholm University.

Based on the results of experimental and theoretical studies of the photoionization and photofragmentation of c-Alanyl-Alanine (c-AlaAla) we proposed that the VUV decomposition of this dipeptide begins below 11 eV binding energy with a ring opening, that can be followed either by fragmentation with the efficient release of prebiotic species, like neutral CO and HNCO, or stabilization of the cation into its isomeric oxazolidinone structure, a well-known precursor for peptide synthesis. Higher binding energies, up to 16 eV, lead to fragmentation. The key mechanism we propose relies on the formation of neutral and charged fragments in peculiar structures: among others, an aziridine three-member ring for the neutral species and an 'amino acid-like' structure [Ala-H-OH] for the charged fragment, which is the core of the peptide sequence.

Via molecular dynamics simulations and potential energy surface calculations we explored the reactivity among these

fragmentation products, that can be formed in the molecular binding energy range up to 16 eV. We found that the interaction between two 'reactive moieties', ionic oxazolidinone and neutral aziridine can give rise to new peptide bonds, reforming cationic dipeptides in either linear or cyclic structure as well as oxazolidinone. Furthermore, they can easily polymerize giving rise to peptide elongation. This suggests that c-AlaAla may have been a suitable oligomer to survive rather hostile environments, where molecules are constantly exposed to radiation. What is even more intriguing, is how the c-AlaAla decomposition may have provided new opportunities for the abiotic synthesis of oligo peptides, see Figure.

The next question we tackled is whether different amino acids composing c-dipeptides, i.e. different side chains attached to the DKP skeleton, may affect the behavior of the irradiated molecules and their potential as prebiotic building blocks. Therefore, we have used the same approach to study two additional c-dipeptides, the c-Alanyl-Glycine (c-AlaGly) and cGlycyl-Glycine (c-GlyGly). In summary, all three cationic dipeptides display a similar evolution just after photoionization, with ring opening at the same bond on the DKP ring. This can be followed either by the loss of CO and HNCO, or by molecular rearrangement into a cationic oxazolidinone structure. Concerning the possibility of peptide bond formation and elongation using fragmentation products as 'reagents', our modelling shows how specific oxazolidinones and aziridines are obtained for each cyclic dipeptide. Thus, depending on the irradiated c-dipeptide, different peptide chains might be formed via different mechanisms, making this process neither trivial nor general for cyclic dipeptides.

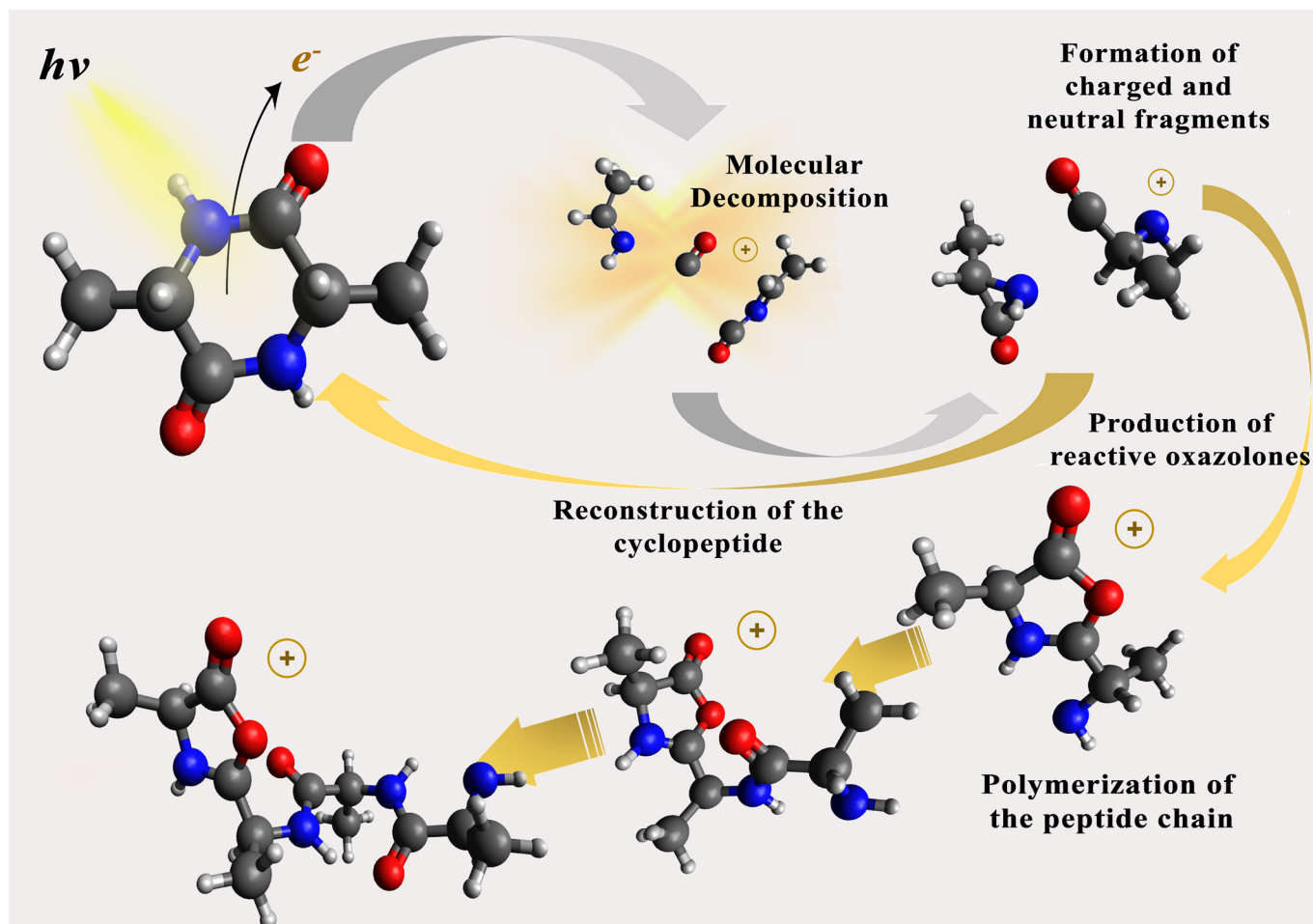


Figure 1. A sketch of the theoretical predictions of the interaction among different products of decomposition of the c-AlaAla dipeptide exposed to VUV irradiation.

Acknowledgments

We acknowledge Elettra Sincrotrone Trieste for providing access to its synchrotron radiation facilities. This work is based upon financial support from Elettra, from COST action CA18212 – Molecular Dynamics in the GAS phase (MD-GAS), supported by COST (European Cooperation in Science and Technology). The authors acknowledge the generous allocation of computer time at the Centro de Computación Científica at the Universidad Autónoma de Madrid (CCC-UAM). This work was partially supported by MICINN (Spanish Ministry of Science and Innovation) project PID2019-110091GB-I00 funded by MCIN/AEI/10.13039/501100011033, the “María de Maeztu” (CEX2018-000805-M) Program for Centers of Excellence in RD, MAECI Italy-Sweden project “Novel molecular tools for the exploration of the nanoworld”, and PRIN 20173B72NB project “Predicting and controlling the fate of bio-molecules driven by extreme-ultraviolet radiation”. D. B.-L. acknowledges the FPI grant associated with MICINN project CTQ2016-76061-P. H. Z. acknowledges the Swedish Research Council for the individual project grant with contract no. 2020-03437. M. H. S. acknowledges the Swedish Research council (Grant no. 2016-03675) and the Carl Trygger Foundation (Grant no. 17:436).

Original paper

D. Barreiro-Lage *et al.*, *Phys. Chem. Chem. Phys.* **25**, 15569 (2023) DOI: 10.1039/d3cp00608e

D. Barreiro-Lage¹, J. Chiarinelli², P. Bolognesi², R. Richter³, H. Zettergren⁴, M. H. Stockett⁴, S. Diaz-Tendero^{1,5,6} and L. Avaldi¹

¹ Departamento de Química, Universidad Autónoma de Madrid, Madrid, Spain

² Institute of Structure of Matter-CNR (ISM-CNR), Monterotondo, Italy

³ Elettra - Sincrotrone Trieste S.C.p.A., Trieste, Italy

⁴ Department of Physics, Stockholm University, Stockholm, Sweden

⁵ Condensed Matter Physics Center (IFIMAC), Universidad Autónoma de Madrid, Madrid, Spain

⁶ Institute for Advanced Research in Chemical Science (AdChem), Universidad Autónoma de Madrid, Madrid, Spain

e-mail: paola.bolognesi@cnr.it; dario.barreiro@uam.es

Shedding light on PTG/PP1 holoenzyme structure – a promising target for Lafora disease

Elettra | Structural Biology, XRD2

Lafora disease (LD) is a rare genetic disorder manifested by catastrophic teenage onset of progressive myoclonus epilepsy. It is caused by alternation in glycogen synthesis pathway that results in formation of insoluble neurotoxic glycogen-like aggregates called Lafora bodies (LB). Currently, no cure has been found and the treatment focuses on managing the severity of the seizures. The LD progresses rapidly and typical patient's life expectancy is 10 years from the symptom occurrence. Based on the ongoing research on LD pathogenicity some therapy development strategies have been proposed, along with targeting brain glycogen synthesis. Glycogen metabolism is tightly coordinated by regulatory enzymes that modulate the activity of glycogen synthase (GYS) and glycogen phosphorylase (PYG), the two key players in glycogen synthesis and degradation. Phosphorylation of both enzymes gives a signal for glycogenolysis, while dephosphorylation, carried out by type 1 protein phosphatase (PP1), triggers the glycogenesis. PP1 is a pleiotropic serine/threonine phosphatase involved in a variety of cellular processes, whose specificity relies on its scaffolding proteins. PTG (protein targeting to glycogen) is one of those regulatory subunits which brings PP1 to GYS and PYG, leading to their dephosphorylation and, thus, initiation of glycogen synthesis. In healthy neurons, the laforin-malin E3-ubiquitin ligase complex downregulates PTG which results in very low glycogen production. In Lafora Disease (LD), mutations in malin or laforin cause PTG accumulation leading to formation of Lafora bodies (LB). In LD mice models, knocking out PTG resulted in a nearly complete disappearance of LB, and resolution of the devastating symptoms, suggesting that interfering with the PTG/PP1 interaction could be a promising approach for LD therapy. In this work, we present the first structural characterization of PTG and PTG/PP1 holoenzyme bound to a carbohydrate,

both *in crystallo* and in solution, revealing their mechanism of interaction and giving the bases for developing small molecules targeting PTG.

In the Protein Facility at the Structural Biology Lab of Elettra, we designed and produced a number of protein constructs of PTG and PP1 proteins that were used for biophysical and structural analysis by x-ray diffraction at XRD2 beamline and SAXS. PTG is a relatively small protein (317 amino acids) composed of the C-terminal carbohydrate binding domain (CBM21) and the N-terminal disordered domain which contains the canonical PP1 recognition signature sequence RVxF (Fig. 1a). First, we determined the crystal structure of the human PTG CBM21 in complex with β -cyclodextrin. Crystals were obtained in two different space groups that diffracted at 1.5 and 2.0 Å resolution, revealing the structure of a typical immunoglobulin-like fold containing two carbohydrate binding sites. The strongest interaction with sugars occurs via site II, which motif is preserved among CBM21 protein family, while site I is hypothesized to play a role as an additional support for binding long-chain polysaccharides, which could further facilitate association to glycogen (Fig. 1b).

Subsequently, we obtained co-crystals of PP1 bound to N-terminal PTG peptide containing the RVxF signature motif that is highly conserved within PP1 regulatory subunits. The x-ray diffraction data show that the binding occurs primarily via hydrophobic and stacking interaction with two principal PP1 grooves (Fig. 1d and 1e).

Finally, after extensive trials, we were able to obtain crystals of PP1 in complex with PTG 70-264 truncated form, encompassing both the PP1-binding region and the CBM21 resulting in first reported x-ray crystal structure of the PTG/PP1 holoenzyme that includes a large portion of PTG regulatory subunit. Our data confirm that the N-terminal RVxF conserved motif is the main driving force of PTG and PP1 interaction. It is

further supported by a downstream SALK sequence, while poor contribution is observed from CBM21 (Fig. 1c). Additionally, the complex assembles itself as a peculiar pseudo-knotted dimer of dimers via a hydrophobic core formed by residues in all four chains (Fig. 1f). In order to understand more the complex architecture, we performed in-solution SAXS experiments at ESRF. The data show that PTG CBM21 appears to oscillate, assuming multiple orientations with respect to PP1, while the N-terminal region stays bound (Fig. 1g). We hypothesize that for CBM21 domain to be able to change its position, SALK sequence detaches from PP1 maintaining the only interaction site via RVxF motif. This could facilitate substrate recognition and recruitment, and would explain the unexpected tetrameric crystal organization observed in the PTG/PP1 crystal structure. To better understand the dynamic properties of the complex, we analyzed the binding kinetics of PTG and PP1 using ITC (Isothermal Titration Calorimetry) and GCI (Grating-Coupled Interferometry) which confirm that the RVxF motif of PTG has the strongest affinity towards PP1 with the additional assistance of SALK sequence, while no interaction was detected from CBM21 domain. In conclusion, our findings contribute to a better understanding of the interplay mechanism between PTG and PP1 and provide the basis for further structural analysis to identify druggable pockets that could lead to the development of small molecules targeting PTG and interfering with complex formations and, thus, inhibition of Lafora bodies accumulation.

PDB accession codes: Data and structures have been deposited in the PDB database under codes: 7QF7 (PTG-CBM21 in complex with β -cyclodextrin, orthorhombic crystal form), 7QFA (PTG-CBM21 in complex with β -cyclodextrin, monoclinic crystal form), 7QFB (PP1/PTG⁸¹⁻¹⁰⁷) and 7QM2 (PP1/PTG⁷⁰⁻²⁶⁴).

Structure and Dynamics

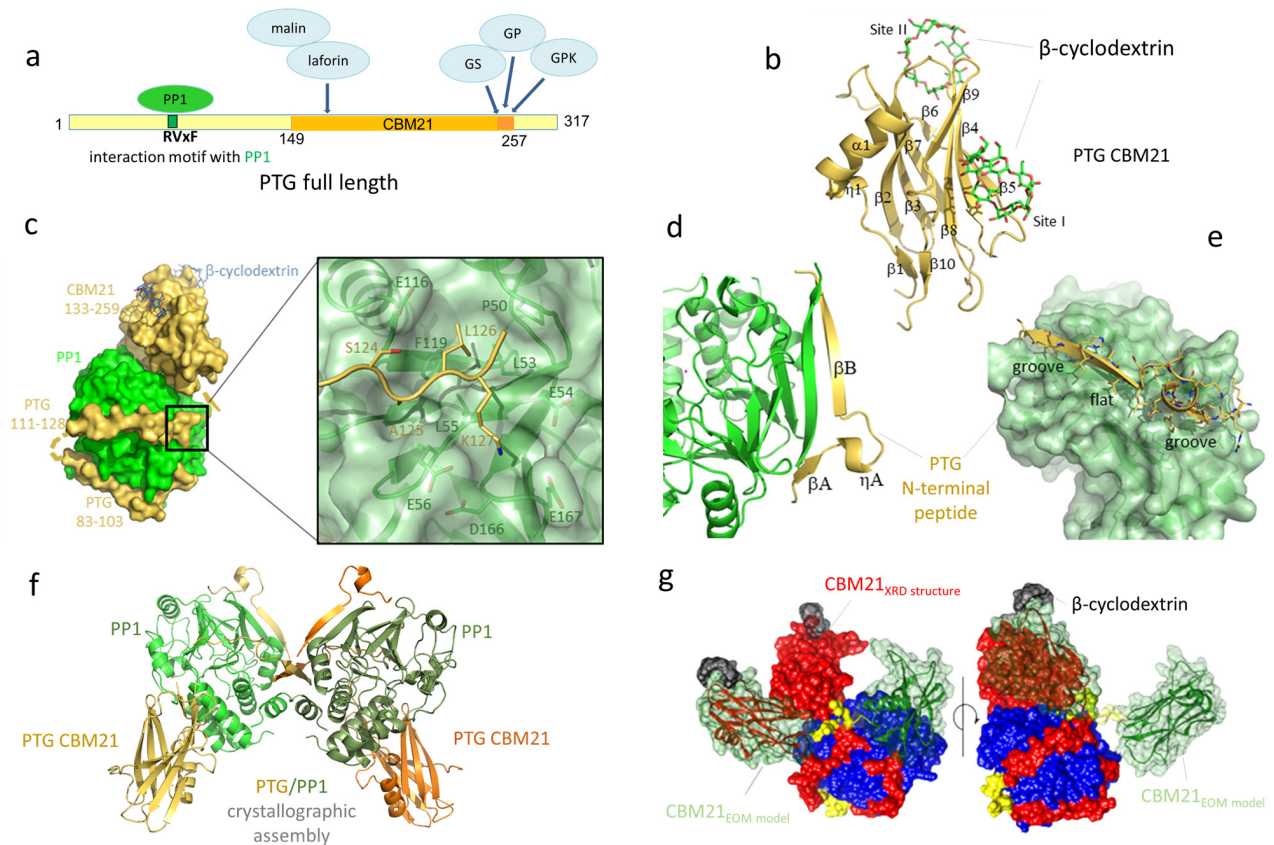


Figure 1. Structural organization of the PP1/PTG/cyclodextrin complex. a) Schematic PTG protein representation indicating conserved PP1 binding motif and other possible binding partners (GS-glycogen synthase, GP-glycogen phosphatase, GPK-glycogen phosphorylase kinase); b) Crystallographic structure of the PTG CBM21 (yellow) in complex with β -cyclodextrin (green) showing two binding sites; c) Crystal structure of PTG/PP1 complex showing that the PTG (yellow) region (aa. 111-128) crosses the PP1 surface (green) to connect its N-terminal stretch to the CBM21 on the opposite PP1 side. d) Crystal structure of PP1 (green) in complex with the PTG peptide 81-107 (yellow). The PTG peptide is arranged in two β -strands and an intervening 310 helix and accommodates itself on PP1 β sheet; e) The peptide (yellow) perfectly adapts to the PP1 surface (green) filling the two grooves with hydrophobic side chains; f) The butterfly-shaped pseudo-knotted PP1/PTG dimer observed in crystal structure; g) SAXS-based structural model of PTG/PP1 complex in solution showing the mobility of the PTG CBM21 domain in respect to PP1.

Acknowledgments

This work was supported by the University of Trento (Starting Grant 2020 to G.L.) and University of Padua (Starting Grant STARS@UNIPD—call 2019 to G.G.). G.L. is also supported by AIRC under MFAG 2017-ID. 19882 project and by the Alzheimer's Association under AARG-NTF-22-923774. We acknowledge Elettra Sincrotrone Trieste for providing access to its synchrotron radiation facilities and we thank Dr. Annie Heroux for assistance in using beamline XRD2. We thank Dr. Mark Tully and Dr. Petra Pernot for help and assistance with data collection at the ESRF BM29 bioSAXS beamline.

Original paper

M.S. Semrau *et al.*, Nat. Commun. **13**, 6199 (2022); DOI: 10.1038/s41467-022-33693-z

M.S. Semrau^{1,2}, G. Giachin³, S. Covaceuszach⁴, A. Cassetta⁴, N. Demitri², P. Storici², G. Lolli¹

¹ Department of Cellular, Computational and Integrative Biology - CIBIO, University of Trento, Trento, Italy

² Elettra-Sincrotrone Trieste S.C.p.A., Trieste, Italy

³ Department of Chemical Sciences (DiSC), University of Padua, Padova, Italy

⁴ Institute of Crystallography - C.N.R. - Trieste Outstation, Trieste, Italy

e-mail: graziano.lolli@unitn.it ; paola.storici@elettra.eu

Targeting 3CL^{pro} for pan-CoVs antiviral drug candidate: medicinal chemistry and X-ray studies

Elettra | Structural Biology, XRD2

Severe Acute Respiratory Syndrome Coronavirus (SARS-CoV-2) is the etiological agent of the COVID-19 pandemic, which represents one of the major global health threats of our time because of its virulence and lethality. The scientific community has been ramping-up efforts to identify COVID-19 treatments and preventives with unprecedented speed and global effort. Vaccines, monoclonal antibodies, and freedom limitation were useful to slow down the pandemic. Despite huge repurposing and focused medicinal chemistry efforts, only three direct-acting antivirals (DAAs) have been globally approved, with moderate efficacy and suboptimal pharmacokinetic. Nirmatrelvir is the only DAA targeting the SARS-CoV-2 3-Chimotrypsin Like Cysteine protease (3CL^{pro}) approved in the late 2021, co-dosed with the pharmacokinetic enhancer Ritonavir (Paxlovid®). Considering the limited therapeutic options, new antivirals are needed for people unable to receive vaccinations in developing countries or to mitigate the harmful consequences of the new infections, and to fight emerging variants. SARS-CoV-2 belongs to the β group of the *Coronaviridae* family together with SARS-CoV and Middle East Respiratory Syndrome Coronavirus (MERS-CoV), which caused the 2003 and the 2011 epidemics, respectively. The SARS-CoV-2 genome is a single strand of 5' - capped (+)-RNA which contains two open reading frames (ORF1a and ORF1ab) and encodes multiple structural and nonstructural proteins. ORF1a and ORF1ab are processed into polypeptides pp1a and pp1ab by the viral 3CL^{pro} and a Papain-Like Cysteine Protease, resulting in 16 mature nonstructural proteins involved in the replication and transcription complex. Among the different viral targets, 3CL^{pro} is one of the most attractive to identify effective, safe, and broad-spectrum DAAs. Indeed, 3CL^{pro}, known also as Main protease or M^{pro}, is a cysteine protease (Cys145) highly conserved in the active site across CoVs, with an almost unique substrate specificity for Leu-Gln in position P2-P1, it is absent in

mammalian cells and has a pivotal role in viral replication, being responsible for the release of the most of viral non-structural proteins including the viral RNA polymerase.

In early 2020, as part of the multi-disciplinary consortium Exscalate4CoV, the first project funded by the European Union to fight COVID-19, we started to work on the identification of new DAAs. In particular, we focused on design and synthesis of a series of peptidomimetics as covalent reversible inhibitors of 3CL^{pro}, functionalized with an aldehydic warhead as a cysteine trap, a cyclic analogue of Gln in P1, and modified P2-P3 residues. Our intuition, supported by docking studies, was to replace the Leu of the natural substrate with functionalized proline residues to obtain the β-turn-like bioactive conformation. Moreover, docking calculations forecast that the P2 proline could allow the P3 residue to make van der Waals interaction with P1 residue. Given the high rate of sequence and structural identity across the 3CL^{pro} from different CoVs, all the compounds were tested in biochemical assays both against SARS-CoV-2 3CL^{pro} and MERS-CoV 3CL^{pro} resulting in sub-to-low-nM potency. The compounds were also evaluated in cell-based assays against SARS-CoV-2 displaying very potent inhibition, and no cell toxicity. Interestingly, the inhibitors displayed notable broad-spectrum potency within other *Coronaviridae*. Overall, derivative 12 resulted in the most promising compound, showing a broad-spectrum activity in the enzymatic assays both against SARS-CoV-2 and MERS 3CL^{pro}, confirming that the bulky bicycloproline nicely fits in P2. Most important, 12 displayed potent antiviral activity against SARS-CoV-2, MERS, and HCoV229E. These results were further confirmed in human epithelial lung adenocarcinoma Calu-3 cells, a cell type more relevant to evaluate the infection of a respiratory virus. Additionally, 12 increased the thermal stability of SARS-CoV-2 3CL^{pro} ($\Delta T_m = +11$ °C in DSF assay) and kinetic assays demonstrated the reversible covalent chemistry of enzyme

inhibition, resulting in an apparent $K_i = 3.2 \pm 0.96$ nM.

X-ray crystallography was exploited in collaboration with the Paola Storici's group at Elettra Sincrotrone Trieste to solve the structures of the four most potent inhibitors, 7, 8, 12, and 14, bound in the catalytic site of SARS-CoV-2 3CL^{pro}, validating our in-silico design hypothesis and being of inspiration for the design of new inhibitors. The protein, produced in the Elettra Protein Facility, allowed to obtain co-crystals that were subsequently measured at XRD2 beamline. The x-ray structures obtained at resolutions in the range of 1.35–1.66 Å unequivocally showed the covalent interaction between the aldehydic warhead and the catalytic Cys145 forming the thiohemiacetal moiety.

In conclusion, in this multidisciplinary study, we designed and synthesized a novel series of proline-based tripeptides as covalent reversible inhibitors of SARS-CoV-2 3CL^{pro} bearing an aldehyde warhead as cysteine trap and a cyclic analogue of Gln in P1, similarly to Nirmatrelvir and other potent known inhibitors. Our design hypothesis was confirmed by x-ray co-crystal structures of representative compounds with the protein target. Notably, most of our newly synthesized compounds showed excellent inhibition of the SARS-CoV-2 and the MERS 3CL^{pro}s and inhibited the replication of the SARS-CoV-2, MERS, and HCoV229E in different cell lines. All these results provide great suggestions to optimize the activity and PK properties of the compounds to obtain broad-spectrum 3CL^{pro} inhibitors as suitable candidates for in vivo studies to counteract the COVID-19 pandemic and other future coronavirus-related diseases.

PDB accession codes: Data and structures generated in this study have been deposited in the PDB database under codes: 8OKK (3CL^{pro}/7); 8OKL (3CL^{pro}/8) ; 8OKM (3CL^{pro}/12); 8OKN (3CL^{pro}/14)

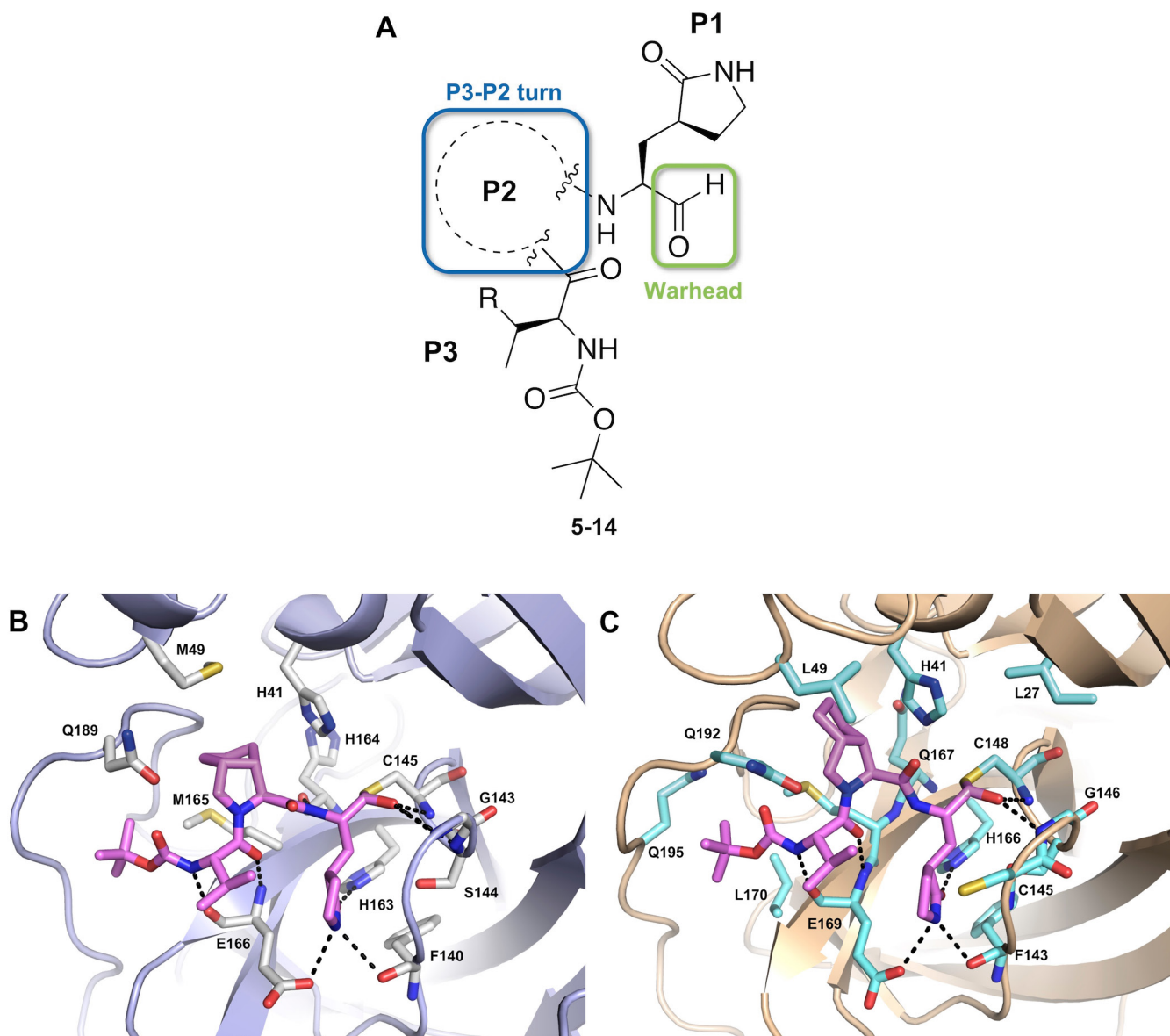


Figure 1. (a) General chemical structures of designed and synthesized aldehyde tripeptides as SARS-CoV-2 3CL^{pro} inhibitors (5-14). (b) Crystal structure of compound 12 (magenta) bound to SARS-CoV-2 3CL^{pro} active site represented as light-blue ribbon model and white sticks residues (PDB: 80KM). (c) Predicted binding mode of 12 into MERS 3CL^{pro} (PDB ID: 4RSP), active site represented as wheat ribbon model and cyan sticks residues

Acknowledgments

This research was supported by the project "EXaScale smArt pLatform Against paThogEns for Corona Virus – Exscalate4CoV" founded by the EU's H2020-SC1-PHE-CORONAVIRUS-2020 call, grant N. 101003551, and by EU funding within the MUR PNRR Extended Partnership initiative on Emerging Infectious Diseases (Project N. PE00000007, INF-ACT). We acknowledge Elettra Sincrotrone Trieste for providing access to its synchrotron radiation facilities and we thank Nicola Demitri for assistance in using beamline XRD2.

Original paper

Stefanelli, I et al. *Eur. J. Med. Chem.* **2023**, 253; 115311 (2022); DOI: 10.1016/j.ejmech.2023.115311

I. Stefanelli¹, A. Corona², C. Cerchia¹, E. Cassese¹, S. Improta¹, E. Costanzi³, S. Pelliccia¹, S. Morasso³, F. Esposito², A. Paulis², S. Scognamiglio², F. Di Leva¹, P. Storicci³, M. Brindisi¹, E. Tramontano², R. Cannalire^{1*}, V. Summa^{1**}

¹ Department of Pharmacy, University of Naples Federico II, Naples, Italy

² Dipartimento di Scienze della Vita e dell'Ambiente, Cagliari, Italy

³ Elettra - Sincrotrone Trieste S.C.p.A., Italy

e-mail: rolando.cannalire@gmail.com (R. Cannalire) ; vincenzo.summa@unina.it (V. Summa)

Unfolding the mysteries of the fascinating interplay of magnetism and electricity in Ni_3TeO_6

Elettra | XAFS

Magnetism and electricity can have a remarkable interplay in certain solid materials, leading to a captivating phenomenon called multiferroicity. In particular, Type-II multiferroics exhibit a strong coupling between magnetic and electric properties. These materials can display a remarkable effect where the application of a magnetic field alters the electric polarization, and vice versa. Investigating multiferroicity in solid materials reveals various underlying mechanisms that give rise to Type-II multiferroic behavior. These mechanisms include inverse Dzyaloshinskii-Moriya interaction through antisymmetric spin-exchange (spin current mechanism), symmetric spin exchange in collinear magnets (Heisenberg exchange striction), and *p*-*d* hybridization between the metal and ligand. It is worth noting that certain cases may involve the presence of multiple mechanisms contributing to the observed multiferroicity.

Among the materials investigated for multiferroicity, Ni_3TeO_6 (NTO), a unique material with a non-centrosymmetric crystal structure, shows an interesting behaviour at low temperatures. While it doesn't exhibit spontaneous polarization, it does display a non-switchable electric polarization along with a magnetoelectric effect. Here we have addressed the origin of the magnetoelectric effect using temperature dependant x-ray diffraction and x-ray absorption spectroscopy. Our study uncovers a significant knowledge on the lattice structure of the material. By analysing temperature-dependent x-ray diffraction spectra, we identify a lattice anomaly characterized by a sharp discontinuity in the lattice volume around the antiferromagnetic transition temperature (Néel temperature, $T_N \sim 52$ K). This observation confirms that the magnetic phase transition is first order in nature. The compound NTO contains NiO_6 type octahedral building blocks, and we observe change in bond distances between nickel (Ni) and oxygen (O)

atoms within the NiO_6 octahedra near T_N . The lattice anomaly observed during the magnetic transition suggests an inherent instability in the system. This is known as exchange striction, arising from the competition between magnetic and lattice energies, resulting in an optimized arrangement of magnetic ions. The application of a magnetic field can disrupt this equilibrium, leading to a further change in the ionic separation within the NiO_6 octahedra, which, in turn, induces the electric polarization. Notably, at 300 K, $\angle[\text{O-Ni-O}]$ in the NiO_6 octahedra are close to 90° . However, as shown in the bottom part of the figure, at lower temperatures, a larger deviation from 90° is observed in all $\angle[\text{O-Ni-O}]$, indicating trigonal distortion in all three Ni-octahedra associated with the exchange striction.

Furthermore, our magnetic measurements unveiled an intriguing thermal hysteresis around T_N , where the heating and cooling data do not follow the same path. These finding challenges previous studies that proposed a second-order continuous magnetic transition.

The previous assumption was that all Ni ions were in a $2+$ state and all Te ions were in a $6+$ state. However, our careful investigation of x-ray absorption study revealed a mixed valency in the system, with a fraction of Ni ions existing as Ni^{3+} [see Fig. 1 (a)] and a fraction of Te ions existing as Te^{4+} . This indicates a charge disproportionation in the system. This finding is further supported by the effective paramagnetic moment (μ_{eff}), which is higher than the spin-only value for Ni^{2+} . Although the coupling between spin and orbital moments of atomic electrons could potentially contribute to a higher paramagnetic moment, neutron diffraction and density functional theory (DFT) calculations suggest that spin-orbit coupling has no significant role in this compound. Therefore, the higher moment can be attributed to the presence of Ni^{3+} ions, which is consistent with the x-ray absorption study.

Our x-ray photoemission study on three

batches of samples (air, vacuum, and oxygen annealed) reveals no significant differences in the O, Ni, and Te peaks. Additionally, the values of μ_{eff} for Ni ions remain consistent, indicating a stable charge state. This suggests that the compound is highly stable, and the oxygen stoichiometry remains largely unchanged throughout the annealing process. These findings highlight the robustness of the mixed valency in NTO, suggesting that it is likely an intrinsic property of the sample.

Multiferroic materials often exhibit mixed valency of magnetic ions, leading to magnetoelectric effects. Examples include $\text{CaMn}_7\text{O}_{12}$, $\text{CaBaFe}_4\text{O}_7$, and RMn_2O_5 , where mixed valency is site-specific. In the case of NTO, the distribution of Ni^{3+} and Ni^{2+} ions in the lattice are random, and it can also contribute to the magnetoelectric effect. In x-ray absorption spectroscopy, often a weak peak is seen just below the main absorption peak, which is called pre-edge (designated as A in Fig. 1 (a)). We observe a clear Ni pre-edge (see Fig. 1 (b)), which is likely to be connected to the lack of inversion symmetry and mixing of *p* and *d* electronic orbitals of Ni due to the distortion of NiO_6 octahedra. Notably, the pre-edge intensity exhibits an anomaly (see inset of Fig. 1 (c)) at the antiferromagnetic ordering temperature, suggesting an indirect effect from the lattice distortion associated with the exchange-striction. Our comprehensive analysis highlights the structural instability at the Néel temperature and the mixed valence states of cations, which contribute to the observed magnetic and electric anomalies in NTO.

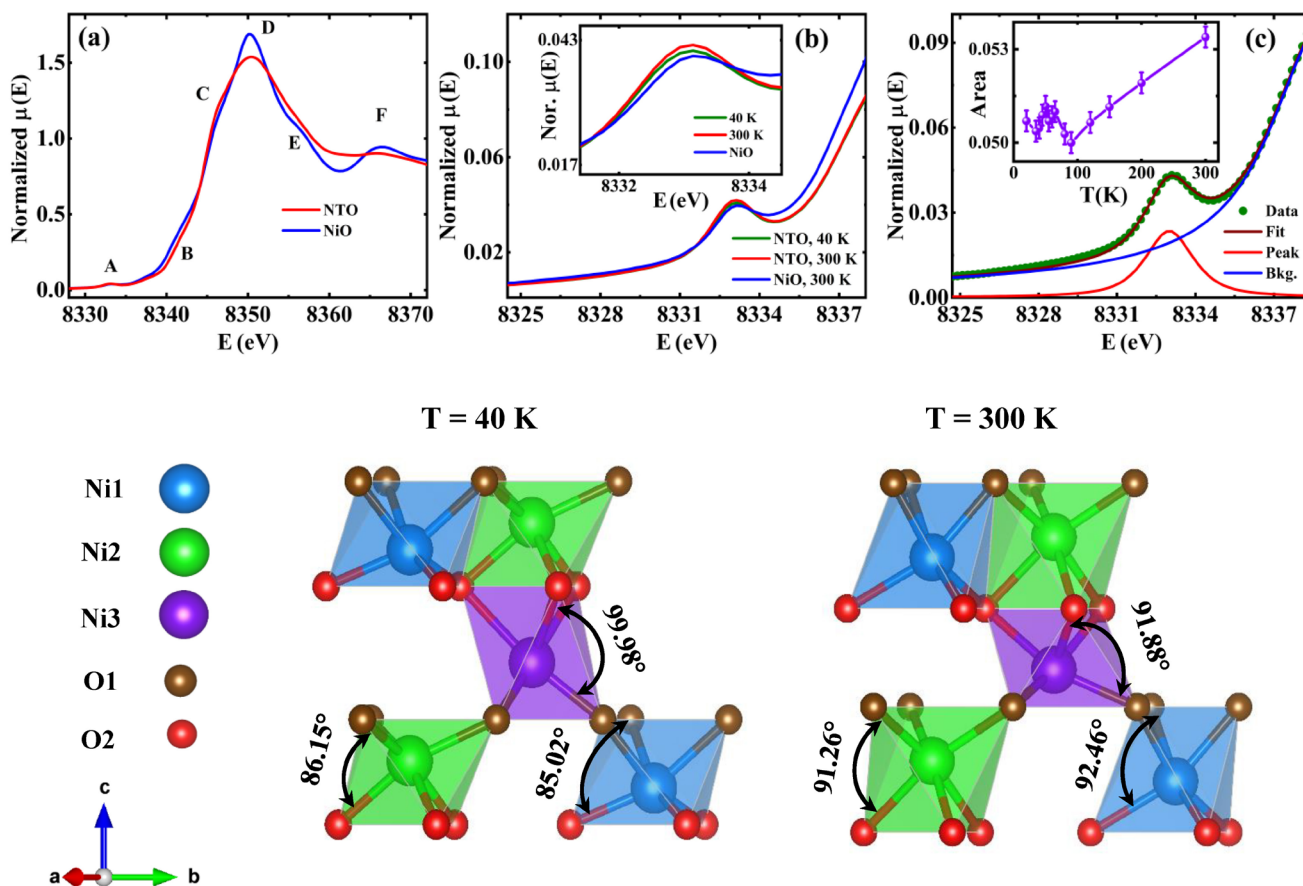


Figure 1. Displays the normalized Ni-K edge x-ray absorption near edge structure of NTO compared to standard NiO in (a). The presence of a higher oxidation state of Nickel ions is indicated by the rising line after the pre-edge, as shown in (b). The inset provides a magnified view of the pre-edge at different temperatures, as well as a comparison with the standard. Additionally, (c) presents the fitting of the pre-edge using a pseudo-Voigt peak function and an arc tangent background function. The inset demonstrates the temperature-dependent variation of the area under the peak. The lower portion of the figure presents a comparison of side-by-side perspective views, illustrating the NiO₆ octahedra at two distinct temperatures: 40 K and 300 K.

Acknowledgments

We sincerely acknowledge Elettra – Sincrotrone Trieste for providing access to its synchrotron radiation facilities at the XAFS beamline (Proposal No. 20210469) under the Indo-Italian cooperation. The Department of Science and Technology (India) is acknowledged for financial support (KEK Proposal No. 2021-IB-32) for facilitating the experiments at the Indian Beam Line, Photon Factory, KEK, Japan. MN would like to thank CSIR, India for his research fellowship [File No. 09/080(1131)/2019-EMR-I].

Original paper

Mohamad Numan *et al.*, Phys. Rev. B **106**, 214437 (2022); DOI: 10.1103/PhysRevB.106.214437

Mohamad Numan¹, Gangadhar Das², Md Salman Khan³, Gouranga Manna⁴, Anupam Banerjee¹, Saurav Giri¹, Giuliana Aquilanti², Subham Majumdar¹

¹ School of Physical Sciences, Indian Association for the Cultivation of Science, 2A & B Raja S. C. Mullick Road, Jadavpur, Kolkata, India

² Elettra - Sincrotrone Trieste S.C.p.A., Trieste, Italy

³ School of Materials Sciences, Indian Association for the Cultivation of Science, Kolkata, India

⁴ New Chemistry Unit, Jawaharlal Nehru Centre For Advanced Scientific Research, Karnataka, India

e-mail: sspsm2@iacs.res.in

Vacancy influence on manganese hexacyanoferrate Na-ion batteries: structural perspective

Elettra | XAFS, MCX

MnHCF (Manganese hexacyanoferrate), as one of the PBAs (Prussian Blue Analogues), has attracted wide attention as promising cathode material for Na-ion batteries, due to its large specific capacity ($>130 \text{ mAh g}^{-1}$), high discharge potential and sustainability. Generally, the electrochemical reaction of MnHCF is accompanied by phase and structural transformation, as well as the JT (Jahn-Teller) distortion of Mn-sites upon the charge process. To understand the effect of the MnHCF structure on its electrochemical performance, two MnHCF materials with the same phase structure (monoclinic), similar particle size, but different $[\text{Fe}(\text{CN})_6]^{4-}$ vacancy content (4% and 11%), were synthesized and tested as cathode material in organic Na-ion battery. The electrochemical results show that the sample with lower vacancy content (4%) exhibits relatively higher capacity retention of 99.1%, 92.6% and 71.1% at 2nd, 10th and 100th cycles, respectively, with respect to 97.4%, 79.3% and 39.4% in the sample with higher vacancy content (11%). To explain the different electrochemical performance of the two MnHCF materials, ex situ XAS (x-ray absorption spectroscopy) data and ex situ XRD (x-ray diffraction) data were collected at XAFS and MCX beamline at Elettra, and the local structural and crystal structure changes of MnHCF samples upon cycling were investigated. From the XANES (x-ray Absorption Near Edge Structure) spectra of Fe and Mn K-edge data, the oxidation/reduction states of Fe and Mn sites at charged/discharged states were observed. While the edge shift of the Mn K-edge is more significant than that of the Fe K-edge at charged states, which is due to the charge effect combined with the local structural changes (JT-distortion) operating exclusively at the Mn sites (Fig. 1a). For pristine MnHCF electrode, the Mn coordination environment consists of a symmetric MnN_6 octahedral, with Mn-N distance being 2.18 Å and 2.19 Å for MnHCF-P and MnHCF-A, respectively. After the first charge, the four equatorial Mn-N

distances contract to 1.95 Å and 1.96 Å for MnHCF-P and MnHCF-A electrodes respectively, i.e., shrinking by 10.55% and 10.50%, respectively. Meanwhile, the axial Mn-N distances remain roughly constant (Fig. 1b). However, a more insightful point is the comparison of the Mn-N distance at the discharged state. The MnHCF-A electrodes experience an irreversible configuration change after the 1st charge and discharge process, which is also kept for the 2nd cycle, with the 4 equatorial Mn-N bonds being always shorter than the axial ones. This irreversible change respect, however, enables MnHCF-A electrodes to undergo less local structure variation during the charge and discharge process. In fact, based on the data above, the low-vacancy-content sample MnHCF-A experiences less effect from the JT-distortion and less structural variations during charge/discharge process. The long-range crystal structure information of MnHCF electrodes, at different charge/discharge states, were studied by ex situ XRD, as observed in Fig. 1(c). A reversible change of XRD patterns between charged (C1, C2, C10) and discharged (D1, D2, D10) electrodes is observed in both MnHCF-P and MnHCF-A electrodes. The XRD pattern of all discharged electrodes share the same pattern as pristine electrode. Thus, all the discharged electrodes were refined with monoclinic phase. While, for all the charged electrodes, the pristine peaks at 1.20 Å⁻¹ and 2.40 Å⁻¹ split into two peaks at around 1.20/1.24 Å⁻¹ and 2.40/2.49 Å⁻¹, respectively. The peaks at around 1.68 Å⁻¹ and 1.71 Å⁻¹ disappeared and were replaced by a single peak at 1.73 Å⁻¹. These changes indicate the potential of a phase change after the charge process. Based on the reports, the monoclinic MnHCF phase, normally, experiences a phase transformation upon extraction of Na⁺: change from monoclinic-to-cubic-to-tetragonal phase. Thus, all the charged electrodes were first refined with tetragonal phase.

The refined a/c ratio results, with $(a/c)_{\text{MnHCF-A}} < (a/c)_{\text{MnHCF-P}} < 0.7071$, which indicates that the crystalline phase of all charged electrodes is not an ideal tetragonal phase (Fig. 1d). Another refinement attempt was conducted by adopting a pseudo-tetragonal phase, which is a monoclinic phase, but with β (beta) value very close to 90°. The results showed that the monoclinic phase exhibits better fitting results than the tetragonal phase. The fitted cell parameters, β value and volume, from both tetragonal phase and monoclinic phase, exhibit the same change trend as Mn-N bond: decreasing upon charging and increasing during discharging process (Fig. 1f, g). Thus, it's concluded that a cooperative JT-effect was observed for both MnHCF-P and MnHCF-A samples. While for MnHCF-P electrodes, the variation of volume value and β values is larger than MnHCF-A electrodes, indicating that a rather larger structure rearrangement is required by the Na⁺ extraction/insertion in MnHCF-P samples, which explained the low cycling stability of MnHCF-P electrode. In summary, the local metal configuration and long-range crystal structure change of the two MnHCF materials with different vacancies content, as well as the effect of its structure on the electrochemical performance, were comprehensively studied by XAS and XRD techniques. It's concluded that a weaker cooperative JT-distortion effect and relatively smaller crystal structure modification occurring for the material with lower vacancies, which well explains the better electrochemical performance, compared to the high-vacancy sample.

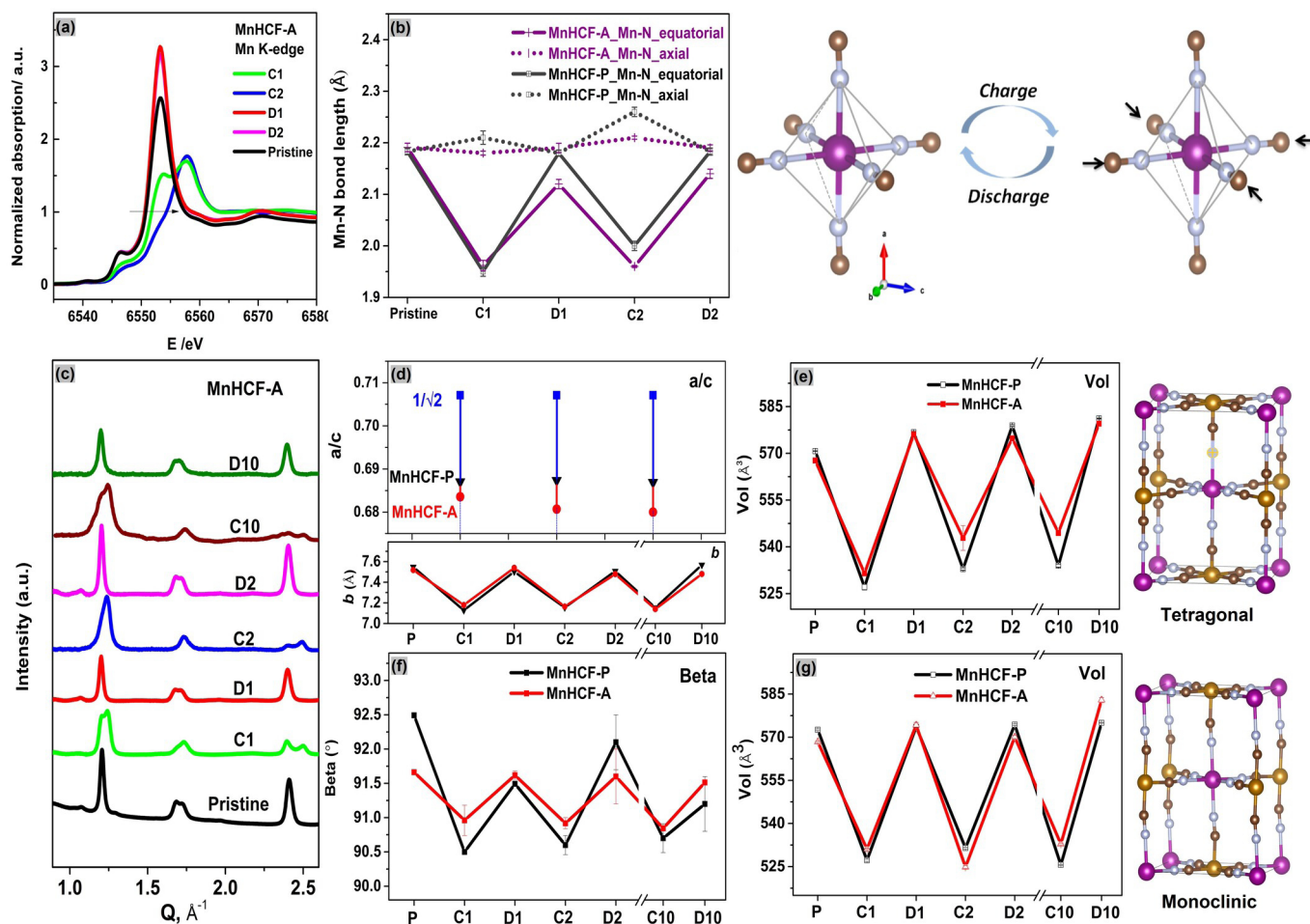


Figure 1. (a) ex situ XANES spectra of Mn K-edge for MnHCF-A electrodes at different charge/discharge states (C1, D1, C2 and D2); (b) Evolution of Mn first shell: Mn-N distances in both axial and equatorial direction for MnHCF-P/A electrodes; (c) ex situ XRD patterns of MnHCF-A at different charge-discharge states (C1, D1, C2, D2 and C10, D10); (d) the a/c value of MnHCF-P and MnHCF-A at charge states, as well as the change of b values; (e) Volume change of MnHCF-P and MnHCF-A, refine results based on tetragonal phase; (f) β value and (g) Volume of MnHCF-P and MnHCF-A, refine results based on monoclinic phase.

Acknowledgments

Measurements at Elettra were supported by CERIC project #20212162 (M. G. as PI). M. L. acknowledges the support of European Energy Research Alliance - Joint Programme Energy Storage (EERA-JPES) Mobility Scheme for providing 3-months scholarship. A. M., M. L., and S. P. acknowledge the basic contribution of the Helmholtz Association. Open Access funding enabled and organized by Projekt DEAL.

Original paper

M. Li *et al.*, ChemSusChem. **16**, e202300201 (2023); DOI:10.1002/cssc.202300201.

M. Li¹, M. Gaboardi², A. Mullaliu^{3,4}, M. Maisuradze¹, X.L. Xue^{3,4}, G. Aquilanti², J. R. Plaisier², S. Passerini^{3,4,5}, M. Giorgetti¹

¹ Department of Industrial Chemistry "Toso Montanari", University of Bologna, Bologna, Italy

² Elettra - Sincrotrone Trieste S.C.p.A., Trieste, Italy

³ Helmholtz Institute Ulm (HIU), Ulm, Germany

⁴ Karlsruhe Institute of Technology (KIT), Karlsruhe, Germany

⁵ Department of Chemistry, Sapienza University of Rome, Rome, Italy

e-mail: marco.giorgetti@unibo.it; stefano.passerini@kit.edu

Depth selective local structure in CoFeB thin film interfaced with W: A standing wave XAFS study

Elettra | XRF

MTJs (magnetic tunnel junctions) are at the heart of spintronics-based non-volatile magnetic random-access memories. CoFeB is the material of choice for the magnetic electrodes in MTJs, owing to its beneficial properties like, low coercivity, large tunnel magnetoresistance, large spin polarization. Interface of such magnetic layers with heavy metals like tungsten, is important in the context of phenomena like SOT (spin-orbit torque), or IDMI (interfacial Dzyaloshinskii–Moriya Interaction), which are especially relevant for the development of high-density, low-power memory devices. These phenomena mainly originate from the intrinsic anisotropy, affecting the local atomic and electronic structure and stress fields. Inhomogeneities and compositional gradients across the film thickness can also affect the macroscopic response. Disentangling these effects can be difficult and requires complementary techniques. XAFS spectroscopy is a chemically selective tool probing the local atomic structure, coordination chemistry and electronic nature of absorbers in complex samples. The SW (standing wave) geometry gives XAFS a depth-selective capability that is particularly suited to the study of layered systems.

Here, a thin layer of $\text{Co}_{40}\text{Fe}_{40}\text{B}_{20}$ sandwiched between two layers of tungsten has been studied at the Elettra XRF beamline. Nominal structure of the sample was $\text{Si}/\text{SiO}_2(\text{substrate})/\text{W } 30\text{nm}/\text{Co}_{40}\text{Fe}_{40}\text{B}_{20} 15\text{nm}/\text{W } 3\text{nm}$. TOF-SIMS (time of flight secondary ion mass spectrometry) laboratory analysis revealed a variation in the composition as a function of film depth. The multilayer structure forms a planar x-ray wave guide with the CoFeB layer being its cavity. Various waveguide modes can be excited when the x-rays fall on the sample at grazing incidence. Excitation of the TE_0 and TE_1 modes of the cavity are clearly visible in the simulated contour plot of the x-ray intensity (Fig. 1(a)). The Fe XRF (x-ray fluorescence) exhibits

two well defined peaks at $q_1=0.053 \text{ \AA}^{-1}$, and $q_2=0.070 \text{ \AA}^{-1}$, corresponding to the resonance enhancement of x-ray intensity inside the multilayer due to excitation of the TE_0 and TE_1 modes, respectively. XRR (X-Ray Reflectivity) exhibits dips at the corresponding positions, due to enhanced absorption in the cavity. The values of the exchanged momentum q as determined from the positions of the two peaks in the XRF yields, were used to carry out depth resolved SW-XAFS at the Fe and Co K edges. Simulations show that the antinode of the TE_0 mode lies in the center of the CoFeB layer, while for TE_1 mode, there are two antinodes close to top and bottom interfaces of the CoFeB layer. SW-XAFS carried out keeping q at the positions of TE_0 or TE_1 resonances provides respectively preferential information about the center or the interfacial regions of the layer.

The normalized XANES spectra measured at the Fe and Co K edges in the CoFeB layer using standard ($\theta=45^\circ$) and SW (TE_0 and TE_1 modes) geometries are presented in Fig. 1(b) together with the spectra of reference Fe and Co samples. It is evident that for both Co and Fe SW-XAFS spectra, the TE_1 spectra, probing the local atomic structure of the absorbers at the interfaces, are very similar to the standard-XANES spectra, but the spectra measured at TE_0 appear quite different, and this effect is larger for Fe than for Co. This finding suggests that: the local coordination chemistry around Fe and Co changes along the film thickness, and that this difference is larger for Fe than for Co.

The analysis of the (SW-)XAFS spectra in the EXAFS (extended) region has provided further quantitative details. The experimental spectra and best fit obtained for the spectra measured in standard and SW-EXAFS geometry at the Co and Fe K edges are presented in Fig. 1(c). Qualitatively slight longer (shorter) wavelength is evident for TE_0 (TE_1) spectra around $k=6.5 \text{ \AA}^{-1}$ (Fig. 1(c))

suggesting some compression of the local structure close to the center of the FeCoB film with respect to the borders.

The data measured in SW geometry depict much larger differences between Fe and Co sites. In general data in SW geometry confirm that the local structure around Fe is averagely more disordered respect to Co. Looking at the TM-B distance, an opposite trend for Fe and Co is revealed: the Fe-B distance close to the film center is significantly compressed with respect to the average Fe-B distance, while at the film borders the Fe-B distance is significantly elongated. While the opposite happens around the Co sites having the Co-B distance elongated in the central region of the film and compressed close at the borders. Looking at the next neighbours the TM_1 shells appear slightly compressed close to the film center for both Co and Fe sites. The Co-TM_2 is slightly compressed close to the film center compared to the borders, while the Fe-TM_2 is only visible in TE_1 spectra due to larger structural disorder around Fe.

To summarise, the SW-XAFS data validate the information obtained from TOF-SIMS by providing fundamental details about the local coordination of transition metals in our nominally $\text{Co}_{40}\text{Fe}_{40}\text{B}_{20}$ film. The SW-XAFS data analysis reveals significant structural differences around Fe and Co, especially in the Fe-B distribution, and allows to detect differences in the local coordination in the film center with respect to the boundaries. Such details are not accessible to other investigation techniques. This structural and morphological information could be relevant to discuss the macroscopic properties of these films and their magnetic response.

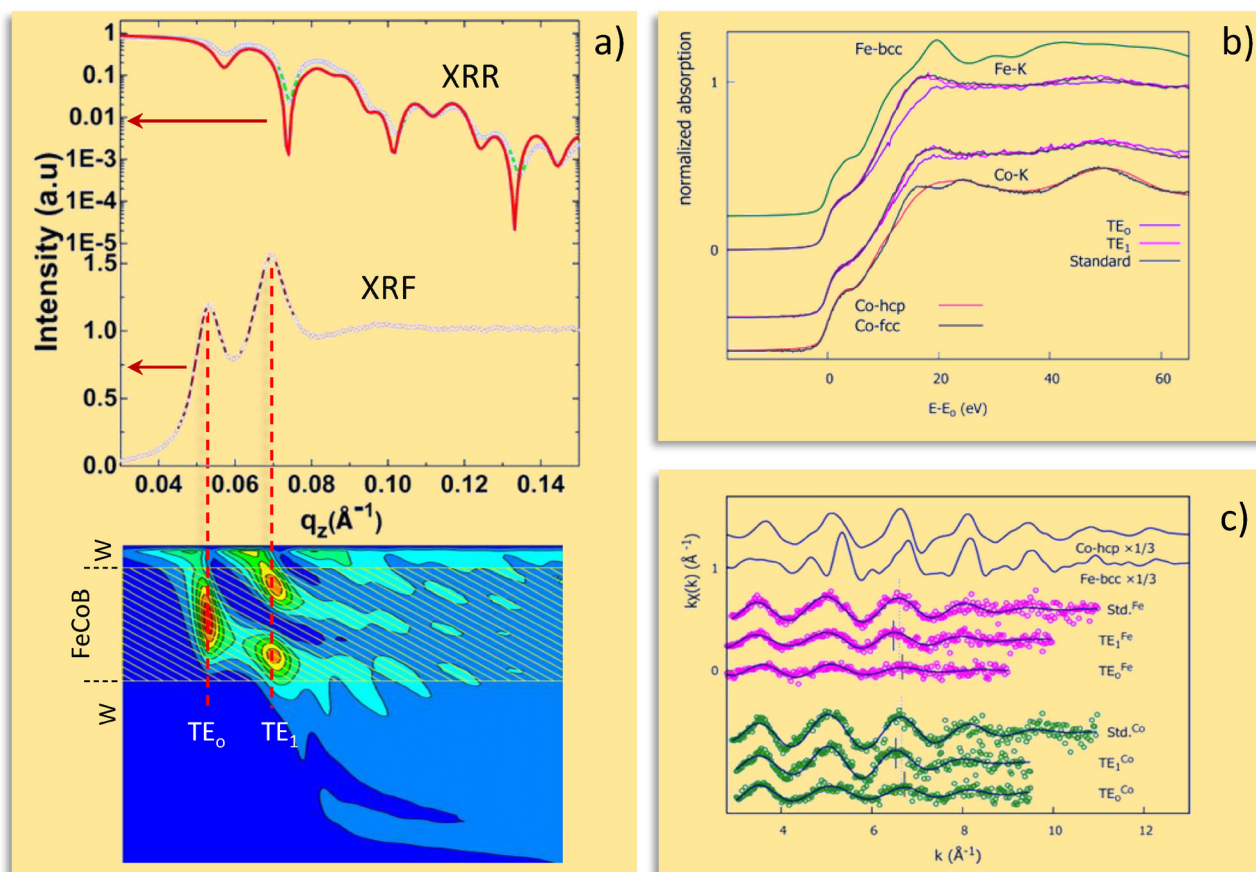


Figure 1. (a) XRR experimental data (open circles) and best fit (continuous line) as a function of the exchanged momentum q are presented. The Fe fluorescence yield is also shown, which allows to individuate the TE_0 and TE_1 SW modes. The calculated contour plot of x-ray SW field intensity is shown below. (b) Normalized XANES spectra measured at the Fe and Co Kedges for the whole film (bulk, black line) and in SW condition (TE_0 -violet, TE_1 -rose). The energies in the abscissa are shown respect to the Fe or Co K edge energies (E_0). The spectra of reference samples are shown for sake of comparison. Spectra are vertically shifted for clarity. (c) Fe and Co k -weighted EXAFS experimental data (magenta and green circles respectively) and best fit (blue lines) for Standard and SW geometries. Data are vertically shifted for clarity, the Fe-bcc and Co-hcp EXAFS spectra are also shown. Figures adopted/ reprinted from M. Singh et al., J. Alloys Compd. **960**, 170588 (2023).

Acknowledgments

We acknowledge Elettra Sincrotrone Trieste for providing access to its synchrotron radiation facilities (proposal 20215789). The beamtime has been supported by the IAEA under the Agreement between IAEA and Elettra - Sincrotrone Trieste. MS is a Jr. Research Fellow supported by UPES, Dehradun.

Original paper

M. Singh et al., J. Alloys Compd. **960**, 170588 (2023); DOI: 10.1016/j.jallcom.2023.170588

M. Singh¹, M. Abdolrahimi^{2,3}, E. Colantoni^{4,5,6}, L. Tortora^{2,4,5}, S. K. Vayalil¹, M. Gupta⁷, V. R. Reddy⁷, I. Carlomagno⁸, G. Das⁸, G. Aquilanti⁸, A. Gupta¹, C. Meneghini²

- ¹ Department of Physics, University of Petroleum and Energy Studies, Dehradun, India
- ² Department of Science, Roma Tre University, Rome, Italy
- ³ Institute of Structure of Matter, National Research Council (CNR), Rome, Italy
- ⁴ LASR3 Surface Analysis Laboratory, Roma Tre University, Rome, Italy
- ⁵ INFN, Roma Tre, Rome, Italy
- ⁶ Department of Mathematics and Physics, Roma Tre University, Rome, Italy
- ⁷ UGC-DAE Consortium for Scientific Research, Indore, India
- ⁸ Elettra - Sincrotrone Trieste S.C.p.A., Trieste, Italy

e-mail: ajay.gupta@ddn.upes.ac.in ; carlo.meneghini@uniroma3.it

All-optical switching of magnetization on a nanometer spatial scale

FERMI | EIS-TIMER

Ultrafast light-driven control of magnetization on the nanometer length scale is key to achieve competitive bit sizes in next generation data storage technology. In this work, we used a novel experimental technique based on the interference of coherent light pulses in the extreme ultraviolet spectral range and successfully demonstrated the ultrafast emergence of nanoscale all-optical magnetization switching. By continuously reducing the wavelength of the light pulses, we optically imprint sinusoidal magnetization gratings with periodicities down to 17 nanometers. Studying the ultrafast evolution of the grating gives insight into the fundamental spatial limits of all-optical switching, ultimately governed by ultrafast lateral energy transport. The experiments were performed at the free electron laser facility FERMI at Elettra in Trieste, Italy.

The physics of optically driven magnetization dynamics on the femtosecond time scale is relevant for the following two main reasons: first, investigations of the microscopic mechanisms responsible for nonequilibrium, ultrafast spin dynamics continue to challenge our fundamental understanding in solid state physics. Second, optical control of magnetization has potential for applications in next generation information technology with a vision to satisfy the need for both faster and more energy efficient data storage devices. AOS (All-Optical Switching) is one of the most interesting and promising mechanisms for this endeavor, where the magnetization state can be reversed between two directions with a single femtosecond laser pulse, serving as "0s" and "1s". While the understanding of the temporal control of AOS has progressed rapidly, knowledge on ultrafast transport phenomena on the nanometer spatial scale, important for the realization of all-optical magnetic reversal in technological applications, has remained mostly unexplored due to the wavelength limitations of

optical radiation. An elegant way to overcome these restrictions is to use short wavelength radiation in the XUV (extreme ultraviolet) spectral range in transient grating experiments. This technique is based on the interference of two XUV beams leading to a nanoscale excitation pattern and has been pioneered at the EIS-TIMER beamline of the free-electron laser FERMI in Trieste, Italy.

In the first experimental run, we excited a TMG (Transient Magnetic Grating) with a periodicity of $\Lambda_{\text{TMG}} = 87$ nm in a ferrimagnetic GdFe alloy sample, known to exhibit AOS. We probed the spatial evolution of the magnetization grating by recording the diffracted intensity of a third XUV pulse for varying time delays after the excitation (cf. Fig. 1 a). By tuning the photon energy of the probe pulse to the Gd N-edge at a wavelength of 8.3 nm (150 eV) and analyzing the polarization state of the light, we ensured exclusive sensitivity to the magnetic moment of the rare earth element Gd. As AOS exhibits a strongly non-linear response to the excitation, one expects characteristic symmetry changes of the evolving magnetic grating distinct from the initial sinusoidal excitation pattern. This information is directly encoded in the diffraction pattern: in case of a linear magnetization response to the excitation and no AOS, a sinusoidal TMG is induced and the second diffraction order is suppressed. However, if AOS occurs, the grating shape changes, now allowing for a pronounced second order diffraction intensity. In other words, we identified the intensity ratio between the second and first order (R_{21}) as a fingerprint observable for AOS in diffraction experiments.

Figure 1 b), c) show the temporal evolution of the diffracted first and second order intensities, respectively. We find comparable decay times of $\tau_{\text{RE,1st}} = (81 \pm 7)$ ps and $\tau_{\text{RE,2nd}} = (90 \pm 24)$ ps, consistent with lateral energy diffusion rates of the nanoscale gratings. Figure 1 d), shows the ratio R_{21} as a

function of the excitation fluence at a constant pump-probe delay of 50 ps. For low fluence below the threshold of AOS, we observed a constant and small value of R_{21} of around 1%. Increasing the excitation to lie within the fluence window for AOS, R_{21} rises to ~8%, providing first evidence for a magnetization reversal on the nanometer length scale. The ratio R_{21} as a function of time is shown in Figure 1 e) for two selected excitation fluences. Only for the larger fluence (red circles) R_{21} exhibits an elevated and constant ratio of about 6% over the measured time interval of 150 ps, indicative of a stable magnetic structure, which we interpret as optically reversed domains, i.e. AOS. Magnetic switching has taken place, transforming the sinusoidal magnetization profile into a prototypical ...01010101... bit pattern. We were able to confirm the observations by complementary all-optical measurements in real space using time-resolved Faraday microscopy, where larger bits can be directly imaged. The combination of the techniques allows us to study the dynamics of the AOS process on the relevant nanometer-scale in great detail.

In a follow-up transient grating experiments, we were able to induce much smaller periodicities down to 17 nm (corresponding to 8.5 nm bit size), leading to a significantly accelerated decay of the magnetic grating contrast with rates of only $\tau_2 = (2 \pm 1)$ ps. Now ultrafast lateral transport processes present an additional channel for energy dissipation on the time scale of demagnetization and will therefore set the fundamental spatial limits of AOS.

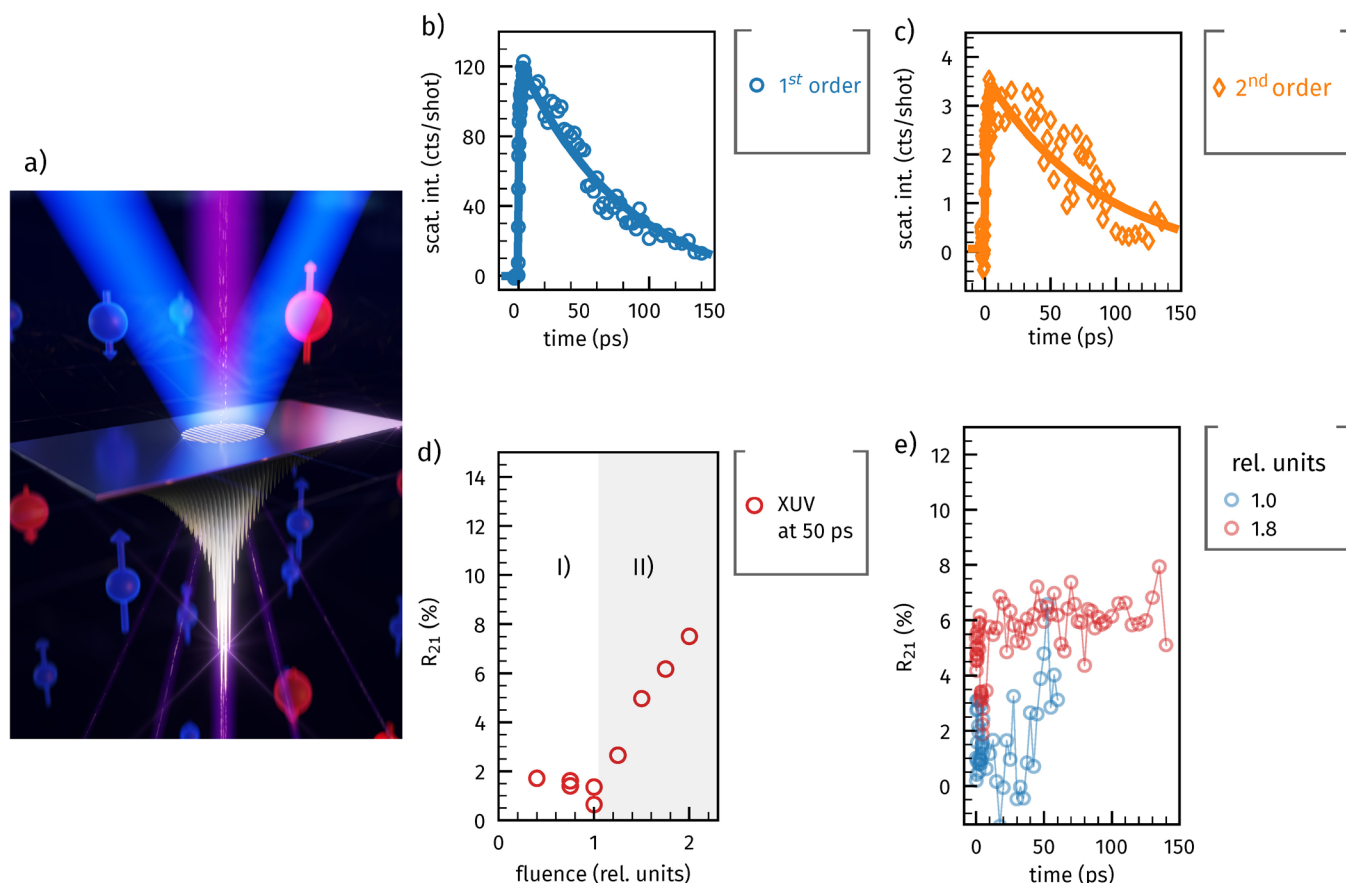


Figure 1. a) Artistic depiction of the transient grating experiment: two XUV beams (blue) interfere and induce a sinusoidal excitation grating. A time-delayed third beam with a wavelength of 8.3 nm (violet) resonantly diffracts of the emerging magnetization pattern. b) First and c) second order diffraction intensity as a function of the time delay between the excitation of the transient magnetic grating and the probe beam. d) Intensity ratio between the second and first diffraction order (R_{21}) as a function of excitation fluence at a delay of 50 ps. At a fluence of 1.3 rel. units, the transient magnetization grating starts to change its shape leading to the emergence of the second diffraction order, a fingerprint for AOS. e) The ratio R_{21} for a high excitation fluence (red circles) exhibits a large and constant ratio, which we identify as the emergence of a stable magnetic structures and therefore as additional evidence for AOS on the nanometer spatial scale.

Original paper

K. Yao *et al.* Nanometer Scale Excited and Probed with Femtosecond Extreme Ultraviolet Pulses." *Nano Letters* **22**, 4452 (2022); DOI:10.1021/acs.nanolett.2c01060.

K. Yao¹, F. Steinbach¹, M. Borchert¹, D. Schick¹, D. Engel¹, F. Bencivenga², R. Mincigrucci², L. Foglia², E. Pedersoli², D. De Angelis², M. Pancaldi², B. Wehinger^{2,4}, F. Capotondi², C. Masciovecchio², S. Eisebitt¹ and C. von Korff Schmising¹

¹ Max-Born-Institute for Nonlinear Optics and Short Pulse Spectroscopy (MBI), Berlin, Germany

² Elettra - Sincrotrone Trieste S.C.p.A., Trieste, Italy

³ Department of Physical and Chemical Sciences, University of L'Aquila, L'Aquila, Italy

⁴ Department of Molecular Sciences and Nanosystems, Ca' Foscari University of Venice, Venezia Mestre, Italy

e-mail: korff@mbi-berlin.de

Extreme ultraviolet transient gratings: a tool for nanoscale photoacoustics

FERMI | EIS-TIMER

The mechanical stiffness of a solid or its capability of transporting heat depend strongly on its dimensions. This becomes particularly relevant when the spatial length scales reduce from macroscopic to microscopic, i.e. to sizes that become comparable to the distance between atoms in a crystal lattice or to the characteristic length scales of nanostructures. For example, in a crystalline solid, heat is transported primarily by vibrations, or phonons, which travel for a finite mean free path L_{ph} . When the dimensions of the solid are much larger than L_{ph} heat is transported diffusively, while it becomes ballistic when the dimensions are much smaller. None of the two descriptions, however, holds when the dimensions are comparable to L_{ph} . A similar situation occurs with the thermal and elastic properties of amorphous solids such as glass. Their vibrational dynamics can be described easily in the macroscopic limit, where the system is approximated as a continuum, and in the single-particle limit, but theory fails in the description of the mesoscopic regime, for length scales on the order of few tens of nanometers.

Measuring and understanding the thermoelastic response of matter at the nanoscale is becoming crucial for technological applications based on nano-, hetero- or confined structures, or those aimed at exploiting or controlling either heat or vibrations such as, for example, thermal barrier coatings, heat assisted magnetic recording, nano-enhanced photovoltaics, thermoelectric energy conversion, high power optoelectronics and many more. Over the years, an obstacle to the full description of thermoelastic responses in this so-called mesoscopic regime was the lack of experimental techniques capable of accessing the nanometer (one billionth of a meter) spatial scale. Optical techniques are typically limited to measurements on the hundreds of nm scale, while inelastic scattering of hard x-ray radiation or neutrons works for length scales shorter than about 1 nm.

These limitations can be overcome by FEL (Free Electron Laser) sources, which offer EUV (Extreme Ultraviolet) pulses of the required brightness to enable TG (Transient Grating) spectroscopy. In this technique the characteristic length scale $\Lambda_{TG} = \lambda / [2 \sin(\theta)]$ is set by the period of the interference pattern formed by two excitation pulses of wavelength λ crossed at an angle 2θ ; the use of FEL radiation enables $\Lambda_{TG} \approx 10$ s of nm. The EUV TG technique pioneered at the EIS-TIMER beamline of the FERMI FEL (Trieste, Italy) has already been applied to studying a wide range of phenomena such as nanoscale thermal transport, ultrahigh-frequency acoustic waves, nonlinear optics, and ultrafast magnetism. In this manuscript, we summarize the experience acquired from EUV TG experiments aimed at studying the thermoelastic response of solids in the sub-100 nm length scale that were carried out at the TIMER instrument in the last 5 years. We focus on the peculiarities related to the use of EUV light both for TG excitation and probing, in both forward and backward diffraction geometries. In the former case, these peculiarities are related mainly to the strong absorption of EUV photons in condensed matter. Indeed, contrary to the optical regime, the photon energy of EUV pulses is always larger than both plasma frequencies and typical electronic bandgaps, making the distinction between dielectrics, semiconductors and metals irrelevant. As depicted in Fig. 1(a), the strong absorption of the excitation pulses leads to a modulated hot electron population that induces a thermal grating in the sample. The accompanying thermal expansion results in a periodic modulation of the material density (density grating). In other words, as depicted in Fig. 1(b), after the initial electronic dynamics and the following electron-lattice relaxation, the material finds itself in a state of alternating hot expanded areas and cold compressed areas remaining at the room temperature. This periodic modulation

of the sample density is measured via diffraction of a third time-delayed EUV pulse. The recovery of the unperturbed state, through mechanical oscillations and heat diffusion, is encoded in the intensity of the diffracted probe beam as a function of the relative delay between the excitation and the probe pulse. We show some selected EUV TG data to illustrate the reliable capability of EUV TG of probing bulk, confined and surface phonon modes, as well as thermal transport, in the sub-100 nm scale, in a totally non-invasive and noncontact manner. Such a capability can be exploited in several fields, such as high frequency surface waves, structural dynamics in disordered systems, and phonon engineering in nanostructures. Additionally, we mention the capability to exploit the electronic core-hole transitions to probe the ultrafast electronic and magnetic responses, with the added value of element specificity. In the case of a magnetic sample with a uniform magnetization, as shown in Fig. 1(b), the contrast arises from the periodic pattern of demagnetized and magnetized sample areas. The transient diffracted signal of the probe encodes the ultrafast process of thermal-induced generation of magnetization grating and the following recovery of a uniform magnetization state (ensured by the presence of an external magnetic field of sufficient strength).

Finally, we discuss the extension of TG both to higher photon energies, changing the experimental paradigm from refractive to diffractive optics, and to high-harmonic-generation-based laboratory setups. The first would open the up the realm of chemical specific spectroscopy and sub-nm periodicities, while the latter would render TG available to a much broader, potentially industry-driven, community.

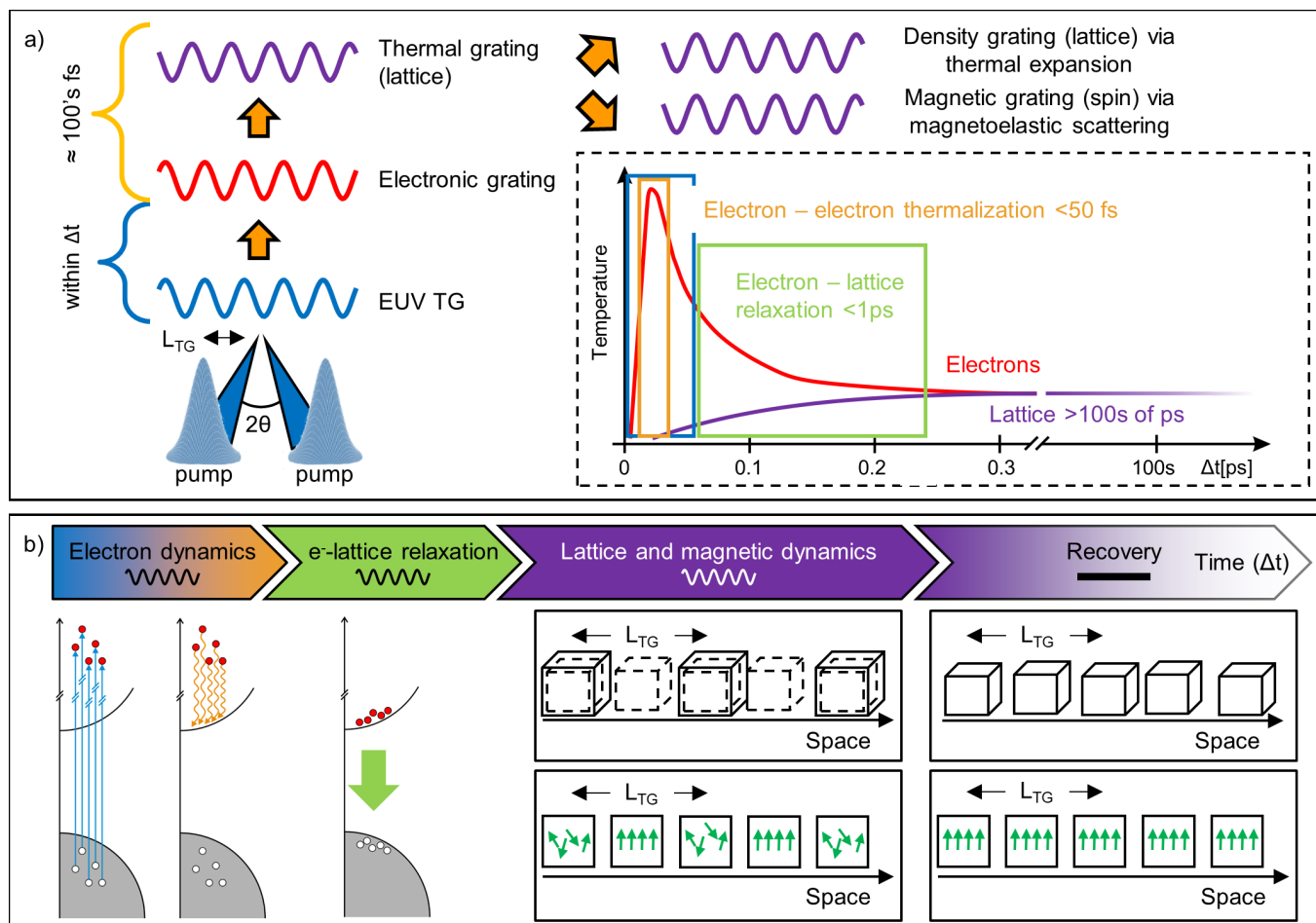


Figure 1. (a) Main excitation pathway for EUV TG: a population grating of electronic excited states is generated “instantaneously”; within 100s of fs, it thermalizes with the lattice leading to temperature, density and/or magnetic gratings, as sketched in the inset for the case of temperature. Here the blue and orange boxes represent, respectively, the time duration of the excitation pulse and the typical timescale for the electron-electron thermalization. The green box indicates the characteristic time scale of the electron-lattice relaxation. (b) After the initial electronic dynamics, the system finds itself in a state of alternating hot / expanded, and cold / compressed areas. In the case of magnetic samples, TG excitation leads to a periodic arrangement of magnetized and demagnetized areas. In both cases the sample recovers to equilibrium conditions in several hundreds of ps to ns.

Acknowledgments

The authors acknowledge the Laboratoire des Matériaux Avancés (LMA-CNRS) for providing the mirror with the standard coating for the LIGO-Virgo collaboration. A.A.M, C.A.O, J.L., R.C., and K.A.N. received support from the Department of Energy, Office of Science, Office of Basic Energy Sciences, under Award Number DE-SC0019126. F.Capor. acknowledges financial support from The Netherlands Organization for Scientific Research (NWO) (Grant Number 680-91-13). G.M. acknowledges support from the research project GLASS@EXTREMES financed by the Cariparo foundation (2021). B.W. acknowledges support from the European Research Council through Starting Grant 715452 “MAGNETIC-SPEED-LIMIT”.

Original paper

L. Foglia, R. Mincigrucci et al., Photoacoustics **29**, 100453 (2023); DOI: 10.1016/j.pacs.2023.100453

L. Foglia¹, R. Mincigrucci¹, A. A. Maznev², G. Baldi³, F. Capotondi¹, F. Caporaletti^{4,5}, R. Comin⁶, D. De Angelis¹, R. A. Duncan², D. Fainozzi¹, G. Kurdi¹, J. Li⁶, A. Martinelli⁷, C. Masciovecchio¹, G. Monaco⁷, A. Milloch⁸, K. A. Nelson², C. A. Occhialini⁶, M. Pancaldi^{1,9}, E. Pedersoli¹, J. S. Pelli-Cresi¹⁰, A. Simoncig¹, F. Travasso^{11,12}, B. Wehinger^{1,9}, M. Zanatta³, F. Bencivenga¹

¹ Elettra - Sincrotrone Trieste S.C.p.A., Trieste, Italy

² Department of Chemistry, Massachusetts Institute of Technology, Cambridge, Massachusetts, USA

³ Department of Physics, University of Trento, Trento, Italy

⁴ Van der Waals-Zeeman Institute, Institute of Physics, University of Amsterdam, Amsterdam, The Netherlands

⁵ Van't Hoff Institute for Molecular Sciences, University of Amsterdam, Amsterdam, The Netherlands

⁶ Department of Physics, Massachusetts Institute of Technology, Cambridge, Massachusetts, USA

⁷ Department of Physics and Astronomy, University of Padova, Padova, Italy

⁸ Department of Mathematics and Physics, Catholic University of Sacred Heart, Brescia, Italy

⁹ Department of Molecular Sciences and Nanosystems, Ca' Foscari University of Venice, Venice, Italy

¹⁰ Italian Institute of Technology, Genoa, Italy

¹¹ University of Camerino, Camerino, Italy

¹² INFN, Section of Perugia, Perugia, Italy

e-mail: laura.foglia@elettra.eu

Revealing all-optical spin injection in silicon in the femtosecond time scale at FERMI

FERMI | MagneDyn

A revolutionary and energy-efficient information technology employing both electron spin and charge - called also *Spintronics* - is being developed worldwide by combining semiconductors and ferromagnets. Encoding digital data in electron spins can ultimately lead to new computer paradigms and novel spin-based multidimensional devices. For instance, Spintronics can result to the merging of the memory and the logic computing functions in the same device, with overall obvious efficiency gains. As a result, the advantages of this new technology would be the inherited non-volatility of magnetic data storage, increased data processing speed and reduced power consumption. Furthermore, spins can act as a natural base for the encoding of quantum-bits, which would permit the progress towards silicon-based quantum computing. The first step to integrate spin-based electronics in current semiconductor technology goes to embedding the spin functionality in silicon, which represents the predominant component in electronic devices. Silicon is an ideal system in that it shows exceptional spin-preserving properties - as several experiments have demonstrated - which allows spin to propagate freely in the semiconductor as it is the case for electrons. However, silicon is non-magnetic at equilibrium, whereas some metals - such as iron and nickel - show a persistent magnetism. To force a magnetic character in silicon, the electron spins must be forced to align along a preferred orientation and a variety of approaches have recently been employed to achieve it, like excitation from circularly polarized light or injection of spin-polarized electrons either direct or through tunnelling or even more through Seebeck effect. In all the last listed cases, the process of inducing magnetism passes through the transfer of spins from a spin-polarized reservoir to the semiconductor via spin-polarized currents. The transfer process can be forced by an external stimulus driving the system out of equilibrium,

as by means of a strong ultrafast laser pulse. Nowadays, there is considerable evidence in literature on achieving spin-polarized currents in silicon via the injection of spin currents from a ferromagnetic contact on the surface of the semiconductor. These currents triggered by ultrafast optical pulses are defined as *superdiffusive* as they achieve a faster diffusion than the normal thermal diffusion, which is responsible of the conduction mechanisms.

The spin injection mechanism is schematically represented in Fig. 1a. In the first place, the optical laser pulse is absorbed by the ferromagnetic metal layer deposited above the semiconductor, kicking off many high-energy electrons of both the spin-majority and minority types. Then, as these electrons diffuse within the metallic film, they interact with the mainly spin-majority polarized electron background. Because this interaction is asymmetric with respect to the spin, within few femtoseconds only the spin-majority component of the excited electrons survives. As a result, the diffusion of electrons leads to a spin diffusion (j_s) away from the irradiated area of the metal. As a second result, this spin diffusion removes also angular momentum from the irradiated area leading to a rapid demagnetization in less than 150 fs.

Then, as the superdiffusive current reaches the metal-semiconductor interfaces, it encounters the Schottky energy barrier which is established when the two materials are placed in contact. If the electron energy is sufficient, it has a nonzero probability to overcome the energy barrier through the tunneling effect and therefore to be injected into the semiconductor. In turn, this leads to a transient magnetization (M_{js}) that is induced in the semiconductor and that is then propagating within the sample. In the proximity of the interface, this transient magnetization can compete with the intrinsic static magnetization in the semiconductor that is induced by the presence of the magnetic metallic film.

In our work, we have investigated the spin injection in silicon in a nickel/silicon heterostructure by means of a pump-probe experiment, which is briefly outlined in Fig. 1b. To control the smoothness of the interface and limit the formation of defects at the metal-semiconductor interface, such as the presence of mixed alloys, the silicon surface has been passivated by an ultrathin silicon nitride layer before the deposition of the metal. In the experimental configuration the optical pump pulse is triggering the superdiffusive spin current, whereas the Free-Electron Laser pulses probe the magnetic state of the sample. Moreover, by tuning the energy of the probe to the core resonances of nickel or silicon, it is possible to study the evolution of the magnetic state in the metal and the semiconductor separately. Magnetization sensitivity has been obtained by measuring the Kerr rotation (MOKE effect) of the photon polarization resulting from the interaction between the photon pulse and the magnetic sample. The evolution of the Kerr rotation has been measured by means of an X-ray polarimeter (TONIX) in the Wollaston configuration. The time-resolved MOKE experiment was carried out at the beamline MagneDyn for magnetodynamics studies at FERMI FEL. The observation of a transient magnetic dynamic signal in silicon - as well as the presence of a static magnetization in the proximity of the interface - represent important results that are beneficial to the design and the development of novel Spintronic paradigms.

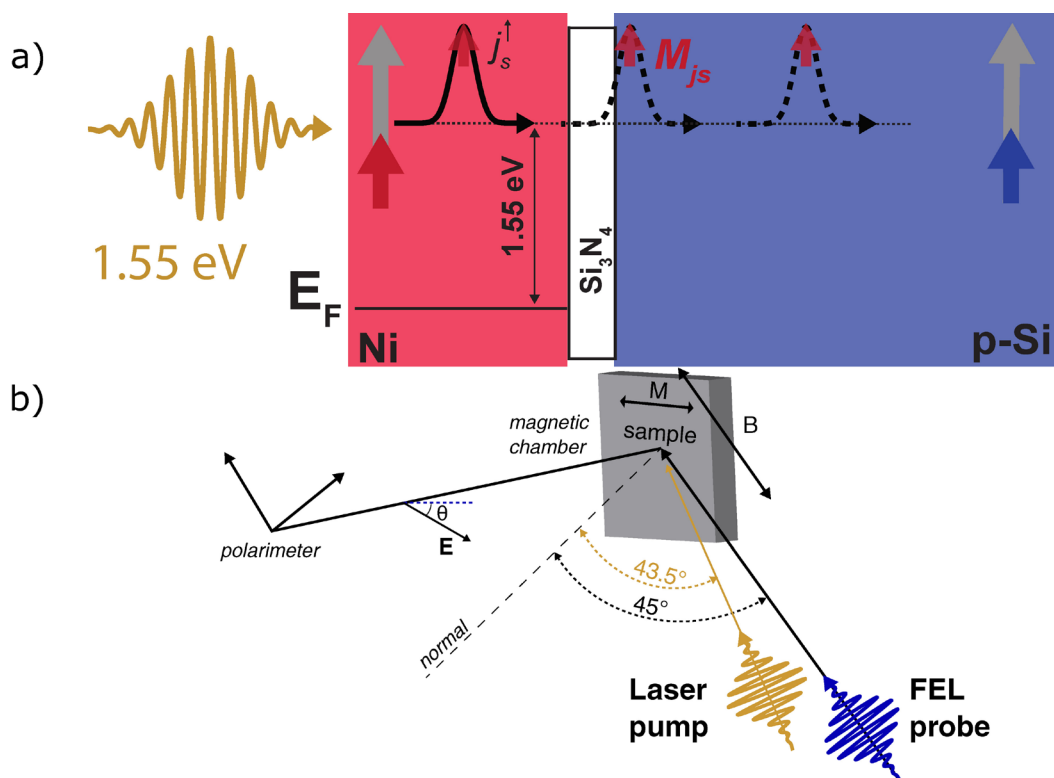


Figure 1. (a) the generation of a spin current pulse in the nickel/silicon heterostructure is triggered by the absorption of an optical pulse (gold arrow) in the nickel film (red). This in turn both reduces the magnetization in nickel (grey to red arrow) and generates high-energetic electrons that travel towards the substrate (black envelope). As these electrons propagate, they become spin-polarized (j_s , small red arrow) and finally get injected and propagate into the substrate (black dashed envelope) causing the insurgence of a transient magnetization in silicon (M_{js} , grey to blue arrow). Figure 1. (b) the time-resolved MOKE setup @ MagneDyn. Laser pump and FEL probe pulses arrive at the sample which is located in the magnetic chamber and subjected to a magnetic field B . After being reflected by the magnetized surface, the probe pulses, which are rotated of an angle θ with respect to the incident polarization E , are analyzed by the TONIX polarimeter.

Acknowledgments

A. C. and F. P. would like to thank Marco Battiato for fruitful discussion. P. M. and M. J. acknowledge financial funding through the project EUROFEL-ROADMAP ESFRI.

Original paper

S. Laterza *et al.*, *Optica* **9**, 11 (2022); DOI: 10.1364/OPTICA.471951

S. Laterza^{1,2}, A. Caretta¹, R. Bhardwaj¹, R. Flammini³, P. Moras⁴, M. Jugovac⁴, P. Rajak⁵, M. Islam⁵, R. Ciancio⁵, V. Bonanni¹, B. Casarin², A. Simoncig¹, M. Zangrando^{1,5}, P. R. Ribic¹, G. Penco¹, G. De Ninno¹, L. Giannessi¹, A. Demidovich¹, M. Danailov¹, F. Parmigiani^{1,6}, M. Malvestuto^{1,5}

¹ Elettra Sincrotrone Trieste S.C.p.A., Trieste, Italy

² Department of Physics, University of Trieste, Trieste, Italy

³ Istituto di Struttura della Materia-CNR (ISM-CNR), Roma, Italy

⁴ Istituto di Struttura della Materia-CNR (ISM-CNR), Trieste, Italy

⁵ Istituto Officina dei Materiali (CNR-IOM), Trieste, Italy

⁶ International Faculty, University of Cologne, Cologne, Germany

e-mail: antonio.caretta@elettra.eu ; simone.laterza@elettra.eu

Layer-by-layer control of the electron dynamics in magnetic topological insulators

FERMI | T-ReX

Stacking layers of two-dimensional materials into heterostructures is an attractive strategy to control the key properties, such as the band gap and the charge transfer efficiency, of advanced spin- and optoelectronic devices. The recently discovered family of van der Waals heterostructures in the form $\text{MnBi}_2\text{Te}_4(\text{Bi}_2\text{Te}_3)_m$ ($m = 1, 2, 3 \dots$) is an interesting target for such approach. Indeed, a layered topological insulator with intrinsic antiferromagnetic ordering, MnBi_2Te_4 , has gained notoriety owing to the realization of exotic phases that support the quantum anomalous Hall effect and axion insulator states. The strength of magnetic interaction in this system can be adjusted by introducing non-magnetic QLs (Quintuple Layers) of Bi_2Te_3 between magnetic SLs (Septuple Layers) of the base material MnBi_2Te_4 , but the influence of interlayer interactions on the ultrafast charge carrier dynamics in this system remained unexplored.

Here, we used the TR-ARPES (Time- and Angle-Resolved Photoemission Spectroscopy) end-station at T-ReX, FERMI, to investigate the ultrafast response of magnetic heterostructures of the form $\text{MnBi}_2\text{Te}_4(\text{Bi}_2\text{Te}_3)_m$ ($m = 0, 1$) to ultrafast infrared optical excitation. ARPES maps are acquired using the fourth harmonics at 6.2 eV of a Ti:Sapphire regenerative amplifier, while photoexcitation is achieved using 1.55 eV pump photons. Measurements were performed at a temperature of 110 K. We found that in MnBi_4Te_7 ($m = 1$), the states derived from Bi_2Te_3 surface layer are preferentially occupied, and that the speed of carrier extraction into the adjacent MnBi_2Te_4 layers is fluence-tunable and may take up to 350 fs at the lowest pump fluence used ($\approx 50 \mu\text{J}/\text{cm}^2$). The thermal relaxation of the excited carriers is mediated by the intralayer phonon scattering, leading to slower decay rates within the SL.

Fig. 1 (a) shows the crystal structures of the materials under investigation. In the case of MnBi_4Te_7 ($m = 1$), mechanical cleaving can expose two surface

terminations with distinct sets of surface states in addition to the common bulk states. This is manifested in Fig. 1 (b), where we show the difference in photoemission intensity between the initial moments after the excitation and the equilibrium conditions before the excitation ($\Delta t < 0$). The red (blue) regions reflect the gain (loss) of photoemission signal, which corresponds to excited electron (hole) population. The time dependence of the electron occupation in MnBi_4Te_7 just above the Fermi level is shown in Fig. 1 (c). At high fluence, the dynamics are comparable across all the two terminations: the signal rises instantaneously, then decays slowly over several picoseconds. At low fluence, however, the build-up of photoemission intensity in the SL termination is delayed to 0.8 ps after the excitation. We investigate the detailed fluence dependence in Fig. 1 (d). The width of sigmoid fit to the rising edge provides the growth rate, τ_0 , of the population just above the Fermi level. While the rise time of QL signal is fast and insensitive to fluence, in the SL, the growth rate becomes slower with decreasing excitation density, reaching the maximum of 0.35 ps at fluence of approx. $50 \mu\text{J}/\text{cm}^2$. The growth rate is influenced by the filling from states at higher energies which are first populated by the pump. One of those states is localized to the QL. At low excitation energy, the intralayer scattering within the QL is more favorable than the interlayer charge transfer to the SL, producing a bottleneck effect. Finally, the signal decays exponentially due to the electron-hole recombination at the Fermi level, which is mediated by electron-phonon interactions in topological insulators. The excited carriers are removed more efficiently in the QL, suggesting that the intralayer phonons play a dominant role in the relaxation. Thanks to this investigation, we determined the ultrafast carrier dynamics of the intrinsic magnetic topological insulator heterostructures MnBi_2Te_4 and MnBi_4Te_7 . The excited carriers exhibit

markedly different dynamics, since these are affected by interlayer interactions between the Bi_2Te_3 quintuple layers and the MnBi_2Te_4 septuple layers. In the regime of low laser fluence, the charge transfer processes into the MnBi_2Te_4 layers display a bottleneck, potentially paving the route to the optical control of the population of spin-polarized carriers in the magnetic layers of these heterostructures. Furthermore, as the subsequent electron-phonon-mediated relaxation is less efficient in the magnetic MnBi_2Te_4 compared to the nonmagnetic Bi_2Te_3 layers, it might be feasible to optically modify the magnetic properties of the heterostructure when designing spintronic and optoelectronic devices with layers of MnBi_2Te_4 . The above results illustrate how the competition between intra- and interlayer processes shapes up the dynamic response in magnetic topological insulators, and may provide guidelines for optical control of spin-polarized charge carriers in their van der Waals heterostructures.

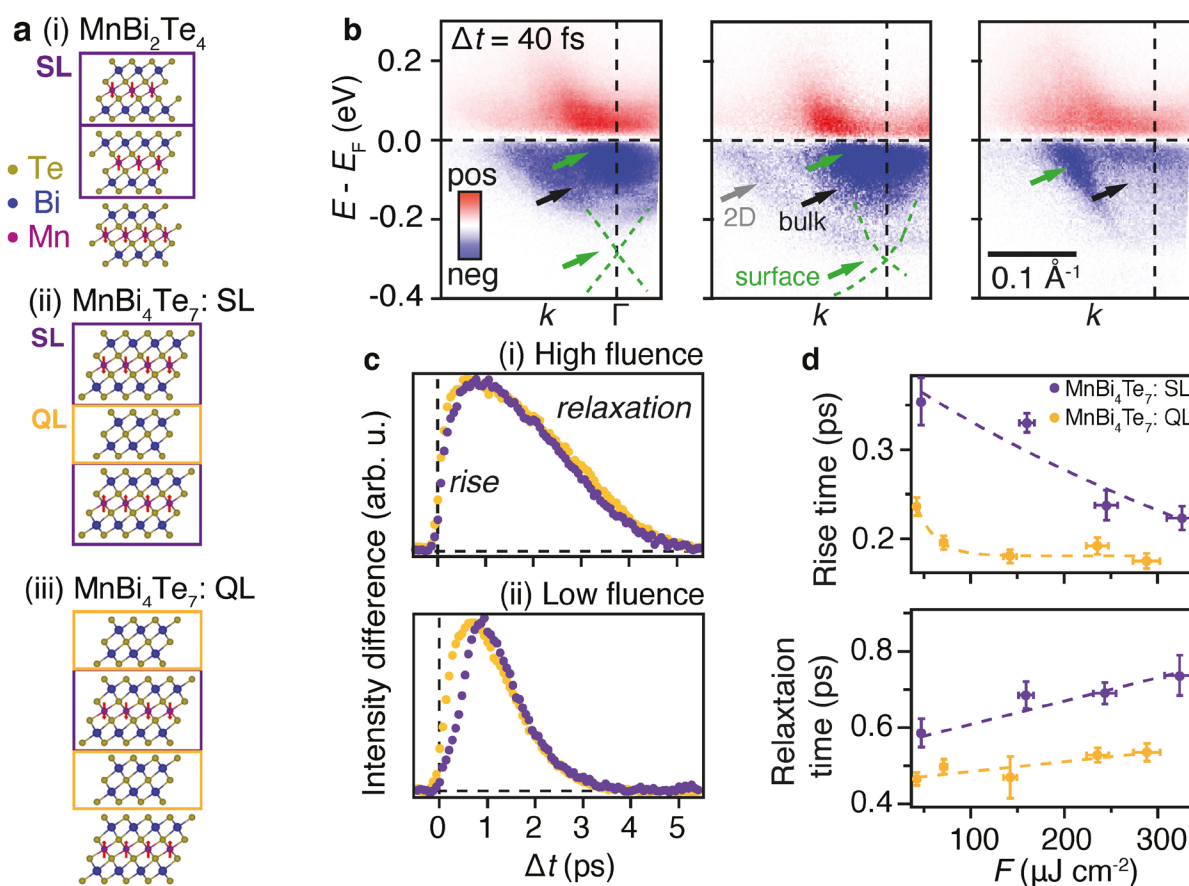


Figure 1. (a) Crystal structures of (i) MnBi_2Te_4 ($m = 0$), (ii) septuple layer (SL)-terminated MnBi_4Te_7 ($m = 1$), (iii) quintuple layer (QL)-terminated MnBi_4Te_7 ($m = 1$). (b) Difference photoemission spectra of the three systems, taken just after the optical excitation. (c) Photoemission intensity integrated over an energy range of 70 meV above the Fermi level, as a function of delay time Δt , for SL (purple) and QL (orange) termination of MnBi_4Te_7 , for (i) high and (ii) low fluence. (d) Fluence dependence of the rise time and decay constant for the two terminations. Dashed curves serve as the guides to the eye. Adapted from P. E. Majchrzak et al., *Nano Lett.* 23, 414 (2023).

Acknowledgments

Funding is acknowledged from VILLUM FONDEN through the Young Investigator Program (Grant No. 15375), the Villum Investigator Program (Grant No. 25931), the Centre of Excellence for Dirac Materials (Grant No. 11744), and the Danish Council for Independent Research, Natural Sciences, under the Sapere Aude program (Grant No. DFF-9064-00057B), WPI-AIMR, JSPS KAKENHI Basic Science A (18H03858), New Science (18H04473 and 20H04623), and Tohoku University FRIID program, Marie Skłodowska-Curie Postdoctoral Fellowship (Proposal Number 101059528), National Key R&D Program of China (Grant No. 2020YFA0308900) and the Center for Computational Science and Engineering of Southern University of Science and Technology.

Original paper

P. E. Majchrzak et al., *Nano Lett.* 23, 414 (2023); DOI: 10.1021/acs.nanolett.2c03075

P. E. Majchrzak¹, Y. Liu², K. Volckaert¹, D. Biswas¹, C. Sahoo¹, D. Puntel³, W. Bronsch⁴, M. Tuniz³, F. Cilento⁴, X.-C. Pan⁵, Q. Liu², Y. P. Chen^{1,5,6}, Søren Ulstrup¹

¹ Department of Physics and Astronomy, Interdisciplinary Nanoscience Center, Aarhus University, Aarhus, Denmark

² Department of Physics and Shenzhen Institute for Quantum Science and Engineering (SIQSE), Southern University of Science and Technology, Shenzhen, China

³ Department of Physics, University of Trieste, Trieste, Italy

⁴ Elettra - Sincrotrone Trieste S.C.p.A., Trieste, Italy

⁵ Advanced Institute for Materials Research, Tohoku University, Sendai, Japan

⁶ Department of Physics and Astronomy and School of Electrical and Computer Engineering and Purdue Quantum Science and Engineering Institute, Purdue University, West Lafayette, USA

e-mail: ulstrup@phys.au.dk

Visualizing excitons in the two-dimensional semiconductor ReSe₂

FERMI | T-ReX

The two-dimensional semiconducting transition metal dichalcogenide ReSe₂ is characterized by an atomic lattice with a reduced dimensionality, owing to an in-plane Jahn-Teller distortion. As a result, the material exhibits a strong linear anisotropy for optical absorption that could be promising to exploit in photodetectors and light-sensitive field-effect transistors for sensors, solar cells and ultra-flat screens.

Monolayer ReSe₂ displays a direct quasiparticle band gap in the range 1.7-2.0 eV, depending on the dielectric screening from the substrate material. Furthermore, an optical gap around 1.51 eV has been determined via photoluminescence measurements. This fact suggests the formation of excitons, bound electron-hole pairs due to strong Coulomb interaction in the bidimensional plane. Excitons with large binding energy dominate the optical properties of several transition metal dichalcogenide compounds. However, the ultrafast dynamics and lifetime of excitons in ReSe₂, as well as the influence on these properties and on the gap sizes of a metallic graphene contact to monolayer ReSe₂ have not been explored, preventing a detailed understanding of the functionality of 2D ReSe₂ devices. In our study, a monolayer of ReSe₂, supported on two graphene layers, is analyzed by means of a TR-ARPES (Time and Angle-Resolved Photoemission Spectroscopy) pump-probe experiment performed at the T-ReX facility. This technique allows to track, with femtosecond resolution, the modification of the electronic band structure of a material (measured by ARPES) as triggered by photoexcitation of the sample with an intense optical pulse. Before the experiments, the sample is annealed in UHV in order to remove the protective Se capping layer. The sample is optically excited using an ultrashort infrared pump pulse at 1.55 eV with tunable linear polarization state. The energy- and momentum-resolved electronic band structure is then measured in the excited state using a

time-delayed ultra-violet probe pulse (see Fig. 1(a)) at 6.2 eV, obtained as the fourth harmonics of the ultrafast driving laser. Both pump and probe pulses are produced by a regenerative amplified Ti:Sapphire laser source providing 50 fs light pulses at 250 kHz. The resulting photoemission intensity reveals that both in-gap states (IGS) and excitons are excited (see Fig. 1(b)). These features show up as additional photoemission intensity (red color in Fig. 1(b)), triggered by photoexcitation, in the vicinity of the Fermi level (EF) and a few hundred meV above EF respectively. The same photoemission experiment allows to determine that the optical gap of the system is 1.53 eV. Importantly, by changing the polarization of the optical pump pulse that excites the sample from p to s, a relative reduction of intensity of 35% of the excitonic feature only is measured. This result is consistent with the expected anisotropy of the exciton in ReSe₂, arising from the lattice distortion. The smearing of the exciton distribution in momentum space is indicative for its real space radial extent. It is therefore possible to estimate the exciton radius by calculating the Fourier transform of the exciton momentum distribution curve. The radius is found to be 17 Å (see Fig. 1(c)), which is substantially larger than the 9.6 Å determined for bulk ReSe₂ excitons. This result is explained by the increased dielectric screening from the metallic graphene substrate, that determines a significant spatial broadening of the distribution.

The lifetime of the exciton is characterized by a bi-exponential decay with time constants of 110 fs and 650 fs (see Fig. 1(d)). Similarly, the IGS decay follows time constants of 210 fs and 1520 fs (see Fig. 1(d)). These comparable time scales suggest a strong interplay of ultrafast exciton decay and electron-hole recombination via the IGS, which likely involves charge transfer to the underlying graphene. Interlayer interactions between monolayer ReSe₂ and graphene play a large role for the observed timescales

and exciton properties. The observed ultrafast charge transfer makes heterostructures of semiconducting ReSe₂ on metallic graphene layers highly attractive for designing efficient optoelectronic devices. For example, by harvesting light using excitons in ReSe₂ followed by ultrafast charge carrier capture and conduction in graphene it is possible to achieve more efficient solar cells.

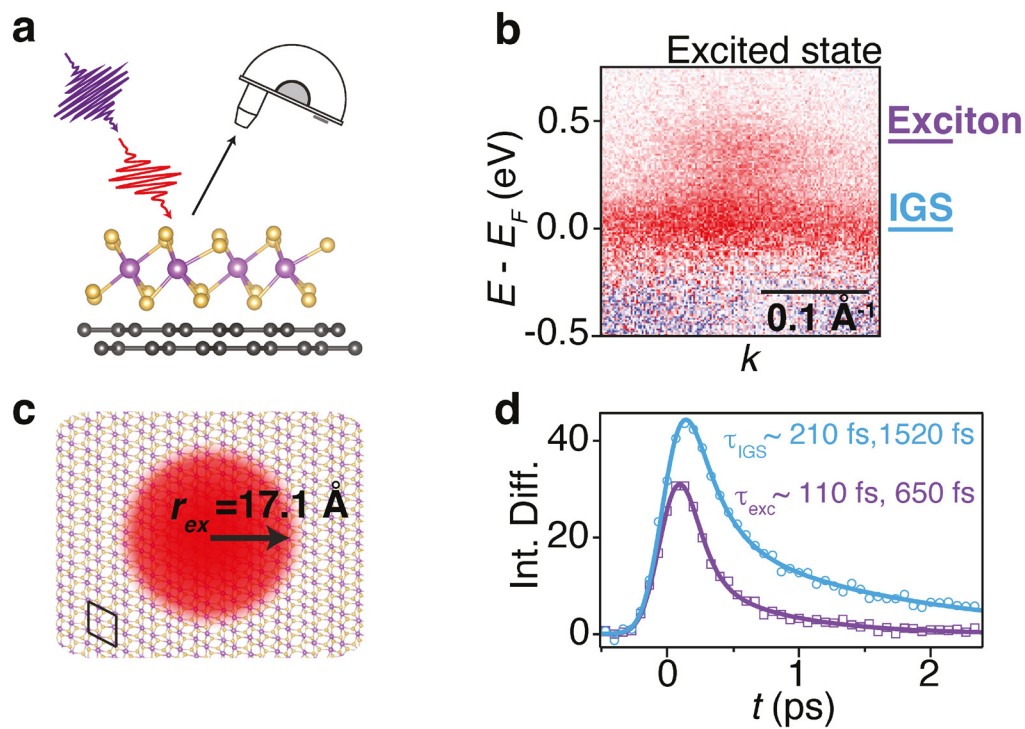


Figure 1. (a) Experimental setup of pump-probe ARPES experiment at T-ReX. (b) Intensity difference measured at time-delay $t = 240$ fs immediately after excitation of the sample. Signal deriving from excitons and in-gap states (IGS) are labeled. (c) Real space exciton radial extent obtained from the data. (d) Transient signal from IGS and exciton states. Adapted from K. Volckaert *et al.*, *Phys. Rev. Mater.* **7**, L041001 (2023) with permission from the American Physical Society.

Acknowledgments

Funding is acknowledged from VILLUM FONDEN through the Young Investigator Program (Grant. No. 15375), the Centre of Excellence for Dirac Materials (Grant. No. 11744), the Danish Council for Independent Research, Natural Sciences under the Sapere Aude program (Grant No. DFF-9064-00057B) and Grants No. NRF- 2019K1A3A7A09033389, No. 2020R1A2C200373211, and No. 2021R1A6A3A14040322 [Innovative Talent Education Program for Smart City] by MOLIT.

Original paper

K. Volckaert *et al.*, *Phys. Rev. Mater.* **7**, L041001 (2023); DOI: 10.1103/PhysRevMaterials.7.L041001

K. Volckaert¹, B.K. Choi^{2,3}, H.J. Kim², D. Biswas¹, D. Puntel⁴, S. Peli⁵, F. Parmigiani^{4,5}, F. Cilento⁵, Y.J. Chang^{2,6}, S. Ulstrup¹

¹ Department of Physics and Astronomy, Aarhus University, Aarhus, Denmark

² Department of Physics, University of Seoul, Seoul, Republic of Korea

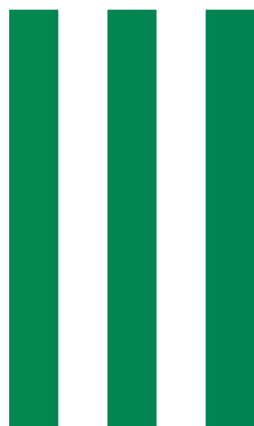
³ Advanced Light Source, E. O. Lawrence Berkeley National Laboratory, Berkeley, California, USA

⁴ Department of Physics, University of Trieste, Trieste, Italy

⁵ Elettra - Sincrotrone Trieste S.C.p.A., Trieste, Italy

⁶ Department of Smart Cities, University of Seoul, Seoul, Republic of Korea

e-mail: ulstrup@phys.au.dk



Surfaces and Interfaces



Orbital symmetry regulates charge transport across a phthalocyanine-graphene interface

Elettra | ALOISA

Functionalization of graphene (Gr)-based materials offers great appeal for several applications, including photonics, optoelectronics, and sensing. However, obtaining clear information on the charge transfer mechanisms at the interface is crucial. In the case of layered materials or two-dimensional (2D) semiconductors, the operation of electronic devices is intertwined with the control of charge carrier generation and flow at the surface or through the junction between layers. Organic molecules are commonly employed to functionalize Gr due to their ability to form covalent bonds with carbon atoms after chemical or electrochemical treatments. Alternatively, they can be physisorbed onto the surface, forming 2D layers. Aromatic scaffolds are often chosen as they allow the formation of cofacially stacked layers, which may interact with the Gr π -orbitals and alter its electronic properties, even without chemical bond formation.

In this study, we deposited a single-molecule thick nickel phthalocyanine (NiPc) layer onto a Gr/SiC sample to investigate the fundamental interactions between the two systems. We first characterized the spatial arrangement and orientation of the molecules with respect to the substrate, followed by an analysis of the photophysics related to the NiPc-to-Gr charge transfer processes. Our investigation involved a combination of experimental and computational methods. The main findings are summarized in Fig. 1: the AFM (Atomic Force Microscopy) images confirmed successful functionalization, showing a homogeneous coverage of the NiPc monolayer with low surface roughness and an absence of clusters. The analysis of high-resolution N 1s and Ni 2p XPS (X-ray Photoelectron Spectroscopy) core-levels (Fig. 1c,d) confirmed the preservation of the NiPc chemical properties, ruling out any decomposition after the sublimation or physisorption processes.

The NEXAFS (Near-Edge X-ray Absorption Fine Structure) spectra taken at the C

K-edge in both p- and s- polarization allowed us to identify the main transitions of Gr from the C 1s core-level to the π^* and σ^* non-occupied levels (found at 285.5 eV and 291.6 eV, respectively). After the NiPc deposition, we observed a strong linear dichroism of the NEXAFS resonances at both the N K-edge and Ni L_3 -edge, indicating a preferentially flat adsorption of NiPc on the Gr surface.

Resorting to DFT (Density Functional Theory) calculations, we evaluated the structure and electronic properties of the Gr-NiPc system. In the framework of the ligand field theory, we focused on the NiPc FMOs (Frontier Molecular Orbitals) mostly involved in the interaction with Gr (Fig. 1g). The HOMO (Highest Occupied Molecular Orbital) exhibited a strong π character, involving exclusively the C p_z states of the pyrrole ring, while the LUMO (Lowest Unoccupied Molecular Orbital), with eg symmetry, mainly involved N and C (pyrrole ring) p_z states. The Ni 3d character contributes to the LUMO+1 (b_{1g} symmetry), which is a σ^* antibonding orbital. Hence, it resonated only in the s-polarization NEXAFS, dominating the Ni L_3 -edge spectrum (Fig. 1e), and was also observed in the N K-edge spectrum slightly above the LUMO energy (Fig. 1d). ResPES (Resonant Photoelectron Spectroscopy) of the valence band disclosed the charge transfer mechanism occurring at the interface. These photoemission spectra were measured in normal emission and with the surface oriented at the magic angle (55° from normal) with respect to the electric field. They are presented in the 2D maps of Fig. 1h,i as a function of the binding energy with respect to the Fermi level (horizontal axis) and of the photon energy (vertical axis). The corresponding NEXAFS profiles, indicating the absorption resonances, are also shown on the left vertical axis. The map recorded at the Ni L_3 -edge exhibited significant photoemission intensity of the occupied molecular orbitals at the LUMO+1 σ -symmetry resonance and a large shift between the

spectator states and the onset of normal Auger decay, indicating a prolonged lifetime of the photoexcited electron in the LUMO+1 orbital compared to the Ni 2p core-hole. In contrast, the corresponding map at the N K-edge shows a complete quenching of the HOMO photoemission at the LUMO π -symmetry resonance and no shift between the spectator and normal Auger onset, suggesting a fast delocalization of the photoexcited electron due to the charge transfer to the Gr layer. Supported by DFT calculations, we concluded that only in the latter case, when the electron occupies a π -symmetry empty orbital (LUMO), a fast and efficient charge transfer can take place (time constant at least ten times lower than 6 fs, that is the N 1s core-hole lifetime).

The computational analysis of the density of states near the Fermi level demonstrated that the Gr Dirac cone feature is preserved after NiPc physisorption, indicating a weak interaction with the adsorbed molecule. Moreover, the π character of both HOMO and LUMO provides the appropriate symmetry for mixing with Gr π states at the same energy. Conversely, the same coupling is not observed for the LUMO+1, due to the symmetry mismatch between the Gr states and an orbital with σ^* character. A possible application of this result has been found in the realization of chemiresistive gas sensors based on the NiPc-Gr heterojunction, whose performances in the detection of NH_3 are quite promising and allowed us to retrieve the p-type nature of the doping in the Gr/SiC system. In our interpretation, the electron donation occurring between the gas molecules and the physisorbed layer, coupled with the Gr substrate, enables the transduction of the NH_3 adsorption process into a (chemi)resistive electrical signal.

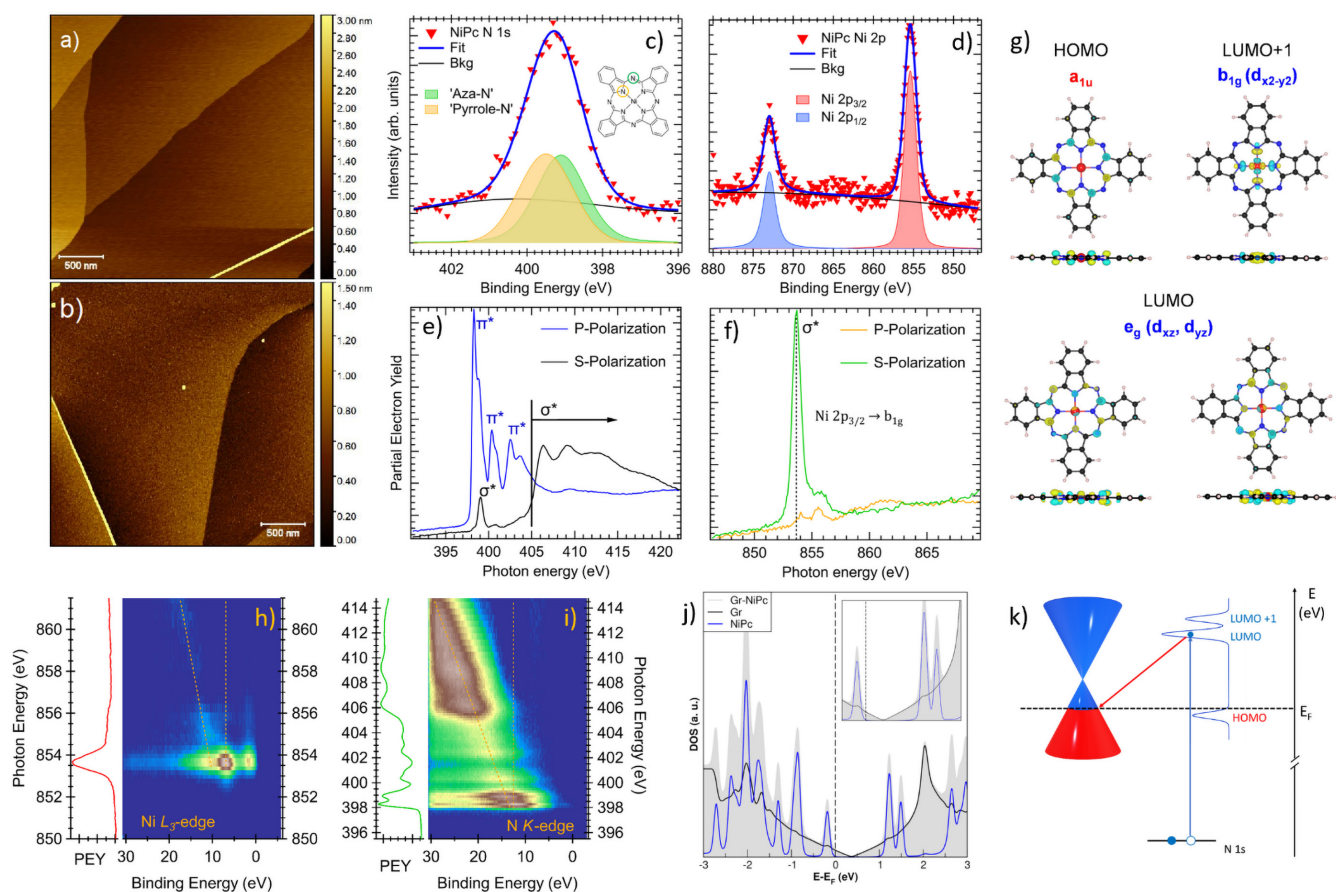


Figure 1. AFM images of (a) pristine and (b) NiPc – functionalized Gr. High-resolution c) N 1s and d) Ni 2p core-level XPS spectra. The inset of panel c) marks the non-equivalent nitrogen atoms in the NiPc structure. e) N K-edge and f) Ni $L_{3,2}$ -edge NEXAFS spectra for the NiPc – functionalized Gr. Both panels include the excitation with s- and p-polarized light, corresponding to transitions to σ^* and π^* -symmetry orbitals, respectively. The dashed line in panel f) points out the main electronic transition Ni $2p_{3/2} \rightarrow b_{1g}$. g) Contour plots for the HOMO, LUMO, and LUMO+1 as calculated for the isolated NiPc molecule in the gas phase. The iso-surface value is set to $4 \times 10^{-3} e^{-\text{\AA}^{-3}}$. Pre-edge subtracted ResPES maps at the (h) Ni $L_{3,2}$ -edge and (i) N K-edge, taken with the surface oriented at the magic angle. On the left panels, NEXAFS spectra at the magic angle, used for the photon energy alignment. j) Total and Projected density of states for Gr-NiPc. In the inset, a zoom-in of the density of states is shown in a range of -0.5 eV/+2 eV with respect to the Fermi level, which is scaled to zero and is indicated by a dashed line. k) Scheme of the relevant energy levels at the Gr-NiPc junction.

Acknowledgments

This work has been supported by the project "MADAM – Metal Activated 2D cArbon-based platforMs" funded by the MIUR Progetti di Ricerca di Rilevante Interesse Nazionale (PRIN) Bando 2017 – grant 2017NYPHN8.

Original paper

A. Casotto *et al.*, *Nanoscale* **14**, 36 (2022); DOI:10.1039/D2NR02647C

A. Casotto^{1,2}, G. Drera¹, D. Perilli³, S. Freddi^{1,4}, S. Pagliara¹, M. Zanotti¹, L. Schio⁵, A. Verdini⁵, L. Floreano⁵, C. Di Valentin³, L. Sangaletti¹

¹ I-LAMP and Department of Mathematics and Physics, Università Cattolica del Sacro Cuore, Brescia, Italy

² Department of Chemistry and Biochemistry, University of Notre Dame, Notre Dame, IN, USA

³ Department of Materials Science, Università degli Studi di Milano-Bicocca, Milano, Italy

⁴ Department of Chemistry, Division of Molecular Imaging and Photonics, KU Leuven, Leuven, Belgium

⁵ TASC Laboratory, IOM-CNR, Trieste, Italy

e-mail: luigi.sangaletti@unicatt.it

Playing with reaction conditions on surfaces

Elettra | ALOISA

MOFs (Metal-Organic Frameworks), highly porous materials composed of metal ions or clusters coordinated to organic ligands, stand out among materials with promising properties for applications such as catalysis, sensing and gas storage. And within this group, two-dimensional (2D) MOFs have also attracted great interest due to their high potential associated to their low dimensionality. The most widely used methodology for the synthesis of these materials is exfoliation, which results in an imperfect product, with the presence of various types of defects. In order to develop non-defective 2D MOFs in a controlled way, we have used the on-surface synthesis approach based on a bottom-up strategy. Molecules of p-AP (para-aminophenol), consisting of a benzene ring with an amine and an alcohol group, have been used as molecular precursors. The surface selected was Cu(111), attractive due its native adatoms, which are essential for the formation of 2D MOF structures. In the fabrication of MOFs, the characteristics of the final product will be substantially determined by a competition between kinetic and thermodynamic control. The reaction control will be sensible to critical factors as the molecular coverage, the amount of surface adatoms, the temperature. In this work, we demonstrate how we obtain two different 2D MOFs structures starting from the same precursor and surface, by varying the experimental conditions. To study the p-AP/Cu(111) system and the corresponding 2D-MOFs, STM (Scanning Tunnelling Microscopy) and SR-XPS (Synchrotron Radiation X-ray Photoelectron Spectroscopy) surface characterization techniques were used in combination with DFT (Density Functional Theory) calculations. Right panel of Fig. 1 shows two STM images of the p-AP molecular networks formed on Cu(111) for two different experimental procedures. The upper image corresponds to the network formed after molecular deposition with the substrate at RT and subsequent

annealing to around 510 K. As it can be observed, this STM image exhibits a network domain of p-AP with a pattern that corresponds to a tessellation composed of hexagons and triangles (Kagome lattice). On the other hand, the lower image of the right panel of Fig. 1 represents the network formed by direct deposition on the hot Cu(111), at around 530 K. In this image, we can observe several molecular domains exhibiting a two-dimensional network based on trigonal arrangements, that in some places suggest the formation of a hexagonal lattice.

The chemical composition of the two phases was measured by XPS and compared with that of as-deposited p-AP on Cu(111) in order to understand the reaction paths and evolution stages. Left panel of Fig. 1 shows the O1s, N1s and C1s XPS core-level peaks for p-AP on Cu(111) just after molecular deposition at RT, after annealing this system from RT to 510 K and after molecular deposition on Cu(111) at 530 K. The O1s spectra exhibit a signal corresponding to the hydroxy group (O-H) and another emission assigned to a phenoxy structure, which suggests the dehydrogenation of the alcohol group when adsorbed on the Cu(111) surface, with the subsequent stabilization via the substrate (Ph-O-Cu emission). The N1s spectra exhibit a peak corresponding to a NH group originated from the partial dehydrogenation of the amine group. At high temperature, an intense component, associated to a N-Cu type structure, appears as a product of a metallation reaction with a Cu adatom of the surface. Finally, all the C1s spectra are similar, with two main emissions, one corresponding to C-C bonds and another one assigned to C-N and C-O components.

Interestingly, the XPS results suggest that the chemical species of the MOFs formed on the Cu(111) by the two different experimental conditions are identical. Upon deposition on the substrate at RT, the molecules undergo a chemical modification (dehydrogenation

and partial dehydrogenation from the alcohol and the amine group, respectively) and become activated. In this case, the precursor density on the surface is very high when the annealing process starts, hindering molecular diffusion and rotation. Thus, these activated molecules will react each other through the easiest way, finding local energy minima. In this procedure, kinetic reaction control seems to prevail in the formation of the metal-organic network. On the other hand, by evaporating the p-AP molecules on the hot substrate, the molecules become activated as soon as they come into contact with the surface, as indicated by XPS, but in this case the coverage increases gradually, leaving enough space for the molecules to rotate and diffuse before reacting with each other to form stable structures. In this case, the reactions leading to the metal-organic network are thermodynamically controlled. Ab initio Density Functional Theory (DFT)-based calculations performed on both systems allowed to elucidate the structure of both networks. As it is shown in the insets of the right panel of Fig. 1, the two networks are based on two different structures, a Kagome and a honeycomb lattice. Consistently with experimental evidences, the calculated molecular adsorption energy for the case of the Kagome network is lower than for the honeycomb one. The latter molecular network thus represents the thermodynamically favored network configuration.

Thus, this work demonstrates the critical role played by reaction conditions in the on-surface synthesis of 2D MOFs, enabling the formation of completely different molecular arrangements. Furthermore, it shows how a combined state-of-the-art structural and chemical analysis is crucial to correctly characterize complex systems on surfaces.

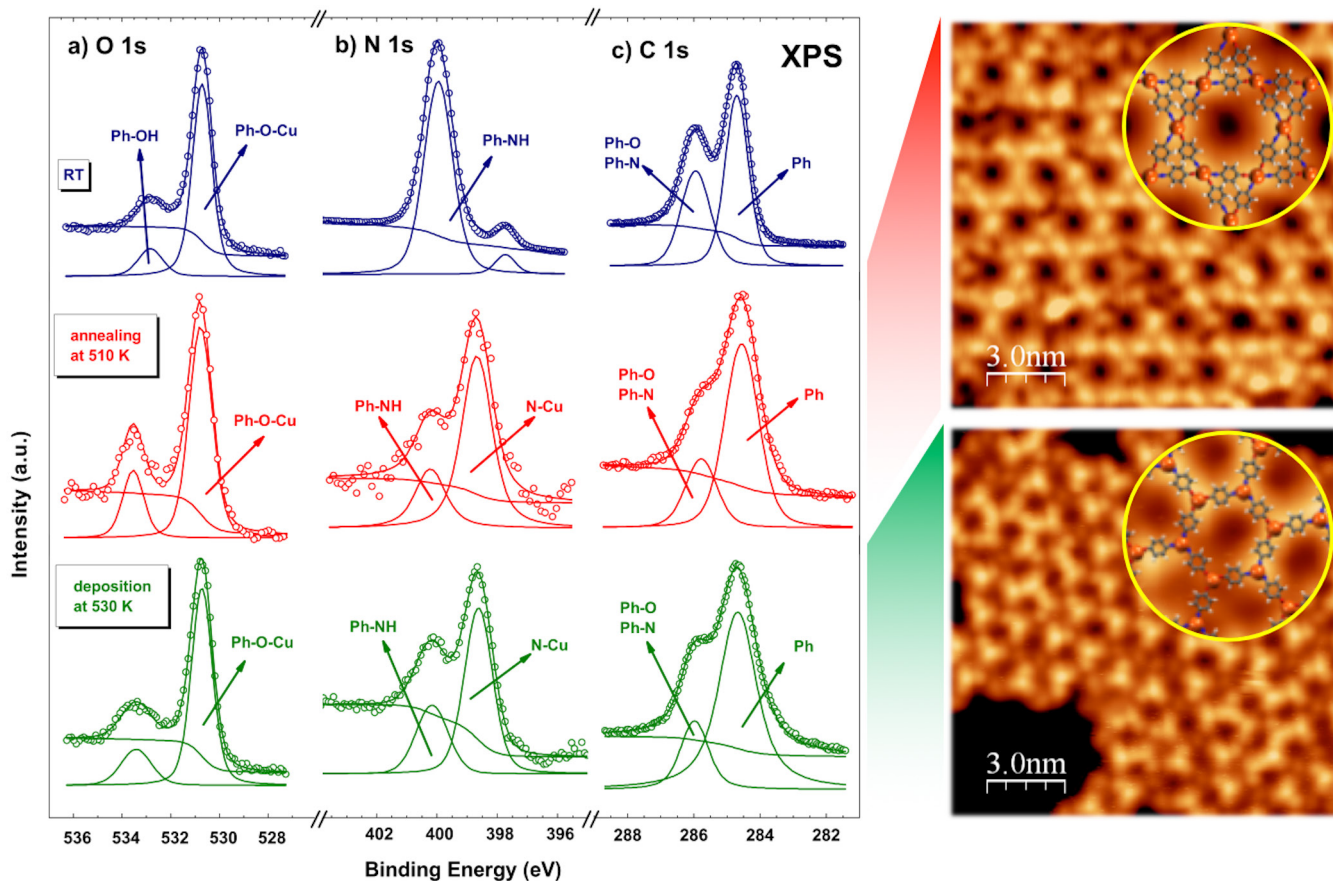


Figure 1. Left: a) O1s, b) N1s and c) C1s XPS spectra of p-AP deposited on Cu(111) at RT (blue), after subsequent annealing at 510K (red) and for direct deposition at 530 K (green). Right: STM images of p-AP on Cu(111) for molecular deposition at RT followed by postgrowth annealing at ~ 500 K ($V_{\text{bias}} = 1$ V, $I_t = 28$ pA) (upper panel) and for molecular deposition on the substrate at ~ 500 K ($V_{\text{bias}} = 0.9$ V, $I_t = 0.13$ nA) (bottom panel). Insets: pictorial top view of the optimized on-surface network structures.

Acknowledgments

This work was supported by the project CALIPSOplus under Grant Agreement 730872 from the EU Framework Programme for Research and Innovation HORIZON 2020, FotoArt-CM (S2018/NMT-4367) and FotoSurf-CM (Y2020/NMT-6469) projects funded by the "Comunidad de Madrid" and co-financed by European Structural Funds, grants PID2020-113142RB-C21, funded by MCIN/AEI/10.13039/501100011033, and PLEC2021-007906 and TED2021-129999B-C31, funded by MCIN/AEI/10.13039/501100011033 and the "European Union NextGenerationEU/PRTR".

Original paper

N. Ruiz del Arbol *et al.*, Chem. Commun. **59**, 2954 (2023); DOI: 10.1039/D3CC00185G

N. Ruiz del Árbol¹, C. Sánchez-Sánchez¹, J. I. Martínez¹, L. Rodríguez¹, D. Serrate^{2,3}, A. Verdini⁴, L. Floreano⁴, P. Jacobson⁵, L. Grill⁵, J. A. Martín-Gago¹, M. F. López¹

- ¹ Instituto de Ciencia de Materiales de Madrid (ICMM), CSIC, Madrid, Spain
- ² Instituto de Nanociencia y Materiales de Aragón (INMA), CSIC-UNIZAR, Zaragoza, Spain
- ³ Laboratorio de Microscopías Avanzadas (LMA), Universidad de Zaragoza, Zaragoza, Spain
- ⁴ CNR-IOM, Laboratorio TASC, Trieste, Italy
- ⁵ Department of Physical Chemistry, University of Graz, Graz, Austria

e-mail: mflopez@icmm.csic.es

Effects of visible light illumination on Photostrictive/Magnetostrictive PMN-PT/Ni Heterostructure

Elettra | APE-HE, Sprint

In recent years, multiferroic heterostructures have gained attention for spintronic applications thanks to the interfacial coupling between ferroelectric and ferromagnetic components. The most exploited interfacial mechanisms are charge, strain, exchange-bias and chemistry-mediated effects, while the possible range of stimuli still needs to be fully investigated. Among them, optical modifications via bulk photovoltaic and photostrictive effects (light-matter interactions resulting in non-thermal shape deformations) are rarely studied. In this study, by combining electrical, structural, magnetic, and spectroscopic characterizations, we show how light illumination modifies significantly the properties of ferroelectric $\text{Pb}(\text{Mg}_{1/3}\text{Nb}_{2/3})\text{O}_3$ - 0.4PbTiO_3 (PMN-PT) substrate, and experimentally prove how these changes affect the magnetic properties of the interfacial magnetostrictive Ni layer. In order to induce bulk photovoltaic effects on ferroelectric substrates, the photon energy of the light illumination impinging on them has to be larger than the energy band gap. By tuning the wavelengths illumination (ranging from 360 to 660 nm) at the Sprint laboratory on the front side of the sample and measuring the resulting photocurrent, it appeared that maximum of photocurrent was found at 412 nm, i.e. 3.01 eV, with a detectable signal in a range from 2.61 to 3.35 eV, consistent with literature (Fig. 1 (a)). In the following, all laser illuminations were done with a continuous 405 nm laser of tunable power, up to 800 mW cm^{-1} . The magnetic properties of pristine PMN-PT/Ni heterostructure were analyzed by MOKE (Magneto-Optic Kerr Effect), both without and with laser illumination of variable intensity. The effects of light illumination for the case of magnetic field $H // [010]$ is shown in Fig. 1 (b). A large coercive field H_c reduction was detected under illumination, up to 45% under light illumination of 800 mW cm^{-2} , while the changes in magnetic remanence were negligible. These magnetic changes are

fully reversible and reproducible, with the magnetic signal fully restored after switching the laser off. After MOKE characterization, XMCD (X-ray Magnetic Circular Dichroism) measurements were carried out at APE-HE beamline. The XMCD spectra at Ni $L_{2,3}$ edges in absence and presence of laser light illumination are shown in Fig. 1(c). The spectra shows a detectable variation of the L_3 edge XMCD intensity upon illumination, passing from $(7.1 \pm 0.1)\%$ with no light to $(7.9 \pm 0.1)\%$ under illumination, while the dichroic signal at L_2 edge does not change (Fig. 1 (c)). This is a signature of a modification of Ni orbital moment induced by PMN-PT photostriction under illumination. By applying sum rules, we derived the spin (m_{spin}) and orbital (m_{orb}) magnetic moments of Ni for both cases. It results that the ratio m_{orb}/m_{spin} was found to be 0.0940 with no light and 0.1149 under illumination. The change of this ratio is a direct experimental proof of the lattice parameter modifications induced at the interface by PMN-PT photostriction when under illumination. The large magnetostrictive coefficient of Ni results ideal in maximizing this effect, with an induced modification of its coercive field. This is to our knowledge the first reported spectroscopic evidence of this interfacial coupling in multiferroic heterostructures. PMN-PT/Ni was electrically polarized out of plane to determine if the presence of a net ferroelectric polarization in PMN-PT would influence the interfacial photostrictive/magnetostrictive coupling. Photocurrent measurements were taken to evaluate the effects of illumination on the three polarization states (Pristine, P_{up} and P_{down}). The resulting curves are shown in Fig. 1(d). In the pristine case, as the light was turned on, an increase in sample current due to bulk photovoltaic effect was observed, with a value of around 0.7 nA. Once turned off the laser, the initial state was sharply restored. On the other hand, slow dynamics with opposite trends were measured in polarized state. As the light was switched on, a photocurrent

peak of opposite sign (positive for P_{down} , negative for P_{up}) appeared, exponentially decaying toward a steady value comparable to the pristine one. Once switched off the illumination, a similar transient effect, but opposite in sign, was observed for both cases, with a relaxation time quite comparable to that under illumination. These transient effects are signature of the presence of a net electric dipole after sample polarization. The steady intensity of the photocurrent under illumination remains almost identical in the three cases; this is important because it means that the amount of bulk photovoltaic effect is unmodified after polarization. Once polarized, the PMN-PT photostrictive effects on interfacial magnetostrictive Ni were verified by combining MOKE and XMCD characterizations, as it was for the pristine case. Here, the observed effects are found to be strongly reduced, with negligible changes under light. We attribute such difference between polarized and pristine PMN-PT states to its structural properties. After polarization, its ferroelectric domain population is mostly out-of-plane oriented, while the in-plane component observed in the pristine case is almost not present anymore. The detected magnetostrictive changes for the pristine case indicate that the in-plane domains play a dominant role in the photostrictive/magnetostrictive coupling. This stimulates further investigations aimed to maximize the interfacial effect.

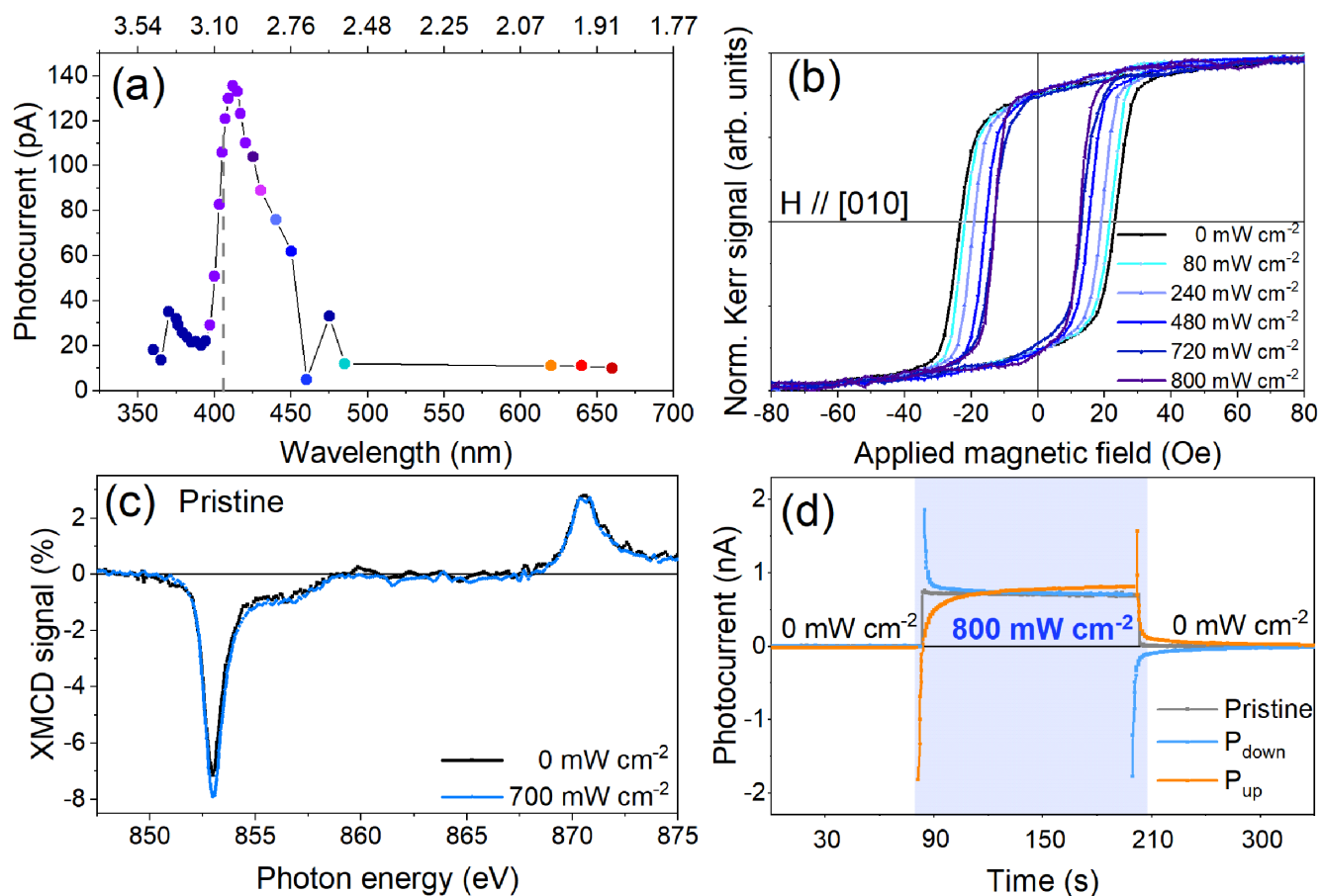


Figure 1. (a) Measured photocurrent as the function of wavelength and corresponding photon energies produced by OPA. The light fluence was kept constant at all wavelengths at 480 mW cm⁻². Vertical dashed line corresponds the photocurrent at 405 nm wavelength, i.e., the photon energy used for continuous illumination. (b) Hysteresis loops measured with the magnetic field applied along the PMN-PT (010) axis under light illumination of variable power (0–800 mW cm⁻²); (c) XMCD dichroic signal at Ni L_{2,3} edges in case of pristine PMN-PT/Ni, in absence and presence of light, applying the magnetic field along (010); (d) Photocurrent evolution of the PMN-PT/Ni heterostructure as a function of time for three different polarization states (Pristine, P_{down} and P_{up}) under 1 V bias. Reproduced with permission under a Creative Commons Attribution-NonCommercial 4.0 International Public License CC BY-NC 4.0 © 2022 The Authors. *Advanced Materials Interfaces* published by Wiley-VCH GmbH

Acknowledgments

This work was performed in the framework of the Nanoscience Foundry and Fine Analysis (NFFA-MUR Italy Progetti Internazionali) project (www.trieste.NFFA.eu).

Original paper

D. Dagur *et al.*, *Adv. Mater. Interfaces*, **9**, 2201337 (2022); DOI: 10.1002/admi.202201337

D. Dagur^{1,2}, V. Polewzyk¹, A. Yu Petrov¹, P. Carrara^{1,3}, M. Brioschi^{1,3}, S. Fiori¹, R. Cucini¹, G. Rossi^{1,3}, G. Panaccione¹, P. Torelli¹, G. Vinai¹

¹ IOM-CNR, Trieste, Italy

² Physics Department, University of Trieste, Trieste, Italy

³ Physics Department, University of Milan, Milan, Italy

e-mail: piero.torelli@elettra.eu

Uncovering the evolution of h-BN-Graphene Heterostructure in oxygen-rich environment

Elettra | BACH, Nanospectroscopy

The interaction between atomically thin 2D materials and molecules abundant in the atmosphere such as oxygen is a crucial focus for a large area of research in materials science. These 2D materials possess a large specific surface area, which is beneficial for their applications including catalysts and sensors. However, their chemical stability under ambient conditions can significantly impact the performance of devices based on these materials. Oxygen adsorption may fundamentally alter the 2D material properties through processes such as oxidation, intercalation, and etching with a profound effect on their applications. Additionally, oxygen plays a crucial role in numerous catalytic reactions.

Of particular interest are lateral heterostructures and their environmental stability. This unique class of materials involves the combination of structurally similar 2D materials, providing an opportunity to simultaneously study the behavior of diverse materials within a single system. One of these is the graphene (Gr)-hexagonal boron nitride (h-BN) heterostructure (h-BNG). Both graphene and h-BN consist of a single layer of atoms arranged in a honeycomb pattern and possess excellent mechanical strength. The h-BNG heterostructure not only combines the distinct electronic properties of conductive Gr and insulating h-BN, but also offers additional catalytically-active sites for the oxygen reduction reaction at the interface between h-BN and Gr.

To assess the stability of the h-BNG heterostructure against oxygen we employed a surface science approach based on synchrotron radiation-based spectroscopy and imaging techniques at the BACH and Nanospectroscopy beamlines of Elettra, respectively. We grow an h-BNG heterostructure single-layer on a well-defined platinum surface, starting from a single molecular precursor, dimethylamine borane (DMAB), and we monitor its evolution

after oxygen exposure using the chemical sensitivity of high-resolution photoemission spectroscopy at the BACH beamline as seen in Figs. 1 a,b.

We find that oxygen molecules can indeed undergo dissociation on in-plane h-BNG structures. Since a large energy barrier would have to be overtaken for O₂ molecules to dissociate on Gr and h-BN, this finding provides experimental support for the existence of catalytically active sites at the boundaries between h-BN and Gr, which contribute to the oxygen reduction reaction. Our experimental finding verifies the theoretical prediction that boundaries between h-BN and Gr domains are highly reactive towards dissociative adsorption of oxygen molecules.

Our results further reveal a more complex relationship/competition between oxygen dissociation, intercalation, and etching processes. Specifically, we find that under well-defined conditions oxygen can intercalate selectively beneath the h-BN layer within the h-BN-Gr lateral heterostructures. Furthermore, we identified that at certain temperature, oxygen exhibited selective etching behavior, primarily targeting the graphene (Gr) component. Instead, the h-BN component of the heterostructure displayed significantly higher stability against oxygen etching in comparison to graphene, indicating a better suitability for coating applications.

Based on this selective etching of graphene we devised a way to engineer the ratios and sizes of h-BN and Gr domains within the h-BNG/Pt system. By employing a series of subsequent cycles involving oxygen etching of Gr followed by the regrowth of h-BNG on the etched graphene patches, we were able to prepare h-BNG layers with controlled and incrementally increasing h-BN/Gr composition. This method offers promising potential for the development of atomically thin

layers suitable for electronic device applications. Advanced imaging methods at the Nanospectroscopy beamline, summarized in Figs. 1 (c-e), reveal that, following multiple etching and regrowth cycles, the resulting layer predominantly consists of h-BN with isolated graphene islands underneath. The presence of bilayer islands signifies a confined growth process within this sample and that in-plane h-BNG can be structurally transformed to islands of graphene covered by a h-BN monolayer.

In addition to our previous findings, we also find out that an oxidized h-BN layer can be generated through the same straightforward etching/regrowth route. The formation of B-O bonds, which occurs at temperatures as low as 100°C within this system, is of great interest in catalysis. Borates, formed through the B-O bonds, can covalently bind to Gr and act as intermediates in the O=O breaking step during the reduction process of O₂, ultimately producing H₂O. It is worth noting that B-O bonds can also be eliminated through vacuum annealing at temperatures equal to or exceeding 730 °C in the presence of the same molecular precursor used for h-BNG growth.

In conclusion, our study provides valuable insight into the intricate interplay between intercalation, etching, and selectivity within the h-BNG/Pt(1 1 1) system under an oxygen-rich environment. Our findings demonstrate the potential for engineering the composition and properties of h-BNG layers using a single precursor through a simple and effective approach.

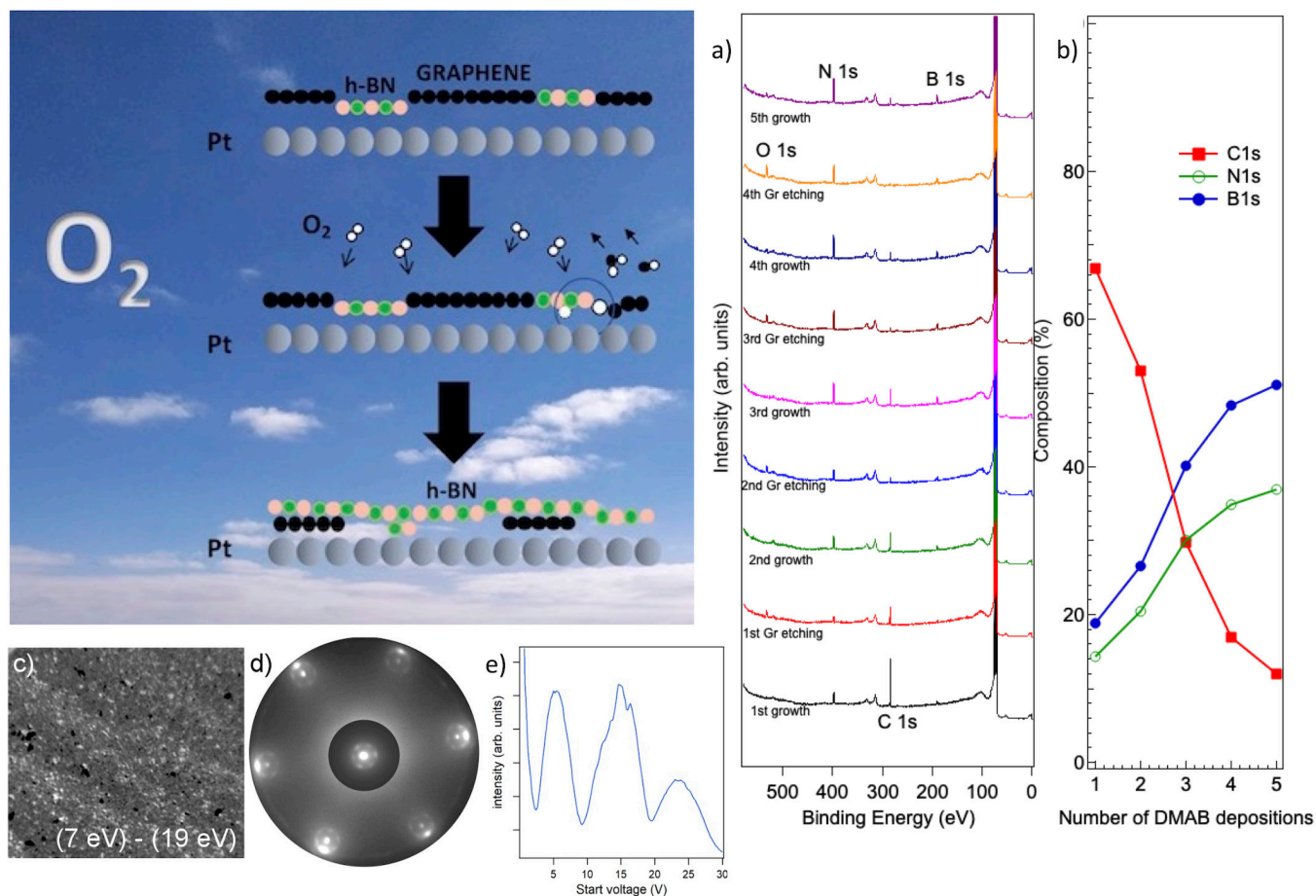


Figure 1. (Top left) Schematic model illustrating the interaction of oxygen with h-BNG/Pt(111) as described in the text. a) XPS data collected after subsequent and repeated growth-etching cycles. The XPS spectra (a) were collected from h-BNG/Pt(111) layers (first growth), after etching of graphene domains, after subsequent exposure of the etched layer to the molecular precursor at 730°C (second growth) and subsequent etching-growth cycles. (b) Relative concentration of carbon, boron, and nitrogen in the grown layers, derived from the total area of corresponding peaks, normalized to their respective photoionization cross sections. (c) Difference between two LEEM images acquired at 19 eV and 7 eV of the final layer obtained after the growth/etching/regrowth cycles. Bright islands of 50–300 nm appear in the differential (area coverage of 20%) (d) LEED pattern of the same layer, with the central part displayed using a different grayscale for better visualization. (e) LEEM IV from the bright islands in the LEEM images after partially subtracting the IV curve from the surrounding regions. This LEEM IV lineshape is characteristic for h-BN/Gr bilayer. Reproduced with permission (licence n. 5582490608650). Copyright 2022, Elsevier.

Acknowledgments

We acknowledge support from MUR (Eurofel project, FOE progetti internazionali) and technical support from Federico Salvador.

Original paper

E. Magnano *et al.*, Applied Surface Science **604**, (154584); DOI: 10.1016/j.apsusc.2022.154584

E. Magnano^{1,2}, S. Nappini¹, I. Piš¹, T.O. Mentes³, F. Genuzio³, A. Locatelli³, F. Bondino¹

¹ IOM-CNR, Trieste, Italy

² Department of Physics, University of Johannesburg, South Africa

³ Elettra - Sincrotrone Trieste S.C.p.A., Trieste, Italy

e-mail: bondino@iom.cnr.it

Moving the Dirac cones of BaNiS₂ by Surface Charge Doping

Elettra | BaDEIPh

In the field of condensed matter physics, the quest for systems with unique electronic properties has driven scientists to explore the fascinating world of Dirac materials, which host Dirac cones - electron bands with linear dispersion - in their band structure. Dirac semimetals, characterized by the presence of Dirac cones in the proximity of the Fermi level, possess remarkable properties such as high carrier mobility and robustness against disorder, making them promising candidates for future electronic devices. However, manipulating and controlling Dirac states in reciprocal space have proven to be challenging due to constraints imposed by crystal symmetry.

Traditionally, manipulating Dirac cones required intricate modifications to the crystal structure or external parameters, limiting the feasibility for practical applications. However, recent discoveries demonstrated the existence of materials with unpinned Dirac cones, allowing for more accessible control of these intriguing electronic states. Materials such as ZrSnTe, Sb, transition-metal dichalcogenides, and layered compounds like ZrSiS and BaNiS₂ have revealed unpinned Dirac cones, providing a fertile ground for exploration and manipulation.

Among these materials, BaNiS₂, a prototype of correlated Dirac semimetal, is attracting considerable attention. Its Dirac states positioned along the Γ -M symmetry line are controlled by the p-d hybridization and by the charge transfer gap. Therefore, BaNiS₂ represents a unique platform to investigate the behavior of Dirac states and explore methods for their control. Previous experiments performed at Elettra demonstrated that in BaCo_{1-x}Ni_xS₂ Dirac cones can be moved along the symmetry line by partially substituting Ni with Co.

In this work, we adopted an alternative approach to manipulate the Dirac states of BaNiS₂ by using surface doping with alkali metal. The adsorbed

atoms donate valence electrons to the substrate, and thus influence the carrier concentration and band structure of the underlying material - in our case BaNiS₂. We employed a combination of ARPES (Angle-Resolved Photoemission Spectroscopy) and first-principles calculations to investigate the effects of surface doping on the electronic structure and in particular on the Dirac cones.

Fig. 1(a-c) illustrate the evolution of the band structure of BaNiS₂ measured by ARPES after each K evaporation step using a photon energy of 25 eV. We observe two clear trends: (i) a downward shift in energy of all electronic bands, as expected in the case of electron transfer from an adsorbed alkali metal atom; (ii) a systematic shift in k-position of the Dirac cone toward Γ with increasing alkali-metal coverage (or electron doping). This shift is evident by comparing the position of the Dirac node, determined by extrapolating the linear dispersion of the Dirac bands.

In order to account for the above experimental results, we model the doped surface layer as a parallel plate capacitor (see Fig. 1e), where the top and bottom plates are respectively the layer of the positively charged K⁺ ions on the surface and the negatively charged layer of Ni atoms near the surface, i.e. the acceptor of the electrons donated by the K atoms. The top Ba and S layers of the BaNiS₂ unit cell lie between these two charged layers, while the bottom Ba and S layers, located below the Ni layer, are unaffected by the transverse electric field created by the charged layers and thus behave as in the bulk of the sample. The above field causes a drop of the effective Kohn-Sham potential probed by the electrons; the on-site energy of the p orbitals of the surface S atoms drops accordingly, thus increasing the charge transfer gap and shifting the Dirac point toward Γ . Our *ab initio* calculations on the above capacitor-like model successfully reproduce the experimental observations and support the above

intuitive considerations. This is seen in Fig. 1f, where we show the evolution of the calculated band structure and the position of the Dirac node as a function of electron doping. In Fig. 1g, we plot the increase of the charge transfer gap with increasing electron content, which explains the shift of the Dirac cone toward Γ . The average of the on-site p and d orbital energies are presented in Fig. 1h. S_{surf} indicates the S atoms at the surface, located between the charged planes; S_{bulk} are the S atoms in the bulk region, unaffected by the electrostatic field. The corresponding averages on the orbital energies show that the main contribution to the increase of the charge transfer gap is the decrease of the S_{surf} p orbital energy.

Our study of BaNiS₂, combined with surface doping using alkali-metal atoms, has demonstrated the potential to shift and modulate Dirac states, offering a pathway towards the design of novel materials with tailored electronic properties. These findings not only contribute to our understanding of topological materials but also open up new possibilities for their utilization in future electronic devices. Furthermore, this approach can be extended to predict and tailor the topological properties of various materials by introducing extra charges into specific atomic layers of nanostructures, surfaces, interfaces, and heterostructures. Overall, it represents another step towards the engineering of topological materials and their diverse applications in the fields of electronics, spintronics, and quantum computing.

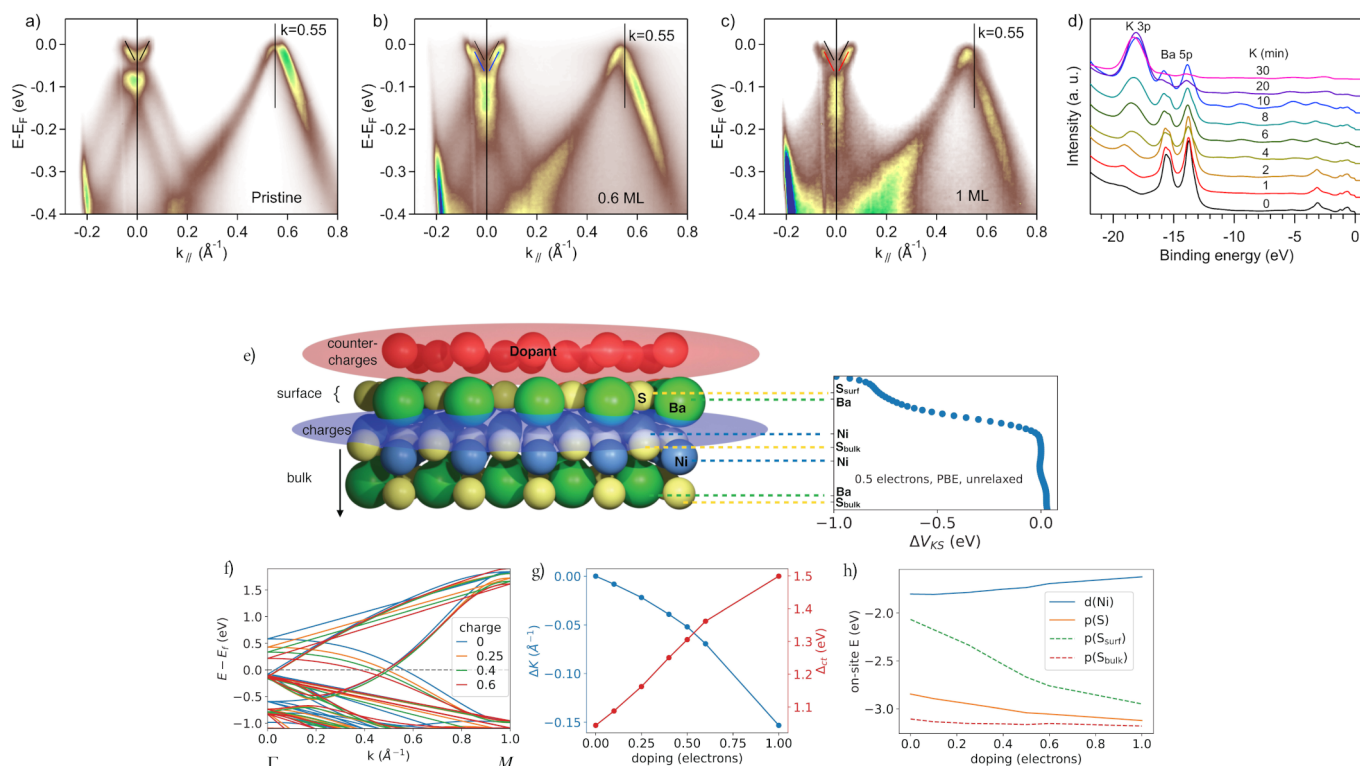


Figure 1. ARPES spectra (25 eV photon energy) for the evolution of the band structure of BaNiS₂ with surface K dosing: (a) pristine surface and after deposition of 0.6 (b) and 1 (c) K monolayer. (d) Evolution of the core levels of BaNiS₂ with surface K dosing (data taken using 31 eV photon energy). All the data were taken at about 100 K. (e) Schematic illustration of the electrostatic effect produced by the K atoms adsorbed on the surface of BaNiS₂ and on the depth profile of the Kohn-Sham potential. (f) Variations of the Wannier band structure as a function of electron doping. (g) Variations in the position of the Dirac cone as well as the charge transfer as a function of doping, as extracted from the Wannier bands. (h) Variations in the on-site energy of Wannier functions associated with Ni and S orbitals, with respect to the Fermi energy. The S p orbitals are decomposed into those of the S atoms at the surface, close to the dopant K atoms, and of the S atoms in the bulk. Adapted from Nano Lett. 2023, 23, 5, 1830-1835 Copyright © 2023 American Chemical Society.

Acknowledgments

We acknowledge Elettra Sincrotrone Trieste for providing access to its synchrotron radiation facilities and we thank Giovanni Di Santo and Luca Sancin for assistance in using beamline BaDElPh. The research leading to this result has been supported by the Grant Agreement 20195527 and 20205499. The work of M.M., L.P., and E.P. was supported by "Investissement d'avenir Labex Palm" (Grant No. ANR-10-LABX-0039-PALM) and by the ANR "Iridoti" (Grant ANR-13-IS04-0001). J.Z. thanks the China Scholarship Council (CSC) for financial support.

Original paper

J. Zhang, *et al.*, Nano Lett., 23, 5(1830); DOI: 10.1021/acs.nanolett.2c04701

J. Zhang¹, T. D. P. Sohler², M. Casula³, Z. Chen¹, J. Caillaux¹, E. Papalazarou¹, L. Perfetti⁴, L. Petaccia⁵, A. Bendounan⁶, A. Taleb-Ibrahimi⁶, D. Santos-Cottin⁷, Y. Klein³, A. Gauzzi³, and M. Marsi¹

¹ Université Paris-Saclay, CNRS, Laboratoire de Physique des Solides, Orsay, France

² Laboratoire Charles Coulomb (L2C), Université de Montpellier, CNRS, Montpellier, France

³ IMPMC, Sorbonne Université, CNRS, IRD, MNHN, Paris, France

⁴ Laboratoire des Solides Irradiés, Ecole Polytechnique, CNRS-UMR 7642, CEA, Palaiseau, France

⁵ Elettra - Sincrotrone Trieste S.C.p.A., Trieste, Italy

⁶ Synchrotron SOLEIL, Gif-sur-Yvette Cedex, France

⁷ Department of Physics, University of Fribourg, Fribourg, Switzerland

e-mail: marino.marsi@universite-paris-saclay.fr

2D ferrimagnetism in quasifreestanding graphene

Elettra | BaDEI Ph

Controlling the spin structure in graphene is one of the most important problems of material science today. To use graphene in spintronics, especially for the realization of dissipation-free transport, it is necessary to be able to control the spin splitting of its electronic states and the topologically nontrivial band gap at the Dirac point. In this context, theoretical and experimental studies of possible magnetic order in 2D carbon systems, such as superatomic graphene, twisted bilayer graphene, triangulene, nanographenes, etc., have attracted particular attention. The experimentally unrealized Haldane model, based on a graphene lattice with inhomogeneous distribution of magnetic field on atomic scale, remains relevant and attractive because it predicts the QAHE (Quantum Anomalous Hall effect) in a honeycomb lattice.

The magnetic proximity effect is a promising way to implement the exchange splitting of electronic states without applying an external magnetic field, which can also be used to implement the QAHE, provided that the topological nontriviality of electronic states is preserved. Previously, it was theoretically shown that the contact of graphene with antiferromagnetic oxide can lead to the QAHE or the quantum valley Hall effect, depending on the direction of magnetization.

In this work, we address the long-standing problem of giant spin-orbit and exchange splittings in graphene, associated with the necessity of their explanation on the basis of spin-ARPES (spin and Angle-Resolved Photoemission Spectroscopy) measurements and DFT (Density Functional Theory) calculations of large-scale structures, including misfit dislocations, for a correct description of graphene magnetization and an explanation of the experimental data. The reason for discrepancy between theoretical and experimental results reported earlier may be structural differences in the synthesized and model systems and the additional effect

of phonon oscillations on the spin-orbit coupling in graphene.

Figure 1a shows the LEED (Low Energy Electron Diffraction) pattern of epitaxial $\sim(9\times 9)$ graphene superlattice formed on the Au/Co(0001)/W(110) interface. It is well known that a Au monolayer forms an alloy with Co with the formation of dislocation loops. These defects are periodic over rather large areas of the sample (see Fig. 1 (b)). In Figures 1 (c,d) we plot the ARPES intensity maps in the ΓK direction of the surface Brillouin zone measured at the BaDEI Ph beamline of Elettra. The band gap opening (E_g) of about 80 meV is connected with the sublattice ferrimagnetism in quasi-freestanding graphene according to our DFT (Fig. 2) and tight-binding calculation results. It was shown that due to the formation of dislocation loops in the Au monolayer under graphene the exchange interaction is transferred to graphene and can be described by the Hamiltonian term in the mean-field Hubbard form. Dislocation loops are self-organized periodic structural defects that induce ferrimagnetic ordering in graphene with a uniform distribution of atomic magnetic moments on each of the graphene sublattices, as shown in Fig. 2 (a). The ferrimagnetic order on graphene sublattices is very stable with respect to the formation of dislocation loops of various sizes under graphene. In general, dislocation loops with displaced gold atoms deep into the cobalt layer lead to ferrimagnetic magnetization on the gold monolayer, which becomes more uniform on the graphene sublattices. Band structure calculations for the relaxed unit cell reveal the formation of the band gap E_g at the Dirac point (Fig. 2 (d)). Moreover, the calculated spin splitting asymmetry near K and K' agrees with the measured spin-ARPES data. Notably, DFT calculation of the (9×9) unit cell, but without dislocation loop, revealed the suppression of sublattice ferrimagnetism and decreasing the corresponding band gap that also confirms its magnetic nature.

Using the tight-binding Hamiltonian, Berry curvatures and Chern numbers were calculated for in-plane magnetization to analyze the implementation of Hall effects. In spite of the Chern numbers being zero, the Berry curvatures for π bands share the dipolar structure and have opposite signs for K and K' valleys. The calculation of the Hall conductivity, taking into account the probability of optical transitions, showed the presence of a robust Hall effect using circular polarized light. This phenomenon is associated with the presence of a dipole structure of Berry curvatures near the K(K') points and nonequal spin-up and spin-down photoexcitation rates in these regions.

Only in-plane magnetized system was experimentally studied, although it is topologically trivial, its Berry curvature dipoles may render it interesting and promising research object from both theoretical and experimental points of view. The out-of-plane magnetization allows nontrivial band topology in ferrimagnetic case, but the anomalous Hall conductance may perfectly quantize in the regime with dominant ferromagnetism only since the nontrivial situation with dominant antiferromagnetism is characterized by a zero global gap. The creation of such out-of-plane magnetized systems remains, of course, an important problem in the context of experimental realization of QAHE in graphene.

Today, the synthesized system is an undeniable candidate for further measurements of the circular dichroism Hall effect that was predicted for topological insulators in 2018 and for antiferromagnetic superatomic graphene in 2021. The new electro-optic effect generates transverse Hall currents of opposite directions for the left- and right-handed circularly polarized light and can be realized by laser-assisted technique.

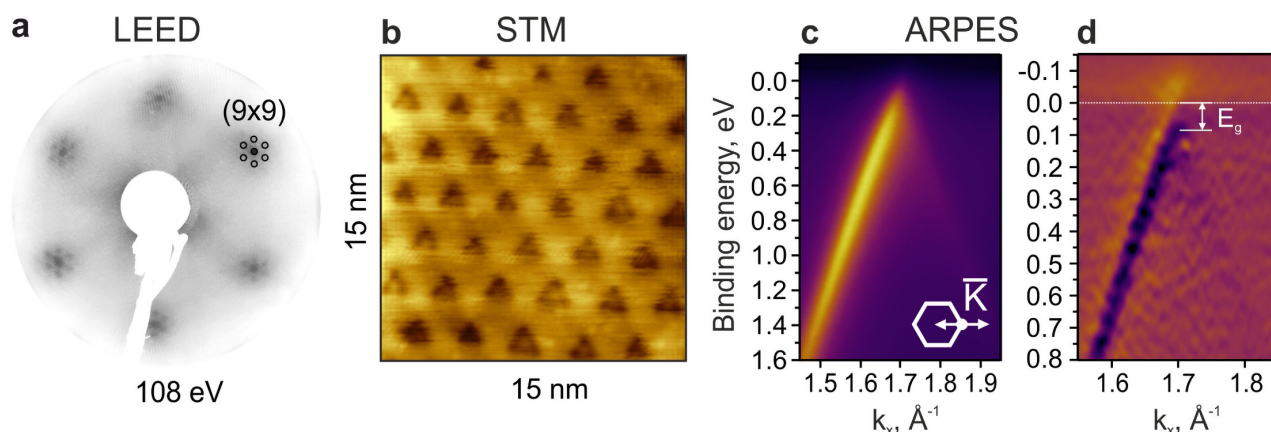


Figure 1. (a) LEED pattern of the epitaxial $\sim(9 \times 9)$ graphene superlattice formed on the Au/Co(0001) interface; (b) STM image of dislocation loops under graphene; (c) ARPES intensity map for the π band, including the second derivative with respect to energy of the enlarged map in (d). The band gap E_g of about 80 meV is also indicated.

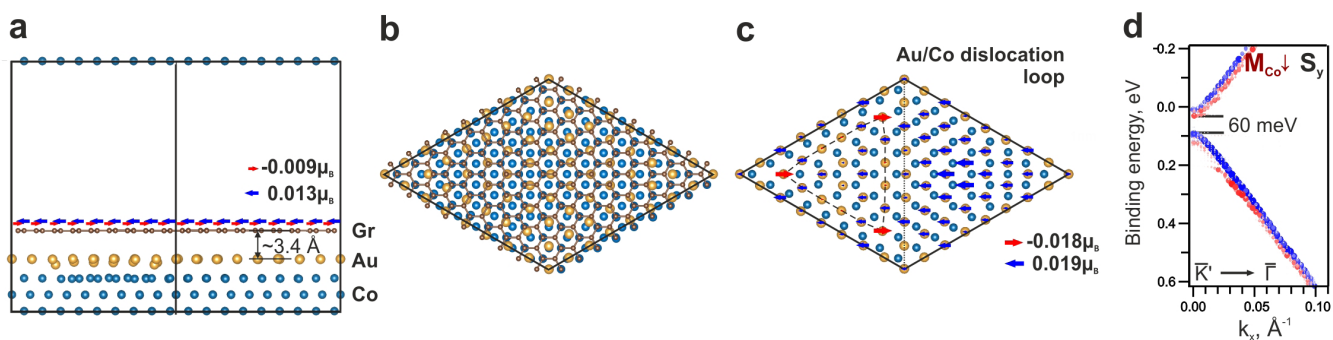


Figure 2. Unit cell of Gr/Au/Co structure with dislocation loop: (a) side view, (b) top view from the vacuum region and (c) top view of Au-Co dislocation loop under graphene. The dislocation loop is marked by a dotted line in (c). Arrow's sizes are proportional to atomic magnetic moment values on gold and carbon atoms. The arrows indicating the maximum magnetic moments in two opposite directions for graphene and Au-Co dislocation loop are included in the legends. The direction of Co layer magnetization points to the right. (d) The unfolded (9×9) band structure of the Gr/Au/Co around the K' point. The symbol size and color represent the Bloch spectral weight for S_y spin component.

Acknowledgments

A.G.R., A.A.R., D.Yu.U., A.A.G., I.I.K. and A.M.S. acknowledge St. Petersburg State University (SPbU) for Research Grant No. 94031444. This work was supported by Russian Science Foundation Grants (No. 20-72-00031 in the part of ab initio calculations and No. 18-12-00062 in the part of synthesis and ARPES measurements with the use of synchrotron radiation), RFBR project No. 20-32-70127 (in the part of ARPES/spin-ARPES measurements with the use of laboratory sources, analysis of experimental data) and the Russian German Laboratory at BESSY II. A.V.T. acknowledge the support by the German-Russian Interdisciplinary Science Center (G-RISC) funded by the German Federal Foreign Office via the German Academic Exchange Service (DAAD). We thank Elettra - Sincrotrone Trieste for providing access to its synchrotron radiation facilities.

Original paper

A.G. Rybkin *et al.*, Phys. Rev. Lett. **129**, 226401 (2022); DOI: 10.1103/PhysRevLett.129.226401

A.G. Rybkin¹, A.V. Tarasov¹, A.A. Rybkina¹, D.Yu. Usachov¹, A.E. Petukhov¹, A.V. Eryzhenkov¹, D.A. Pudikov¹, A. A. Gogina¹, I.I. Klimovskikh^{1,2}, G. Di Santo³, L. Petaccia³, A. Varykhalov⁴, A.M. Shikin¹

¹ St. Petersburg State University, St. Petersburg, Russia

² Center for Advanced Mesoscience and Nanotechnology, Moscow Institute of Physics and Technology, Dolgoprudny, Russia

³ Elettra - Sincrotrone Trieste S.C.p.A., Trieste, Italy

⁴ Helmholtz-Zentrum Berlin für Materialien und Energie, Elektronenspeicherring BESSY II, Berlin, Germany

e-mail: artem.rybkin@spbu.ru

Understanding carbide evolution and surface chemistry during deep cryogenic treatment in high-alloyed ferrous alloy

Elettra | ESCA Microscopy

Cryogenic treatment is a type of heat treatment under which the material is subjected to extreme cooling in order to change the microstructure of the material and improve its final properties, such as hardness, corrosion resistance, wear resistance etc. is a type of treatment under which materials are exposed to temperatures below 123 K (usually liquid nitrogen or liquid helium temperature), inducing changes in the microstructure and properties of the material. Much remains to be learned about the mechanisms of DCT (Deep Cryogenic Treatment), particularly in regards to surface modification and the changes of surface chemistry and surface properties, which is considered as the primary origin of the improved corrosion and wear resistance of treated materials. In this study, the investigation of the effect of DCT on a HAFA (High-Alloyed Ferrous Alloy) and its effectiveness on carbide formation and chemical shifts of alloying elements was carried out using both *ex-situ* and *operando* (performed at cryogenic temperatures) SPEM (Scanning Photoelectron Microscopy) to investigate the chemical changes induced by DCT. Microstructural analysis and local chemical probing were conducted with SEM (Scanning Electron Microscopy), EDS (Energy Dispersive X-ray Spectroscopy), APT (Atomic Probe Tomography) and SANS (Small-Angle Neutron Scattering). The results determined that the main phases in the material are martensite, $M_{23}C_6$ (has Cr-rich shell, but lower-alloyed inner centre of Cr, V and Mo, where M represents alloying element(s) and C stands for carbon) and M_7C_3 (enriched with Mo, where M represents molybdenum and C stands for carbon) carbides. The evolution and behaviour of selected alloying elements during the nucleation of carbides formed during the different heat treatment routes was studied using *ex-situ* SPEM: Conventional Heat Treatment (CHT) with samples austenitized at $T_a = 1323$ K for 2 min, quenched in nitrogen gas and triple

annealed at $T_t = 873$ K for 2 h and DCT samples austenitized at $T_a = 1323$ K for 2 min, quenched in nitrogen gas, exposed to liquid nitrogen temperatures at $T = 77$ K for 24 h and finally annealed at $T_t = 873$ K for 2 h.

Altogether, the SPEM maps (Fig. 1 a-b) show the distinct segregation of two additional type of carbides MC and M_6C by their V and W content. Furthermore, the micro-spectroscopic C 1s analysis (Fig. 1 c-d) of carbides present in CHT or DCT shows a difference in the C binding state, the C 1s spectrum is shifted towards lower BE (~ 283 eV) in MC type carbides compared to M_6C (~ 284 eV BE). This correlates with the highly C enriched state of MC carbides. In M_6C carbides, C is located within the octahedral interstitials, which are less tightly bound to metal atoms due to its high ligancy. As a result, the C 1s chemical shift is similar to the shift within the matrix. In addition, the double peak character of C 1s confirms the core-shell structure of MC carbides. SPEM also identified the different evolution pathways of $M_{23}C_6$ carbides with CHT and DCT, indicating higher alloying and larger size in the CHT sample compared to the DCT one (Fig. 1 a -b). Analysis of the core level spectra confirms that $M_{23}C_6$ carbides evolve towards the M_6C composition with the slight presence of Mo, W and V. Comparison of the two heat treatments (CHT and DCT) shows that the V content of CHT carbides is higher than that of DCT carbides. In addition, CHT $M_{23}C_6$ carbides do not show this trend, but have higher Cr and C contents, whereas DCT induces higher Mo contents in $M_{23}C_6$ (Fig. 1 c-d). The underlying mechanism of C redistribution and changes in the chemical state of the alloying elements was revealed by *in-situ* SPEM at cryogenic temperatures. The results indicate that C is redistributed towards the vicinity of pre-existing carbides and defects, which does not affect the bonding states of C during DCT cooling, but only after the material is heated once more through tempering.

In addition, a change in the bonding state of Mo is recorded, which shows a slight shift of 0.1 - 0.2 eV during the DCT. Around the smaller previous M_6C carbides the observed phenomenon is particularly visible. A line scan of the Mo spectra over selected carbides and the surrounding matrix before and after DCT confirms that the chemical shift changes are caused by the matrix and not by the carbides themselves. The shift returned to a binding state similar to the pre-DCT state after heating to 873 K. This indicates a metastable transition state of Mo with DCT, which is relaxed by applying thermal energy that causes precipitation and growth of carbides. The non-uniform oxidation of the sample and the newly formed Cr-enriched $M_{23}C_6$ carbides can be seen by deconvoluting the metallic and oxide portions of the Cr spectra. In addition, SPEM performed during DCT cooling showed that only C undergoes a change in spatial distribution during DCT cooling. Fig. 1e-g shows that C segregation can be effectively visualised at micrometre resolution, which has not been reported previously. The observed changes in C and Mo spectra are associated with the evolution of loosely formed primordial M_2C carbides. These act as nucleation points for the next generations of carbides. The enhanced formation of Mo-enriched M_7C_3 carbides was observed during Mo modification with DCT. A subtype of M_7C_3 that develops at cryogenic temperatures is associated with the newly modified M_7C_3 carbides. *In-situ* SPEM observations also showed that the increase in the number of M_7C_3 carbides corresponds to increased nucleation and precipitation of $M_{23}C_6$ carbides with DCT.

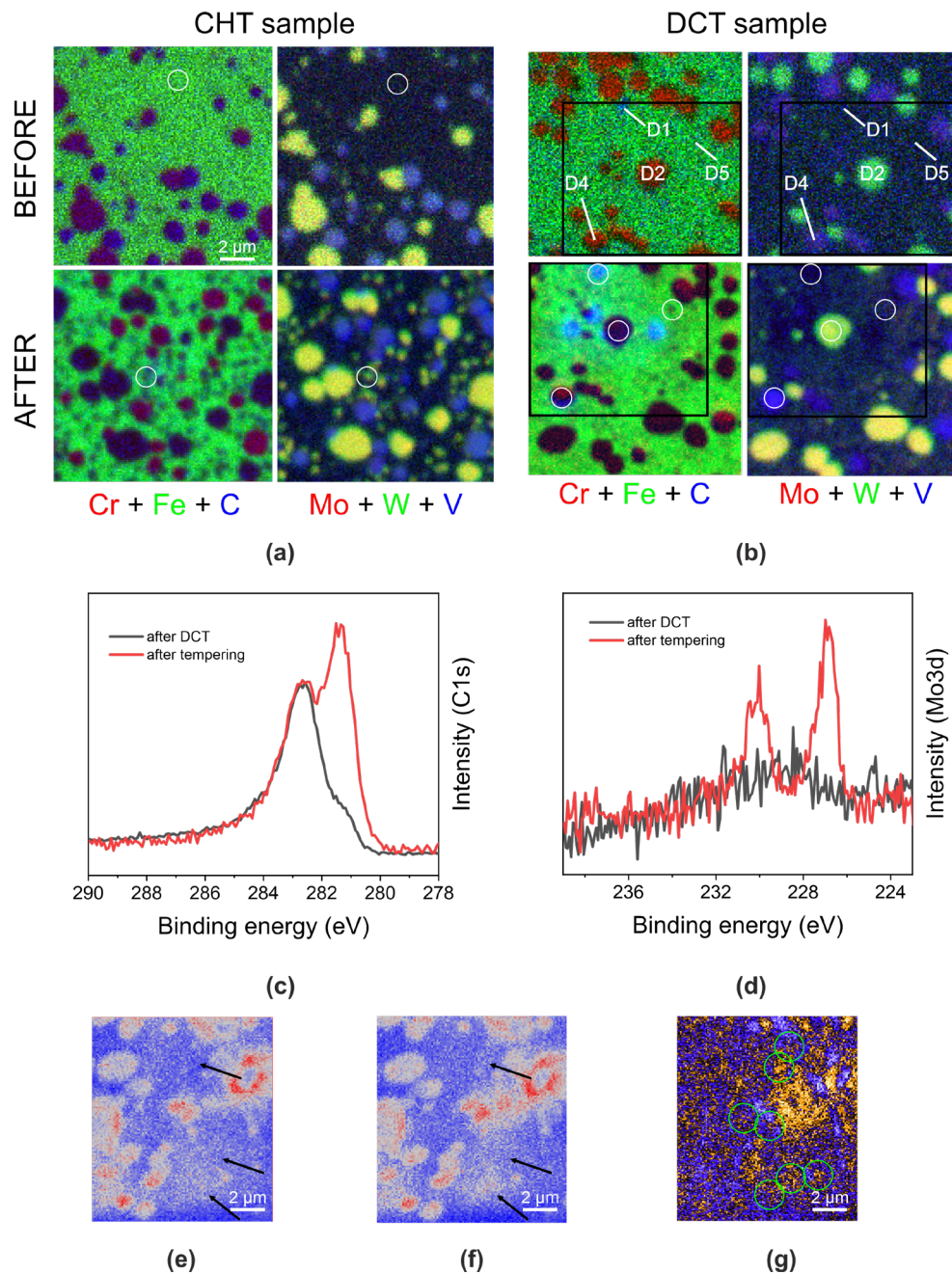


Figure 1. SPTEM color-coded maps of the scanned area for CHT (a) and DCT (b) samples before and after heating up to 873 K. SPTEM spectra (C 1s and Mo 3d) for MC carbide in DCT samples; after DCT and after heating up to 873 K (c)-(d). (e)-(g) in-situ color-coded C 1s concentration maps of the DCT sample, (e) before DCT, (f) after DCT and tempering and (g) after 24 h in DCT. The green circles in (g) indicate changes in the C signal from the quenched state to the 24 h DCT.

Acknowledgments

The synchrotron experiments were performed at the ESCA Microscopy beamline at Elettra Sincrotrone Trieste (proposal number:20205083).

Original paper

P. Jovicevic-Klug *et al.*, *Appl. Surf. Sci.* **610** (2023); DOI: 10.1016/j.apsusc.2022.155497.

P. Jovicevic-Klug¹, L. Tegg^{2,3}, M. Jovicevic-Klug¹, R. Parmar⁴, M. Amati⁴, L. Gregoratti⁴, L. Almasy⁵, J.M. Cairney^{2,3}, B. Podgornik⁶

¹ Max-Planck-Institute for Iron Research, Düsseldorf, Germany

² School of Aerospace, Mechanical and Mechatronics Engineering, The University of Sydney, Camperdown, Australia

³ Australian Centre for Microscopy and Microanalysis, The University of Sydney, Camperdown, Australia

⁴ Elettra - Sincrotrone Trieste S.C.p.A., Trieste, Italy

⁵ Institute for Energy Security and Environmental Safety, Centre for Energy Research, Budapest, Hungary

⁶ Institute of Metals and Technology, Ljubljana, Slovenia

e-mail: p.jovicevic-klug@mpie.de

Identifying charge distribution and support effects in Au catalysts under reaction conditions

Elettra | Materials Science Beamline

Au/ceria-based materials are well-known catalysts for low-temperature oxidation of CO, dangerous for human health, into relatively safer CO₂. The main factor responsible for the catalytic activity of ceria-based catalysts is the reversible reducibility and Ce⁴⁺/Ce³⁺ transition in ceria. This process determines the ability of the catalysts to transport oxygen to the active sites, an essential step in Mars-van Krevelen (MvK) reaction mechanism. Also, MSI (Metal-Support Interactions) at the interface between ceria and metal NPs (nanoparticles) influence the charge state of interface atoms within metal nanoparticles, a crucial factor in both MvK and LH (Langmuir-Hinshelwood) reaction mechanisms. It makes understanding how reaction conditions affect MSI in catalytic materials a challenging task in heterogeneous catalysis research. Metal nanoparticles and their supports often undergo changes in structure and oxidation state when exposed to reactants, hindering a straightforward elucidation of the structure-activity relations using only ex-situ or UHV (Ultra-High Vacuum) techniques. Overcoming these limitations, we explored the MSI between gold nanoparticles and ceria supports in ultrahigh vacuum and during exposure to CO. A combination of in situ and NAP (Near Ambient Pressure) methods such as XPS (X-ray Photoemission Spectroscopy), SRPES (Synchrotron Resonant Photoemission Spectroscopy) and DRIFTS (Diffuse Reflectance Infrared Fourier Transform Spectroscopy), and theoretical calculations based on DFT (Density Functional Theory) was applied to investigate the gold/ceria interface and its reactivity toward CO exposure. Special attention was paid to XPS measurements – a direct and unambiguous method for determining a catalyst's chemical and charge state. Using synchrotron irradiation in SRPES experiments allows determining charge distribution in Au NPs in Au/CeO₂ catalysts.

First, we focused on the electronic structure of the ceria-supported Au particle as induced by the MSI. Applying various XPS techniques (UHV-XPS, NAP-XPS, and SRPES), we found that in classic Au/CeO₂ samples (where Au NPs are deposited on the ceria support) mainly two oxidation states of gold are present: metallic Au⁰ and ionic Au⁺. There is also a tiny amount of Au³⁺ species in samples with a mixed stoichiometric Au-CeO₂ layer. In contrast, there are no Au³⁺ species in the reduced Au-CeO_{2-x} sample and samples of Au NPs deposited on CeO₂(111), which suggests that Au³⁺ species are incorporated in the ceria lattice during the co-deposition of Au and Ce in the samples with a mixed Au-CeO₂ layer. Acquiring the spectra at various photon energies allowed us to evaluate the depth profile of the different Au oxidation states and assign of Au⁺ species to interface Au atoms in contact with the ceria support. A comparison of SRPES (hν = 180 eV) and UHV-XPS (hν = 1487 eV) measurements on fully oxidized (stoichiometric) Au/CeO₂ sample revealed a significantly lower fraction of Au⁺ when using the lower photon energy, indicating that such species do not preferentially occupy surface positions of Au NPs. This indicates that Au⁺ sites are mainly localized in the Au-ceria interface but not on the surface of Au NPs (Figure 1). This is in good agreement with the results of CO DRIFTS under conditions resembling those of the CO oxidation reaction. Moreover, CO also serves as a probe molecule to scrutinize the nature and abundance of various adsorption sites. It was found that the major C-O stretching DRIFTS band (2121–2138 cm⁻¹) for CO adsorbed on the Au/CeO₂ catalyst is assigned to CO adsorbed on metallic Au⁰ (majorly) and slightly positively charged (minorly) Au^{δ+} sites. Thus, based on XPS and CO DRIFTS data, we concluded that in Au/CeO₂ systems most of the Au⁺ sites are localized at the Au-ceria interface and not in contact with the gas phase. In turn, surface Au sites on Au NPs, considered active sites in

CO oxidation, are metallic or just slightly positively charged.

We next focused on how charge redistributes upon reduction of the ceria surface, whereby some electrons are transferred back to the supported Au NPs. Our DFT calculations predicted that ceria reduction can lead to the formation of strongly negatively charged interface Au^{δ-} sites that adhere to oxygen vacancies, or to the transfer of electrons that delocalize in several atoms of the Au NP. According to our DFT calculations the formation of the former interface Au^{δ-} site does not have a clear core-level shift fingerprint, whereas the later electron transfer and delocalization is associated to a chemical shift of tenths of eV. XPS studies confirmed this prediction and showed that the partial reduction of the ceria support resulted in a 0.1–0.3 eV shift of the entire Au 4f doublet toward lower binding energies (Figure 1). This tendency was the same for both model samples we studied: Au/CeO₂ model catalysts (where Au NPs are deposited on a well-defined ceria surface) and Au-CeO₂ (where gold is dispersed on nanostructured ceria powder). Considering that some authors mentioned Au^{δ-} species as an active site in CO oxidation, we also tried to study the possibility of CO adsorption on negatively charged gold atoms. Our CO DRIFTS studies show the slight shoulder with frequencies (2060–2090 cm⁻¹) assigned by many authors to CO molecules adsorbed on Au^{δ-} species. However, our DFT calculation shows that CO does not adsorb on the strongly negatively charged Au^{δ-} formed at the Au/ceria interface. Thus, we tentatively assign the lowest wavenumber band to CO adsorbed on low-coordinated Au centers, which acquire smaller positive charges after binding CO.

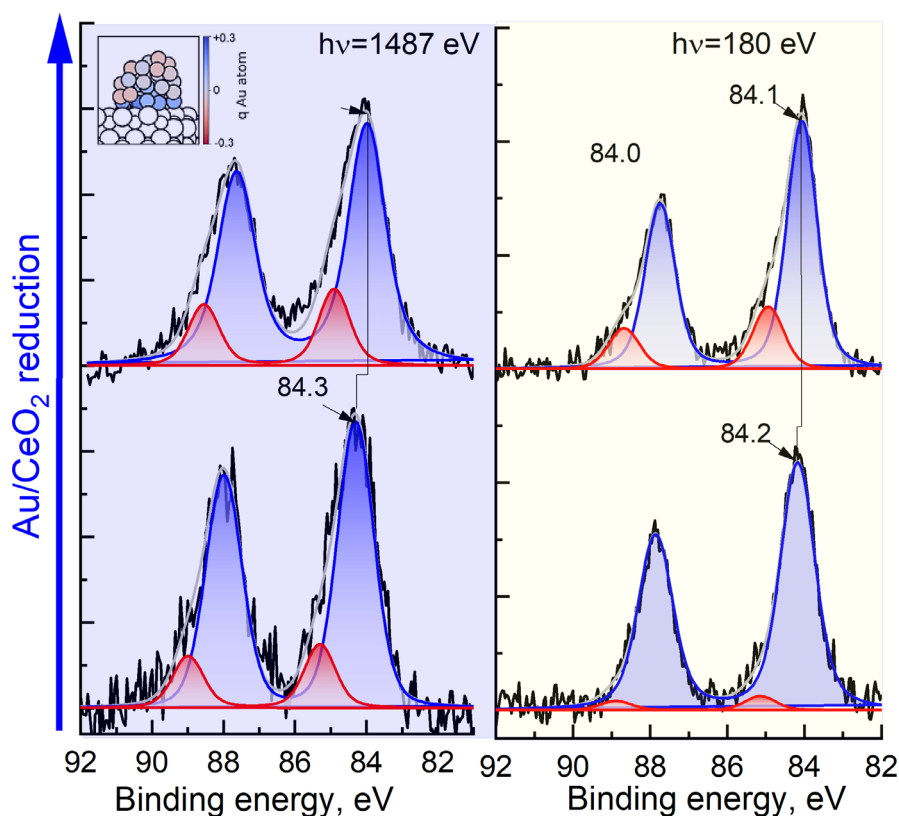


Figure 1. Normalized XPS Au 4f spectra of stoichiometric and reduced Au/CeO₂ samples. Color-coding: measured spectra (black), fitted components Au⁺ (red), Au⁰ (blue), and their sum (gray). In the insert – side view of the most stable state found for the Au₃₁/CeO₂(111) model. Au atoms are colored according to their calculated Bader charge *q*.

Acknowledgments

O.B., P.K., and L.K. thank the National Science Centre (Poland) for financial support, under Project No. UMO-2017/27/N/ST5/02731, and the CERIC-ERIC Consortium for access to experimental facilities and financial support. L.P., I.K., T.S., M.V., and I.M. would like to thank the Czech Science Foundation for financial support, under Project No. 20-13573S. A.B. and K.M.N. gratefully acknowledge support by the Spanish/FEDER grants (Nos. PGC2018-093863-B-C22 and MDM-2017-0767), as well as by Grant Nos. 2018BPO0190 (for A.B.) and 2017SGR13 of the Generalitat de Catalunya. Computational resources have been partly provided by the Red Española de Supercomputación. M.P. is thankful for financial support under the Excellence Initiative - Research University program. The authors also thankfully acknowledge funding of the Deutsche Forschungsgemeinschaft (DFG) and acknowledge additional support by the DFG from the Excellence Cluster "Engineering of Advanced Materials" (Bridge Funding). This study was also supported by the European COST Action CA18234.

Reproduced with permission under a Creative Commons Attribution-NonCommercial 4.0 International Public License CC BY 4.0 Copyright © 2022 The Authors. Published by American Chemical Society

Original paper

O. Bezkrovnyi *et al.*, Chem. Mater. **34**, 17 (2022); DOI:10.1021/acs.chemmater.2c01659

O. Bezkrovnyi¹, A. Bruix², D. Blaumeiser³, L. Piliáí⁴, Simon Schötz³, T. Bauer³, I Khalakhan⁴, T. Skála⁴, P. Matvija⁴, P Kraszkiewicz¹, M. Pawlyta⁵, M. Vorokhta⁴, I. Matolínová⁴, J. Libuda³, K.M. Neyman^{2,6}, L. Kępiński¹

¹ W. Trzebiatowski Institute of Low Temperature and Structure Research, Polish Academy of Sciences, Wrocław, Poland

² Departament de Ciència de Materials i Química Física and Institut de Química Teòrica i Computacional (IQTCUB), Universitat de Barcelona, Barcelona, Spain

³ Interface Research and Catalysis, Erlangen Center for Interface Research and Catalysis, Friedrich-Alexander Universität Erlangen-Nürnberg, Erlangen, Germany

⁴ Department of Surface and Plasma Science, Charles University, Prague, Czech Republic

⁵ Materials Research Laboratory, Silesian University of Technology, Gliwice, Poland

⁶ ICREA (Institució Catalana de Recerca i Estudis Avançats), Barcelona, Spain

e-mail: o.bezkrovnyi@intibs.pl ; abruix@ub.edu

Single-active site character in a bottom-up constructed π -conjugated nickel-porphyrin network

Elettra | NanoESCA, ALOISA

The technological exploitation of molecule-based materials relies on more robust nanostructures composed of covalently linked units. Covalent transition metal porphyrin-based catalytic materials that exhibit improved charge transport and carrier separation properties were proven to outperform their single-molecule counterparts in electro- and photochemical conversion reactions. On-surface synthesis is the method of choice in order to achieve π -conjugated conductive nanomeshes with red-shifted absorption characteristics at the interface. Thereby, we have chosen a Au(111) substrate as a catalyst to induce Ullmann coupling of NiTBrPP (Nickel Tetra(4-BromoPhenyl) Porphyrin) precursor layer. The weak charge transfer at the interface to the molecular layer allows elucidating the intrinsic properties of the fabricated molecular network, which is composed of in-plane covalently linked NiTPP (Nickel TetraPhenylPorphyrin) units. Here, joint findings obtained by photoemission and absorption spectroscopy, as well as STM (Scanning Tunneling Microscopy) experiments are provided. In Figure 1a we present a region measured by STM of a covalent NiTPP-based nanomesh created by annealing at 673 K, which allows concluding that the phenyl substituents are flattened as a consequence of the formation of a π -extended macromolecule due to intermolecular coupling. When analyzing monomeric units in the network, deviations from a perfect four-fold symmetry that make the porphyrin nanomesh amorphous become evident. The appearance of the molecular constituents allows us to conclude that these irregularities originate from cyclodehydrogenation side reactions. Indeed, four TPP derivative products have been reported upon annealing pristine molecules on Au(111) and these species are incorporated into the covalent porphyrin network reported here, as confirmed by the STM images. Moreover, the partial dehydrogenation of the monomeric units

restricts the growth direction when the covalent nanostructure is formed and causes the monomeric units to exhibit a random azimuthal orientation. Covalently linking NiTPP units leads to drastic changes in the valence band spectrum. The discrete molecular levels disappear upon annealing the molecular precursor and evolve into a continuum of states that is largely spread in energy and arising from few tenths of eV below the Fermi level. This evidence is related to the formation of an extended covalent nanostructure. Looking at the photoelectron $k_{||}$ distribution along the Au(111) substrate $\bar{M}-\bar{\Gamma}-\bar{M}$ direction after NiTPP network creation that is shown in Figure 1b, the formation of a dispersive band of parabolic shape is evident. The molecule-related states are fully absent when using s-polarized light instead of p-polarized light indicating the π -delocalization in the covalent nanomesh. All directions in reciprocal space yield the same dispersion relation for the molecular network when using p-polarized light. The band structure is equally broadened along any direction and within the full energy range. The covalent nanomesh produces a ring structure observed in the 2D momentum maps that is closing with the binding energy increasing. Similar findings were observed for graphene when more than one rotational domain was present. It is very peculiar, that the present graphene-related NiTPP-based polymer structure, though amorphous and defect-rich, is also characterized by broad, and yet, continuous spectrum of states. This supports the picture of a uniform and efficient charge transport across the metal-like molecular layer, the stability of which is increased as a consequence of creating an extended aromatic system. We also emphasize that, so far, dispersive electronic features that are exhibited by bottom-up constructed nanostructures were rarely observed, limited to smaller monomeric units without any transition metal ions embedded.

Information on the Ni cores stabilized

within the porphyrin N-moiety is of major interest in order to evaluate to what extent their main single-molecule functionalities are retained when embedded in more stable π -delocalized covalent nanomeshes. NEXAFS (Near-Edge X-ray Absorption Fine Structure) spectra recorded across the Ni L_3 thresholds and reported on Figure 1c allow us to get a better insight into the details of the electronic structure of the functional porphyrin center provided by NiTPP network and the single-molecule layer counterpart. Since no changes characteristic for the Ni(II) low-spin state in both the spectral shape and satellite structure are observed, we can assume the Ni core single-active site character to be preserved upon NiTPP-based network formation. The Ni ion cores embedded in the polymeric molecular backbone are barely involved in the extended π -bonding as desired for a multifunctional device with active centers, whose performance benefits from the larger stability of the polymerized backbone. It should be emphasized that the imperfections in the covalent nanomesh reported here do not lead to any visible broadening of the Ni-related states indicating a well-defined functionality that is uniform across the interface.

In conclusion, despite deviations from perfect order inherent to the coupling scheme applied, namely by thermal activation, the extended conductive nanomeshes reported here are characterized by exciting functional properties. The creation of a π -delocalized porphyrin network across the surface is reflected by the appearance of continuous energy-dispersive electronic valence states that were not observed before for this class of materials. At the same time, the single-active site character of the Ni cores embedded in the conductive molecular backbone is retained. Thus, our strategy is particularly interesting for advanced devices given the possibility of relying on precisely defined central metal ion functionality.

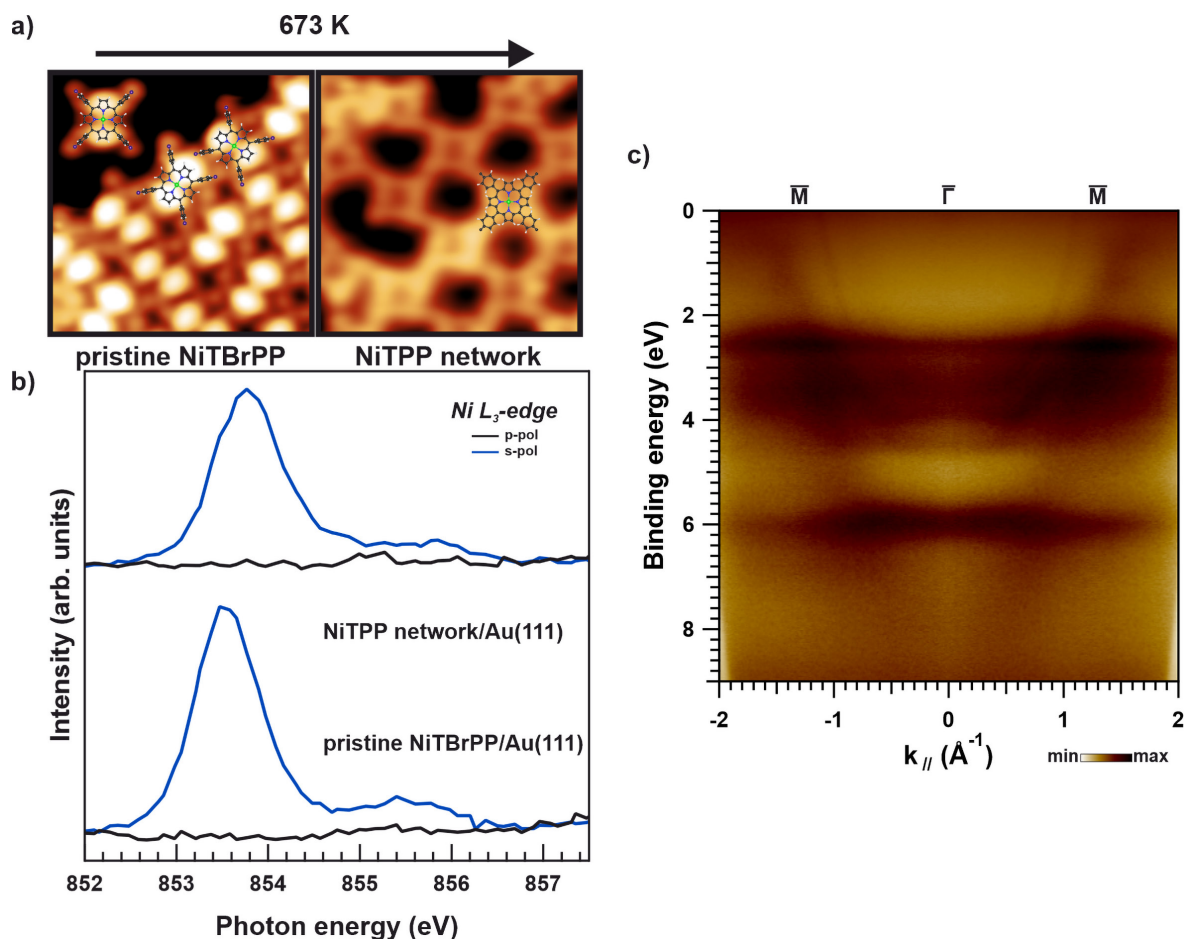


Figure 1. a) STM images ($5.2 \times 5.2 \text{ nm}^2$) of pristine NiTBrPP layer and annealed to 673 K that induces the formation of NiTPP-based covalent network; b) photoelectron $k_{||}$ distribution obtained for covalent NiTPP-based network on Au(111) along the substrate M- Γ -M direction recorded at a photon energy of 30 eV using p-polarized light; c) NEXAFS spectra recorded across Ni L₃-edge for both the pristine NiTBrPP layer and NiTPP-based network.

Original paper

D. Baranowski *et al.*, *Angewandte Chemie International Edition* **61**, e202210326 (2022); DOI: 10.1002/ange.202201916

D. Baranowski^{1*}, I. Cojocariu¹, A. Sala², C. Africh², G. Comelli^{2,3}, L. Schio², M. Tormen², L. Floreano², V. Feyer^{1,4*}, C. M. Schneider^{1,4,5}

¹ Peter Grünberg Institute (PGI-6) Jülich Research Center, Jülich, Germany

² TASC Laboratory, IOM-CNR, Trieste, Italy

³ Physics Department, University of Trieste, Trieste, Italy

⁴ Faculty of Physics and Center for Nanointegration Duisburg-Essen (CENIDE), University of Duisburg-Essen, Duisburg, Germany

⁵ Department of Physics and Astronomy, UC Davis, Davis, USA

e-mail: d.baranowski@fz-juelich.de ; v.feyer@fz-juelich.de

Epitaxially-aligned and rotated graphene on cobalt: exploring spin-polarized hybrid states

Elettra | Nanospectroscopy, NanoESCA

Markings produced by dragging an ordinary pencil on paper can generate great elation in an infant learning how to draw. It is amusing to think that the layered nature of graphite responsible for those markings has stirred an equal amount of excitement in some of the best minds in the physics community in the last decade. The possibility to dissect graphite into individual single atomic layers, famously termed as graphene, gave rise to a plethora of surprising observations in part due to graphene's exceptional electronic properties. Our research aims at understanding the spin degree of freedom in the electronic structure of graphene, especially when it is interfaced to a ferromagnetic metal.

Regarding spin-related phenomena, the graphene-Co interface is particular as it gives rise to efficient spin injection, spin reorientation transitions in Co, and a Rashba-type DMI (Dzaloshinski-Moriya) interaction. The basis of such spin effects may be sought in the Gr-Co orbital hybridization, which results in a spin-polarized state near the Fermi level, termed as minicone in the literature. On the other hand, all studies to date focused on those cases in which the graphene's crystallographic orientation matches that of the Co support. Instead, in order to understand more realistic systems, in the present work, we have investigated the spin-polarized electronic structure of azimuthally-rotated Gr-Co interfaces. High-resolution ARPES (angle-resolved photoemission spectroscopy) data collected at the BadElph and NanoESCA beamlines were complemented by the SPELEEM (spectroscopic photoemission and low energy electron microscopy) measurements carried out at the Nanospectroscopy beamline.

The sample used for these investigations was a graphene monolayer grown by CVD (chemical vapor deposition) on top of a 10 nm thick cobalt film. In particular, the hot catalytic surface was exposed to ethylene backpressure, allowing for the

formation of a surface carbide phase, followed by the formation of graphene. Under these growth conditions, graphene grows mainly with the crystalline axes rotated with respect to the substrate ones. However, the rotated graphene domains can be transformed into aligned ones by a carbon dissolution-segregation procedure, allowing for obtaining a sample with coexisting aligned and rotated domains.

From the structural point of view, we identified the most prominent graphene rotational domains on Co(0001). As seen in Fig. 1 (a), ARPES data near the Fermi level shows the presence of several rotated patterns with hexagonal symmetry. The same can be observed in the LEED (low-energy electron diffraction) pattern in Fig. 1 (b). A detailed analysis of the LEED profile identifies several azimuthal angles (Fig. 1 (c)). The intensity profile reveals the presence of four broad diffraction peaks rather than a featureless diffraction ring expected from an entirely incoherent azimuthal distribution. The rotations are determined to be $\varphi = 9.6^\circ, 16.5^\circ, 19.2^\circ, 22.4^\circ$ by fitting the intensity profile with Gaussian peaks. The relative abundance of the $\varphi \neq 0$ peaks are 4.7%, 38.2%, 40.6%, 16.5%, respectively. These angles nearly coincide with commensurate Gr-Co superlattices, which are also used in the theoretical modeling of each rotational angle.

The electronic structures of epitaxially-oriented and rotated graphene domains were studied both experimentally by ARPES and theoretically by DFT (density functional theory). Figs. 1 (d-h) summarizes the most important findings. The maximum of the minicone state intersects the Fermi level at a slightly larger in-plane momentum transfer with respect to the epitaxially-aligned case, consistent with the structural relaxation of the rotated graphene domains, as also observed in LEED. Most importantly, Figs. 1 (d) and (e) clearly show the same minicone band

feature both for epitaxially-oriented and rotated graphene domains. The binding energy of the minicone state is found unchanged between rotated and epitaxially-oriented domains, whereas the Fermi velocity is slightly higher for the rotated domains. Moreover, the π band apex of rotated graphene is shifted towards lower binding energies. All experimental observations are confirmed by our DFT calculations and point to a slightly weaker average C-Co bond in the case of rotated domains compared to the epitaxially-oriented ones.

Importantly, the minicone band feature is found to be highly spin-polarized for all azimuthal rotations, as seen in Fig. 1 (f). The theoretical confirmation is given in Figs. 1 (g-h), in which the same band feature appears only in one spin state for the 19° azimuthal rotation case. Notably, the same theoretical observation is made for all other commensurate Gr/Co structures studied.

The correspondence between the band structure of epitaxially-aligned and azimuthally-rotated graphene domains can be understood by the primitive-cell character calculated for each rotation. Even in the rotated phases, the primitive cell character is found to be about 60%. In all the rotated phases considered, the states at the \bar{K} . Of the graphene primitive cell are unfolded exclusively from the \bar{K} points of the superstructure unit cell. This results in the appearance of the minicones both at the primitive and supercell \bar{K} points and explains the observation that the minicone appears at the \bar{K} point of the primitive cell even in the rotated phases. Considering the presence of different rotational alignments of graphene is unavoidably expected, especially on ultrathin Co films, our findings provide a solid experimental and theoretical basis for exploiting CVD (chemical vapor deposition) synthesized graphene/Co(0001) interfaces in spintronics.

Surfaces and Interfaces

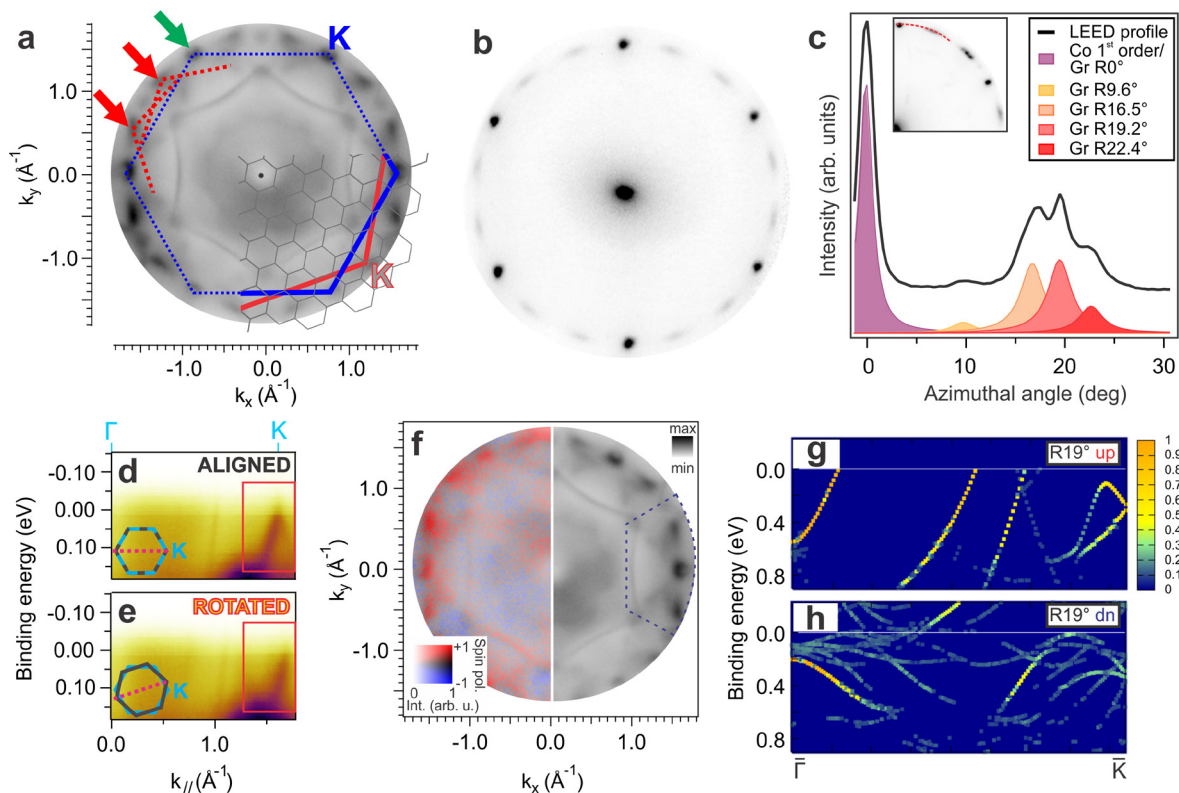


Figure 1. (a) ARPES pattern showing both rotated and epitaxially-oriented graphene phases, along with the primitive cell and supercell overlays. (b) LEED pattern from the same surface. (c) LEED intensity profile along the azimuthal direction showing distinct rotational domains. Binding energy-dependent ARPES profiles are shown for d) aligned and e) rotated graphene domains along the direction shown by a dashed red line in the inset. f) ARPES pattern near the Fermi level. Spin-polarized ARPES is shown on the left half. g)-h) DFT calculated electronic structure is shown for both spin states for the 19° rotation after unfolding to the primitive cell. The color bar indicates the strength of the primitive-cell character of the unfolded states.

Acknowledgments

We acknowledge Prof. Sebastian Günther for fruitful discussions.

Original paper

M. Jugovac *et al.*, *Carbon* **198**, 188 (2022); DOI: 10.1016/j.carbon.2022.07.011

M. Jugovac^{1,3}, **E.D. Donkor**², **P. Moras**³, **I. Cojocariu**^{1,4}, **F. Genuzio**¹, **G. Zamborlini**⁴, **G. Di Santo**¹, **L. Petaccia**¹, **N. Stojić**², **V. Feyer**^{4,5}, **C.M. Schneider**^{4,5}, **A. Locatelli**¹, **T.O. Montes**¹

¹ Elettra - Sincrotrone Trieste S.C.p.A., Trieste, Italy

² Abdus Salam International Centre for Theoretical Physics, Trieste, Italy

³ ISM-CNR, Trieste, Italy

⁴ Peter Grünberg Institute (PGI-6), Forschungszentrum Jülich GmbH, Jülich, Germany

⁵ Fakultät f. Physik and Center for Nanointegration Duisburg-Essen (CENIDE), Universität Duisburg-Essen, Duisburg, Germany

e-mail: matteo.jugovac@elettra.eu ; tevfik.montes@elettra.eu

Stripy domain of striped electronic phase

Elettra | Spectromicroscopy

In solids undergoing symmetry breaking phase transitions, the low symmetry phases form domains with various morphological shapes that are usually unrelated to the nature of symmetry breaking. It would be interesting if the domain shapes are directly associated with the geometry of the symmetry breaking. Among various systems showing symmetry breaking transitions, the layered IrTe_2 with a triangular lattice of Ir exhibits a structural phase transition from trigonal to monoclinic or triclinic at about 280 K and an additional transition below 180 K. The structural phase transition at about 280 K is governed by the breaking of the three-fold symmetry of the triangular lattice due to Ir 5d orbital ordering which is accompanied by the lattice periodicity change due to Ir-Ir dimerization and charge ordering. The possible charge-orbital ordering patterns are schematically shown in Fig. 1(a). The direction of the dimerized Ir-Ir bond is determined by the Ir 5d orbital ordering which breaks the three-fold symmetry. The Ir-Ir dimers form the striped charge ordering pattern in which the direction of the Ir-Ir bond and that of the stripe have one-to-one correspondence. The other phase transition below 180 K is due to the additional periodicity change of the striped charge ordering. It was known that the anisotropic charge-orbital ordered state harbors anisotropic Fermi surfaces as schematically shown in Fig. 1(b). The straight Fermi surfaces (Fermi arcs) are expected at the cleaved surface, and the direction of the Fermi arcs should be perpendicular to the stripes since the Ir 5d band exhibits large dispersion along the stripes. Such domain dependent electronic structure has been studied by means of SPEM (Scanning Photoelectron SpectroMicroscopy) and nano-ARPES (Angle Resolved Photoemission Spectroscopy with submicron space resolution) at the spectromicroscopy beamline.

Figure 1(c) shows a SPEM image taken at 250 K for the cleaved IrTe_2 . The crystal was cleaved at 300 K and slowly cooled

across the phase transition temperature of 280 K. Figure 1(d) shows a zoomed over the area with the striped domains of length $\sim 50\text{--}100\ \mu\text{m}$. The high intensity (bright) and low intensity (dark) regions may correspond to the striped charge ordering of the three possible directions in Fig. 1(a). It is interesting that the low symmetry electronic phases with striped charge ordering form the striped domains. Temperature evolution of the striped domains are indicated in Figs. 1(e) and 1(f). The cooling rate of $\sim 2\ \text{K}/\text{min}$ is slow enough to allow formation of the striped domains. Interestingly, the domain boundaries became ambiguous in going from 120 K to 47 K, indicating change of the domain shapes. The domain's morphological change would be related to the periodicity change of the striped charge ordering at 180 K or below.

Figures 1(g) and 1(h) show SPEM images at 47 K which are obtained by different energy windows. This permits to extract domain boundaries between three different striped charge orderings (labeled as #1, #2, and #3) which are summarized in Figs. 1(i), 1(j), and 1(k) for 250 K, 120 K, and 47 K, respectively. These results indicate that the striped domain boundaries at 250 K is created by two out of the three different striped charge orderings. Domain-dependent electronic band structure can be observed by nano-ARPES. Figures 1(l), 1(m), and 1(n) showing Fermi surfaces measured in the three different domains, respectively. In addition to the Fermi surfaces from the bulk, straight and fragmented Fermi surfaces derived from the surface bands are observed for each domain. The directions of the straight and fragmented Fermi surfaces roughly correspond to the Fermi arcs illustrated in Fig. 1(c). The surface bands in domain #1 are dispersive along the direction of the horizontal charge stripes and exhibit the Fermi arcs perpendicular to them as indicated by the broken lines in Figure 1(l). Interestingly, the Fermi arcs for domain #1 are relatively sharp compared to those of domains #2 and #3 as

indicated by the broken lines in Figs. 1(m) and 1(n). Most likely, the charge-orbital stripes are well established in newly developed domain #1 whereas they are somewhat disordered in domains #2 and #3 during the evolution from the intermediate temperature striped charge ordering to the low temperature striped charge ordering with different periodicity.

The SPEM/nano-ARPES of the spectromicroscopy beamline, Elettra enabled us to observe the interesting domain textures and the domain-dependent Fermi surfaces of the striped charge ordering phases in IrTe_2 . The striped domain texture at 250 K is obtained by the two directions of the striped charge ordering forming about 60 degrees at the boundary as shown in Fig. 1(i). The striped domain of the electronic stripe phase can be stabilized under the anisotropic strain from the neighboring domains. At 47 K, the striped texture is replaced by the trijunction texture of the three types of domains of the three striped charge ordering phases as shown in Fig. 1(k).

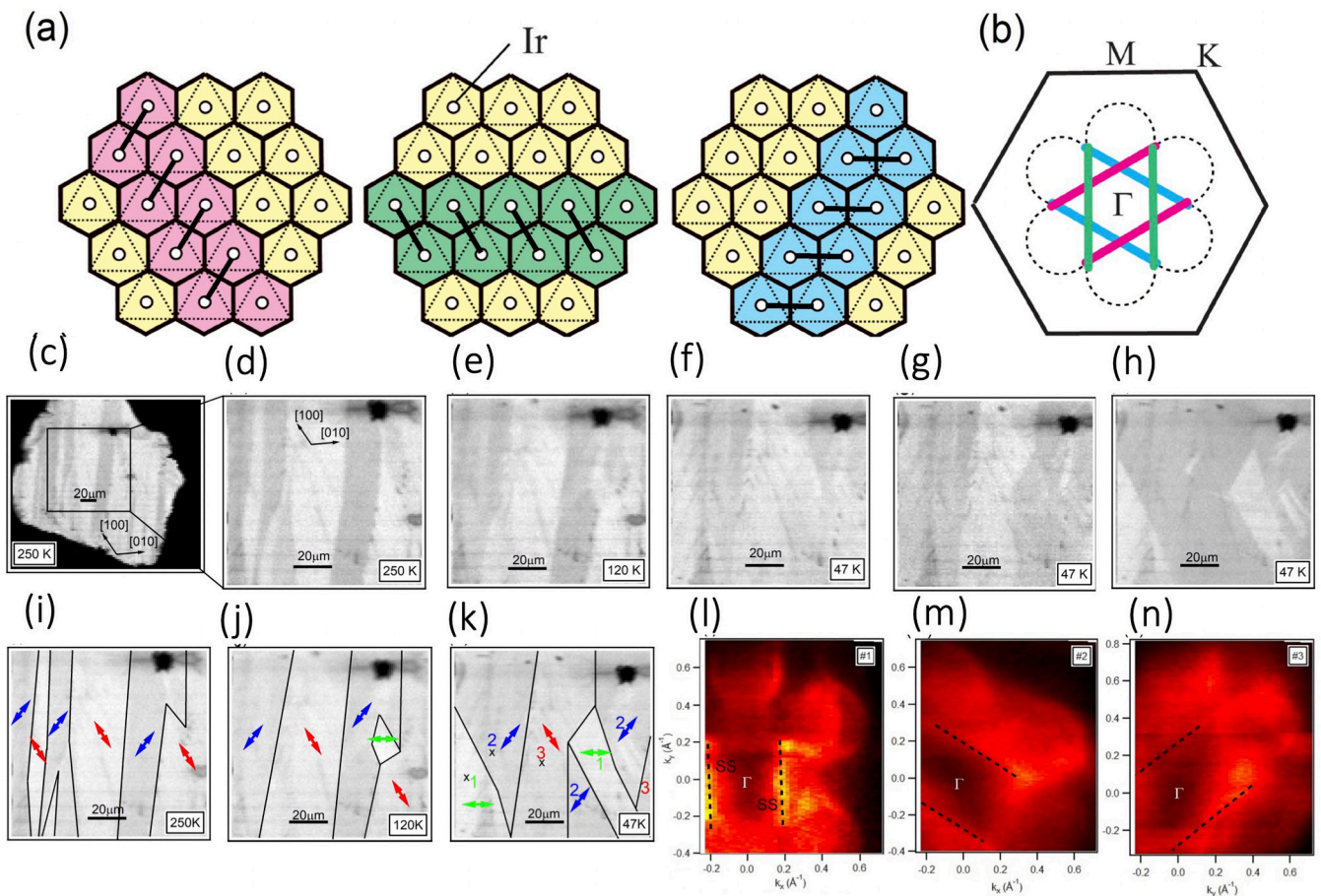


Figure 1. (a) Three directions of the striped charge ordering in the IrTe₂ layer. (b) Three directions of the Fermi arcs in the Brillouin zone corresponding to the three directions of the striped charge ordering. The dotted curves schematically show the bulk Fermi surfaces. (c) Photoemission intensity image of the wide area at 250 K. (d,e,f) Photoemission intensity image of the selected area at 250 K, 120 K, and 47 K. (g, h) Domain textures at 47 K visualized by different energy windows. All the images were taken at $h\nu=27$ eV with linear polarization (horizontal). (i, j, k) Domain textures at 250 K, 120 K, and 47 K. The solid lines indicate domain boundaries. The arrows indicate the directions of charge/orbital stripes. (l, m, n) Fermi surfaces of the three different domains at 47 K. The broken lines indicate Fermi arcs derived from the surface states.

Acknowledgments

This work was partially supported by Elettra, the JSPS/MEXT KAKENHI, and the joint research program of ZAIKEN, Waseda University (Project No. 31010). We also acknowledge Elettra Sincrotrone Trieste for providing access to its synchrotron radiation facilities and the partial support.

Original paper

T. Mizokawa *et al.*, *Adv. Quantum Technol.* **5**, 2200029 (2022); DOI: 10.1002/qute.202200029

A. Barinov², V. Kandyba², A. Giampietri², R. Matsumoto¹, Y. Okamoto¹, K. Takubo³, K. Miyamoto⁴, T. Okuda⁴, S. Pyon⁵, H. Ishii⁶, K. Kudo⁷, M. Nohara⁸, and N. L. Saini⁹

¹ Department of Applied Physics, Waseda University, Tokyo, Japan

² Elettra - Sincrotrone Trieste S.C.p.A., Trieste, Italy

³ Department of Chemistry, Tokyo Institute of Technology, Tokyo, Japan

⁴ Hiroshima Synchrotron Radiation Center, Hiroshima University, Hiroshima, Japan

⁵ Department of Applied Physics, The University of Tokyo, Tokyo, Japan

⁶ Department of Physics, Okayama University, Okayama, Japan

⁷ Department of Physics, Osaka University, Toyonaka, Osaka, Japan

⁸ Department of Quantum Matter, Hiroshima University, Hiroshima, Japan

⁹ Department of Physics, Sapienza University of Rome, Rome, Italy

e-mail: mizokawa@waseda.jp ; naurang.saini@roma1.infn.it

Time-resolved x-ray spectroscopy reveals atomic and electronic dynamics in adsorbates

FERMI | DiProl

Fundamental dynamical processes of adsorbates on surfaces, *e. g.* energy or charge transfer, desorption, etc. often define catalytic and especially photocatalytic activity and selectivity. These processes are typically in the femtosecond regime. Exploiting the unique capabilities of the seeded x-ray free electron laser at FERMI, we perform pump-probe experiments on C/Ni(100) to gain insight into these processes, using an optical laser to drive the dynamics and an x-ray laser pulse to probe the system. Since the x-ray spectroscopic probe can measure element-specific changes in the electron structure, much more detailed information about the chemistry occurring in the ultrafast time regime can be obtained than in pure optical pump-probe experiments. For the first time, we could detect electronic structure changes in an adsorbate prior to induced nuclear dynamics and associated equilibration.

The carbon adsorbate is a prototypical strongly bonded atomic adsorbate that has previously been well characterized with x-ray-spectroscopy-based synchrotron radiation measurements. We directly follow the changes in the occupied and unoccupied local density-of-state of a strongly adsorbed C atom, using XAS (X-ray Absorption Spectroscopy) and XES (X-ray Emission Spectroscopy), after intense laser excitation (at 400 nm) of the Ni(100) substrate. Using externally seeded x-ray laser beams, it is possible to probe the adsorbate electronic structure dynamics with a time resolution of ≈ 100 fs.

We probe the energy region around the x-ray absorption onset at 283 eV, which corresponds to electronic states close to the Fermi level E_F . In the time-dependent XAS shown in Fig. 1 (a-b) we observe changes for both the holes below 283 eV (orange) and electrons above (turquoise) with a rise time of around 0.1 ps, and with a slower recovery of around 0.2 ps. The long-term spectral change (grey) is delayed until 0.5 ps with a rise time of 0.2 ps and with no detectable recovery

within the measured 4.0 ps. The XES spectral changes shown in Fig. 1 (c-d) around the main peak (green and red) appear to be faster with the onset at almost 0 ps and with a slightly faster rise time; the recovery time of ~ 0.25 ps appears somewhat slower than in the XAS. Both the XAS and XES rapid changes have decayed within 0.5 ps. The changes above the Fermi level (blue) in the XES spectra have an onset of 0.1 ps and then remain, similar to the long-term time component in the XAS.

With the help of theoretical spectra from density functional theory calculations, we interpret the observed features in terms of elevated temperatures of the electronic and phononic subsystems. For the optical fluence used, we estimate a peak electronic temperature of 5000 K within ~ 100 fs of the optical laser excitation, followed by a surface equilibration to 1000 K after ~ 2 ps via electron-phonon coupling. Thermalization of the hot electrons and holes occurs on a time scale of ~ 100 fs. The changes around the adsorption onset at 283 eV can be explained by the 5000 K electronic temperature giving a broad Fermi-Dirac distribution of occupied electrons, consistent between the XAS (orange/turquoise lines) and XES (blue line). In contrast, the increase at the high-energy side of the main XAS peak at 4 ps delay could be reproduced in the simulation of the spectrum from a fully thermalized system at 800 K. The increasing intensity in this (grey in Fig. 1 (a-b)) region is consistent with thermal motion of C atoms towards lower coordinated bonding geometries than the four-fold hollow sites they occupy initially. The excited e-h population seen in the XAS decays on a time scale of ~ 300 fs, simultaneous with an increase in the intensity ~ 1 eV above EF. Thus, these spectral changes are consistent with a decreasing electronic temperature via electron-phonon coupling and corresponding heating of the phonon modes, and is in good agreement with expected time scales from theoretical modeling. In the XES we also observed

a similar decay of the intensity around EF but it does not return to the intensity prior to the pump. This is most likely related to the broadening and shift of the Fermi level at the equilibrated 800 K temperature.

We also observe an immediate short time redshift of the main XES peak where the mechanism is more elusive. We suggest this could be due to ultrafast excitation of in-plane adsorbate vibrations but also many-body effects in the electronic system itself.

In conclusion, the simultaneous measurement of x-ray absorption and emission spectra reveals details of the dynamics on distinct timescales. We see a direct effect on both XAS and XES of the initially high electronic temperature, which manifests itself as clearly identifiable changes in the line shape close to the Fermi level and only persists during the first ps. We can identify this as the timescale of thermal electronic excitation. Our observation constitutes direct experimental evidence that ultrafast laser excitation immediately leads to a highly excited e-h pair distribution not just in the substrate, but also in the adsorbate. The XAS high-energy shoulder at longer delays is a clear signature of a high overall temperature, and its gradual build-up indicates equilibration of the system, which takes place over several ps. We identify this timescale as that of phonon excitation and the response of all substrate degrees of freedom to the excitation pulse. Our results underscore the importance of taking high electronic temperature into account when studying *e.g.* adsorbate dynamics or excitation spectra within a few ps after intense optical pumping.

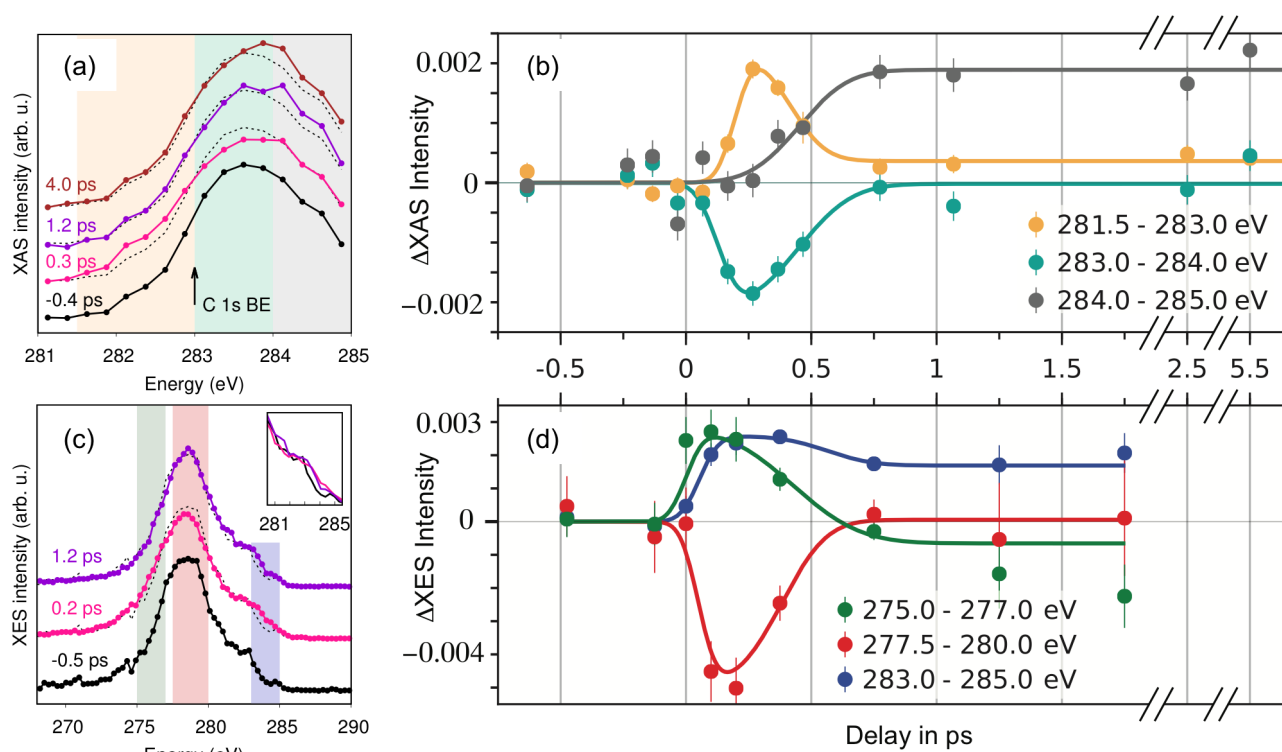


Figure 1. Time-resolved XAS and XES spectroscopy of C/Ni(100). (a) XAS spectra measured with the E-vector parallel to the surface at different delay times between the optical and soft X-ray laser beams. The arrow indicates the C 1s binding energy used for calibration. (b) XAS time trace; the color of each time trace represents different spectral regions indicated in Fig. 1 (a). (c) XES spectra in grazing emission using an excitation energy of 284 eV. (d) XES time traces. The transient shifts in intensity around the C 1s binding energy (orange/turquoise regions of the XAS and blue region in the XES) are attributed to a high electronic temperature, which decreases within the first ps transferring energy to adsorbate vibrations. This high vibrational temperature gives a long-lived intensity increase in the XAS grey region. Adapted from Phys. Rev. Lett. 129, 276001 (2022); Copyright 2022 American Physical Society.

Acknowledgments

This research was supported by the U.S. Department of Energy, Office of Science, Office of Basic Energy Sciences, Chemical Sciences, Geosciences, and Biosciences Division, Catalysis Science Program to the Ultrafast Catalysis FWP 100435 at SLAC National Accelerator Laboratory under Contract No. DE-AC02-76SF00515, Knut and Alice Wallenberg Foundation under Grant No 2016.0042, the Swedish Research Council under Grant No 2013-8823, U.S. This research used resources of the National Energy Research Scientific Computing Center, a DOE Office of Science User Facility supported by the Office of Science of the U.S. Department of Energy under Contract No. DE-AC02-05CH11231. The authors acknowledge the continuous support of the FERMI team during the setting up and operation of the FEL source for the experiment. M.B and P.S.M acknowledge funding from the Helmholtz association (VH-NG-1005). M.D.A and R.C. acknowledge support from the SIR grant SUNDYN [Nr RBS114G7TL, CUP B82115000910001] of the Italian MIUR. Part of calculations were performed using resources provided by the Swedish National Infrastructure for Computing (SNIC) at the HPC2N and NSC centers. We acknowledge valuable discussions with Lars G. M. Pettersson.

Original paper

S. Schreck *et al.*, Phys. Rev. Lett. **129**, 276001 (2022); DOI: 10.1103/PhysRevLett.129.276001

S. Schreck¹, E. Diesen², M. Dell'Angela³, C. Liu¹, M. Weston¹, F. Capotondi⁴, H. Ogasawara⁵, J. LaRue⁶, R. Costantini^{3,7}, M. Beye⁸, P. S. Miedema⁶, J. Halldin Stenlid^{1,2}, J. Gladh^{1,5}, B. Liu¹, H.-Y. Wang¹, F. Perakis¹, F. Cavalca¹, S. Koroidov¹, P. Amann¹, E. Pedersoli⁴, D. Naumenko⁴, I. Nikolov⁴, L. Raimondi⁴, F. Abild-Pedersen², T. F. Heinz^{5,9}, J. Voss², A. C. Luntz², A. Nilsson¹

¹ Department of Physics, AlbaNova University Center, Stockholm University, Stockholm, Sweden

² SUNCAT Center for Interface Science and Catalysis, SLAC National Accelerator Laboratory, Menlo Park, California, USA

³ CNR-IOM, Trieste, Italy

⁴ Elettra-Sincrotrone Trieste, Trieste, Italy

⁵ SLAC National Accelerator Laboratory, Menlo Park, California, USA

⁶ Schmid College of Science and Technology, Chapman University, Orange, California, USA

⁷ Department of Physics, University of Trieste, Trieste, Italy

⁸ Deutsches Elektronen-Synchrotron DESY, Hamburg, Germany

⁹ Department of Applied Physics, Stanford University, Stanford, California, USA

e-mail: diesen@fhi.mpg.de

Unique adsorption configuration of M(II)-tetraphenylporphyrins on the r-TiO₂(110) surface

MiNaC
Elettra | ALOISA

Titanium dioxide, TiO₂, is the most widely employed reducible oxide in photocatalysis and photovoltaics applications. It is a wide gap (3.0–3.2 eV) Vis-transparent insulator in its stoichiometric form, with exceptional electronic properties due to the close proximity of the empty Ti 3d band to the Fermi edge. Upon charge injection, a new state at the upper edge of the band gap appears, typically associated with the most common point defects found in TiO₂, which makes it reactive and conductive. The rutile polymorph is the most stable form among the TiO₂ crystalline structures, can be easily synthesized in large size single crystal, and its non-polar (110) orientation closely matches the highest reactivity and conductivity of the anatase form. The coupling of suitable donor molecules to r-TiO₂(110) makes the substrate an archetypal dye-sensitized interface for light harvesting: the donor molecules extend the energy range of the adsorption spectrum and rapidly transfer the photoexcited electrons to the acceptor substrate, where they can be extracted or made available to trigger chemical reactions.

Among heteroaromatic semiconductors, metal-porphyrins incorporating first row transition metals are known to strongly absorb in the visible region. Their metal-complexed macrocycles mimic the biological activity of the enzymes at the basis of life, such as chlorophyll (Mg), heme (Fe), vitamin B12 (Co), F₄₃₀ coenzyme (Ni), and their absorption energy window may be tuned by suitable choice of the metal center, peripheral functionalization, as well as substrate interaction. The porphyrin/TiO₂(110) interfacial charge transfer (static and dynamic) is governed by the molecular adsorption configuration, which requires an investigation at an atomistic level for the appropriate modeling. We performed Synchrotron radiation XPS (X-ray Photoemission Spectroscopy) at the ALOISA beamline and STM (Scanning Tunneling Microscopy) in ultra-high-

vacuum at the CNR/Elettra-MiNaC joint laboratory for microscopy (OSMOS). By combination with DFT (Density Functional Theory) calculations, we provided a deeper insight in the adsorption mechanism of TPPs (TetraPhenylPorphyrins) containing first period transition metals, namely M(II)-TPPs with M = Co, Ni, Cu, Zn. Despite having different tendency to axial metal coordination in their oxidation state (II), all molecules are found to adsorb on the O_{br} rows protruding off the TiO₂(110) surface, where they adopt the same molecular conformation and aggregate into a commensurate phase with the same symmetry.

The chemical state of M-TPPs in contact with the surface can be probed by XPS. When coordinated to a central metal atom, the four nitrogen atoms of the tetrapyrrolic ring become equivalent and a single peak is observed in XPS of N 1s. The corresponding binding energy changes slightly from Zn- (398.17 eV) to Cu- (398.35 eV) and then Ni-TPP (398.6 eV), displaying a trend consistent with the element group, but for Co-TPP (398.5 eV), which may indicate a slightly larger interaction with the substrate. Looking at the corresponding spectra of the metal 2p_{3/2} peaks, we found that the binding energies correspond to the metals in the oxidation state (II), as confirmed by comparison with XPS of multilayers either grown in-situ or taken from literature, indicating that no significant static charge transfer takes place between the substrate and the macrocycle.

The absorption geometry of the M(II)-TPPs on the r-TiO₂ (110) surface can be elucidated by STM topography. The molecular features can be easily recognized in STM images by a characteristic saddle-shape with the nodal plane oriented transverse to the substrate atomic rows; all the four M(II)-TPPs adsorb atop the O_{br} rows. At a coverage > 0.3 ML, shown in Fig. 1, the onset of molecular aggregation

into ordered domains is observed, where the molecules preserve both the adsorption site on the O_{br} rows and the intramolecular saddle-shape, with few degrees of in-plane azimuthal rotation compared to the isolated molecules. From images where the substrate Ti_{sf} rows are resolved together with molecular domains, we could unequivocally identify a commensurate (2 × 4)-oblique phase symmetry (Fig. 2a), as previously reported also for Zn-TPP, 2H-/4H-TPP, as well as its self-metalated TiO₂^{br}-TPP. In order to shed light on the adsorption site we calculated their adsorption energy for the case of an isolated molecule. Adsorption on the Ti_{sf} rows is always unfavoured with respect to the O_{br} ones by 0.6–0.9 eV. Moreover, adsorption on the O_{br} rows shows an increase of the adsorption energy along the Zn-, Cu-, Ni-, Co-TPP series, with Co-TPP giving the largest adsorption energy (0.4 eV greater than Zn-TPP). DFT calculations found also that Co- and Zn-TPP display a clear preference for adsorption on top of an O_{br} atom, while the bridge site is favoured for Ni- and Cu-TPP, as drawn in Fig. 2b. From a detailed analysis of the molecular components interaction, the molecular adsorption site results from the balance between the strenght of coordination to O_{br} of the metal ion (prevailing for Co-/Zn-TPP) and the optimization of the network of peripheral hydrogen bonds to the adjacent O_{br} rows (prevailing for Ni-/Cu-TPP). Most importantly, DFT calculations predict a different degree of metal coupling to the substrate (stronger for Co/Zn than for Ni/Cu), which is reflected by the adsorption height of Ni(II) and Cu(II) being ~0.4 Å higher than that of Co(II) and Zn(II), in agreement with the overall larger bias required by STM for imaging Ni-/Cu-TPP with respect to Zn-/Co-TPP.

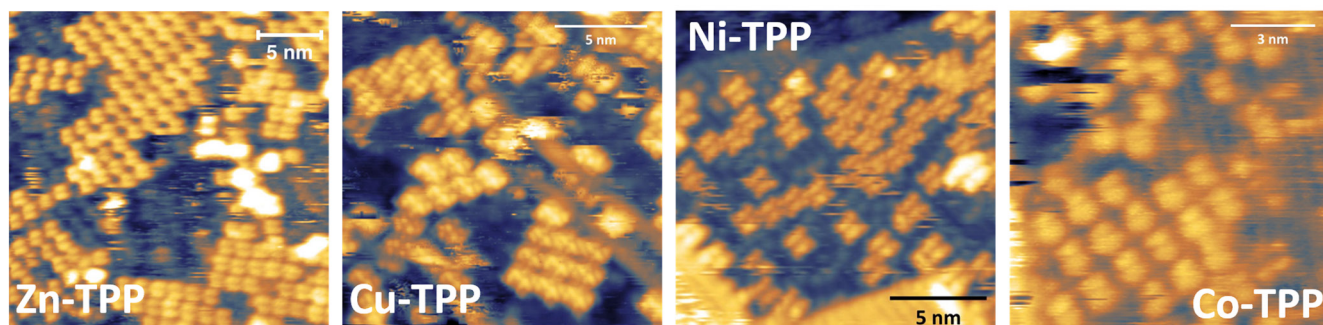


Figure 1. STM topographic images of Zn-, Cu-, Ni- and Co-TPPs on the $\text{TiO}_2(110)$ surface (from left to right, respectively); molecules adsorb on the dark (O_{br}) rows (bright rows correspond to the Ti_{5f} ones) and display a characteristic saddle-shape contrast; at room temperature, molecules aggregate into commensurate domains with (2×4) -oblique symmetry.

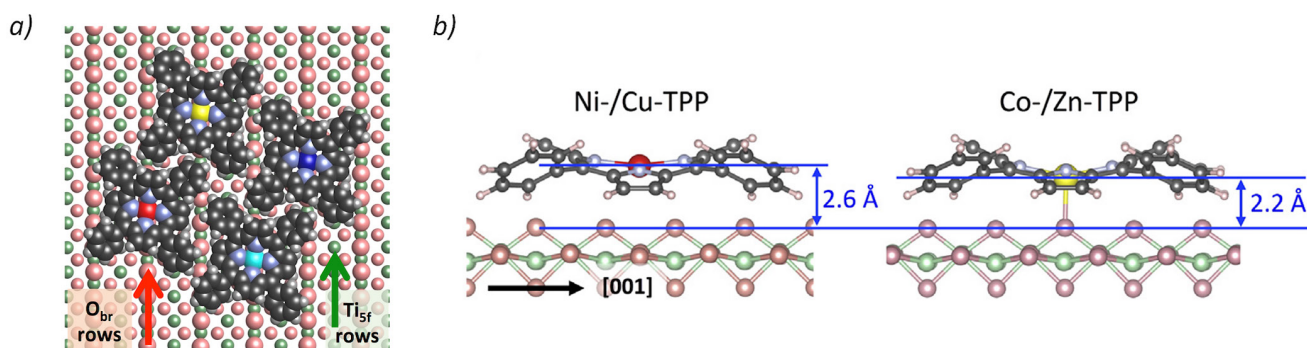


Figure 2. (a) top view of the adsorption configuration of M-TPPs in the (2×4) -oblique phase symmetry; red (green) vertical arrows mark the O_{br} (Ti_{5f}) rows along the substrate $[001]$ direction. (b) Side view across the $[1-10]$ direction of the most stable adsorption configuration for Ni-/Cu-TPP (left panel) and Co-/Zn-TPP molecules (right panel) adsorbed on O_{br} rows, as predicted by DFT calculations; in agreement with coordination chemistry arguments, Co-/Zn-TPP species display a preferential axial coordination on top of an O_{br} atom, where the metal atoms display a distance from the surface significantly shorter than that of Cu and Ni (as highlighted by the blue horizontal lines); in absence of axial coordination, the adsorption of Cu-/Ni-TPP on bridge O_{br} sites is driven by hydrogen bonding of phenyl terminations to the adjacent O_{br} rows.

Acknowledgments

C.G.B. acknowledges financial support through IAEA-Marie Skłodowska Curie fellowship program, Italy.

Original paper

L. Schio *et al.*, Appl. Surf. Sci. **616**, 156548 (2023); DOI: 10.1016/j.apsusc.2023.156548

L. Schio¹, G. Bavdek², C. Grazioli¹, C. G. Bolaños³, A. Goldoni³, A. Vittadini⁴, M. Tormen¹, L. Floreano¹

¹ TASC Laboratory, IOM-CNR, Trieste, Italy

² Faculty of Education, University of Ljubljana, Ljubljana, Slovenia

³ Elettra-Sincrotrone Trieste S.C.p.A, Trieste, Italy

⁴ ICMATE-CNR and INSTM, Padova, Italy

e-mail: schio@iom.cnr.it ; floreano@iom.cnr.it

The oxidation of sub-nanometer graphene-supported Fe clusters

Nanoscale Materials Laboratory
Elettra | SuperESCA

The pursuit of newly designed and efficient catalysts is a key focus that has attracted the attention of numerous researchers. This is because catalysts play a crucial role in enhancing the sustainability of various chemical processes in industrial settings. Recently, the scientific community has shown growing interest in the potential groundbreaking impact of metallic-based nanostructures on improving the efficiency of traditional catalyst designs. One class of nanostructured materials, known as size-selected atomic clusters, has exhibited remarkable catalytic performances, and their properties are strongly influenced by the number of atoms they contain. Iron, traditionally used in industrially relevant reactions such as the Haber-Bosch process, has recently found application in atomic clusters. These iron atomic clusters have demonstrated potential as cost-effective substitutes for expensive noble metal-based catalysts in reactions including oxygen reduction, ammonia synthesis, and alkene epoxidation. Furthermore, the interest in iron-based nanostructures extends to include iron oxides, which have found applications in various technological fields like magnetic storage media and biomedicine, as well as serving as catalysts in chemical reactions such as CO oxidation, water splitting, and the Water Gas Shift.

In this study, we investigated the oxidation of size-selected Fe_n clusters with n = 11, 12, 13, 15, and 20, supported on graphene epitaxially grown on Ru(0001). Size-selected Fe clusters were produced using the ENAC (Exact Number of Atoms in each Cluster) cluster source developed and built by the Nanoscale Materials Laboratory. ENAC was directly connected to the experimental chamber of the SuperESCA beamline of Elettra, enabling the study of cluster properties in situ. The choice of this substrate, combined with keeping the substrate at 20 K throughout the experiment, avoids cluster sintering, thereby preserving the properties related to the specific cluster size. Subsequently, the clusters

were oxidized using a photodissociation approach. In detail, O₂ was adsorbed on the sample at 20 K, and atomic O was produced by dissociating physisorbed O₂ through soft X-ray irradiation. The entire process is schematically described in Figure 1(a).

The Fe 2p_{3/2} core levels were measured on both the pristine and oxidized clusters to highlight differences in lineshape due to the size of each cluster and reveal any effects on oxidation that could be attributed to the specific number of atoms in each cluster. The main component in the spectra acquired after cluster deposition, represented by the gray component in Figure 1(b), was associated with metallic iron. The second component, indicated by orange, was assigned to oxidized iron atoms, indicating that our clusters were already slightly oxidized after deposition. The Fe 2p_{3/2} core levels of metallic clusters exhibited shifts towards higher binding energies compared to the nominal values of iron bulk and solid surfaces, with the magnitude of the shift depending on the cluster size. These shifts were attributed mainly to initial state effects, particularly the contraction of Fe-Fe bond lengths, as previous theoretical calculations have shown that lattice strain causes positive core level shifts. The magnitude of the shift is also correlated with the reactivity of the system, with a larger core level shift in correspondence of a stabler cluster. Data analysis revealed that Fe₁₃ exhibited the largest core level shift, making it the most stable cluster among those examined, in agreement with the fact that 13 is a magic number for iron clusters and associated with a particularly stable configuration.

After oxidation, the main component in the spectra, depicted in orange in Figure 1(c), could be associated with iron atoms in the Fe(II) oxidation state. The additional component, indicated in light red and observed in Fe₁₃ and Fe₂₀ clusters, was linked to the interaction between iron and graphene carbon atoms. The same trend observed in

metallic clusters was also observed in oxidized clusters, with the Fe 2p_{3/2} core levels of oxidized clusters exhibiting a positive shift attributed to Fe-O bond length contraction compared to bulk and surface iron oxide compounds. Notably, oxidized Fe₁₃ clusters showed the largest core level shift. Since our clusters are electrically neutralized upon impact and no components due to metallic iron or iron atoms in the Fe(III) oxidation state were observed in the spectra, we can conclude that the Fe-to-O ratio in the clusters is close to 1:1. Further exposure to oxygen did not lead to any modifications in the cluster spectra, indicating that Fe(II) is the highest observed oxidation state for iron oxide clusters under these experimental conditions. Our research reveals significant differences in the oxidation mechanisms between supported iron nanoclusters and iron solid surfaces. While iron surfaces undergo multilayer oxidation at room temperature driven by inward oxygen diffusion at the metal-oxide-gas interface, resulting in two oxide phases, the oxidation of Fe nanoclusters leads to the formation of a stable Fe(II) oxide compound. These findings provide evidence that matter at the sub-nanoscale exhibits distinct behaviors with respect to the bulk counterpart. Our results contribute to expand the understanding the oxidation properties nanoscale materials.

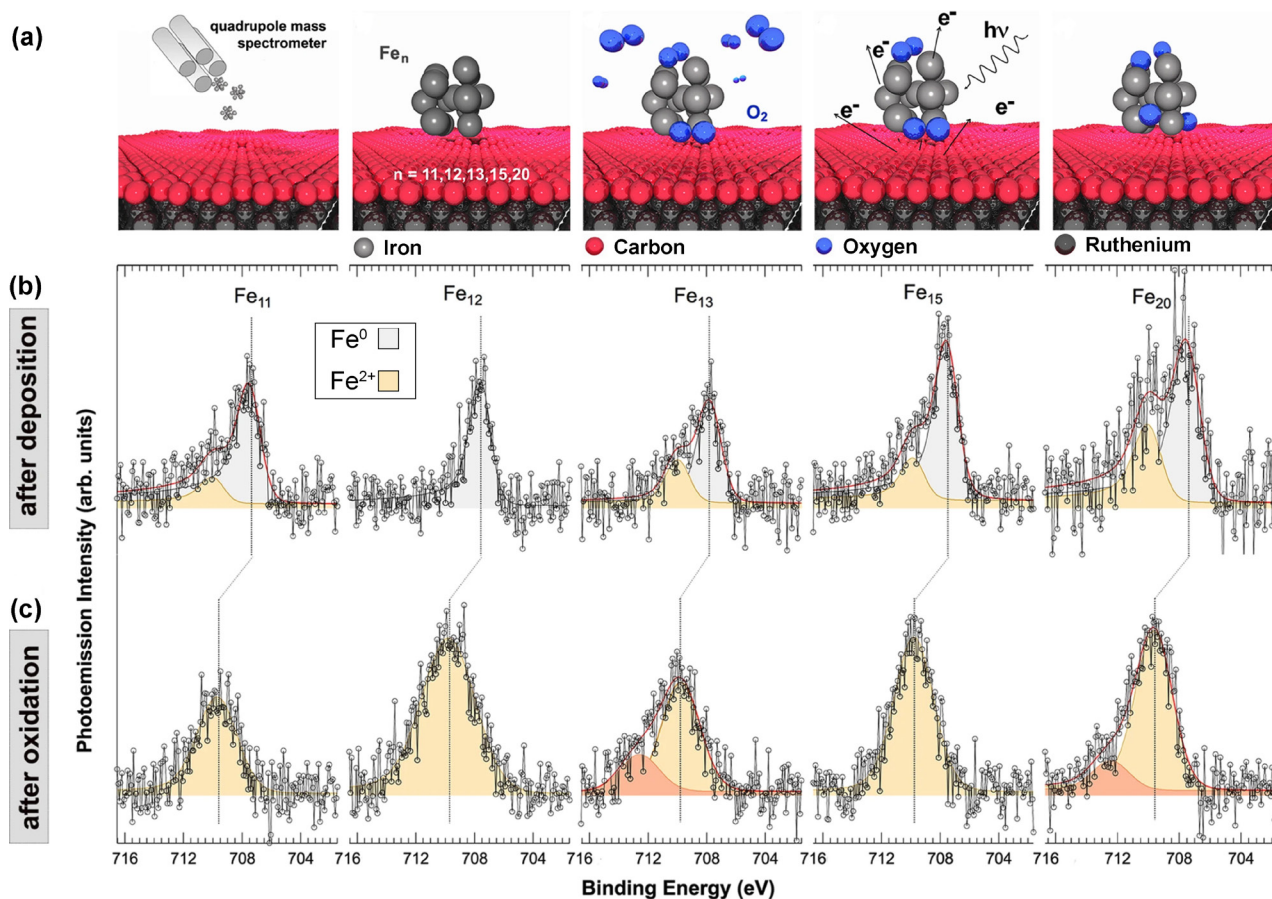


Figure 1. (a) Scheme of the soft-landing deposition and oxidation process of Fe clusters on graphene; Fe 2p_{3/2} for the size-selected clusters, (b) as-deposited and (c) after the exposure to molecular oxygen at 20 K. The size of each cluster is reported near the corresponding spectrum.

Acknowledgments

The authors thank Elettra-Sincrotrone Trieste for the support received during the beamtime allocated at the SuperESCA beamline. We thank G. Panaccione and J. Fuji for very fruitful discussions. A.B. acknowledges funding within the framework of PNR MUR Project PE0000023-NQSTI and from the University of Trieste through the METAMAT project. L.B. acknowledges funding from the University of Trieste through the D55 Microgrants funding initiative. U.H and A.K. acknowledge funding from DFG (HE3454/23-2).

Original paper

D. Perco *et al.*, *Commun. Chem.* **6**, 61 (2023); DOI: 10.1038/s42004-023-00865-x

D. Perco¹, F. Loi¹, L. Bignardi¹, L. Sbuelz¹, P. Lacovig², E. Tosi², S. Lizzit², A. Kartouzian³, U. Heiz³, and A. Baraldi^{1,2}

¹ Physics Department, University of Trieste, Trieste, Italy

² Elettra - Sincrotrone Trieste S.C.p.A., Trieste, Italy

³ Department of Chemistry, Technical University of Munich, Garching, Germany

e-mail: alessandro.baraldi@elettra.eu



Photon Sources and Instrumentation



Elettra status

Elettra | Machine

The operational status of the Italian 2.4/2.0 GeV third generation light source Elettra is presented together with the latest developments.

Status

Elettra operates 24 hours/day, seven days a week delivering 5000 hours/year of synchrotron light from IR to hard x-rays to 28 operating beam lines, 9 of which are served from dipoles and 19 from many types of insertion devices, such as such as planar, polarizing, electromagnetic, superconducting including canted APPLE II type undulators occupying all the eleven available long straights while some dispersive short straights are also used for short insertion devices such as the one 1m long serving the TwinMic, namely a double short APU (Adjustable Phase Undulator).

For 75% of user's dedicated time Elettra operates at 2 GeV, while for the remaining 25% at 2.4 GeV being the only facility to operate at two energies (both in top-up). The main operating modes are multi-bunch with a dark gap of 42 ns and hybrid (42% of the total user beam

time) i.e. multi-bunch with one (for time resolved experiments) or two single bunches (distant 40 ns in a dark gap of 120 ns for pump and probe experiments). The operating beam currents are 310 mA at 2 GeV and 160 mA at 2.4 GeV with 5 mA single bunch added when in hybrid mode.

In Fig. 1, the total availability including surges (interruptions of the power grid, green bars) is shown for the past 10 years of top-up operation. Another important number indicative of the reliability of a light source is the mean time between failures (mtbf, red bars). In 2018 the mtbf decreased due to balance loss of the magnet cooling system after a general maintenance; however, the beam dumps were of very short duration thus not affecting the total uptime. In 2019 a decreased total availability was observed mainly due to an abnormal increase of surges) due to unusually stormy weather.

The number of surges is shown by the solid blue line (right y axis).

An increase of the maximum time between failures is also observed, currently about 360 hours with peaks at 470 hours.

The top-up availability as compared to the total user time is currently 99.0%.

The remaining 1.0% reflects decay-mode operation resulting from some system failure. However, it is considered to be downtime when in decay mode and below a certain current threshold (270 mA at 2 GeV and 130 mA at 2.4 GeV). The injectors themselves did not cause any measurable downtime.

Top-up contributes also to very good long- and short-term orbit stability. Currently the long term (2 to 5 days) stability is $\pm 5 \mu\text{m}$ maximum while the short term (24 hours) at 2% of the beam size ($1.7 \mu\text{m}$ horizontally and $1.2 \mu\text{m}$ vertically).

Developments

A series of projects are in progress in the framework of the development of the new Elettra2.0 DLSR source. Those developments were identified as the ones that can serve both the present and the next machine. Those include:

- Three klystron RF stations have already been replaced with solid state amplifiers that are performing very well while in summer 2023 the last RF station replacement will be completed.

- A spare gun has been constructed that reached 80 kV with 1 A peak current. This gun will be used in Elettra 2.0 but at the moment is a spare in case of

failures of the current gun of Elettra. At the same time the new timing system that will serve also Elettra 2.0 has been successfully tested.

- The production of the Elettra Electron Beam Position Monitors (E2BPM) the novel electron BPM front end with submicron resolution based on pilot tone compensation continues, after the successful test of the prototype within the control system.

- The realization of the MOST beam line which will merge the CiPo and the GasPhase beam lines (Fig. 2). It consists of a fixed gap (low energy undulator

with period of 132 mm, 2.6 m length with minimum photon energy 15 eV for circular polarization and 10 eV for vertical polarization at 2 GeV) and a gap adjustable high energy undulator with period of 50 mm, length 1.5 m and minimum energy 100 eV for circular polarization and 80 eV for horizontal polarization. Both undulators have been manufactured by KYMA S.p.A. and have been installed together with the low gap chamber. During the winter shutdown the light exit will also be installed.

Photon Sources and Instrumentation

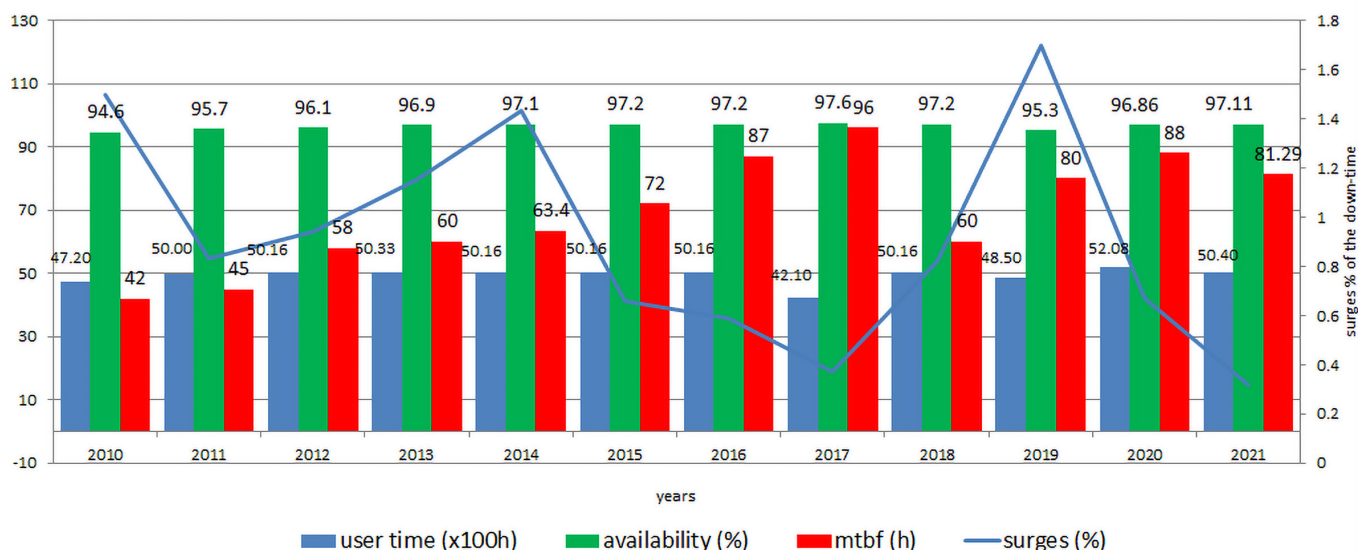


Figure 1. The 10-year user dedicated time (blue), availability (green) and mean time between failures (red bars). The solid line shows the surges.

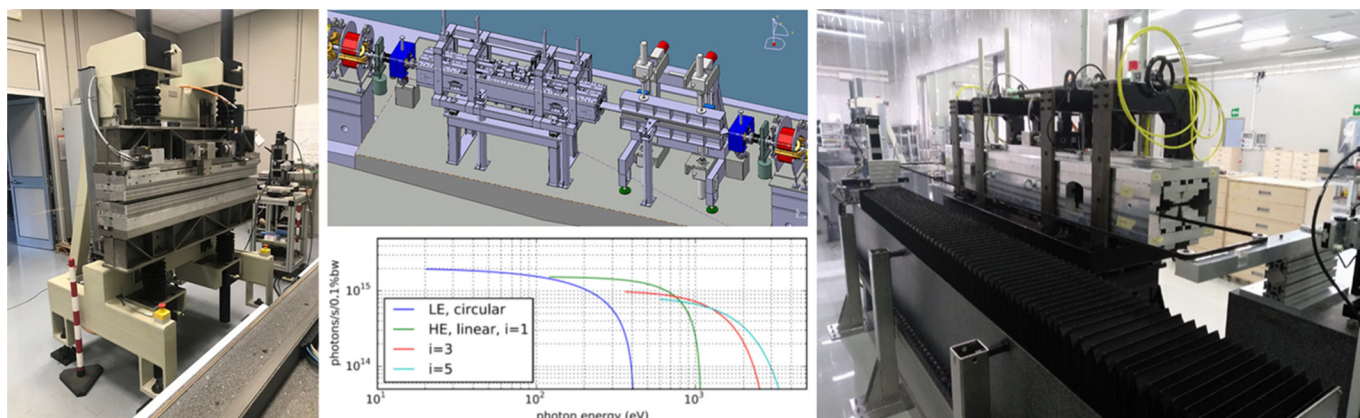


Figure 2. On the left the high energy movable gap undulator and on the right the low energy fixed gap undulator. In the central part both IDs installed in Elettra.

Emanuel Karantzoulis on behalf of the Elettra team

Elettra - Sincrotrone Trieste S.C.p.A., Trieste, Italy

e-mail: emanuel.karantzoulis@elettra.eu

Elettra 2.0

Elettra | Machine

Elettra 2.0 will be a fourth-generation upgrade replacing the existing Elettra light source. This article illustrates the technical choices to meet multiple and sometimes conflicting requirements, in order to make Elettra 2.0 a fully transversely coherent source up to 0.5 keV-photon energy, diversify the type of experiments through a very broad range of photon energies, from the infrared and extreme ultra-violet to hard x-ray range, maximize the number of photon beamlines and produce picosecond-long light pulses at MHz repetition rate at several beamlines with full coherence without interference with the standard multi-bunch operation.

Elettra, that operates as a user facility at two energies, 2 and 2.4 GeV and is optimized to provide the scientific community with photons in the energy range from a few to several tens of keV will be replaced in 2026 by its successor Elettra 2.0 a 4th generation light source. The upgrade project is already running and it is expected to provide new much brighter and coherent light to friendly users in winter 2026 and to all in January 2027.

After many discussions with staff scientists and users and after a few workshops on the future of Elettra, the final requirements for Elettra 2.0 have been determined as follows:

- Operating energy 2.4 GeV (and for some limited time at 2 GeV)
- Reduce the horizontal equilibrium emittance
- Conserve the existing ID beam lines in LS at the same position
- Conserve the existing dipole magnet beam-lines
- Increase the slots available for insertion devices
- Preserve the time structure of the beam and increase the beam intensity to 400 mA
- Let open the possibility for installing bunch compression scheme
- Include super-bends and in-vacuum undulators
- Keep the present injection scheme and injection complex
- Keep the same building and the same ring circumference (259.2 m)
- Minimize the downtime for installation and commissioning to about 18 months maximum.

Based on the final requirements an enhanced version of the previously created S6BA (symmetric six bend achromat being the base of the first CDR available in 2017) was produced, namely S6BA-E by using longitudinal gradient (LG) dipoles (4 per achromat) and reverse bends (shifted quadrupoles, 8 per achromat).

The present version has a bare emittance of 140 pm-rad at 2.0 GeV and 212 pm-rad at 2.4 GeV and consists of 12 identical sectors having long and short straight sections. The net length of the short straights is 1.26 m whereas the net length of the long straights is 4.94 m; with that choice of lengths, the transverse position of the beam lines on the long straight sections compared to the ones in the actual Elettra is almost coincident. For the full intensity case (400 mA), a superconductive third harmonic cavity lengthens the bunch for stability and lifetime, in this case the Touschek lifetime will be about 15 h at 3% coupling and 1 mA/bunch. The beam dimensions in the long and short straights are shown below. Prototypes of magnets, vacuum chambers, girders etc. are being characterized. Calls for tenders have been launched for most machine components. The new machine will have 3 new micro-spot beam lines using in vacuum undulators and three beamlines served by three super-bends (6 T field) in the range of 35 to 50 keV with flux higher than 10^{13} ph/sec.

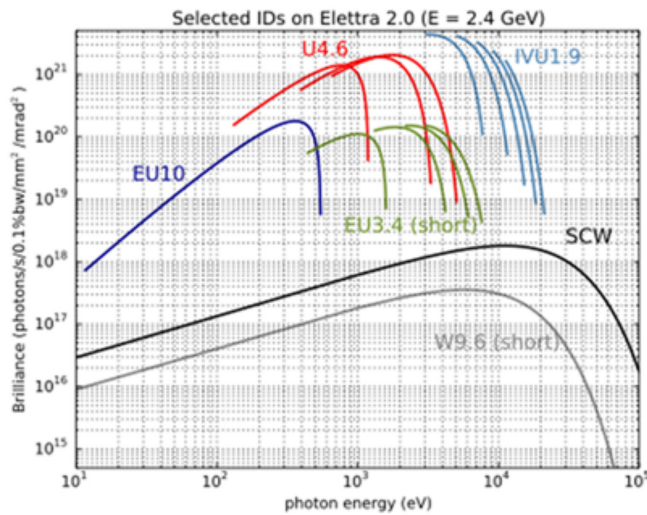
At the same time it seems possible to create at some beam lines short pulses of the order of a few ps (fwhm) by using rf deflecting cavities (See rightmost

panel of Fig 1).

The beam dimensions for 3% and 10% coupling (cpl) in the long straight (LS) and the short straight (SS) sections are shown in Table 1.

Reduction of emittance, flat-beam configuration (transverse emittance ratio $< 5\%$) and increase of the total average current at the higher beam energy, will produce a brilliance increase of up to 3 orders of magnitude and 60-fold higher coherence at 1 keV. This will have a strong impact on pushing the lateral resolution down to a few nanometre scale, since in all experiments using focusing optics this translates directly into an increase in focal flux density. This opens in turn the possibility of performing all types of spectroscopies with nano-sized photon beams (e.g., nano-PES, nano-ARPES) approaching the X-ray imaging spatial resolution of a few nm. Complemented with nano-scale IR and VUV microscopy, the large coherent fraction of the light pulse will allow unprecedented investigations of structure and dynamics in three and four dimensions with variable probing depths. The high coherence of the source will open unique opportunities for coherence-hungry methods. Coherent diffraction imaging with chemical specificity, its scanning mode ptychography and closely related XPCS (X-ray Photon Correlation Spectroscopy), will approach the wavelength-limited spatial resolution with chemical specificity and improved temporal resolution.

Photon Sources and Instrumentation



Section	Beamline	Lowest photon energy				Highest photon energy			
		Δt_{FWHM} (ps)		$\Delta F/F$ (%)		Δt_{FWHM} (ps)		$\Delta F/F$ (%)	
		DR	IM	DR	IM	DR	IM	DR	IM
1.2	Nanospectroscopy	16.5	10	1	3	2	1.8	0.2	3
2.1	TwinMic	48	1.2	1	1.6	45	0.8	0.5	1.7
3.2	Spectro μ	47	10	1	1.6	45	2.9	1	2
4.2	MOST	14	18	0.5	8	2.8	4.5	0.1	10
5.1	XRD1	1.8	1.4	0.2	3	1.3	1.4	0.2	3
5.2	μ XRD	9	0.9	1	2	5.8	0.8	1	2
6.2	CDI	3.5	5.3	0.5	5	1	2.4	0.1	5
7.2	μ XRF	5.5	1	0.4	2	2.4	0.9	0.4	2
8.1	Aloisa	27	1.1	1	1.6	9.4	0.8	0.3	2
8.2	BACH	15	6	0.5	3	2.5	1.8	1	4
9.2	APE LE	38	7	0.2	2	13	1.9	1.5	2
9.2	APE HE	15	2.2	1.5	2	5	1.2	1	2
10.1	APE TX	17	0.8	0.5	1.6	7	0.7	0.5	1.6
10.2	HB-SAXS	1.2	1.3	0.1	3	0.9	1.2	0.1	3
11.1	XAS-mW	1.4	23	0.1	50	1	22	0.1	50
11.2	Xpress (SCW)	30	1.1	0.5	2	17	1.1	1	2.5

Figure 1. The brilliance of some old and new insertion devices (left) and the short pulse duration (*fwhm*) for each beamline (right). DR stands for drift and IM for imaging optics. In yellow are marked pulses that are less than 3 ps.

Energy 2.4 GeV	LS at 3% cpl	LS at 10% cpl	SS at 3% cpl	SS at 10% cpl
σ_x (um) / σ'_x (urad)	36 / 5.7	35 / 5.5	63 / 6	63 / 5.8
σ_y (um) / σ'_y (urad)	3.2 / 1.9	5.7 / 3.4	3.5 / 1.8	6 / 3

Energy 2.0 GeV	LS at 3% cpl	LS at 10% cpl	SS at 3% cpl	SS at 10% cpl
σ_x (um) / σ'_x (urad)	30 / 4.8	29 / 4.6	53 / 5	52 / 4.8
σ_y (um) / σ'_y (urad)	2.7 / 1.6	4.7 / 2.8	2.9 / 1.5	5.1 / 2.6

Table 1.

References

A. Abrami, A. Amenitsch, L. Avaldi, A. Barinov, A. Barla, D. Baron, S. Bassanese, A. Bianco, F. Billè, R. Borges, P. Borsi, A. Buonanno, E. Busetto, C. Carbone, A. Carniel, D. Castronovo, K. Casarin, M. Cautero, V. Chenda, S. Cleva, A. Coronica, I. Cudin, S. Dastan, S. Di Mitri, R. De Monte, B. Diviacco, A. Fabris, R. Fabris, I. Ferigutti, A. Franciosi, P. Furlan Radivo, G. Gaio, A. Galimberti, F. Giacuzzo, A. Goldoni, L. Gregorati, E. Karantzoulis, M. Kiskinova, G. Kourousias, S. Krecic, R. Laghi, S. Lizzit, G. Loda, M. Lonza, S. Lupi, A. Locatelli, C. Macsiovecchio, K. Manukyan, A. Martinolli, E. Mazzucco, P. Michelini, M. Miculin, P. Moras, L. Novinec, G. Pangon, G. Paolucci, C. Pasotti, R. Passuello, L. Pivetta, M. Polentarutti, K. Prince, R. Pugliese, L. Raimondi, L. Rumiz, R. Sauro, L. Sturari, C. Scafuri, G. Stopar, M. Svandrlik, P. Tosolini, M. Trevi, G. Tromba, L. Vaccari, A. Vascotto, R. Visintini, D. Vivoda, M. Zaccaria, D. Zangrando "Elettra 2.0 Technical Design Report", ST/M-21/01, Elettra–Sincrotrone Trieste, internal document (2021).

e-mail: emanuel.karantzoulis@elettra.eu

Polarizers for solar physics at key spectral lines

Elettra | BEAR

The magnetic structure and thermodynamics of the solar corona and chromosphere have broad implications for solar atmosphere and they are essential research goals in solar physics. These research fields require measuring the magnetic field in the chromosphere and solar corona.

The solar magnetic field is best observed through light polarization. Line-radiation that is resonantly scattered by an anisotropic illuminating source turns linearly polarized. The presence of a magnetic field modifies such polarization in a process known as the Hanle effect. By measuring the polarization degree and direction we can diagnose the magnetic field orientation and strength. The majority of the sensitive spectral lines to the magnetic field are localized at the UV (ultraviolet) and FUV (far ultraviolet) spectral ranges, which makes UV-FUV polarimetry a powerful tool to measure the magnetic field. Due to the absorption of the atmosphere of the UV-FUV radiation, solar polarimetry must be performed outside the atmosphere or at a high enough orbit.

A key spectral line for solar atmosphere's polarimetry is H I Lyman α (121.6 nm), which is the brightest line that is sensitive to Hanle effect. Complementarily, the C IV doublet (155 nm) is one of the most important transitions for optical diagnostics of hot plasmas in the stellar atmospheres. Last but not least, the Mg II line (280 nm) is the most important radiator of the chromosphere. Hence our research has addressed these three key spectral lines.

Central elements for polarimetry are linear polarizers. In addition to imaging instrumentation for astrophysics and solar physics, linear polarizers are used in many technological applications. Bulk polarizers, such as Wollaston and Rochon prisms, are available in the UV and in parts of the FUV. These devices require ultrasmooth polished surfaces to minimize absorption, which

is complicated to reach in the FUV. They also turn bulky for large-aperture optics, which is a difficulty for space instruments.

Instead, a multilayer coating is a choice of an efficient UV-FUV polarizer. The coating can be tuned at the desired wavelength(s) through layer thickness optimization. A coating polarizer can be designed as a beamsplitter, so that film thicknesses are selected to provide the required reflective and transmissive profiles. Being a single device to separate the two crossed polarization components, multilayer beamsplitter polarizers are a useful tool that allows reducing energy losses and weight in a future more compact space polarimeter. Due to their coating nature, they can be easily scaled up compared to bulk devices.

Multilayer beamsplitter polarizers were prepared at GOLD-Instituto de Optica-CSIC in a 75-cm diameter, 100-cm height, cylindrical, stainless-steel chamber installed in an ISO-6 cleanroom dedicated to coat space optics. Coatings were designed to preferentially reflecting one polarization component (s polarization, i.e., transverse electric) and transmitting the other (p polarization, i.e., transverse magnetic). Polarizers simultaneously tuned at 155 nm and 280 nm were prepared by depositing an (Al/AlF₃)₃ multilayer on a quartz substrate. Polarizers tuned at 121.6 nm were prepared by depositing an (Al/MgF₂)₂ multilayer on an MgF₂ substrate.

The polarizers were measured at BEAR/Elettra. Radiation emitted by the storage ring is linearly polarized in the storage plane, which is an essential property to measure the polarizers. Anyway, some proportion of the crossed polarization is present as soon as the light beam used to measure the polarizers contains some light coming from slightly away from the storage ring plane. In practice, the proportion of light with crossed polarization is minimized by limiting the emission angle through a double-slit device. Since light arrives at BEAR

reflectometer chamber with a given polarization, measurements were performed with the chamber (which is able to rotate) oriented with respect to the beam at an angle of 0° (for s polarization) or 90° (for p polarization). Figure 1 presents the performance of the polarizer tuned at 155 and 280 nm. The polarizer is successful for the referred application since it provides a large difference in reflectance (Rs over Rp) and in transmittance (Tp over Ts). The polarizer is more efficient in reflectance than in transmittance; the presence of Al films in the coating involves radiation absorption, which is responsible for the reduced efficiency in transmittance. Yet, the polarizer working in transmittance also performs some filtering mainly of longer wavelengths, which can compensate for the smaller polarizer performance in transmittance. Good results were also obtained for beamsplitter polarizers tuned at 121.6 nm. A sample aged of 4 years had a performance at an angle of incidence of 70° of 72% (Rs), 13% (Rp), 1.4% (Ts), and 13.3% (Tp), which again are promising values to apply in a solar polarimeter.

The usefulness of the present beamsplitter polarizers was assessed by comparing their performance with more conventional polarizers, such as a parallel plate of MgF₂ at Brewster angle and a pile of plates made of LiF. The presented coating polarizers were found to be more efficient than the more conventional ones when the polarization capacity is combined with the overall performance for unpolarized light.

In conclusion, the presented multilayer beamsplitter polarizers display unique properties: 1) high polarization contrast in a broad angle range compared to Rochon polarizers; 2) cost-effective to apply over large optics, also compared to Rochon polarizers; 3) by transmission, they filter the long wavelengths, so that they can be useful in presence of heat load, such as in solar observations.

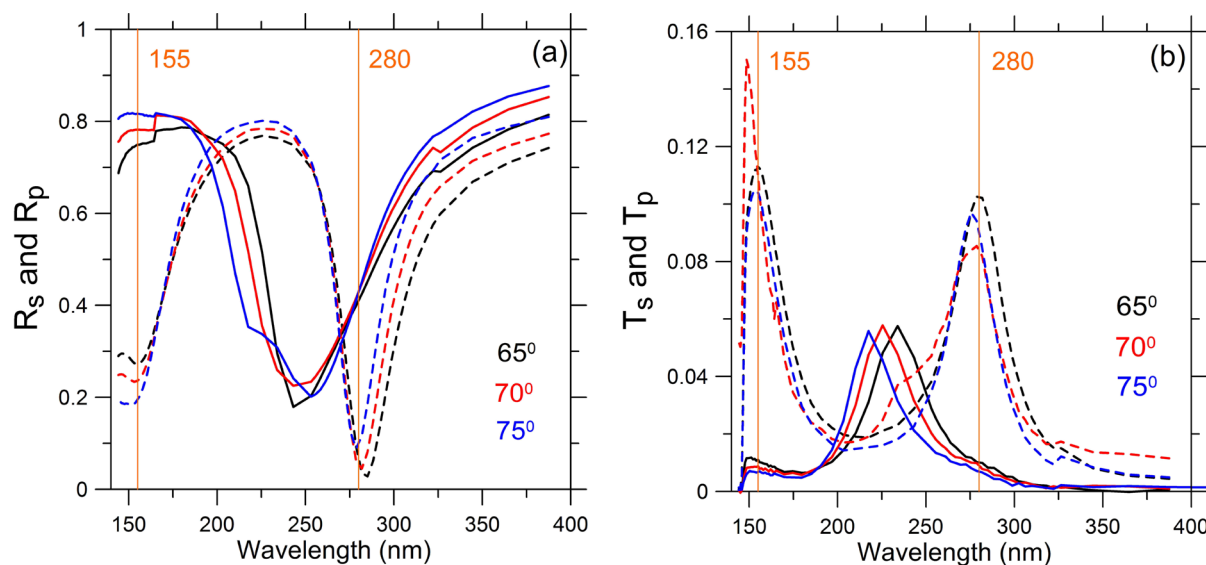


Figure 1. (a) Reflectance and (b) transmittance measured at s polarization (solid lines) and p polarization (dashed lines) for a beamsplitter polarizer simultaneously tuned at the C IV line (155 nm) and at the Mg II line (280 nm). The polarizer was designed to operate at an angle of incidence of 70°; measurements were performed at this angle and also at 65° and 75°. Measurements correspond to a sample aged of 3 years. The large difference in reflectance (R_s over R_p) and in transmittance (T_p over T_s) makes this coating useful as a linear polarizer for solar polarimetry. Reproduced from N. Gutiérrez-Luna et al, *Opt. Express* **30**, 16 (29735)

Acknowledgments

We acknowledge support by the European Community-Research Infrastructure Action under the FP6 'Structuring the European Research Area' Programme (through the Integrated Infrastructure Initiative 'Integrating Activity on Synchrotron and Free Electron Laser Science'); measurements were performed under Elettra proposal numbers 20150344, 20155497, 20165506, 20170445, 20180233, 20190371, 20210186 and AHEAD2020 proposal 871158. We acknowledge support by "Subdirección General de Proyectos de Investigación, Ministerio de Ciencia e Innovación", projects number ESP2016-76591-P and PID2019-105156GB-I00. LRM acknowledges CRESST II cooperative agreement supported by NASA under award number 80GSFC21M0002.

Original paper

N. Gutiérrez-Luna et al., *Opt. Express* **30**, 16 (29735) ; DOI:10.1364/OE.463215

N. Gutiérrez-Luna¹, G. Capobianco², A.M. Malvezzi^{2,3}, C. Honrado-Benitez¹, L.V. Rodríguez-De Marcos^{1,4}, J.I. Larruquert¹, A. Giglia³, N. Mahne³, S. Nannarone³, S. Fineschi²

¹ Instituto de Optica-Consejo Superior de Investigaciones Científicas, Madrid, Spain

² Turin Astrophysical Observatory, INAF, Torino, Italy

³ IOM-CNR, Trieste, Italy

⁴ Catholic University of America and NASA Goddard Space Flight Center (CRESST II), Greenbelt, MD, USA

e-mail: nuria.gutierrez@csic.es; j.larruquert@csic.es

Synchrotron radiation study of GaAs avalanche photodiodes for hard x-ray

Instrumentation and Detectors Laboratory
Elettra | TwinMic

APD (Avalanche Photodiodes) are semiconductor devices used to detect light, operating on the principle of avalanche multiplication, which allows them to achieve higher sensitivity and lower noise compared to standard photodiodes.

In an APD, the incident photons generate electron-hole pairs in the depletion region of the device. These charge carriers are accelerated by a high electric field present in the APD, causing them to gain energy and create additional electron-hole pairs through impact ionization. This multiplication process leads to an internal current gain, enabling APDs to achieve higher levels of signal detection by amplifying the photo-current above the noise floor of the read-out circuit, significantly improving the SNR (signal-to-noise ratio). This property makes them very effective in sensing extremely weak signals.

SAM-APDs (Separate Adsorption Multiplication - APD) are specific devices designed to enhance APD performance. In a standard APD, the absorption and multiplication regions are combined within a single material while, in a SAM-APD, these regions are physically separated, allowing for better optimization of their respective properties.

This design can lead to improved efficiency, higher gain, and lower noise, making SAM-APDs particularly useful in applications that require high sensitivity and single photon detection.

For photons in the visible up to soft x-ray range, the best-known and most widely used SAM-APDs are based on silicon. For shorter wavelengths (<1 nm), i.e., in the x-ray region, absorption capabilities of silicon SAM-APDs decrease rapidly with increasing photon energy. This limits their use in many synchrotron radiation and free-electron laser experiments, since x-ray absorption scales with a high power of the atomic number, at least in the energy range dominated by the photoelectric effect.

Compared to silicon devices, compound semiconductors based on III-V elements,

such as GaAs, have some unique properties, such as a higher density, a high effective atomic number, a direct energy band gap, high electric-breakdown fields, and a high electron mobility, which makes them suitable for photonic, radiofrequency, and high-power device technologies.

The absorption lengths for medium and hard x-ray energies are substantially shorter in GaAs than in Si, owing to the higher effective atomic number. This results in a much higher absorption coefficient and higher detection efficiency when compared to Si sensors of the same thickness.

Thanks to the characteristics listed above, in recent years GaAs has been studied as Si alternatives for the production of x-ray detectors. In particular their use is of great interest for high-energy fluorescence spectroscopy, not only for the aforementioned higher efficiency compared to silicon but also for the possibility of working at room temperature, as opposed to the germanium-based detectors currently used for high energies, which require liquid nitrogen cooling.

Over the past decade, a fruitful collaboration has emerged between CNR-IOM, University of Udine, and the Instrumentation and Detectors Laboratory at Elettra Sincrotrone Trieste. This partnership aims to develop cutting-edge GaAs SAM-APDs tailored for the detection of hard x-rays. These devices are characterized by the use of band gap engineering to create multiplication layers based on the superlattice resulting in a staircase profile of the conduction band, which greatly reduces the multiplication noise, that is the main traditional limitation of GaAs-based APD devices.

This study focuses on the characterization of developed GaAs SAM-APD (Fig. 1a), with particular emphasis on investigating the impact of the absorption region's thickness. In fact, this parameter plays a critical role when detecting high-energy photons, as significant thickness is needed to optimize the absorption efficiency.

Initially, the devices were subjected to a comprehensive characterization using laser light. Subsequently, synchrotron light was employed to perform measurements on the TwinMic beamline of Elettra, aiming to examine the relationship between devices efficiency and radiation penetration depth in the absorption region.

Laser measurements have shown gains of the order of some tens (Fig. 1b) with low multiplication noise thanks to the staircase structure of the multiplication region. The multiplication noise ENF (Excess Noise Factor) in APD is related to the ratio of the ionization coefficients for electrons and holes: when this ratio is close to 1 the noise is very high. Unfortunately, this is precisely the situation with GaAs. For this reason, the staircase structure is necessary, which reduces the probability of multiplication by impact of the holes and the ratio k between the two coefficients deviates from one, which results in a better SNR (Fig. 1c).

Then, measurements performed with synchrotron light enabled the creation of high-resolution x-ray fluorescence images of the devices (Fig. 1d). Moreover, thanks to the availability of a micrometric radiation beam and the presence of entrance windows (not covered by the Cr/Au anode, Fig. 1d), photocurrents could be generated without interactions between the beam and the electrode; this allowed assessing the net role of the interface between the anode and semiconductor.

Finally, the impact of the absorption region thickness was carefully analyzed, allowing to create the photocurrents at different depths in the absorption layer, irradiating the devices featuring different thicknesses of the absorption layer with photons of different energies.

The measurements have shown that the efficiency substantially does not change by varying the point of electron-hole creation within the absorption region nor by varying the thickness of the absorption region from 300 nm to 15 microns (Fig. 1e).

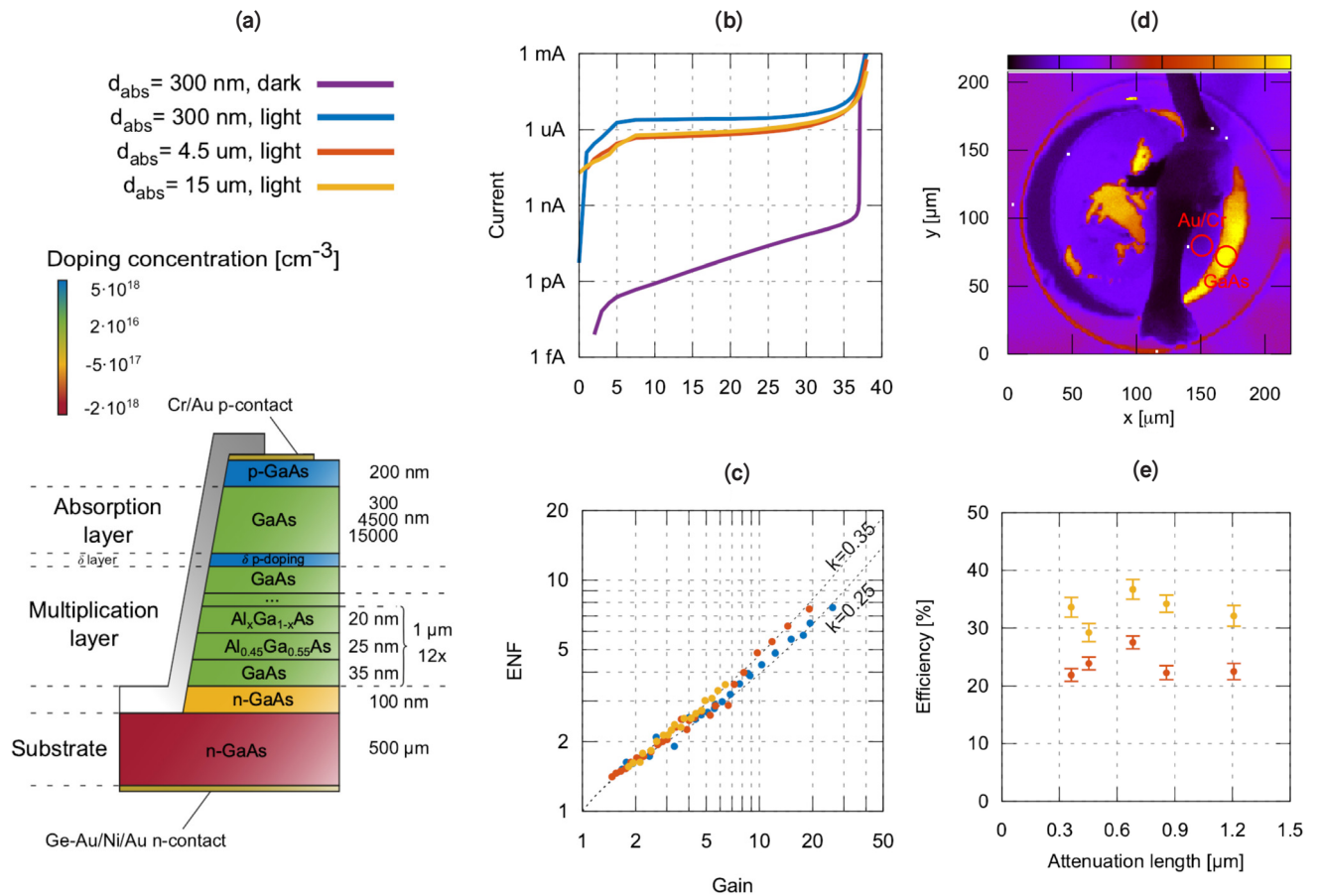


Figure 1: (a) Sketch of the GaAs APDs considered in this work (not to scale). The grown layered structure is depicted, where the layer color represents its doping concentration; (b) Dark I–V characteristics of the device with $d_{\text{abs}} = 300 \text{ nm}$ compared to light I–V measurements (Plaser $\approx 50 \text{ μW}$, $\lambda = 532 \text{ nm}$) of the three types of devices; (c) Calculated ENF for the three devices as function of k , which is the ratio of the ionization coefficients for electrons and holes; (d) x-ray fluorescence image of the As La line; the dark shadow is the Al wire-bond. The unexposed half-moon shaped areas of devices are clearly visible; (e) Efficiency as a function of attenuation length (function of the photon energy) of the 15 μm (yellow dots) and 4.5 μm (red dots) devices.

Acknowledgments

This work was financially supported by statutory funds from Elettra-Sincrotrone Trieste S.C.p.A. and IOM CNR, Laboratorio TASC.

Original paper

M. Colja *et al.* *Sensors* 2022, **22**, 4598.
 DOI:10.3390/s22124598

M. Colja¹, M. Cautero¹, R.H. Menk^{2,3,4}, P. Palestri⁵, A. Gianoncelli², M. Antonelli³, G. Biasiol⁶, S. Dal Zilio⁶, T. Steinhartova⁶, C. Nichetti⁷, F. Arfelli^{3,7}, D. De Angelis², F. Driussi⁵, V. Bonanni², A. Pilotto⁵, G. Gariani², S. Carrato¹, G. Cautero^{2,3}

¹ Department of Engineering and Architecture, University of Trieste, Trieste, Italy

² Elettra - Sincrotrone Trieste S.C.p.A., Trieste, Italy

³ Istituto Nazionale di Fisica Nucleare Sezione di Trieste, Trieste, Italy

⁴ Department of Medical Imaging, University of Saskatchewan, Saskatoon, Canada

⁵ Polytechnic Department of Engineering and Architecture, University of Udine, Udine, Italy

⁶ CNR-IOM, Laboratorio TASC, Trieste, Italy

⁷ Department of Physics, University of Trieste, Trieste, Italy

e-mail: Matija.colja@elettra.eu

FERMI Status Report

FERMI | Machine

We report on the status of FERMI, the machine and beamlines developments. In 2022, FERMI was operating for the majority of the time to carry out external users and in-house experiments. The availability of the FEL source reached 95.5% in 2022, a significant improvement compared to previous years. The upgrade plan for FERMI 2.0 also saw progress, with the installation of the new accelerating cavities, the development of the spherical compressor and the upgrade of FEL-1 to the EEHG configuration, that was partially completed, with the remaining work scheduled for 2023.

In 2022, FERMI focused primarily on developing and conducting experiments with external users. Throughout the year, FERMI was operational for a total of 5,856 hours. Out of this, 92% of the time was dedicated to operating the source for external users and in-house experiments, while the remaining 8% was allocated to machine physics studies. These percentages remained consistent with those of 2021. In 2022 the impact of the SARS-COV-2 pandemic on experimental activities was minimal, mainly limiting the maximum number of researchers allowed at the experimental stations. The implementation of automated control methods started in 2021 was ameliorated during 2022 enabling the successful execution of all planned experiments with extensive remote user participation. The number of experiments conducted with external users in 2022 was 29, which is comparable to the pre-pandemic phase (31 experiments in 2019). This demonstrates FERMI's ability to maintain a robust level of user engagement despite the prevailing circumstances. The actual availability of the FEL source for experiments, in relation to the scheduled time, reached 95.5% in 2022, excluding downtime resulting from thunderstorms. This marks an improvement from the 93.5% availability recorded in 2021. Achieving such a high level of reliability was made possible through proactive maintenance of critical equipment, such as klystrons and laser systems, and the

implementation of algorithms based on automatic optimization procedures. These algorithms played a vital role in automating and optimizing machine performance. Overall, FERMI's activities in 2022 demonstrated a strong commitment to facilitating experimental research and ensuring a high level of reliability and user satisfaction. FERMI continues to be an international point of reference in the field of free electron lasers research infrastructures. In fact, in 2022 the number of publications with a high scientific impact was 14, which is almost 50% of the total number of publications equal to 29, demonstrating the very high scientific quality of the results produced by FERMI users. Among the relevant publications it is important to mention the use of beams with optical angular momentum which allowed to study the magnetic response on both macroscopic systems, at the DiProl experimental station, and nanometric systems on the LDM beamline. The MagneDyn beamline was used to inject and probe spin-polarized currents in silicon. This result is a first step towards the development of technologies that allow magnetic storage to be combined with electronic reading in a single semiconductor device, with a series of important advantages for the microelectronics industry. The use of the non-linear response of a magnetic multilayer system has highlighted, with an experiment carried out on the TIMER experimental station, the possibility of realizing optical switching processes

at the nanoscale. This result is of particular interest for the development of new technologies that allow a considerable improvement in the speed of transmission and storage of digital data. Moreover a fluorescence imaging system has been developed on TIMER, which was used in combination with sub-micrometric structured illumination provided by EUV transient grating to determine Fourier components of the image beyond the limit imposed by the numerical aperture of the microscope and the fluorescence wavelength (structured illumination microscopy). The obtained results are very promising and demonstrate how this approach allows for spatial information to be obtained on a scale of 100 nm. During 2022, FERMI made significant progress in both the exploration of new configurations for scientific applications and the launch of the "early" upgrade plan outlined in the FERMI 2.0 CDR (Conceptual Design Report). One notable achievement was the utilization of higher-order harmonics to conduct user experiments at the L-edge of iron. Although the number of photons available was approximately 10^3 times lower than the estimated amount for the machine after the completion of the upgrade process described in the CDR, significant advancements were still made in this area (Fig. 1). FERMI's early upgrade process commenced with the replacement of the horizontal deflector and the last accelerating section, employing the back travelling wave BTW (Backward

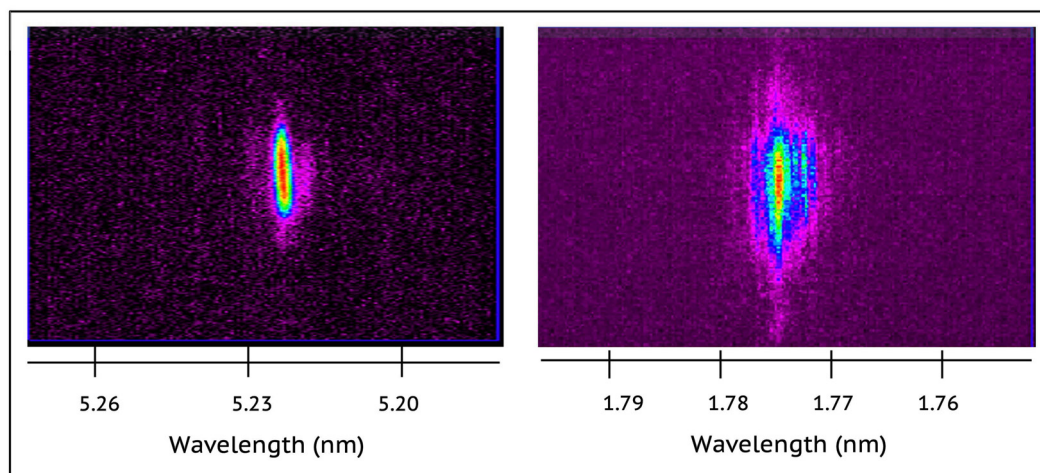


Figure 1. FEL spectrum at the 5.2 nm (fundamental) and at third harmonic (1.7 nm). The two spectra are simultaneously measured at the PRESTO and WEST spectrometers, on TIMEX. Using a combination of filters (Cu-100nm, Pd-100 nm and Cu-200 nm) it was possible to estimate a pulse energy at 1.7 nm of about 100 nJ.

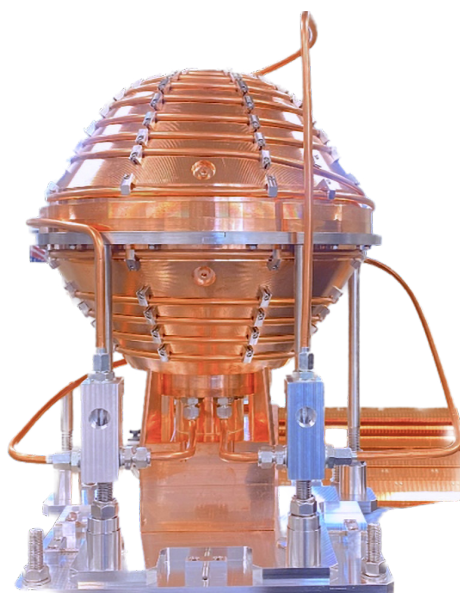


Figure 2. Final fabricated version of the first spherical pulse compressor

Travelling Wave) scheme, with two high-gradient prototype accelerating sections. These sections were developed in collaboration with PSI and were received by the FERMI LINAC & RF team during 2022. The first section underwent bench conditioning in full compliance with project parameters, while the second section, received just before the summer shutdown, was directly installed in the LINAC. Additionally, the development of the spherical compressor (Fig. 2), which will replace the currently installed SLAC Linac energy doubler (SLED) in

the BTW sections of the machine, was successfully completed. The device met all design parameters, and the conditioning process progressed smoothly. The spherical compressor offers a compact and cost-effective solution for power amplification while replacing outdated and bulky SLEDs. Simultaneously, the upgrade process of FEL-1 to the EEHG (Echo-Enabled Harmonic Generation) configuration continued. This involved the installation of undulators in their final configuration, the implementation of a new modulator, and the installation of supports and

modified vacuum chambers, as required by the new configuration. Following the modifications, the operation of FEL-1 in the HGHG configuration was verified, showcasing performance at least equivalent to the previous configuration. However, due to a delay in the delivery of dipoles for the dispersive section of FEL-1, the conversion work planned for the 2022 winter shutdown could not be completed as originally scheduled. This installation has been postponed to 2023 pending the delivery of the missing components.

C. Masciovecchio¹ and L. Giannessi^{1,2} on behalf of the FERMI team

¹ Elettra Sincrotrone Trieste S.C.p.A., Trieste, Italy

² INFN - Laboratori Nazionali di Frascati, Rome, Italy

e-mail: claudio.masciovecchio@elettra.eu; luca.giannessi@elettra.eu

Free electron laser stochastic spectroscopy revealing silicon bond softening dynamics

FERMI | EIS-TIMEX, DiProI

The absorption spectroscopy in EUV (Extreme Ultraviolet) regime is one of the most robust and diffused methods for the investigation of the chemical and structural properties of matter. Historically, this kind of spectroscopy has been developed at synchrotron facilities with the aim of improving the energy resolution and signal to noise ratio. Nowadays, synchrotron spectroscopy is extensively used in a large number of scientific fields, ranging among condensed matter, organic and inorganic chemistry, nanotechnology, photo-catalysis, and molecular biology. In the last decades, another challenge has been addressed, consisting in the development of time resolved spectroscopy to investigate the condensed matter dynamics in the range of pico- and femtoseconds. The development of this experimental approach proceeded on two opposite photon energy regimes, i.e. x-ray and UV-visible. With this work we filled the photon energy gap across EUV, by exploiting the flexible capabilities of the FERMI FEL (Free Electron Laser) source operating in SASE (Self Amplified Stimulated Emission) mode.

In the UV range, HHG (High Harmonic Generation) sources-based techniques are the most used, despite they suffer from low intensity at higher photon energy. Their use in the far UV and EUV is therefore not advised. FELs provide much higher photon fluxes, but there are few sources in the world, so that access is limited. For this reason, the efficient use of FEL sources is paramount: it requires the implementation of novel approaches to spectroscopy, which benefit from the high-peak brightness and broad spectral bandwidth typical of self amplified FEL pulses. In this respect, it is highly desirable to develop multiplexing approaches capable of simultaneously exploiting a large spectral bandwidth without the need for spectral filtering and photon-energy scanning. An elegant and effective solution to multiplex-based spectroscopy is

represented by correlation spectroscopy methods based on the determination of the statistical fluctuations introduced by the interaction of the light pulses with the sample; such approaches have been realized both in the optical region as well as in the x-ray range.

In our case we had the FERMI FEL operated in an analogous of the self amplified regime (called optical klystron mode) to obtain a stochastic energy distribution of the photons within each pulse. We developed a method for accumulating single pulse spectra measured before and after the sample, by using the two available spectrometers (PRESTO and WEST, upstream and downstream the sample, respectively). On the basis of regularized matrix inversion methods, we developed an analytic tool to extract correlation information between the two sets of spectra (upstream and downstream) after accumulating about 100 thousand pulses. We were able to reconstruct the elastic and inelastic response 2D map of the sample (Fig. 1 a), from which it was possible to extract EUV emission (Fig. 1 a, inset) and transmission spectra (Figs. 1 b).

The time resolution of this correlation technique emerges from the intrinsic pulsed regime of the lightsource, which is capable of producing light pulses of the order of 1 ps time duration. We applied this feature to investigate the dynamics of a silicon crystal excited by a visible light pulse at a fluence regime at which Si covalent bonds start to weaken in virtue of the large amount of free charges within the crystal structure. This phenomenon, that implies a transient structural modification of the material is known as Bond-Softening (BSO). With our setup we had the possibility to track the variation of the $L_{2,3}$ absorption edge of Silicon as a function of the delay between the visible pump and the EUV probe (Figs. 1 c,d). In particular, we observed two opposite dynamics for the pre- and post-edge. At the same time, we could observe

the dynamics of the emission features highlighted in fig. 1a.

In the XAS spectra, we identified two distinct dynamics: (i) an increase (decrease) of the sample transmission in the pre-(post)-edge region during the first 2 ps after excitation; and (ii) an inflection (increase) of the transmission between 2 and 50 ps, slightly faster in the pre-edge region with respect to the post-edge one, which progressively recovers the transmission of the sample before excitation.

In the XES spectra we also observed a dynamics with a recovery time of ~50 ps. We could therefore infer that the transmission and emission dynamics are related to the same electronic/structural phenomenon in the excited c-Si during the first 50 ps after the laser pulse. A schematic representation of the electronic structure modification is depicted in Fig. 1 for the pre-edge (e) and post-edge (f) photon energy states, respectively: the excited and delocalized electrons generated by the pump pulse are expected to occupy non-bonding and anti-bonding states in the conduction band and to weaken the atomic covalent bonds. In the 50 ps time scale, during the thermalization of the system, lattice modifications are expected to occur. We believe that our correlation spectroscopy approach offers great advantages in the study of electronic dynamics due to its ability to extract information from both occupied and unoccupied electronic states simultaneously.

In a more general context, EUV stochastic correlation spectroscopy provides comparable information to synchrotron-based measurements in terms of acquisition time, signal-to-noise ratio and energy resolution, with the valuable additional advantage of allowing time-resolved measurements with sub-picosecond resolution and the simultaneous determination of the XES response.

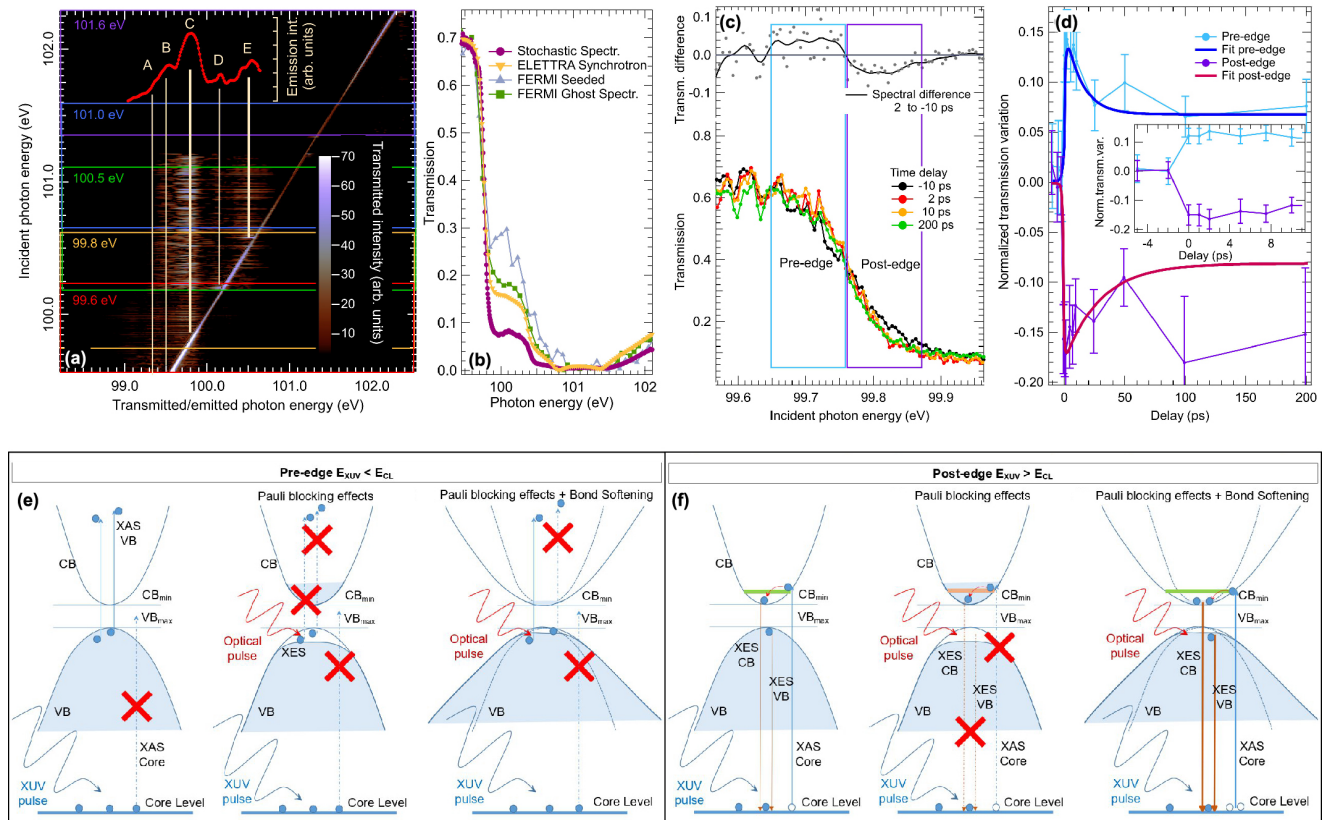


Figure 1. (a) Reconstructed sample response map at equilibrium. Colored rectangles refer to five photon-energy settings of the SASE-like emission, while vertical white lines indicate the emission features. Inset in red represents the integrated emission spectrum; (b) Transmission profile of c-Si $L_{2,3}$ -edge, as obtained from the diagonal terms of the sample response map (purple dots connected by lines; here, error bars are $<2\%$ and cannot be resolved on this scale), is compared to other spectroscopic methods, as detailed in the legend; (c) Selected transmission spectra before and after optical excitation, as indicated in the legend. Light blue and purple rectangles define the “pre-edge” (99.65–99.76 eV) and “post-edge” (99.76–99.87 eV) spectral regions. (d) Light blue and purple data refer to the time dependence of the normalized variation of the transmitted intensity in the pre-edge and post-edge regions, respectively; fit results are shown in the same plot. Inset shows an enlargement of the initial part of the dynamics; (e, f) Schematic representation of the electronic processes described in the text, related to EUV absorption for the pre- (e) and post-edge (f). In each panel: from the left, i) static case, i.e., EUV absorption in the absence of the laser pump pulse; ii) EUV absorption occurring after laser pump, in the absence of the BSo effect; iii) EUV absorption occurring after laser pump in the presence of the BSo effect.

Acknowledgments

We acknowledge FERMI staff for the support during the data collection campaign, in particular Luca Giannessi and Giuseppe Penco for the discussion on the optical klystron lasing scheme. J. S. acknowledges partial support from the National Science Centre (Poland) under Grant No. 2017/27/B/ST2/01890.

Original paper

D. De Angelis *et al.*, Phys. Rev. B **107**, 214305 (2023); DOI: 10.1103/PhysRevB.107.214305

D. De Angelis^{1,2}, E. Principi¹, F. Bencivenga¹, D. Fausti^{1,3,4}, L. Foglia¹, Y. Klein⁵, M. Manfreda¹, R. Mincigrucci¹, A. Montanaro^{1,3,4}, E. Pedersoli¹, J. S. Pelli Cresi¹, G. Perosa¹, K. C. Prince¹, E. Razzoli⁶, S. Shwartz⁵, A. Simoncig¹, S. Spampinati¹, C. Svetina⁷, J. Szlachetko⁸, A. Tripathi⁵, I. A. Vartanyants⁹, M. Zangrando^{1,2}, F. Capotondi¹

¹ Elettra - Sincrotrone Trieste, Trieste, Italy

² IOM-CNR, Trieste, Italy

³ Department of Physics, University of Trieste, Trieste, Italy

⁴ Chair of Solid State Physics, Friedrich-Alexander-Universität Erlangen-Nürnberg, Erlangen, Germany

⁵ Physics Department and Institute of Nanotechnology and advanced Materials, Bar Ilan University, Ramat Gan, Israel

⁶ Paul Scherrer Institut, Switzerland

⁷ Madrid Institute for Advanced Studies, IMDEA Nanociencia, Madrid, Spain

⁸ SOLARIS National Synchrotron Radiation Centre, Jagiellonian University, Krakow, Poland

⁹ Deutsches Elektronen-Synchrotron DESY, Hamburg, Germany

e-mail: deangelis@iom.cnr.it

Polarization shaping of ultrashort extreme-ultraviolet light pulses

FERMI | LDM

Generation of laser pulses whose polarization is varying on an ultrashort time scale is an established technique in the visible spectrum. It has been successfully used in a number of applications, especially for the characterization and (coherent) control of electronic properties.

The ability to generate polarization-shaped pulses in the XUV (extreme-ultraviolet) and x-ray spectral regions would improve spatio-temporal resolution and element selectivity, and potentially lead to the development of new coherent control methods for probing and manipulating tightly bound electrons in matter. Unfortunately, tailoring the polarization profile of short and intense XUV or x-ray pulses cannot be achieved by using pulse shapers developed for conventional lasers, which operate in the visible spectrum. However, a seeded FEL (Free-Electron Laser), which amplifies light generated by tailored relativistic electron beam, provides an answer to this problem. The proposed and experimentally demonstrated layout is sketched in Fig. 1(a). After interacting with the seed laser (a conventional visible or UV laser) in the modulator and traversing a magnetic chicane, the modulated portion of the electron beam emits a RC (right-circularly) polarized FEL pulse at an integer harmonic of the seed frequency in the downstream radiator R1. The electron beam is then delayed with respect to this FEL pulse using a highly dispersive element such as a magnetic chicane. It then traverses R2, generating a LC (left-circularly) polarized FEL pulse. A phase shifter PS (a small magnetic chicane) located just before R2 is used to fine tune the relative delay (or phase) between the two counter-rotating (cross-polarized) FEL sub-pulses. Two linearly polarized sub-pulses with orthogonal polarizations are also possible using linearly polarized radiators.

The properties of the composite output pulse are shown in Fig. 1(b) for two identical, cross-polarized sub-pulses

separated in time by 60 fs and with a relative phase of $\pi/4$. The top panel shows the on-axis x and y components of the total electric field E_x , E_y and the total intensity I . We analyze the pulses in terms of their Stokes parameters, which are a set of values that describe the polarization state of light. Unlike pulses with time-independent polarization (e.g., pure circular or pure linear), ours have time-dependent Stokes parameters S_1 (which describes linear horizontal/vertical polarization), S_2 (linear diagonal polarization) and S_3 (circular polarization), which are in general all different from zero. For the case in the bottom panel of Fig. 1(b), the polarization evolves from RC in the pulse head ($t < -50$ fs), to linear in the pulse center ($t = 0$), to LC in the pulse tail ($t > 50$ fs). By modifying the relative phase between the sub-pulses, we can control the polarization of the composite pulse, in particular the direction of the (purely linear) polarization at $t = 0$; the latter rotates in the polarization plane as the phase is varied.

We confirmed the time-varying polarization profile by measuring photoelectron distributions from helium atoms excited by such FEL pulses using a VMI (Velocity Map Imaging) detector that is sensitive to the polarization state of light. By decomposing VMI images into a weighted sum of images corresponding to pure linear horizontal and vertical polarizations, which are shown in Fig. 1(c), we extracted the intensity-normalized, time-integrated Stokes parameter S_1 , and found that it oscillates as a function of the relative phase between the FEL sub-pulses; see Fig. 1(d). The measurements were performed for synchronous pulses (no delay) and for a 30 fs delay. The fact that the oscillation amplitude of S_1/S_0 decreases when going from 0 to 30 fs with the sub-pulse delay (as expected from theory) is direct evidence that we are producing two delayed FEL pulses that will generate the FEL output shown in Fig. 1(b).

Because FELs are accelerator based, electron-beam energy fluctuations

introduce unwanted relative phase fluctuations between the sub-pulses, leading to a fluctuating output polarization. This shows up in our measurements as increased error bars in Fig. 1(d), especially when going to larger delays. However, a clear oscillation of S_1/S_0 for a delay of 30 fs indicates that phase fluctuations are at a level that will not compromise potential experiments. The FEL pulses were probed further using ATI (above-threshold ionization) in the presence of an optical dressing field. By spatially and temporally overlapping the FEL pulse with a short and intense linearly polarized infrared (IR) laser, we observed a modulation of the photoionization yield of helium atoms when varying both the delay between the FEL and IR pulses and the relative phase between the FEL sub-pulses, confirming a time varying polarization profile (not shown).

With our method, we will be able to directly test the prediction of generating electron vortices by absorbing a single XUV photon. Potential applications in atomic and molecular physics include coherent control of electron wave packets and observing photoelectron circular dichroism within a single measurement. Such experiments can now be performed without the need to absorb many photons. In addition, our scheme is likely to find extensive application in dichroic spectroscopy of molecules e.g., by varying the delay between pulses to extract chiral dynamics. We also envisage applications in condensed matter, especially in the field of ultrafast magnetism, where magnetic dynamics may proceed on a femtosecond time scale. Having XUV sources generating polarization-shaped pulses on such time scales opens the door to pump-probe studies of coherent spin-dependent processes with element selectivity.

Photon Sources and Instrumentation

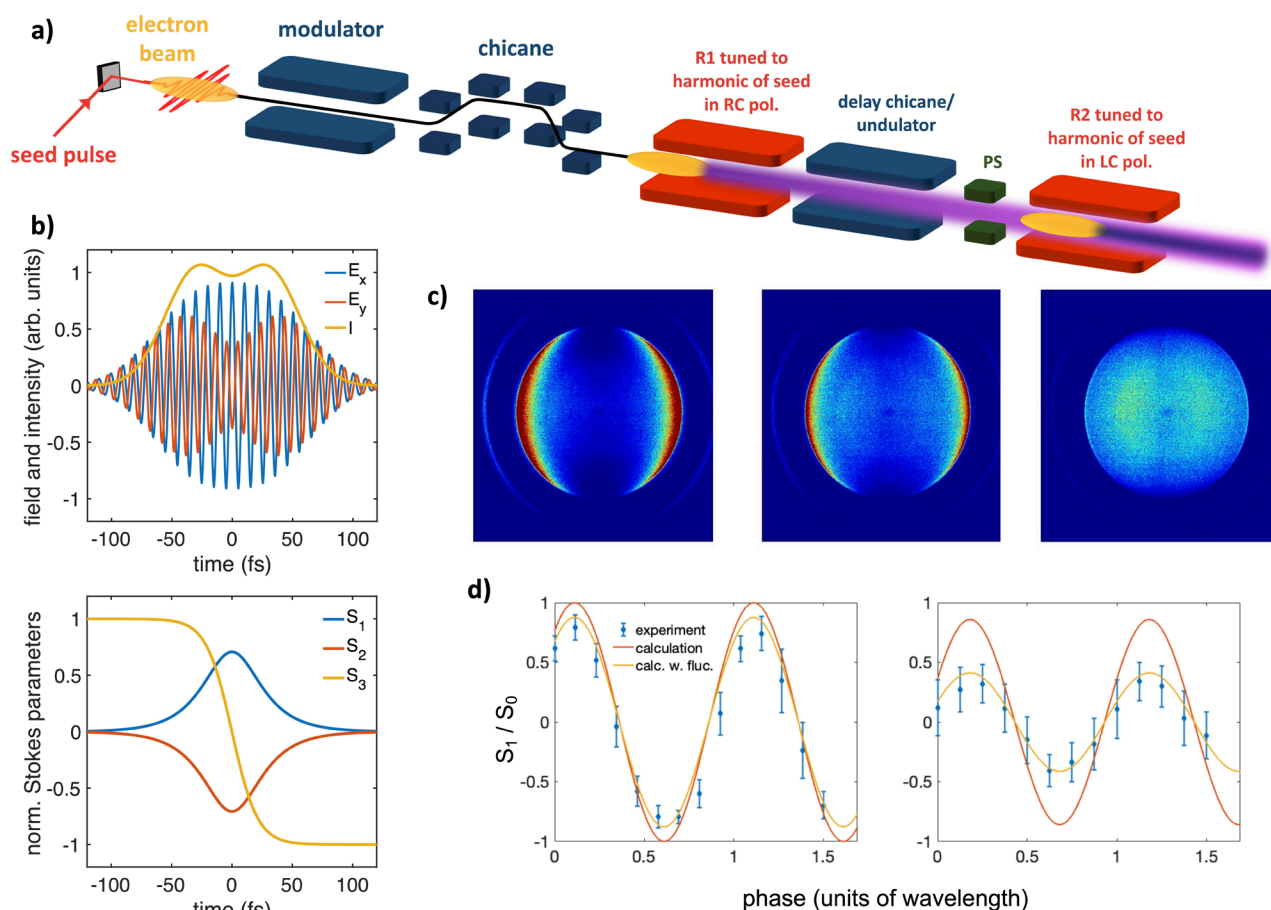


Figure 1. (a) The scheme for generating an XUV FEL pulse with time-dependent polarization by combining two counter-rotating FEL sub-pulses. (b) Schematic output of the setup shown in (a) for a separation between the sub-pulse envelopes equal to their FWHM durations (60 fs) and a relative phase (set by PS before R2 in (a)) equal to $\pi/4$. Top: components of the total electric field and total intensity. The FEL wavelength is exaggerated to visualize oscillations of the fields. Bottom: temporal profiles of the intensity-normalized Stokes parameters. (c) VMI images obtained from photoionization of helium atoms for a zero delay between the sub-pulse envelopes as a function of the relative phase: the polarization varies from almost pure horizontal (phase = 0, left), to diagonal (phase = $\pi/2$, middle), to almost pure vertical (phase = π , right). (d) Intensity-normalized, time-integrated Stokes parameter S_1 as a function of the relative phase for zero (left) and 30 fs (right) delay between the sub-pulse envelopes.

Acknowledgments

We acknowledge financial support from: Deutsche Forschungsgemeinschaft (project nos. 429194455 and 429805582, and Research Training Group 2717); Swedish Research Council and the Knut and Alice Wallenberg Foundation, Sweden; U.S. Department of Energy (award no. 2021-SLAC-100732); Slovenian Research Agency (project no. J1-3012).

Original paper

G. Perosa *et al.*, Phys. Rev. Lett. **131**, 045001 (2023); DOI: <https://doi.org/10.1103/PhysRevLett.131.045001>

G. Perosa^{1,2}, J. Wätzel³, D. Garzella¹, E. Allaria¹, M. Bonanomi^{4,5}, M. B. Danailov¹, A. Brynes¹, C. Callegari¹, G. De Ninno^{1,6}, A. Demidovich¹, M. Di Fraia^{1,7}, S. Di Mitri^{1,2}, L. Giannessi^{1,8}, M. Manfreda¹, L. Novinec¹, N. Pal¹, G. Penco¹, O. Plekan¹, K. C. Prince¹, A. Simoncig¹, S. Spampinati¹, C. Spezzani¹, M. Zangrando^{1,7}, J. Berakdar³, R. Feifel⁹, R. J. Squibb⁹, R. Coffee¹⁰, E. Hemsing¹⁰, E. Roussel¹¹, G. Sansone¹², B. W. J. McNeil^{13,14,15}, P. R. Ribic¹

¹ Elettra - Sincrotrone Trieste S.C.p.A., Trieste, Italy

² Physics Department, University of Trieste, Trieste, Italy

³ Institut für Physik, Martin-Luther-Universität Halle-Wittenberg, Halle, Germany

⁴ Politecnico di Milano, Milano, Italy

⁵ Istituto di Fotonica e Nanotecnologie, Milano, Italy

⁶ Laboratory of Quantum Optics, University of Nova Gorica, Nova Gorica, Slovenia

⁷ CNR-IOM, Trieste, Italy

⁸ ENEA C.R. Frascati, Frascati (Roma), Italy

⁹ Department of Physics, University of Gothenburg, Gothenburg, Sweden

¹⁰ SLAC National Accelerator Laboratory, Menlo Park, California, USA

¹¹ Univ. Lille, CNRS, UMR 8523 - PhLAM - Physique des Lasers Atomes et Molécules, Lille, France

¹² Physikalisches Institut, Albert-Ludwigs-Universität Freiburg, Freiburg, Germany

¹³ University of Strathclyde (SUPA), Glasgow, United Kingdom

¹⁴ Cockcroft Institute, Warrington, United Kingdom

¹⁵ ASTeC, STFC Daresbury Laboratory, Warrington, United Kingdom

e-mail: primoz.rebernik@elettra.eu

MagneDyn: a tool for the study of ultrafast magnetic phenomena in solids

FERMI | MagneDyn

Ultrafast magneto-optics, the study of how light interacts with magnetic materials, has come a long way in the past 30 years. Research is providing fascinating insights into the hidden world of spin dynamics - the dance of the tiny magnetic moments inside materials. By shining ultrafast laser pulses, lasting less than 50 femtoseconds, onto these materials, we have started to understand not only their microscopic behavior, but also how they function on a larger scale. This includes how charge and spin - the basic properties of electrons - move around, and how these elements interact with quasiparticles like phonons and magnons, which are disturbances in a solid that behave like particles.

The journey of ultrafast magneto-optics has been quite intriguing. Initially, these ultrafast lasers were a revolutionary tool, enabling us to propel a solid's spin system into a state far from its equilibrium and monitor its electronic and magnetic responses. What followed was an unexpected discovery of rapid light-induced demagnetization events, fueling intrigue about the suspected transient states of the spintronic configuration and sparking lively debates about the complex interplay at work. However, while our conventional laser methods of studying magnetism offer an interesting glimpse, they do not tell the full story. As the field evolves, cutting-edge techniques to track magnetic moments are taking center stage. These include femtosecond slicing at synchrotron sources, high harmonic generation (HHG) in labs, and free-electron laser (FEL) experiments. Each has helped deepen our understanding of the interplay between light, matter, and the ephemeral properties of spin systems, all within an incredibly short time frame.

One method to examine the extremely rapid changes in magnetism within matter involves harnessing the polarization of light. This is where ultrafast resonant magneto-optics come in. It is a unique tool that not only differentiates the magnetic properties

but can also focus on specific elements with nanoscale precision, all thanks to the short wavelength of x-rays. Light polarization defines the direction in which a light wave oscillates as it travels. When this light interacts with matter, the amplitude and polarization change based on the material's properties. The altered polarization can tell us about the material's properties like symmetry, order, and its magnetic state. When we conduct experiments sensitive to polarization in the x-ray range, we can gain insights about the magnetic state of specific atomic components of the material.

In simple terms, by observing the polarization - or the way the x-rays bounce back - from the magnetic material under study, scientists can gain insights into the intricate and invisible magnetic interactions occurring within. This is incredibly valuable because it helps us to understand and potentially control magnetic materials better, which could lead to all sorts of new technologies.

MagneDyn, which is a dedicated experimental station for these studies, is stationed at the FERMI free-electron laser (FEL) facility. Open to users since 2019, MagneDyn employs the variable circular and linear polarized femtosecond pulses emitted by the FERMI FEL to conduct advanced time-resolved magnetic dichroic experiments. These experiments involve probing the magnetic properties of elements such as 3d-transition-metals and rare earth elements.

The central capability of this beamline revolves around controlling and observing magnetization using light, which is achieved by both FEL and optical lasers. These lasers generate synchronized super short light pulses. The precision and stability of the FERMI FEL pulses, alongside the control of polarization and the ability to adjust photon energy, make MagneDyn a highly versatile station.

In order to be useful to a wide range of applications, MagneDyn has two

separate experimental areas, each filled with distinct features. The main end-station installed at MagneDyn has been specifically designed for time resolved magnetic dichroism experiments. This end-station is equipped with a dedicated electromagnet, that can generate variable magnetic fields up to 1.5 Tesla. The Earth's magnetic field is much weaker than this. It varies between 30-65 millionths of a Tesla. The experimental chamber is also equipped with a cryostat, a device that gets really cold for cooling down the systems that are under study. Finally, there is a polarimeter, a tool to measure light polarization, which is essential for these experiments. This polarimeter offers high angular sensitivity, reproducibility, flexibility, and user-friendliness, as well as the capability for energy and time fast scanning.

The second station is specially designed for carry-in user instruments, providing additional capabilities such as a spectrometer for pump-probe resonant x-ray emission and inelastic spectroscopy experiments. This approach uses a pump-probe scheme that combines a XUV polarimeter with tunable photon energy polarized FEL pulses and a synchronized optical laser system. The spectrometer employed in this process permits the recording of time resolved x-ray emission spectra with a high signal-to-noise ratio in a reasonable time.

In conclusion, the MagneDyn beamline offers researchers an advanced tool for studying ultrafast magnetic dynamics in various solids. With planned upgrades to the FERMI FEL source, the beamline's utility is set to extend even further, expanding the photon energy range to the water window and up to $L_{2,3}$ edges of transition metals. As the mysteries of magnetization in solids continue to unravel, MagneDyn stands at the frontier, offering a glimpse into the enigmatic dance of spins.

Photon Sources and Instrumentation

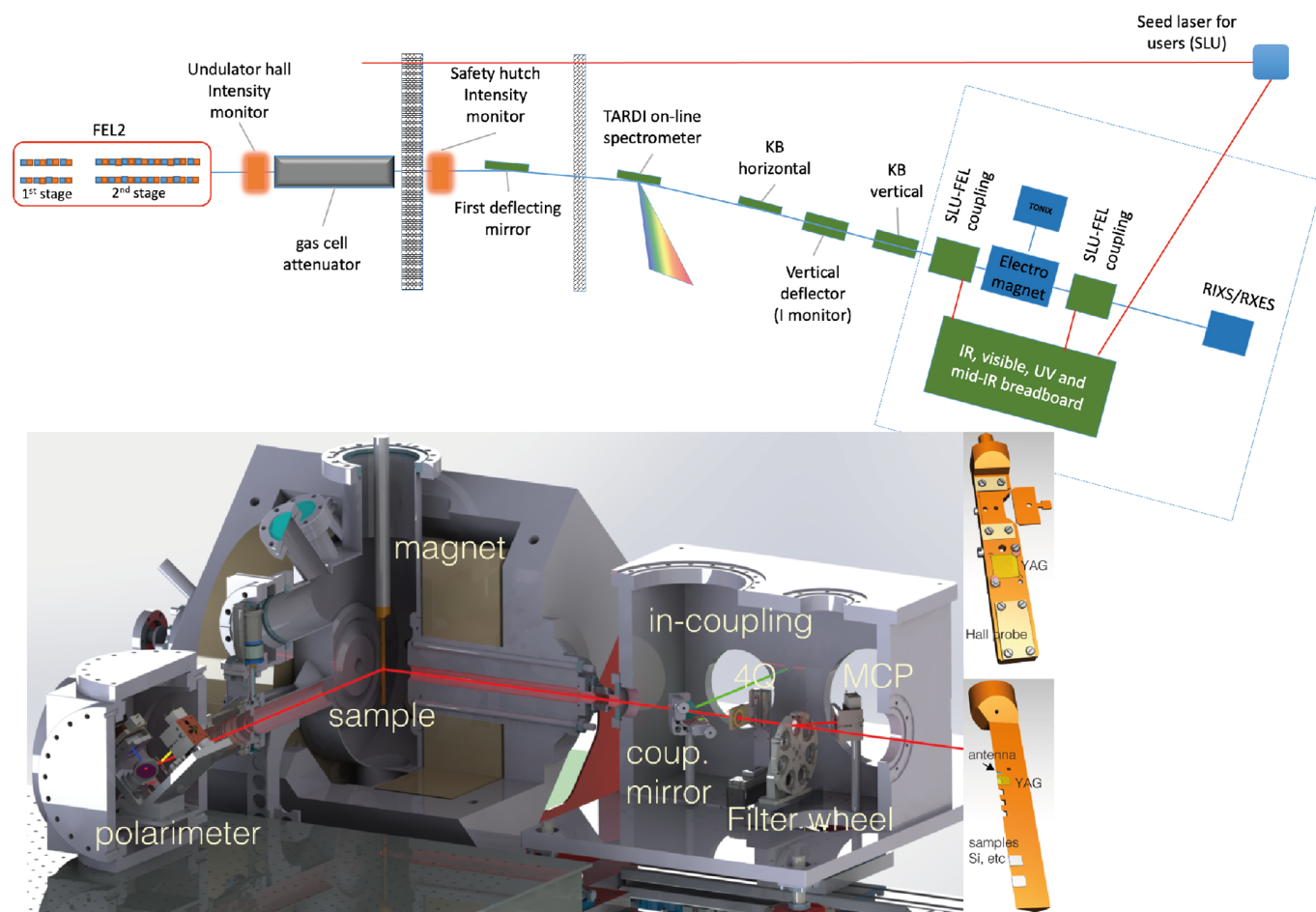


Figure 1. General layout of the FEL2 and the seed laser for users (SLU) photon delivery systems at MagneDyn. Pulse-to-pulse spectral monitoring is performed by means of a high resolution spectrometer (TARDI). The pulses are then refocused by means of the Kirkpatrick-Baez active optics (KAOS) mirror bending system. A dedicated beamline delivers the SLU to MagneDyn, where a breadboard is assigned for the control and manipulation of the optical laser.

View of the magnetic chamber: the focused FEL beam propagates through the in-coupling chamber where the beam is filtered and its intensity is monitored. The FEL beam enters the magnetic chamber through the magnetic expansion and impinges on the sample mounted on the shaft of a closed-cycle cryostat. Quasi-collinear to the FEL path, the optical beam is driven to the sample through an in-coupling mirror. The FEL reflected beam is then collected by the polarimeter. A schematic of the two sample holders available at MagneDyn is also shown. The sample holders are equipped with standard tools such as an antenna, YAG, Si sample, etc., for temporal and spatial overlaps, temperature, and magnetic field readings.

Original paper

M. Malvestuto *et al.*, The MagneDyn beamline at the FERMI free electron laser. *Rev Sci Instrum* **93**, 115109 (2022); DOI:10.1063/5.0105261

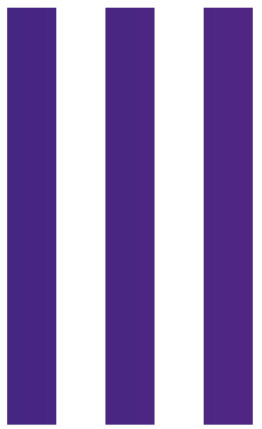
M. Malvestuto^{1,2}, A. Caretta¹, R. Bhardwaj¹, S. Laterza^{1,3}, F. Parmigiani^{1,3}, A. Gessini¹, M. Zamolo¹, F. Galassi¹, R. Sergo¹, G. Cautero¹, M. B. Danailov¹, A. Demidovic¹, P. Sigalotti¹, M. Lonza¹, R. Borghes¹, A. Contillo¹, A. Simoncig¹, M. Manfredda¹, L. Raimondi¹, M. Zangrando^{1,2}

¹ Elettra-Sincrotrone Trieste S.C.p.A., Trieste, Italy

² CNR-IOM Istituto Officina Dei Materiali, Trieste, Italy

³ Physics Department, University of Trieste, Trieste, Italy

e-mail: marco.malvestuto@elettra.eu



Facts & Figures

Events



Elettra and FERMI lightsources



Elettra Sincrotrone Trieste S.C.p.A. is a company of national interest managing an international research and multidisciplinary center of excellence, the hallmark of which is the study of materials through the light generated by two sources, Elettra and FERMI.

This light has the ability to unveil the structural and behavioral details of matter at atomic and molecular level to delve into their characteristics and provide solutions to the most diverse problems, in fields such as electronics, environmental sciences, pharmacology, diagnostics, engineering, nanotechnology and the preservation of cultural heritage.

The generated light feeds 34 experimental stations at Elettra and FERMI, which use it to study the matter and its properties at atomic level. Many laboratories of chemistry, biology, science of materials, electronics and computer science complement the Center's investigative capabilities.

The Company mission is the promotion of cultural, social and economic growth, thanks to basic and applied research, technology and knowledge transfer, high technical, scientific and management education, and the creation and coordination of national and international scientific networks.

Elettra hosts two different light sources: Elettra, a third-generation storage ring and FERMI, a cutting-edge free electron laser, together with a number of support laboratories.

A new 4th generation synchrotron radiation source, Elettra 2.0, is under development.

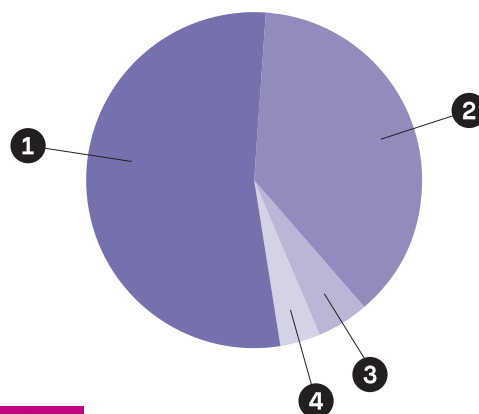
Elettra takes part in major European and international research programs, collaborating with the most important research universities and organizations, both in Italy and abroad. The Center is affiliated with the International Atomic Energy Agency (IAEA), and participates, as Representing Entity of the Italian Government, in the European Research Infrastructure Consortium (ERIC-ERIC).

Shareholders

The Center is managed by Elettra – Sincrotrone Trieste S.C.p.A., a non-profit Share Company (Società Consortile per Azioni) of national interest pursuant to Law 370/99.

The shareholders are:

- 1 Area Science Park Consortium (53.7%),
- 2 Autonomous Region of Friuli Venezia Giulia (37.63%)
- 3 CNR (Italian National Research Council) (4.85%)
- 4 Invitalia Partecipazioni S.p.A. (3.82%)



Partnerships and Alliances

Aarhus University

Academy of Sciences of the Czech Republic

AIAR – Italian Archaeometric Society

Alma Mater Studiorum – Dept. of Biological, Geological and Environmental Sciences

University of Bologna

AIRC – AIRC Foundation for Cancer Research

ANL – Argonne National Laboratory

Area Science Park

BAM Bundesanstalt für

Materialforschung und -prüfung

BNL – Brookhaven National Laboratory

CLS – Canadian Light Source Inc.

CELLS – Consortium for the Construction, Equipping and Exploitation of the Synchrotron Light Source ALBA

CERIC – ERIC (Central European Research Infrastructure Consortium - ERIC)

CERN – European Organization for Nuclear Research

Charles University – Prague

Clemson University

CNR – Italian National Research Council

CNRS – Centre National de la Recherche Scientifique

Democenter-Sipe Foundation

DESY – Deutsches Elektronen-Synchrotron

Euro-BioImaging ERIC

European Spallation Source ERIC

European XFEL

FELs of Europe

Fondazione Bruno Kessler

Forschungszentrum Jülich

Hochschule Fresenius University of Applied Sciences

HZB – Helmholtz-Zentrum Berlin für Materialien und Energie GmbH

IAEA – International Atomic Energy Agency

ICGEB – International Centre for Genetic Engineering and Biotechnology

ICTP – International Centre for Theoretical Physics

Indian Institute of Science, Bangalore

INAF-OATs National Institute for Astrophysics – Astronomical Observatory of Trieste

INFN – Institute of Nuclear Physics

INGV – Istituto Nazionale di Geofisica e Vulcanologia

INSTM – National Inter-University

Consortium for Materials Science and Technology

ISAS/SISSA – International School of Advanced Studies

IIT – Italian Institute of Technology

Katholieke Universiteit Leuven

LENS – European Laboratory for Non-linear Spectroscopy

LIS – Science Centre Immaginario Scientifico

MUR – Italian Ministry of University and Research

NIMP – National Institute of Material Physics

PAL – Pohang Accelerator Laboratory

PLUS – Paris Lodron University of Salzburg

Politecnico di Milano

Salzburg University of Applied Sciences

Scuola Normale Superiore of Pisa

SESAME – International Center for Synchrotron-light for Experimental Science and Applications in the

Middle East

PSI Paul Sherrer Institute,

SLS – Swiss Light Source

Stazione Zoologica Anton Dohrn

Synchrotron SOLEIL

TU Graz – Graz University of Technology

UKRI – United Kingdom

Research and Innovation

Universidad Complutense

- Facultad de Ciencias Fisicas

University of LAquila

University of Campania

University of Calabria

University of Genoa

University of Marche – Environmental Sciences and Civil Protection Dep (DISVA)

University of Milan

University of Modena and

Reggio Emilia UniMoRe

University of Naples "Federico II"

University of Nova Gorica

University of Padua

University of Palermo

University of Perugia

University of Pisa

University of Rome "Sapienza"

University of Rome "Tor Vergata"

University of "Roma Tre"

– Dep. of Science

University of Sydney

University of Trento

University of Trieste

University of Udine

University of Uppsala – Institute of Cell and Molecular Biology

University of Valencia

University of Venice "Ca' Foscari" – Dep. of Environmental Sciences,

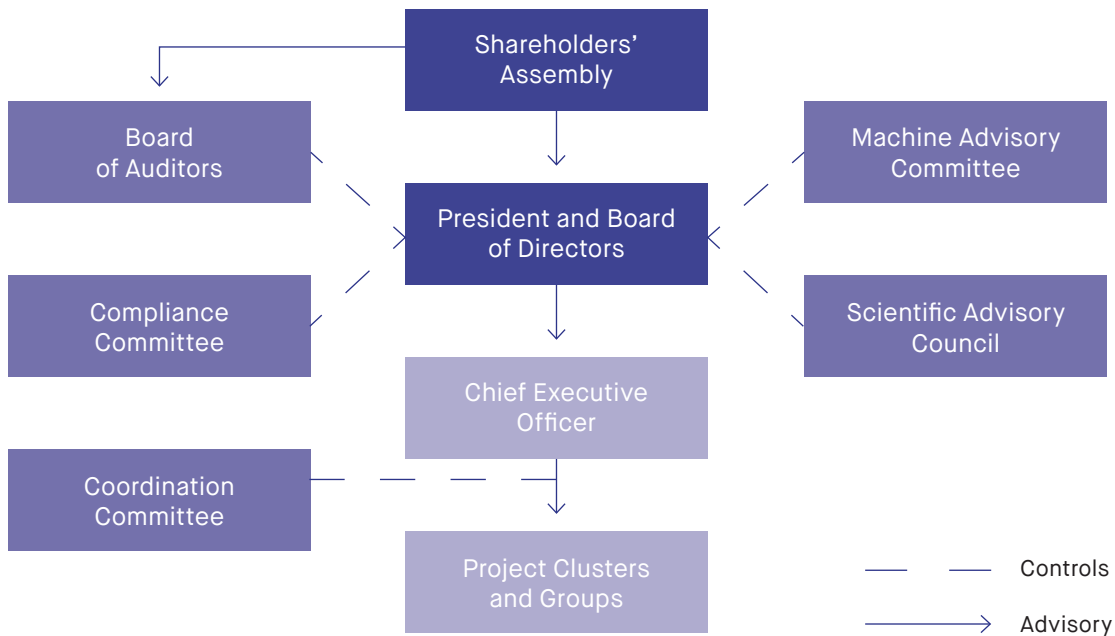
Informatics and Statistics

University of Venice "Ca' Foscari" – Dep. of Molecular Sciences and Nanosystems

UPOL – Palacky University Olomouc

Organization

Elettra Sincrotrone Trieste is managed by a Board of Directors, assisted by a shareholder-appointed Board of Auditors, and advised by board-appointed international committees such as the Scientific Advisory Council for scientific programs and the Machine Advisory Committee for accelerator development.



Board of Directors

President and CEO:

Alfonso Franciosi
 Alberto Aloisio
 Giovanni Comelli
 Anna Gregorio
 Caterina Vozzi

Board of Auditors

President: Gianpaolo Graberi

Francesco Battaglia
 Luca Bicocchi
 Maria Brogna
 Sara Rossi

Compliance Committee

Chairman: Vincenzo Di Felice

Giorgio Pani
 Melissa Valentino

Machine Advisory Committee (MAC)

Chairman: Pedro Fernandes Tavares

Masamitsu Aiba
 Johannes Bahrtd
 Riccardo Bartolini
 Jim Clarke (2023-)
 Gianluca Geloni (2020-2023)
 Agostino Marinelli (2023-)
 Ryutaro Nagaoka
 Marco Pedrozzi
 Francisco Perez
 Fulvia Pilat
 Tor Raubenheimer (2020-2023)

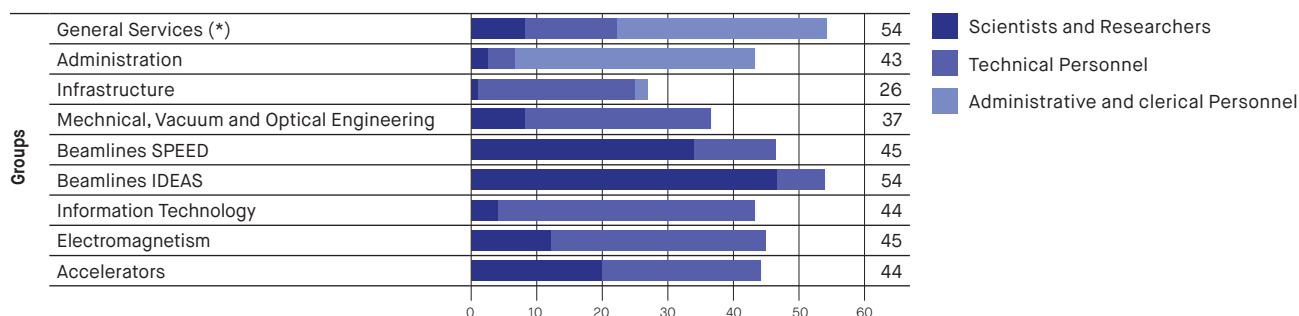
Scientific Advisory Council (SAC)

Chairman: Stefan Eisebitt

Miguel Angel Garcia Aranda
 Martin Beye
 Kristina Djinovic Carugo
 Dean Chapman
 Martin Gruebele
 Giancarlo Ruocco
 Thomas R. Schneider
 Marco Stampanoni
 Amina Taleb
 Andrew Thompson
 Philippe Wernet

Staff

Elettra Sincrotrone Trieste has adopted a matrix-type of organization. There are five Strategic Initiatives, which correspond to distinct Project Clusters: Elettra, FERMI, Research, Technology Platform and International Projects, grouped together based on the complementarity of the different project goals. The human and instrumental resources required by the different projects are managed within nine Groups of staff members with similar or related expertise.



Total 392 **

* including human resources, legal, industrial liaison office, users office, etc.

** situation at 30.06.2023

Budget allocation 2023

General costs	€ 2.200.000
Insurance	€ 550.000
Utilities	€ 10.969.662
Agreements	€ 1.500.000
Operation	€ 500.000
Coordination Group	€ 850.000
Administration Group	€ 100.000
Accelerator Group	€ 60.000
Beamlines Group	€ 700.000
Electromagnetism Group	€ 200.000
IT Group	€ 300.000
Mechanical, Vacuum and Optical Group	€ 200.000
Infrastructure Group	€ 900.000
ODAC Project	€ 675.000
Ordinary expenses	€ 19.704.662
BEI Loan amortization	€ 6.750.000
Industrial Liason Office	€ 600.000
Ordinary projects	€ 350.000
FERMI Operation	€ 3.700.000
Elettra Upgrade	€ 52.742.530
Additional International Projects and Partner contributions	€ 380.000
External projects	€ 2.070.000
Project expenses	€ 66.592.530
Personnel	€ 24.300.000
General total	€ 110.597.192

Elettra Sincrotrone Trieste has top-quality research and training in its Mission.

Our researchers are leaders and partners in **Regional, National, European and Global collaborations**.

In 2022–2023 we have been involved in 32 European / International projects, 19 National ones, 2 Regional ones and 7 granted by CERIC-ERIC, with new funding acquired for nearly 4 Million Euro.

The years 2022–2023 have been extremely successful with respect to the Horizon Europe funding programme, with 11 new projects: two financed under the Health Programme, five Marie Skłodowska-Curie Actions, one ERC Advanced Grant with Elettra as Host Institution. In addition, we have just been granted 3 projects from the INFRA-SERV call, that will all start in 2024.

The **canSERV**¹ (Providing cutting edge cancer research services across Europe) project provides cutting edge, interdisciplinary and customized oncology services across the entire cancer continuum. It is coordinated by BBMRI-ERIC and the Elettra SYRMEP beamline is offering access as part of the Euro-BioImaging² phase contrast imaging node.

The **AVITHRAPID**³ (Antiviral Therapeutics for Rapid Response Against Pandemic Infectious Diseases) project will improve Europe's research capacities becoming a key instrument to support research on viral pathogens with epidemic and pandemic potential. It is coordinated by the Fraunhofer Gesellschaft and Elettra is involved with its Protein facility and the XRD2 beamline, to provide x-ray crystal structures supporting lead compound optimization against selected targets.

Two excellent researchers will join Elettra for their MSCA post-doctoral fellowships, starting in autumn 2023: Dr. S. Lemmers for her ENIGMA⁴ project, and Dr. S. Sarkar for her MI-CORE⁵ project.

ENIGMA (Neanderthal virtual bone histology deciphering hominin Growth rate activity and environmental Adaptation) is dedicated to bone virtual histology of Neanderthal bones from Krapina, Croatia (ca 130 kyears ago). High-resolution micro-Computed Tomography, available at the SYRMEP beamline and at the Tomolab laboratory, is a non-destructive technique able to provide unprecedented insight into the anatomy and growth rates of our closest ancient human relatives (*homo neanderthalensis*).

MI-CORE (Mechanistic Insights into e-CO₂ REduction on various alloys and intermetallics based systems) aims at developing new materials and operando techniques to study novel catalysts for the electrochemical CO₂ reduction reaction and metal-ion batteries. The beamlines involved will be MCX and XAFS, offering state of the art X-ray Diffraction and Spectroscopy capabilities.

Elettra is attractive also for Global MSCA fellowships: the SISSI beamline will host the secondment of Dr. D. Bedolla, for her **IR4FTD**⁶ Project. The project aims

to understand and diagnose Frontal Temporal Dementia using infrared spectroscopy among other techniques. She will spend the out-going phase at Monash University (Australia) and come back to ICGEB for the incoming one.

The **GAP** (image Guided computational and experimental Analysis of fractured Patients)⁷ Doctoral Network, coordinated by Politecnico di Milano, groups 13 participants including Research Centers, Hospitals and Citizen Associations. Ten PhD students will dedicate their research to improve the comprehension of bone damage mechanisms for a better reliability of fracture risk and a more accurate diagnosis of bone pathologies, in a truly interdisciplinary and inter-sectoral approach.

Finally, the **DOC-FAM**⁸ COFUND project will recruit 26 early-stage researchers to work in the field of synthesis and characterization of advanced functional materials, including those used in batteries, while at the same time offering a complete training experience to the recruited fellows.



Figure 1: canSERV project logo.



Figure 2: Marie Skłodowska-Curie Actions logo

¹ <https://www.canserv.eu/>, GA n. 101058620.

² <https://www.eurobioimaging.eu/>

³ GA n. 101137192

⁴ GA n. 101065448

⁵ GA n. 101065933

⁶ GA n. 101106307

⁷ GA n. 101120290

⁸ GA n. 101081337, <https://docfam.icmab.es//>

⁹ GA n. 101095012

Elettra Sincrotrone Trieste is proud to be the Host Institution of one of the 14 **ERC Advanced Grants** awarded to Italian institutions in the last call: the **CHIRAX**⁹ project (X-ray spectroscopy of molecular chirality in solutions) with **Principal Investigator prof. M. Chergui**. Chirality is a property of biomolecules to have a left and a right handed form (so-called enantiomers), which are mirror images of each other but cannot be superimposed (Figure 4). Nature is however homochiral, therefore identifying the right-or-left enantiomers of biomolecules is central to analytical (bio)chemistry, toxicology and drug design. The project comes at a turning point thanks to the recent developments in X-ray sources, flat liquid jets samples and theoretical concepts. Starting in November 2023, prof. Chergui will setup a new research group at Elettra and FERMI, including 4 post-docs students and 3 PhDs hired at University of Trieste as Additional Beneficiary. CHIRAX will implement steady-state X-ray circular/helical dichroism of molecules in solution, and establish them as analytical tools. A further development is to add the temporal resolution, with the ultimate goal of

detecting in real-time the evolution of molecular systems with element-and enantio-selectivity.

The three INFRA-SERV projects in which Elettra is involved are centered around the storage ring and FEL analytical capabilities and are the result of more than 20 years of collaboration among the European facilities: **RIANA** (Research Infrastructure Access in NANoscience & nanotechnology), **NEPHEWS** (NEutrons and PHotons Elevating Worldwide Science) and **Lasers4EU** (European Laser Research Infrastructures Serving Science and Industry for our Future).

Elettra Sincrotrone Trieste has also been involved in quite a number of National PRIN applications, with the role of "sub-unit"; we have been successful in 8 PRIN projects.



European Research Council

Established by the European Commission

Figure 3: European Research Council logo.

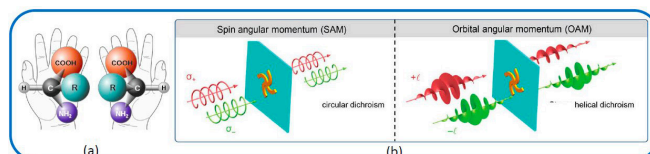


Figure 4: (a) a chiral amino acid and its two enantiomers (b) principle of circular and helical dichroism spectroscopy.

Ongoing research contracts

NAME	SHORT NAME	COORDINATOR
European/International Research Projects		
DNA helicases in genomic maintenance: from mechanism to specific inhibitors as potential drugs	AntiHelix	Consiglio Nazionale delle Ricerche - Istituto di Biochimica delle Proteine, Italy
Antiviral Therapeutics for Rapid Response Against Pandemic Infectious Diseases	AVITHRAPID	Fraunhofer Gesellschaft
Beamline for Tomography at SESAME	BEATS	European Synchrotron Radiation Facility, France
Platform for Biosciences and Human Health in Cyprus: MicroCT Enabled and Synchrotron Radiation Enabled Analyses	BioMERA	The Cyprus Institute, Cyprus
Improve EuBI ERIC research in response to cancer	canSERV	BBMRI-ERIC - Biobanks and Biomolecular Resources Research Infrastructure
X-ray spectroscopy of molecular chirality in solutions	CHIRAX	Elettra - Sincrotrone Trieste S.C.p.A.
DESTINY: European Doctorate Program on Materials for Energy Storage	DESTINY	Université de Picardie Jules Verne, France
DOctoral training programme in Functional Advanced Materials for grand challenges	DOC-FAM+	CSIC - Consejo Superior de Investigaciones Científicas - ICMA B - Instituto de Ciencia de Materiales
European Network for Chemical Elemental Analysis with TXRF	ENFORCE	Consorzio Interuniversitario Nazionale per la Scienza e Tecnologia dei Materiali, Italy
nEanderthal virtual boNe Hstology: deciphering hominin Growth rates, activity and environMental Adaption	ENIGMA	Elettra - Sincrotrone Trieste S.C.p.A.
EuPRAXIA Preparatory Phase Project	EUPRAXIA	I.N.F.N. - Istituto Nazionale di Fisica Nucleare - Laboratorio Nazionale di Frascati
EOSC Photon and Neutron Data Services	ExPaNDs	DESY - Deutsches Elektronen - Synchrotron, Germany
GAP: image Guided computational and experimental Analysis of fractured Patients	GAP	Politecnico di Milano - Dipartimento di Meccanica
Micromechanical Bolometers arrays for Terahertz hyperspectral	H - CUBE	CNR - IOM - Consiglio Nazionale delle Ricerche - Istituto Officina dei Materiali - c/o Dipartimento di Fisica - Università di Perugia
Innovation Fostering in Accelerator Science and Technology	I.FAST	C.E.R.N. - European Organization for Nuclear Research
IMPULSE - Integrated Management and reliable oPerations for Userbased Laser Scientific Excellence	IMPULSE	Extreme Light Infrastructure - Delivery Consortium, Belgium
INhomogenities and fluctuations in quantum CohErent matter Phases by ultrafast optical Tomography	INCEPT	Università degli Studi di Trieste, Italy
Heterogeneous biocatalytic reaction cascades training network	INTERfaces	Aarhus University, Denmark
Improve EuBI ERIC research in response to infectious disease epidemics	ISIDORE	E.M.B.L. - European Molecular Biology Laboratory
Knowledge-driven fine-tuning of mixed oxides for Chem-X devices	KNOWSKITE - X	CNRS - Centre National de la Recherche Scientifique - SPM - Sciences Physiques et Mathématiques
The Integrated Initiative of European Laser Research Infrastructures	Laserlab Europe	Lund University, Sweden
EUROPEAN LASER RESEARCH INFRASTRUCTURES SERVING SCIENCE AND INDUSTRY FOR OUR FUTURE	Lasers4EU	LASERLAB-EUROPE
LEAPS pilot to foster open innovation for accelerator-based light sources in Europe	LEAPS-INNOV	DESY - Deutsches Elektronen-Synchrotron - A Research Centre of the Helmholtz Association
Mechanistic Insights into e-CO2 REDuction on various alloys and intermetallics based systems	MI-CORE	Elettra - Sincrotrone Trieste S.C.p.A.
Participation as partner organisation in the Innovative Training Network "NanED"	NanED	IIT - Istituto Italiano di Tecnologia - Italian Institute of Technology, Italy
NEutrons and PHotons Elevating Worldwide Science	NEPHEWS	Jagiellonian University - Uniwersytet Jagiellonski - SOLARIS - National Synchrotron Radiation Centre
An international network for Non-linear Extreme ultraviolet to hard X-ray Techniques	NEXT	Instituto Madrileño de Estudios Avanzados (IMDEA Nanoscience)
NFFA-Europe PILOT	NFFA - Europe PILOT	CNR - IOM - Consiglio Nazionale delle Ricerche - Istituto Officina dei Materiali - Sezione di Trieste
ReMade-at-ARIE	ReMade-at-ARI	HZDR - Helmholtz-Zentrum Dresden-Rossendorf e. V
Research Infrastructure Access in NANoscience & nanotechnology	RIANA	DESY - Deutsches Elektronen-Synchrotron - A Research Centre of the Helmholtz Association
Scattering-Based X-ray Imaging and Tomography	S-BaXIT	Università degli Studi di Trieste - Dipartimento di Fisica, Italy
Study of carrier transport in MAterials by time-Resolved specTroscopy by ultrashort soft X-ray light	SMART-X	CNR - IFN - Consiglio Nazionale delle Ricerche - Istituto di Fotonica e Nanotecnologie - Sede di Milano, Italy

National Research Projects*		
Non-covalent Epigallocatechin-3-gallate-based targeting EGFR to overcome T790M and C797S resistance in Advanced NSCLC	AIRC_SISSI	Università Politecnica delle Marche - Dipartimento di Scienze della vita e dell'Ambiente (DISVA)
Understanding the role of RecQ4 in cancer development and progression	AIRC-RECQ4	Elettra - Sincrotrone Trieste S.C.p.A.
A fracture mechanics approach for addressing micro-scale bone damage mechanisms	ARCHIMEDES	Politecnico di Milano - Dipartimento di Meccanica
Plastic pollution in the Antarctic terrestrial ecosystems	EXPLORA	Università degli Studi di Siena - Dipartimento di Scienze Fisiche, della Terra e dell'Ambiente
Flexible molecular crystals with embedded permanent electrical fields (PRIN)	FLEXPOLY_PRIN	Università degli Studi di Trieste - Dipartimento di Scienze Chimiche e Farmaceutiche
Formazione Fondimpresa 2020-2021	FORFOND 2020 - 2021	Fondimpresa c/o Confindustria Friuli Venezia Giulia
Formazione Fondimpresa 2023-2024	FORFOND 2023 - 2024	Fondimpresa c/o Confindustria Friuli Venezia Giulia
Access to the beamlines of Elettra and FERMI Laboratories by the Indian scientific institutions	Italia-India 2021 - 2022	Elettra - Sincrotrone Trieste S.C.p.A.
Access to the beamlines of Elettra and FERMI Laboratories by the Indian scientific institutions	Italia -India 2023	Elettra - Sincrotrone Trieste S.C.p.A.
Therapeutic opportunities in Lafora Disease, a rare juvenile neurodegenerative epilepsy with no-cure	LAFORA-PRIN	Università degli Studi di Trento - CIBIO - Centre for Integrative Biology
MultiExciton Generation in Synthesized molecular heterojunctions	MEGS	CNR - IOM - Consiglio Nazionale delle Ricerche - Istituto Officina dei Materiali - Sezione di Trieste
Open Lab - A System of Open Research Facilities	OPEN LAB	AREA Science Park - Consorzio per l'AREA di ricerca Scientifica e Tecnologica di Trieste
Operando studies of High-Entropy oxide-based active materials for Na-Ion battery cathodes (OPHELIA)	OPHELIA	Alma Mater Studiorum - Università di Bologna - Dipartimento di Chimica Industriale "Toso Montanari"
PLASMA acceleration, beam Manipulation and Advanced Radiation sources	PLASMAR	Istituto Nazionale di Fisica Nucleare - Laboratorio Nazionale di Frascati, Italy
Acquisizioni di beni per il potenziamento dell'Infrastruttura di Ricerca Elettra a valere sul Fondo per la promozione e lo sviluppo delle politiche del Programma nazionale per la ricerca (PNR)	PNR 2021 - 2022	Elettra - Sincrotrone Trieste S.C.p.A.
Assembly of macromolecular complexes at the origin of replication in Mycobacterium tuberculosis	PRIN-OriTB	Università degli Studi di Parma - Dipartimento di Scienze degli Alimenti e del Farmaco
QUest for BOron Phosphide	QUBOP	Università degli Studi di Trieste - Dipartimento di Fisica - Scuola di Dottorato in Nanotecnologie
Short Heterochiral Assembling peptides that Zip into smart AntiMicrobials	SHAZAM	Università degli Studi di Trieste - Dipartimento di Scienze Chimiche e Farmaceutiche
Synchrotron light investigation of environmental radioactivity sources in the Chihuahua deser	U- Water	Centro de Investigación en Materiales Avanzados, S.C.
Regional Research Projects		
Request to activate a Cost Unit for the TomoLab activity at Elettra	CC_TomoLab	Elettra - Sincrotrone Trieste S.C.p.A.
InCIMA for Science and SMEs	InCIMA4	Elettra - Sincrotrone Trieste S.C.p.A.
CERIC - Related Research Projects		
CERIC-ERIC for Battery Research	BatERIC	Elettra - Sincrotrone Trieste S.C.p.A.
CERIC-ERIC for Cultural Heritage Research	CH-ERIC	Elettra - Sincrotrone Trieste S.C.p.A.
Electron microscopy for Structural Biology at CERIC-ERIC	ESBY	Elettra - Sincrotrone Trieste S.C.p.A.
Flexible Apparatus for Imaging and Tomography	FAITH	Elettra - Sincrotrone Trieste S.C.p.A.
The first step to enhance CERIC-ERIC's life science capabilities	INTEGRA	University of Graz, Austria
Photon and Neutron Open Science Cloud	PANOSC	European Synchrotron Radiation Facility, France
multiScale TERahertz iMaging	STEAM	Elettra - Sincrotrone Trieste S.C.p.A.

*FOE Projects not included in this list; for more info, see: <https://www.elettra.eu/about/projects/international-projects.html>

Novel technological ICT developments for Elettra 2.0

The main focus of the IT group was both on consolidation and improvement of the whole scientific workflow according to FAIR principles and to be ready for Elettra 2.0 upgrade, working towards satisfying the forecasted needs and future requirements. This required an intense collaboration with the beamline scientist to refine every single step from experimental station control, to scientific data acquisition and annotation, archiving and curation, in order to be really sustainable in everyday operations. Moreover this requires the creative use of existing technologies but also the development of novel IT approaches. We are testing and developing processing methods that require complex Python setups (ie. optimised ML libraries like Tensorflow) and specialised hardware (ie. GPUs and fast NFS I/O). Those methods are exposed through minimalistic REST API so that they can be utilised as blackbox remote methods from other systems including Python based data

acquisition, legacy LabView installations, Igor Pro, Jupyter Notebooks, Java and last and not least web based front ends for data analysis. This approach allows for standard development and later exposure as a remote API with similarities to the old RPC model by using standard web technologies such as REST. By intelligent choice of hardware and setups, I/O can be highly optimised through privileged 1-100 Gbps access to the data (server-side), remote calculation and serving only the reduced result to the client. Existing systems included web-analysis for XRF fitting leading to in-house published research [Fig.1] of the Scientific Computing team, including raytracing sample topography reconstructions and novel application for scanning control system using Compressive Sensing. Even if experimentation and development is going, the key takeaways of this novel approach is increased flexibility and extensibility, on-line computing on the cloud but without special tools easy to

integrate with any acquisition system and rapid Application Development even during beamtimes. The system is already in use in 4 beamlines (SYRMEP, TwinMic, XAFS, DiProl) and has been used in multiple experiments.

The IT Group is also developing a large number of technologies to support **Elettra 2.0 project management**. The VUO platform has been fully integrated with MS Project and Oracle Primavera Risk Analysis. The Elettra 2.0 Document Management System is under development and will be soon capable of tracking physical objects and instruments to support coordination and logistics and the whole components life cycle. In the same line it will be able to visualize IFC files to support the BIM process.

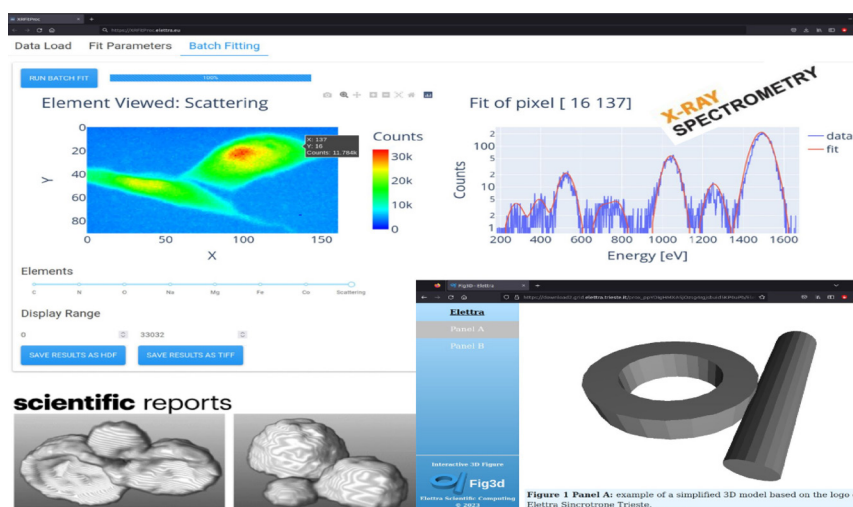


Figure 1: Examples of SciComp apps based on the mentioned approach: inc. Ray tracing topography, XRF fitting, and 3d figure visualisation



Figure 2: GeCo Beamline Control System logo.

Kalculus, the Elettra 2.0 HPC Hybrid (CPU/GPU) Cluster, in full operation has been further improved. The system is now offering 1776 cores (3552 threads) and 27 TB of RAM over 37 blades and 20736 CUDA cores and 1296 Tensor cores with 120GB of GPU HBM2 memory over 3 blades. The interconnection between the blades is at 25 Gb/s, the connection to the LAN and other virtualisation clusters is at 100 Gb/s. Kalculus is dedicated to all the computations required for Elettra 2.0 design and much more. Kalculus deeply interacts with hyperconvergent virtualization and storage clusters dedicated to on line processing for the beamlines and experimental stations. At the moment we are expanding and reorganizing the central and the two satellite server rooms in order to be able to grow gradually to support the Elettra 2.0.

Advanced data storage solutions are an essential part of the Open and FAIR remote data strategy. Elettra has an online storage capacity of about 8PB and an

offline storage capacity that can grow up to 60PB. Data are acquired, associated with metadata and support data in most of the beamlines. DOIs are associated with the datasets and can be directly used in publications. KPIs have been associated to each beamline in order to monitor and evaluate quality, occupation status and balance of the whole system.

GeCo, the new Elettra 2.0 Beamline Control System, has been designed and developed. The main target of this development is the standardization and renewal of the interlock and motion systems for all the beamlines. The present infrastructure needs to be replaced using state of the art technologies. In the first 2023 shutdown, the control system (BCS) of the beamline 1.2 has been completely replaced with a new interlock system named GeCo (Gestione e Controllo). A Siemens PLCs is used for low level instrumentation control, while higher level applications are developed using the Tango framework.

In the upgrade process also the original motion controllers have been completely replaced with the new standard YAMS system, based on Galil network controllers.

Essential for the future challenges are the control systems. Since 2003 Elettra has been an active member of Tango Controls, an international collaboration which develops Tango, the control system framework used at Elettra and FERMI, that will be adopted as control system framework for Elettra 2.0 as well. Elettra is contributing to the development of the Tango core library and managing the development of the alarm and historical archiving subsystems. At the moment we are designing parts of the machine control systems and their digital twin counterpart.

References

Ray tracing topography:
<https://doi.org/10.1038/s41598-022-24059-y>
XRF fitting: <https://doi.org/10.1002/xrs.3341>
3d visualisation: <https://doi.org/10.5281/zenodo.7802829R>.

R. Pugliese¹, G. Kourousias¹, F. Billè¹, R. Borghes¹, L. Pivetta¹, R. Passuello¹, C. Scafuri¹

¹ Elettra - Sincrotrone Trieste S.C.p.A., Trieste, Italy

e-mail: roberto.pugliese@elettra.eu; george.kourousias@elettra.eu; fulvio.bille@elettra.eu; roberto.passuello@elettra.eu; roberto.borghes@elettra.eu; lorenzo.pivetta@elettra.eu; claudio.scafuri@elettra.eu

CERIC

Central European Research Infrastructure Consortium

CERIC-ERIC (in the following, CERIC) integrates and provides open access to some of the most advanced analytical facilities in Europe to help science and industry advance in all fields of materials, biomaterials and nanotechnology, with a focus on energy materials and life sciences. It enables the delivery of innovative societal challenges in the fields of energy, health, food, cultural heritage and more.

The Consortium is an ERIC (European Research Infrastructure Consortium), a distributed research infrastructure based on Council Regulation 723/2009. Its statutory seat is in Italy and is hosted by Elettra Sincrotrone Trieste. In addition to Italy, CERIC's members include Austria, Croatia, the Czech Republic, Hungary, Poland, Romania and Slovenia. Other associated facilities are located in France, Greece and the Netherlands. Serbia is an observer.

Open Access

Between the second half of 2022 and the first half of 2023, CERIC published two calls for proposals for access to research infrastructures in its offer. Research groups from 37 countries submitted 354 applications, equivalent to 506 single-instrument proposals.

186 proposals from 29 countries were allocated instrument time to 277 single instruments.

Below is a selection of papers published by CERIC users in 2022-2023:

Fig. 1: Antibiotics are among the most popular pharmaceuticals. However, their broad application is causing the contamination of water bodies, heavily contributing to the growing problem of antibiotic resistance. CERIC users tested the effectiveness of black titanium dioxide in promoting the degradation of amoxicillin, a common antibiotic, under sunlight.

Fig. 2: Copper-based antitumoral drugs are a promising treatment options thanks to their in vitro and in vivo properties, which include improved selectivity toward tumour cells, reduced side effects, and efficacy against tumours resistant to other medication. Several copper-based complexes have been synthesised, and their structure and stability tested using Synchrotron light-based techniques.

Fig. 3: Ammonia, a widely used chemical, is also a critical substance for producing nitrogen-containing fertilisers. Photoelectrochemical nitrogen reduction reaction (NRR) is a way to synthesise it in

a green and sustainable way using solar power. CERIC scientists at the Materials Science Beamline (MSB) tested and characterized electrochemical Lithium (Li)-mediated NRR, showing that this method could provide ammonia with a high yield rate and excellent faradaic efficiency.

In the same period, CERIC continued offering dedicated Fast Track Access to a selected number of instruments. Such access mode has allowed selected applicants to use the available instruments undergoing a fast evaluation procedure and experiments to be scheduled within one month from the submission of the proposal based on the feasibility evaluation performed by the facility.

Furthermore, in solidarity with the Ukrainian researchers, CERIC also launched in 2022 a call for Ukrainian post-doc researchers to enable their continuous research activities at CERIC's Partner Facilities. The project with Dr. Anatolii Nagorny as principal investigator, which started in early 2022 and aims to investigate novel fuel cell materials using synchrotron beamlines, is still active, as well as the call for Ukrainian researchers.

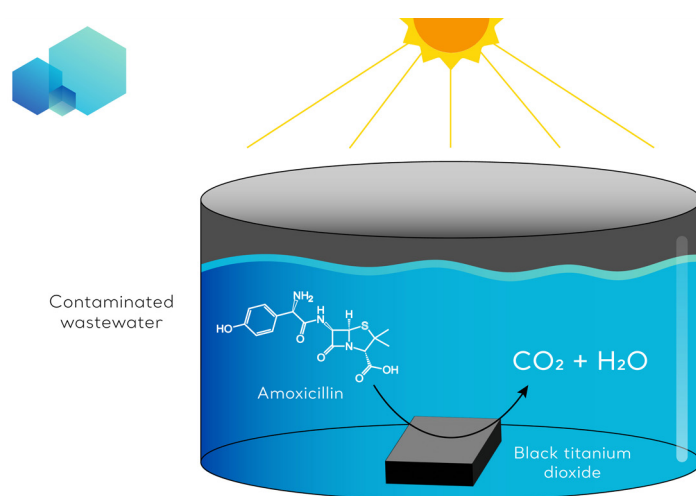


Figure 1. Visible-Light-Active Black TiO₂ Nanoparticles with Efficient Photocatalytic Performance for Degradation of Pharmaceuticals, Andronic L., Ghica D., Stefan M., Mihalcea C. G., Vlaicu A. M., & Karazhanov S., *Nanomaterials*, **2022**.

Facts & Figures

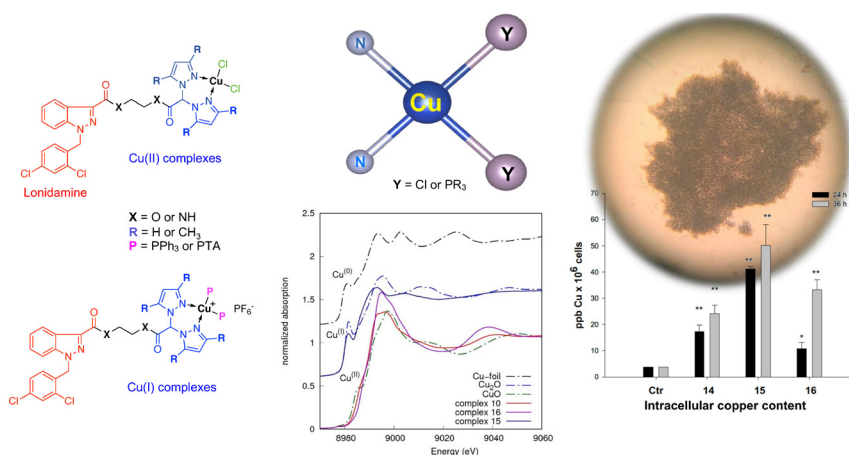


Figure 2. Cu (I) and Cu (II) Complexes Based on Lonidamine-Conjugated Ligands Designed to Promote Synergistic Antitumor Effects. Del Bello F., Pellei M., Bagnarelli L., Santini C., Giorgioni G., Piergentili A., Quaglia W., Battocchio C., Iucci G., Schiesaro I., Meneghini C., Venditti I., Ramanan N., De Franco F., Sgarbossa P., Marzano C., & Gandin V., *Inorganic Chemistry*, **2022**.

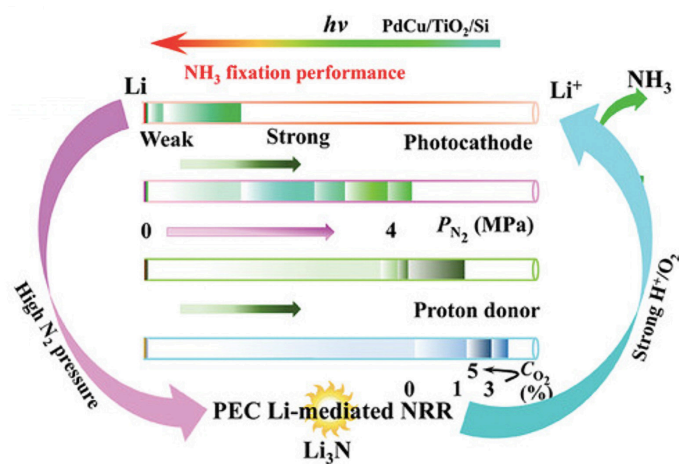


Figure 3. Photoelectrochemical N₂-to-NH₃ Fixation with High Efficiency and Rates via Optimized Si-Based System at Positive Potential versus Li^{0/+}. Zhang X., Lyu Y., Zhou H., Zheng J., Huang A., Ding J., Xie C., De Marco R., Tsud N., Kalinovykh V., Jiang S.P., Dai L., Wang S., *Advanced Materials*, **2023**, DOI.

CERIC for FAIR data

The Photon and Neutron Open Science Cloud – PaNOSC project came to an end in November 2022; the project aimed to address the FAIR principles in the workflows of photon and neutron (PaN) facilities by developing tools and software for data management, data handling, analysis and simulation, as well as the required legal and administrative frameworks preparation (e.g., data policy adoption). Within the PaNOSC framework, CERIC and project partners made data produced at PaN facilities across Europe available under an Open FAIR Data policy. Moreover, the project consortium developed and adopted a federated search API (Application Programming Interface) for PaN data catalogues, crucial for the functioning of an Open Data portal, as well as a

common protocol for harvesting data and metadata. Finally, to make data reusable, a community metadata standard for PaN sources (NeXus/HDF5) has been widely adopted at several CERIC instruments.

CERIC response to global challenges

CERIC has contributed to the UN Sustainable Development Goals (SDGs) and to tackling grand societal challenges. The main focus is on the development of services in the fields of energy and life sciences, providing ground-breaking discoveries that contribute to different SDGs (SDG3 - Good Health and Well-being, SDG 7 - Affordable and Clean Energy, SDG 12 - Responsible Consumption and Production, SDG 15 - Life on Land). Regarding energy research, CERIC continued and increased its efforts in

the fields of batteries, fuel cells and solar cells. Between 2022 and 2023, 12 papers were published in these domains. Moreover in 2023, two European Commission's Joint Research Centre (JRC) facilities in the Netherlands have been added, as associated facilities, to CERIC's open access offer for research in the energy field.

To promote a circular economy approach in terms of sustainable materials in the production process, the European research infrastructure project ReMade@ARI kicked off in September 2022: CERIC is a project partner involved in activities such as project management, academic and industrial access support, and four of its Partner Facilities are involved in providing access for innovative research.

Our beamlines, laboratories and services

Elettra Beamlines		Acronym explanation and/or short description of the main techniques	source*	energy range (eV)
1.1L	TwinMic	Soft X-ray transmission and emission microscope	id	400 – 2200
1.2L	Nanospectroscopy	Spectroscopic photoemission and low energy electron microscope (SPELEEM)	id	25 – 1000
1.2R	NanoESCA	Imaging XPEEM spectroscopy, microprobe ARPES and XPS	id	25 – 1000
2.2L	ESCA Microscopy	Scanning photoelectron microscopy (SPEM)	id	400 – 1200
2.2R	SuperESCA	High energy resolution photoemission and x-ray absorption spectroscopy	id	90 – 1800
3.2L	Spectromicroscopy	Angle-resolved photoemission microscopy	id	27; 74
3.2R	VUV-Photoemission	Vacuum UltraViolet photoemission	id	20 – 750
4.2	CiPo	Circular Polarization - (Dichroic measurements on chiral systems)	id	7 – 900
5.2R	XRD1	X-Ray Diffraction	id	4000 – 21500
5.2L	SAXS	Small Angle X-ray Scattering	id	5400; 8000; 16000
6.1L	MSB	Materials Science Beamline (Photoemission and x-ray absorption)	bm	22 – 1000
6.1R	SYRMEP	SYNchrotron Radiation for MEDical Physics	bm	9000 – 40000
6.2L	GasPhase	Gas Phase Photoemission - Photoelectron and fluorescence spectroscopy	id	13 – 900
7.1R	MCX	Materials Characterisation by X-ray diffraction	bm	6000 – 20000
7.2	ALOISA	Advanced Line for Overlayer, Interface and Surface Analysis	id	130 – 1500
8.1L	BEAR	Bending source for Emission Absorption and Reflectivity	bm	2.75 – 1600
8.2	BACH	Beamline for Advanced diChroism	id	44 – 1600
9.1	SISSI-Bio	Synchrotron Infrared Source for Spectroscopy and Imaging Chemical and Life Sciences	bm	0.001 – 2.5
9.1	SISSI-Mat	Synchrotron Infrared Source for Spectroscopy and Imaging Materials Science	bm	0.001 – 2.5
9.2R	APE-LE	Advanced Photoelectric Effect - Low Energy	id	10 – 100
9.2L	APE-HE	Advanced Photoelectric Effect - High Energy	id	200 – 1600
10.1L	XRF	X-Ray Fluorescence	bm	700 – 14000
10.1R	DXRL	Deep X-Ray Lithography	bm	2 – 20000
10.2L	IUVS	Inelastic UltraViolet Scattering	id	5 – 11
10.2R	BaDElPh	BAnd Dispersion ELection-PHOnon coupling (LE-ARPES)	id	4.6 – 40
11.1R	XAFS	X-Ray Absorption Fine Structure	bm	2400 – 25000
11.2C	XRD2	X-Ray Diffraction (Macromolecular Crystallography)	id	8000 – 35000
11.2R	Xpress	High pressure X-ray diffraction	id	25000

source* **id** = insertion Device (wiggler or undulator) / **bm** = bending magnet

FERMI Beamlines		source	energy range (eV)
TeraFERMI	TeraHertz beamline at FERMI	THz	0,001 - 0,05
MagneDyn	Magneto Dynamics Studies	FEL-2	40-310
LDM	Low Density Matter: atomic, molecular, and optical science with rarefied targets	FEL-1 / FEL-2	12 - 310
DiProl	Diffraction and Projection Imaging	FEL-1 / FEL-2	12 - 310
EIS-TIMEX	Elastic and Inelastic Scattering: Ultrafast Time-resolved studies of Matter under EXtreme and metastable conditions	FEL-1 / FEL-2	12 - 310
EIS-TIMER	Elastic and Inelastic Scattering: TIME-Resolved spectroscopy of nanoscale dynamics in condensed matter physics	FEL-1 / FEL-2	12 - 200

Laboratories & Services	
CITIUS	Interregional Centre of Ultrafast Photonic Technology for Spectroscopies
MiNaC	Micro and Nano Carbon Laboratory
NanoLab	NanoInnovation Laboratory
OptimaTo	Optimal Imaging and Tomography
SciComp	Scientific Computing & Software for Experiments
SPRINT	Spin Polarized Research Instrument in the Nanoscale and Time Laboratory
Structural Biology	Structural Biology Laboratory
Nanoscale Materials Laboratory	Nanoscale Materials Laboratory
TomoLab	TomoLab
T-Rex	T-Rex Laboratory
Q4Q	Quantum Spectroscopy for Quantum Materials

Proposal Review Panels

Access to Elettra and FERMI beamlines is offered every year to scientists from more than 50 different countries based on the scientific merit of the proposals they submit. The most deserving proposals are selected by independent Proposal Review Panels of world-renowned experts in synchrotron radiation research and applications, appointed by the laboratory management.

The Panels are divided into subpanels, each of them reflecting different research areas. These panels meet twice a year, producing a written report for each proposal. Best ranked proposals are allocated according to the amount of available user dedicated beamtime.

Elettra Proposal Review Panel Enrique Garcia Michel (Chairman)

Atoms Molecules and Plasma

Edwin Kukk (Chairman)
Christian Alcaraz
Andras Bodi
Patrick Hemberger

Catalytic Materials/ Surface Science

Luca Ottaviano (Chairman)
Carla Bittencourt
Martina Corso
Ana Cremades
Valentina De Renzi
Sebastian Guenther
Georg Franz Konrad Held
Jose Angel Martin Gago
Yaroslava Lykhach
Jill Miwa
Celia Rogero Blanco
Gopinathan Sankar

Condensed matter – Electronic and Magnetic Structure

Enrique Garcia Michel (Chairman)
Benedetta Casu
Mirko Cinchetti
Hugo Dil
Alexei V. Fedorov
Marino Marsi
Pascale Roy
Stefano Rusponi
Tomasz Slezak
Anna Tamai
Elio Vescovo

Hard condensed matter – Structures

Giuseppe Cruciani (Chairman)
Tiziana Boffa Ballaran
Wilson Crichton
Natalia Doubrovinkaia
Patrick Frank
Chiara Maurizio
Carlo Meneghini
Lorenzo Mino
Vittoria Pischetta
Gloria Subias Perugia
Ian Swainson
Rosario Isabel Cerda' Vilaplana

Instrumentation, Technological and Soft Materials – Life and Medical Sciences (including Crystallography)

Mariangela Cestelli Guidi (Chairman)
Frauke Alves
Sam Bayat
Hugh James Byrne
Francesco De Carlo
Elisabetta Giorgini
Enzo Lombi
Kamilla Malek
Giorgio Margaritondo
Rajmund Mosko
Mark Tobin
Naoto Yagi

Macromolecular, Protein and Polymer Crystallography

Beatrice Vallone (Chairman)
Michele Cianci
Silvano Geremia
Balasubramanian Gopal
Natasa Novak Tusar
Aravind Penmatsa

Scattering

Maurizio Musso (Chairman)
Anuradha Ramoji
Paola Sassi
Giulietta Smulevich

FERMI Proposal Review Panel Wolfgang Eberhardt (Chairman)

FERMI subpanel

Wolfgang Eberhardt (Chairman)
Nora Berrah
John Bozek
Stefan Eisebitt
Manfred Helm
Alexey Kimel
Jonathan Marangos
Christopher Milne
Matteo Mitrano
Giulio Monaco
Shaul Mukamel
Luca Perfetti
Claus Michael Schneider
Robert Schoenlein
Svante Svensson
Amina Taleb-Ibrahimi
Paulus H.M. Van Loosdrecht
Michel Viret
Gwyn Philip Williams

TeraFERMI subpanel

Wolfgang Eberhardt (Chairman)
Claus Michael Schneider (Chairman)
Manfred Helm
Alexey Kimel
Luca Perfetti
Robert William Schoenlein
Paulus H.M. Van Loosdrecht
Gwyn Philip Williams

TREX & CITIUS subpanel

Wolfgang Eberhardt (Chairman)
Claus Michael Schneider (Chairman)
John Bozek
Stefan Eisebitt
Manfred Helm
Alexey Kimel
Matteo Mitrano
Luca Perfetti
Svante Svensson
Paulus H.M. Van Loosdrecht

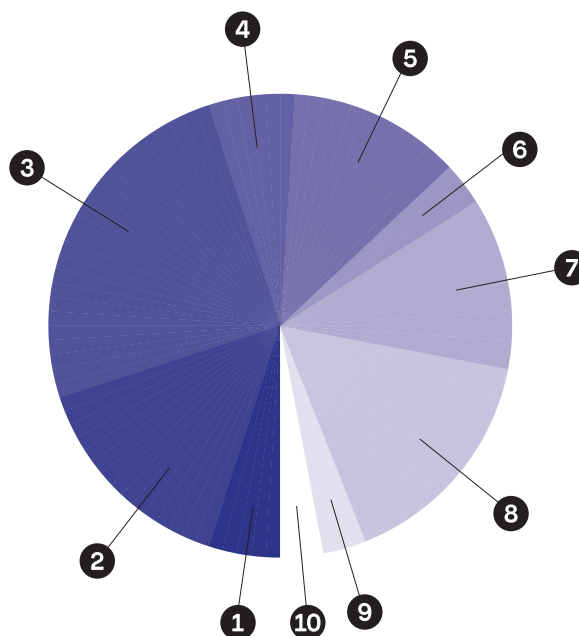
Users at Elettra

II semester 2022 - I semester 2023

Proposals submitted: 831 (+ 154 through CERIC-ERIC)
 Proposals allocated: 400 (+ 88 through CERIC-ERIC)

Elettra proposals allocated by Research Area:

- 1 Atoms Molecules and Plasmas (4%)
- 2 Catalytic Materials/Surface Science (17%)
- 3 Condensed matter - Electronic and Magnetic Structure (22%)
- 4 Environmental and Earth Science (5%)
- 5 Hard condensed matter - Structures (12%)
- 6 Instrumentation and Technological materials (1%)
- 7 Life and Medical Sciences (excluding Crystallography) (13%)
- 8 Macromolecular, Protein and Polymer Crystallography (22%)
- 9 Polymers and Soft Matter (1%)
- 10 Scattering (3%)



Elettra and CERIC-ERIC users on site by country

Australia	6	Netherlands	11
Austria	68	Norway	13
Belgium	24	Pakistan	3
Brazil	21	Poland	16
Cameroon	2	Portugal	3
Canada	1	Romania	11
China	3	Russian Federation	19
Croatia	20	Saudi Arabia	1
Cyprus	1	Slovenia	62
Czech Republic	43	Spain	27
Denmark	9	Sudan	1
Egypt	2	Sweden	6
Finland	5	Switzerland	32
France	39	Turkey	1
Hungary	10	United Kingdom	28
Germany	166	United States of America	17
India	98	Grand Total	1379
Iran, Islamic Republic Of	7		
Ireland	3		
Israel	3		
Italy	579		
Japan	9		
Jordan	1		
Mexico	8		

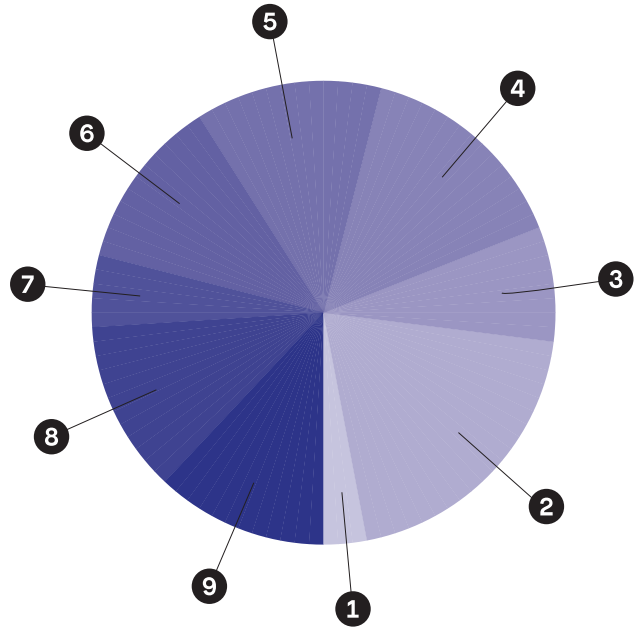
Users at FERMI

Call 14 and Call 15 May 2022 - May 2023

Proposals submitted: 129 (May 2022 - May 2023)
 Proposals allocated: 36

FERMI proposals allocated by research area:

- ❶ Atoms Molecules and Plasmas Polymers and Soft Matter (3%)
- ❷ Condensed matter - Electronic and Magnetic Structure (22%)
- ❸ Diffraction and Projection Imaging (8%)
- ❹ Elastic and Inelastic Scattering (14%)
- ❺ Low Density Matter (11%)
- ❻ Magnetism (11%)
- ❼ Novel methods (6%)
- ❽ THz-science (14%)
- ❾ Time Resolved photoemission (11%)



FERMI users on site by country

Austria	2
Belgium	1
Canada	1
Croatia	2
Denmark	3
France	13
Germany	39
Italy	96
Japan	1
Luxembourg	1
Netherlands	2
Slovenia	1
Spain	1
Sweden	3
Switzerland	5
United Kingdom	5
United States of America	16
Grand Total	192

Industrial Liaison Office News



In the pharmaceutical field, in recent years Elettra has collaborated and stipulated research contracts with many of the main Italian pharmaceutical companies most important in terms of turnover. In particular, the consolidated collaborations with the market leader in the development of drugs for the respiratory system and neonatology led to the evaluation of new, broader projects of common interest involving the SISSI beamline and the Structural Biology Laboratory.

Collaborations involving the XRD1 and XRD2 lines continued for the study of the molecular structures of active pharmaceutical ingredients (APIs) on behalf of some Polish and Italian pharmaceutical companies. Elettra has acquired the rights to exploit the patent of an innovative protocol that allows high sensitivity purity analyzes to be carried out on active ingredients and finished products, with significant implications in the pharmaceutical, biotechnological, nutraceutical and diagnostic sectors.

In the materials analysis sector, new collaborations were started with national companies that produce components for the automotive sector on the SISSI line and the XRF and XAFS lines; for applications in Life Sciences with the involvement of the Nanoinnovation Lab and in the field of metallurgy with the involvement of the XAFS and Materials Science line.

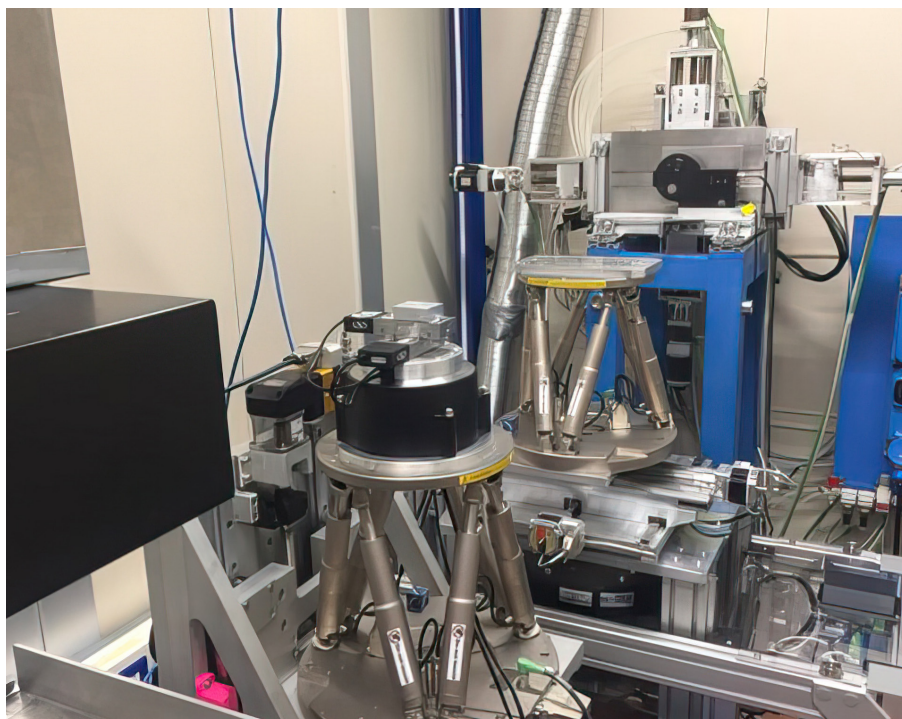
Synchrotron radiation based techniques at the forefront of research for energy storage technologies

Synchrotron radiation-based techniques have emerged as transformative tools in the realm of energy storage technologies, bridging the microscopic and macroscopic worlds by probing an array of length scales with varying depth sensitivities and spatial/temporal resolutions. Batteries, a crucial component of these energy storage systems, are especially benefiting from these advanced methodologies. Elettra, with its cutting-edge synchrotron techniques, embodies this innovation in the field.

By harnessing synchrotron radiation, scientists are now capable of mapping the distribution of chemical species within a battery. Such insights are invaluable, shedding light on the movement of ions during charge and discharge cycles, thereby paving the way for enhancements in battery design. Furthermore, the powerful X-rays emitted by synchrotrons can penetrate the battery materials, revealing a detailed snapshot of their intricate internal structure. This capability provides an avenue for experts to monitor structural changes during battery operation. One of the most groundbreaking advantages of these techniques is the ability to capture data at incredible speeds, enabling

real-time or near real-time observations. Researchers can now closely observe and analyze the dynamic processes within batteries, such as the evolution of their structure with use. Additionally, by closely watching batteries as they undergo charge and discharge cycles, deeper insights into the degradation mechanisms become apparent. This knowledge is pivotal in the quest to develop new materials and innovative designs that significantly prolong battery life.

Elettra, thanks to its partnership with CERIC (the European Research Infrastructure Consortium), supported BASF's research and development unit in the USA in studying materials and technologies related to its energy storage activities. BASF, a European multinational company, is the world's largest chemical producer, with subsidiaries and joint ventures in more than 80 countries and over 390 production sites in Europe, Asia, Australia, the Americas, and Africa.



Revolutionizing Insertion Device Design and Manufacturing at Kyma S.p.A.: A Cutting-Edge Approach



Unleashing the Power of Light with uncompromising quality

Step into a world where science meets innovation, and technological marvels come to life! Welcome to Kyma S.p.A., the trendsetter in designing, manufacturing, and commissioning cutting-edge insertion devices for light sources, captivating the scientific community worldwide.



Illuminating the Path to Breakthroughs: Kyma's Journey

Established in August 2007, Kyma S.p.A. set its sights on a remarkable mission: to redefine the possibilities of light sources and empower researchers with unparalleled tools. Driven by experience and relentless passion, Kyma quickly emerged as a dominant force in the market, with unparalleled expertise and unwavering reliability.



Where Brilliance Takes Shape

At Kyma, we don't just build devices; we push the boundaries of what's technically possible. With over 50 large insertion devices delivered and a diverse range of groundbreaking equipment, including laser heater undulators, phase shifters, and magnetic measurement benches, Kyma's portfolio is a demonstration to its remarkable expertise.



A Global Symphony of Scientific Partnerships

Collaborating with prestigious institutions across the globe, Kyma's work resonates with excellence. From the Argonne National Laboratory in the USA to the European XFEL, and the Elettra-Sincrotrone Trieste in Italy, our journey is a symphony of extraordinary partnerships.



The Power to Illuminate: Join Kyma in this extraordinary journey

We invite scientists, technicians, and innovators to become part of the Kyma family. Together, we shall illuminate the world with breakthroughs that turn scientific research into real-world technological.



Discover more about Kyma S.p.A. and our groundbreaking Permanent Magnet Devices

With over a decade of experience in the industry and a proven track record of successfully manufacturing and installing numerous permanent magnet devices worldwide, Kyma has solidified its position as a well-established and highly trusted company in the permanent magnet devices segment and accelerator market. Our dedication to innovation, reliability, and exceptional craftsmanship sets us apart, making Kyma the go-to choice for those seeking cutting-edge solutions for their accelerator-based research and experiments.



How to Contact Us:

Kyma S.p.A.

S.S. 14 - km 163,5 in AREA Science Park
IT-34149 Trieste, Italy, EU

Tel. +39 040 375 8472

Fax +39 040 375 8209

info@kyma-undulators.eu

kyma-undulators.com

Institutional Visits and Events

New Quaestor of Trieste Ostuni

(Trieste, 21 September 2022)

On September 21, 2022, the Quaestor of Trieste, Dr. Pietro Ostuni, paid a visit to Elettra. Welcomed by the President and CEO Professor Alfonso Franciosi for a brief institutional presentation, he then proceeded to visit the experimental hall, to visit the experimental hall led by the deputy coordinator-general Marco Marazzi and the Spectroscopy, Photoemission and Dynamics cluster coordinator Andrea Locatelli. The colleagues Giuliana Tromba and Nicola Demitri spoke on the SYRMEP and XRD2 lines, while Filippo Bencivenga led the visit for FERMI.



Members of the Permanent Conference of General Directors of Italian Public Research Institutions

(Trieste, 25 October 2022)

On the occasion of the event "CODIGER 2022 'The Challenge of Growth' organized by AREA Science Park and its Director General Anna Sirica, seeking to enhance Italy's research system's administrative capacity, a delegation of CO.DI.G.E.R., General Directors of Italian Public Research Institutions, visited Elettra. Welcomed by Alfonso Franciosi, Elettra President and CEO, and Giorgio Paolucci Elettra Chief Scientific Officer, they visited Elettra and FERMI experimental halls, including the CiPo, Twin Mic, SYRMEP, XRD1, XRD2 and LDM beamlines. Technical and scientific aspects of the research and techniques used were discussed.



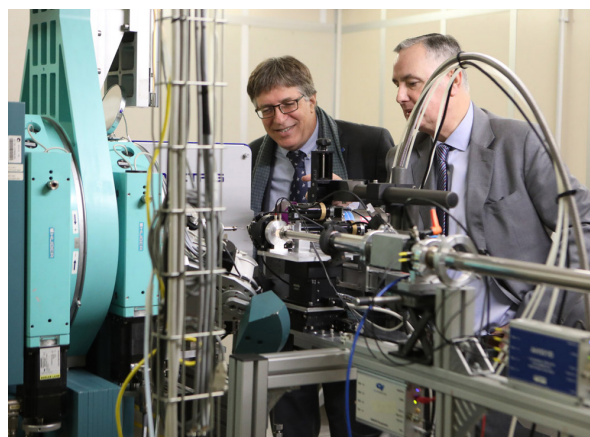
H.E. Ambassador of Israel to Italy Alon Bar

(Trieste, 24 January 2023)

After a meeting at AREA Science Park with President Caterina Petrillo and Director General Anna Sirica on January 24 2023 Elettra Sincrotrone Trieste received a visit from His Excellency Alon Bar, Israel's Ambassador to Italy.

Welcomed by Giorgio Paolucci, Chief Scientific Officer, he visited the experimental halls and some beamlines for an insight into applications and research.

At the end of the visit, H.E. Alon Bar left a dedication in the Elettra's signature book: "Impressive facility, with top scientists and researchers. Thanks for the very interesting visit. Wishing you success on the next stage. A. Bar."



Johanna Leissner, Fraunhofer Scientific Representative and member of the EU Expert Group "Cultural Heritage"

(Trieste, 27 January 2023)

On the occasion of the Workshop 'Cultura e Creatività: nuove leve per l'innovazione multisettoriale' (Culture and Creativity: new levers for multi-sectoral innovation) organised by AREA Science Park within the framework of the activities of the Culture and Creativity Region Cluster, Johanna Leissner, Fraunhofer Scientific Representative and member of the EU Expert Group "Cultural Heritage", visited Elettra. Welcomed by Marco Marazzi, Deputy Coordinator General and Marco Peloi Head of the Industrial Liaison Office and after an institutional presentation by Giorgio Paolucci, she toured Elettra and FERMI's experimental halls, where she learnt more about the technical and scientific aspects of the research and techniques used.



Institutional Visits and Events

SIRIUS Brazil's Director Harry Westfahl in Elettra for a round table discussion and a webinar

(Trieste, 2 February 2023)

Prof. Harry Westfahl Jr., Director of Brazil's National Synchrotron Light Laboratory (LNLS,) presented "Sirius: A New Era for Latin American Science with a Fourth-Generation Storage Ring" during a visit to Elettra. He highlighted the Sirius project's scientific opportunities in biological, condensed matter research, emphasizing its fourth-generation storage ring's capabilities. Following a round table, Prof. Alfonso Franciosi, Elettra's President and CEO, illustrated Elettra 2.0 and FERMI 2.0 projects. The main objective of the initiative was to acquaint the Italian scientific community with the SIRIUS particle accelerator, the SIRIUS facility, to promote greater dissemination of its potential by increasing academic exchanges between Brazilian and Italian researchers.



New Prefect of Trieste and Government Commissioner for the Friuli Venezia Giulia Region Pietro Signoriello

(Trieste, 1 March 2023)

On March 1, 2023, the new Prefect of Trieste and Government Commissioner for Friuli Venezia Giulia Region, Pietro Signoriello, visited Elettra with Vice Prefect Ms. Beatrice Musolino. Welcomed by Elettra's President and CEO Alfonso Franciosi, the visit included an introduction to the Centre's history and excellence. The delegation, led by Marco Marazzi, Deputy Coordinator General, into Elettra and FERMI experimental halls, met Andrea Locatelli, Nanospectroscopy beamline Head, and Claudio Masciovecchio, FERMI's Head of time-resolved techniques. The guests expressed great appreciation and keen interest in the possible uses of the analysis techniques in a wide variety of fields, particularly in relation to the Elettra 2.0 project.



The Minister of University and Research Anna Maria Bernini

(Trieste, 9 June 2023)

On June 9, 2023 the University and Research Minister Sen. Anna Maria Bernini visited AREA Science Park and Elettra. After a meeting with the representatives of regional institutions at AREA Science Park where the Research and Innovation system in Friuli Venezia Giulia was illustrated, Minister Bernini visited few of the scientific realities present on the two campuses, including Modefinance, LAGE Genomics and Epigenomics Laboratory, Alifax R&D laboratories, and the ICGEB International Centre for Genetic Engineering and Biotechnology laboratory.

At Elettra she was welcomed by President and CEO Prof. Alfonso Franciosi, General Coordinator Michele Svandrlík, Chief Financial Officer Michele De Franceschi, and Marco Marazzi, Deputy General Coordinator.

After an overview of the infrastructure and future developments provided by the President, the group moved on to the TwinMic, Xpress, and XRD2 lines where they met with the beamline coordinators Alessandra Gianoncelli, Bobby Joseph, and Annie Heroux to learn more about the techniques, experiments, and international cooperations.

She ended her tour on N/R Laura Bassi of the OGS National Institute of Oceanography and Experimental Geophysics.



Conferences

IPAC'23

co-organized by Elettra in Venice Italy

(Venice Lido, 7-12 May 2023)

IPAC'23, the 14th International Particle Accelerator Conference, took place at the Venice Convention Center, Venice Lido from 7 to 12 May, 2023. IPAC is the world's leading international event in the field of particle accelerators. The Conference was hosted by Elettra and INFN and organized under the auspices of the European Physical Society Accelerator Group (EPS- AG) and the International Union of Pure and Applied Physics (IUPAP).

The fully in-person event had record attendance with 1,660 registered participants, including 273 students, from 37 different countries, and 121 industrial exhibitors, illustrating the need for real life interactions in the global accelerator landscape after the end of the COVID-19 pandemic. The Organising Committee and the Scientific Programme Committee were chaired, respectively, by Ralph Assmann and Peter McIntosh (STFC). The Local Organising Committee was co-chaired by Alessandro Fabris (Elettra) and Giovanni Bisoffi (INFN).

Following the opening speeches by Antonio Zoccoli (INFN president) and Alfonso Franciosi (Elettra president), the scientific programme got under way. It included 87 talks and 1790 posters covering all particles (electrons, positrons, protons, ions, muons, neutrons, ...), all types of accelerators (storage rings, linacs, cyclotrons, plasma accelerators, ...), all use-cases (particle physics, photon science, neutron science, medical and industrial applications, material physics, biological and chemical, ...) and institutes involved across the world. On Friday 12 May, after the closing session, participants were offered the opportunity to visit either Elettra or INFN Legnaro.

The prize session saw Xingchen Xu (Fermilab), Mikhail Krasilnikov (DESY/Zeuthen) and Katsunobu Oide (KEK) receive the 2023 EPS-AG accelerator prizes. In addition, the Bruno Touschek prize was awarded to Matthew Signorelli (Cornell University), while two student poster prizes went to Sunar Ezgi (Goethe Universität Frankfurt) and Jonathan Christie (University of Liverpool).

Elettra's scientific participation included 5 talks, selected by the Scientific Programme Committee, and more than 30 posters presented during the conference, covering the results and future perspectives of FERMI, Elettra and Elettra 2.0. Both the talks and the poster interactions demonstrated widespread interest for developments being carried on at our Laboratory.

Additional information, full programme and pictures on ipac23.org.



Workshops, Meetings and Schools

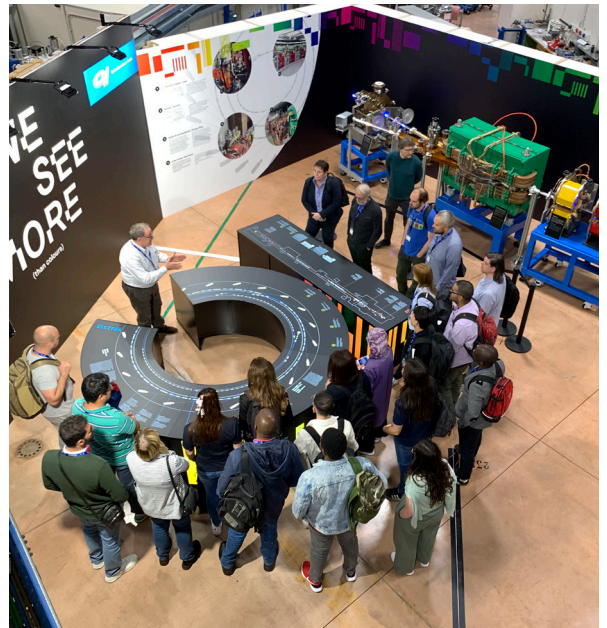
Workshop on Geomaterials, the importance of X-ray applications (Trieste, 27-28 September 2022)

The international workshop 'Synchrotron and laboratory-based X-ray computed microtomography: Applications in the Earth sciences' took place on September 27-28 with 50 participants from different countries. Organized by Elettra in cooperation with the University of Catania, it aimed to familiarize young researchers in geomaterials with X-ray applications for microscale structure analysis. Activities included analyzing geological samples and practical sessions. Among the organizers Rosalda Punturo (lecturer at Dsbga and scientific referee for the University of Catania), Gabriele Lanzafame (Dsbga Catania), Lucia Mancini (ZAG - Slovenian National Institute for Building and Civil Engineering), and Giuliana Tromba (Elettra Sincrotrone Trieste). The initiative was part of the PhD programme in "Earth and Environmental Sciences" of the University of Catania.



"Joint ICTP-IAEA Advanced Workshop on Future Trends in Multidisciplinary Ion Beam Analysis" (Trieste, 12 October 2022)

On October 12, 2022, Elettra has welcomed a group of about 20 participants to the 'Joint ICTP-IAEA Advanced Workshop on Future Trends in Multidisciplinary Ion Beam Analysis'. The group visited the Elettra Exhibition area, the DXRL, X-Ray Fluorescence XRF, XAFS, SISSI, SYRMEP, Twin-Mic beamlines and the FERMI experimental hall where they followed the researchers' explanations with great interest and had the chance to deepen some technical and practical aspects. Since 2005 Elettra has been an "IAEA Collaborating Centre" and has been endorsing the Agency's activities in disseminating scientific and technical culture and promoting international networks among the research communities worldwide. IAEA has been partnering with the XRF beamline at Elettra since 2012.



2023 ICTP Winter College on Optics (Trieste, 10 February 2023)

On February 10, 2023, Elettra hosted over 55 participants for the '2023 ICTP Winter College on Optics: Terahertz Optics and Photonics'. This two-week program involved researchers from developing nations into the field of Optics, Lasers and their applications. Miltcho Danailov, Elettra Laser Lab's Senior Researcher, collaborated with the ICTP organizer Joe Niemela to shape the program. This edition explored Terahertz Optics and Photonics. It was the occasion for students to visit both Elettra and FERMI focusing on SISSI and TeraFermi beamlines strongly related to the College topic, engaging with researchers to delve into technical nuances.



HERCULES School back in presence at Elettra (Trieste, 20-24 March 2023)

The European school "HERCULES: neutrons and synchrotron radiation for science", founded in 1991, is dedicated to young students who wish to use the synchrotron radiation in fields such as physics, chemistry and biology. In 2023 the school was held from March 20 to 24. The main objective of the school is to train a generation of young researchers capable of exploiting the exceptional experimental research potentials of advanced light sources with practical activities carried out by seven Elettra beamlines (ALOISA, NANOSPECTROSCOPY, NANOESCA, DXRL, SISSI, XPRESS, IUVS) and Elettra and FERMI laboratories (Nanoinnovation lab, structural Biology lab, TOMOLAB in Elettra; Terafermi and T-ReX in FERMI).



Workshops, Meetings and Schools

Training for 15 PhD Students of the Destiny Doctorate Programme (Trieste, 15-19 May 2023)

From May 15th until May 19th 2023, 15 students selected within the DESTINY European Doctorate Programme exploited the Elettra beamlines' capabilities in a theoretical and hands-on training school entitled «Operando studies using synchrotron radiation».

The students had the possibility to train on two different beamlines XAFS and MCX, and the Tomolab laboratory. Interactive sessions were organized to prepare students to deal with basic data analysis as well as to write their own proposals.

The final aim of this school was to increase the awareness of the potential of synchrotron radiation for the DESTINY students, and to provide them the basis for the possible integration of such techniques in their PhD projects.



Held in Italy for the first time, the 19th edition of the P4EU Annual Meeting (Trieste, 23 May 2023)

On May 23 a group of participants in the Protein Production and Purification Partnership in Europe (P4EU) annual meeting, visited Elettra.

The event was organised in Trieste at Area Science Park by Elettra Sincrotrone Trieste - the first Italian member to join the network - in cooperation with ICGEB and under the patronage of Area Science Park. The theme of this edition was cutting-edge technologies for protein production.

Attended by more than 100 researchers from leading laboratories as well as international experts in this important scientific and experimental field, the meeting dealt with state-of-the-art methods for producing multi-protein systems, complex and difficult to obtain, but essential for studying the molecular mechanisms of the cell using cryo-microscopy. The group visited the NanoInnovationlab, the Elettra Experimental Room and the Structural Biology Laboratory.



Joint ICTP-IAEA Advanced Workshop on Accelerator Mass Spectrometry Radiocarbon Dating for Heritage and Forensic Sciences (Trieste, 25 May 2023)

On May 25, 2023, Elettra welcomed the 40 participants of the 'Joint ICTP-IAEA Advanced Workshop on Accelerator Mass Spectrometry Radiocarbon Dating for Heritage and Forensic Sciences'.

Visitors were welcomed by Giuliana Aquilanti, Coordinator of the Research Projects Cluster and Head of XAFS and XRF beamlines. Afterwards, Franco Zanini, researcher at SYRMEP beamline, gave the lectures 'Alternative synchrotron radiation methods for dating of heritage and forensic samples' and 'Synchrotron infrared spectroscopies and chemometrics for forensic application'. Participants were then accompanied in the exhibition area and the experimental hall where they visited SISSI, XRF, MCX, TWINMIC and SYRMEP, deepening some technical and practical aspects.



Workshops, Meetings and Schools

"Elettra 2.0: New Structural Biology Opportunities" Workshop (Trieste, 3-4 July 2023)

The workshop was held on July 3, 2023 at Area Science Park, bringing together international experts and the community of present and future users of the structural biology platform under development.

The new Elettra 2.0 lightsource and the funding from the PNRR project PRP@CERIC are the key to a renewed synergy between Elettra, Area Science Park and CNR, for the IOM and IC institutes, in the field of structural biology, aimed at the integration of the new macromolecule micro-diffraction beamline, the electron cryo-microscopy facility and the structural biology laboratory for sample preparation and characterization.



Workshop "μ-XRF at Elettra 2.0: Challenges and Opportunities" (Trieste, 11-12 September 2023)

Held at Elettra on September 11 and 12, 2023, this event hosted key users of the present XRF beamline and colleagues from other facilities gathering to discuss the present needs and future perspectives over diverse scientific domains for the new beamline μ-XRF that will be part of the Elettra 2.0 offer.

The invited speakers highlighted the challenges encountered in similar beamlines in other diffraction-limited synchrotron facilities and discussed about scientific opportunities offered by the micrometric spatial resolution of X-ray fluorescence coupled with other x-ray techniques. Their ideas and vision will help to set the final project of μ-XRF beamline and its experimental station.



PhotonMeadow23 Workshop (Trieste, 12-14 September 2023)

The workshop was held at ICTP Trieste from September 12 to 14, 2023. This edition was a merge of two different workshops:

MEADOW - 10 years after, aiming to celebrate the 10th anniversary of the original "METrology, Astronomy, Diagnostics and Optics Workshop", held in the same venue in 2013, and PhotonDiag 2023 representing the 6th edition of the "FELs of Europe Workshop on FEL Photon Diagnostics, Instrumentation, and Beamlines Design"

The three days event has been a real success, welcoming over 110 attendees from all over the world, and giving the audience the chance to focus on several topics such as, among all, X-ray optics, Photon diagnostics, Scientific computing.



Public Engagement Events

Trieste Next 2023

(Trieste, 22-24 September 2023)

From 22 to 24 September Elettra has been one of the leading institutes of the twelfth edition of 'Trieste Next', entitled 'A New World, Science, Culture, Innovation for a Sustainable Future'. The festival registered as usual thousands of Italian and foreign visitors that participated in the many activities organized in this occasion.

Fully booked the two conferences coordinated by Elettra.

Research frontiers in the treatment of brain tumours

Chair: Roberto Pugliese, Deputy General Coordinator and Director of the IT Division of Elettra Sincrotrone Trieste President of Glioblastoma.IT ODV.

Invited speakers Elena Longo, Researcher at SYRMEP beamline of Elettra; Daniela Cesselli, Associate Professor in Pathology – University of Udine; Marco Vindigni, Medical Director at the Operative Unit of Neurosurgery – Department of Head, Neck and Neuroscience – ASUFC Udine, and with the facilitation of the comedians "I PAPU", Andrea Appi and Ramiro Besa.



Proteins, supercomputing and space stations: researching new drugs

Chair: Paola Storici, Researcher at Elettra and head of the Protein Laboratory.

Invited Speakers Emiliano Biasini, Associate Professor at the Department of Cell, Computational and Integrated Biology – Trento University; Pietro Faccioli, Associate Professor at the 'G. Occhialini' Department of Physics – Milano-Bicocca University; Marta S. Semrau, Researcher at Protein Facility of Elettra Sincrotrone Trieste.

In the three-day large exhibition area in Piazza Unità, organized with Area Science Park, Istituto Officina dei Materiali CNR-IOM, International Centre for Genetic Engineering and Biotechnology (ICGEB), Fondazione Italiana Fegato - FIF and in collaboration with Idrostudi and Alifax, Elettra Sincrotrone Trieste presented three activities/labs for the general public.



And there was light!

Lasers, microscopes and X-rays to analyse matter

With Sumea Klokic, CERIC-ERIC Post-Doc researcher at Elettra Sincrotrone Trieste; Benedetta Marmiroli, Senior Researcher at Elettra Sincrotrone Trieste on the CERIC-ERIC SAXS beamline and the DXRL beamline; Christian Morello, Engineer at Elettra Sincrotrone Trieste; Barbara Sartori, Senior Researcher at Elettra Sincrotrone Trieste on the CERIC-ERIC SAXS beamline; Philipp Aldo Wieser, PhD Student at Elettra Sincrotrone Trieste on the CERIC-ERIC SAXS beamline.



Bacteria: can we exploit them?

With Valentina Bonanni, Scientist of the TwinMic beamline at Elettra Sincrotrone Trieste; Alessandra Gianoncelli, Head of the TwinMic beamline at Elettra Sincrotrone Trieste; Milan Zizic, PostDoc of the TwinMic beamline at Elettra Sincrotrone Trieste.

Tune the metronomes!

With Cecilia Blasetti, International Project Officer at Elettra Sincrotrone Trieste; Carlo Callegari, Head of the LDM Beamline at Elettra Sincrotrone Trieste; Angela Montanaro, PhD Researcher in Q4Q labs; Ettore Paltanin, PhD Student at EIS-TIMEX at Elettra Sincrotrone Trieste; Giuseppe Penco, Head of FERMI Machine Operation and member of the FERMI Project Office. Senior Accelerator Physicist.



Public Engagement Events

SHARPER 2023 – European Researchers' night 2023

(Trieste, 29 September 2023)

As every year Elettra again took part in the initiatives promoted by the European Commission, SHARPER - European Researchers' Night, on Friday 29 September 2023.

The event involves thousands of researchers and institutions in all European countries every year. In Trieste the Night is organised by Immaginario Scientifico, in cooperation with the Education and Family Policies Department of the Municipality of Trieste and the scientific bodies of Trieste City of Knowledge.

Through various types of activities, games, performances, workshops, demonstrations and talks, researchers working in Trieste's institutes presented topics such as climate change, sustainable development, artificial intelligence, astronomy, sustainability, geophysics and medicine, health and sociology and science in a simple, concrete and interactive way.

Elettra participated with:

Simone Lemmers - MSCA research fellow at Elettra Sincrotrone Trieste, as part of the initiative 'An hour with the researcher', led an interactive lesson in English in the Aula Magna of the Liceo Galilei. In front of over 120 students, Simone spoke about *'The Secrets inside our skeletons. A story of resilience and adaptivity in an ever-changing world'* exploring how the study of bones can help us understand the past, present and future, and how the cutting-edge techniques of the Elettra Sincrotrone Trieste particle accelerator can push us into new and unknown territories.

In the late afternoon, a visit for 100 people was organized by the researchers through FERMI's control room and Elettra's experimental hall. The groups stopped at a number of experimental stations where they were shown the techniques used to investigate matter based on spectroscopy, diffraction, absorption, scattering and imaging, and the fields of application ranging from electronics to environmental science, from pharmacology to diagnostics, and from engineering to nanotechnology.



Other News

Elettra and Paul Scherrer Institut joint meeting and workshop

(Trieste, 10-11 November 2022)

Elettra Sincrotrone Trieste and the Paul Scherrer Institut (Villigen - Switzerland) have a decades-long tradition of cooperation in the field of particle accelerators. Both laboratories have advanced projects to upgrade their synchrotron light sources, for the realization of the fourth-generation sources Elettra 2.0 and SLS 2.0. A framework agreement has been concluded that provides for collaborations in the fields of superconducting magnets and magnetic measurements, power converters for magnets and kickers for multibunch feedback. A collaboration is also active in the development of high-gradient accelerator structures, implemented with innovative construction techniques for the FERMI linac.

From November 10 to 11, The 'Elettra and Paul Scherrer Institut Workshop' was organised and held in Trieste at NH Hotel Trieste aiming to assess the progress of these collaborations and explore further potential for expand to other areas.



100 years of CNR celebration in Trieste, and renewal signature of the Framework Agreement

(Trieste, 21 April 2023)

On April 21, 2023 - CNR President Maria Chiara Carrozza visited Trieste on the occasion of CNR's centennial celebrations, part of which took place inside Elettra. It has also been the occasion for the important signing of the new Framework Agreement between the two institutions.

Object of the agreement is the cooperation designed to maintain and develop forms of collaboration for the joint realization of scientific programs of common interest aimed primarily at promoting and encouraging research in the field of fine matter analysis, nanotechnology and nanoscience, in the development of innovative materials, and in the development of advanced instrumentation, particularly for the use of synchrotron radiation.

In addition, Elettra and CNR intend to promote the use of synchrotron radiation by Italian and international scientific users by cooperating in the management of existing beamlines and laboratories, promoting investment in maintaining, securing and renewing the scientific instrumentation of beamlines and laboratories, and in assisting users in carrying out research activities.



MAECI's "We Love Science" Art and Science Project Inaugurated

(Trieste, 2 May 2023)

On the occasion of the celebration of the Day of Italian Research in the World, the traveling exhibition "WE LOVE SCIENCE" was inaugurated at the Italian Cultural Institute in Krakow. This is a project of interaction between art and science by the Ministry of Foreign Affairs and International Cooperation aimed specifically at promoting and enhancing the dialogue between artistic and technological research. The traveling exhibition brings together eight original artworks and audiovisual content created by eight Italian artists inspired by the activities of as many Italian research laboratories including Elettra Sincrotrone Trieste.

The artist Irene Fenara, following an artistic residency at our research center, displays 'Supervision' which represents a close-up and abstracted view of a light source, in which the subject of the image is observed from the inside, which thus becomes invisible.



Other News

In this way, the subject is no longer just a filmed object, but is transformed into the light itself. The exhibition opened in Krakow, but will then be in Warsaw, Pristina and then it will continue its international tour with the support of the Italian Embassies, Consulates and Italian Cultural Institutes network.

Inaugurated at Elettra the new "OptImaTo" laboratory of the University of Trieste

(Trieste, 17 May 2023)

On May 17, 2023 – Elettra and the University of Trieste inaugurated a new state-of-the-art laboratory: the OptImaTo (Optimal Imaging and Tomography) laboratory, set up at Elettra and led by Pierre Thibault, full professor of applied physics at the university.

OptImaTo is equipped with state-of-the-art combined instruments that make the laboratory unique: a robotic arm manipulates the samples to be analysed on a micrometer scale, while the powerful liquid anode X-ray source and the photon-counting detector provide top-quality images in very short times.

The uniqueness of the laboratory lies in the combined method of using these instruments: the potential for acquiring new results and developing innovative techniques is therefore extraordinary.



Empowering Women in Science Workshop in Trieste explores science and technology opportunities at Elettra

(Trieste, 31 May 2023)

The Organization for Women in Science for the Developing World fellowship program supports outstanding women scientists from developing countries to lead research projects and establish research teams at their home institutions to maintain an international standard of research and attract scholars from around the world to collaborate.

Part of the training program that took place in Trieste at ICTP also featured a meeting session at Elettra.

After the welcome and a brief overview on Elettra by Loredana Casalis, head of the Nanoinnovation Laboratory, the participants attended lectures especially tailored for the event, including 'Technology Transfer: Experiences and Challenges' by Mojca Franceskin and Maria Cristina Cringoli of the Industrial Liaison Office, 'Scientific Computing' by George Kourousias, Head of the Essential Remotization internal project, 'Exploring the Frontiers of Energy Research' at Elettra by Giuliana Aquilanti, researcher head of XAFS and XRF beamlines, and 'Synchrotron Application for Agriculture' by Alessandra Gianoncelli, Head of the TwinMic beamline. They also visited the Protein Production Facility with Paola Storici, Head of the Protein Facility, as well as the Elettra experimental hall and FERMI with Filippo Bencivenga, researcher at FERMI.



Elettra Fellows

The Board of Directors of Elettra Sincrotrone Trieste appoints as "Elettra Fellows" distinguished scientists and administrators who have greatly helped Elettra to pursue its mission and achieve its institutional goals. By appointing an Elettra Fellow, Elettra expresses its gratitude for his/her contributions and looks forward to maintaining a long-term scientific relation in the future.

Elettra Fellow to Dr. Dr. Peter Kuske

(Trieste, 12 July 2023)

On Wednesday 12 July, at the dinner of the Machine Advisory Committee, President and CEO Prof. Alfonso Franciosi, on behalf of the Board of Directors of Elettra Sincrotrone Trieste, conferred the title of Elettra Fellow on Dr. Peter Kuske, with the following motivation:

Dr. Peter Kuske is a distinguished accelerator physicist who has given fundamental contributions to the understanding of non-linear transverse and longitudinal beam dynamics and instabilities, in particular longitudinal single bunch instabilities driven by coherent synchrotron radiation. He made important contribution to beam diagnostics and later to beam injection techniques. He designed the multipole pulsed injector element tested, constructed and currently used in MAX IV.

Dr. Kuske has been a member of the Machine Advisory Committee of Elettra Sincrotrone Trieste and over the last years has provided our institution with many valuable contributions in areas ranging from beam dynamics and instabilities to machine injection strategies, greatly contributing to the success of our organization.



Elettra Fellow to Prof. Richard Walker

(Trieste, 12 July 2023)

On Wednesday 12 July, at the dinner of the Machine Advisory Committee, President and CEO Prof. Alfonso Franciosi, on behalf of the Board of Directors of Elettra Sincrotrone Trieste, conferred the title of Elettra Fellow on Prof. Richard P. Walker, with the following motivation:

Prof. Richard P. Walker is an illustrious physicist of international repute who has given fundamental contributions to the understanding and development of the insertion devices that produce the electromagnetic radiation in third-generation synchrotron radiation sources and in free-electron laser sources.

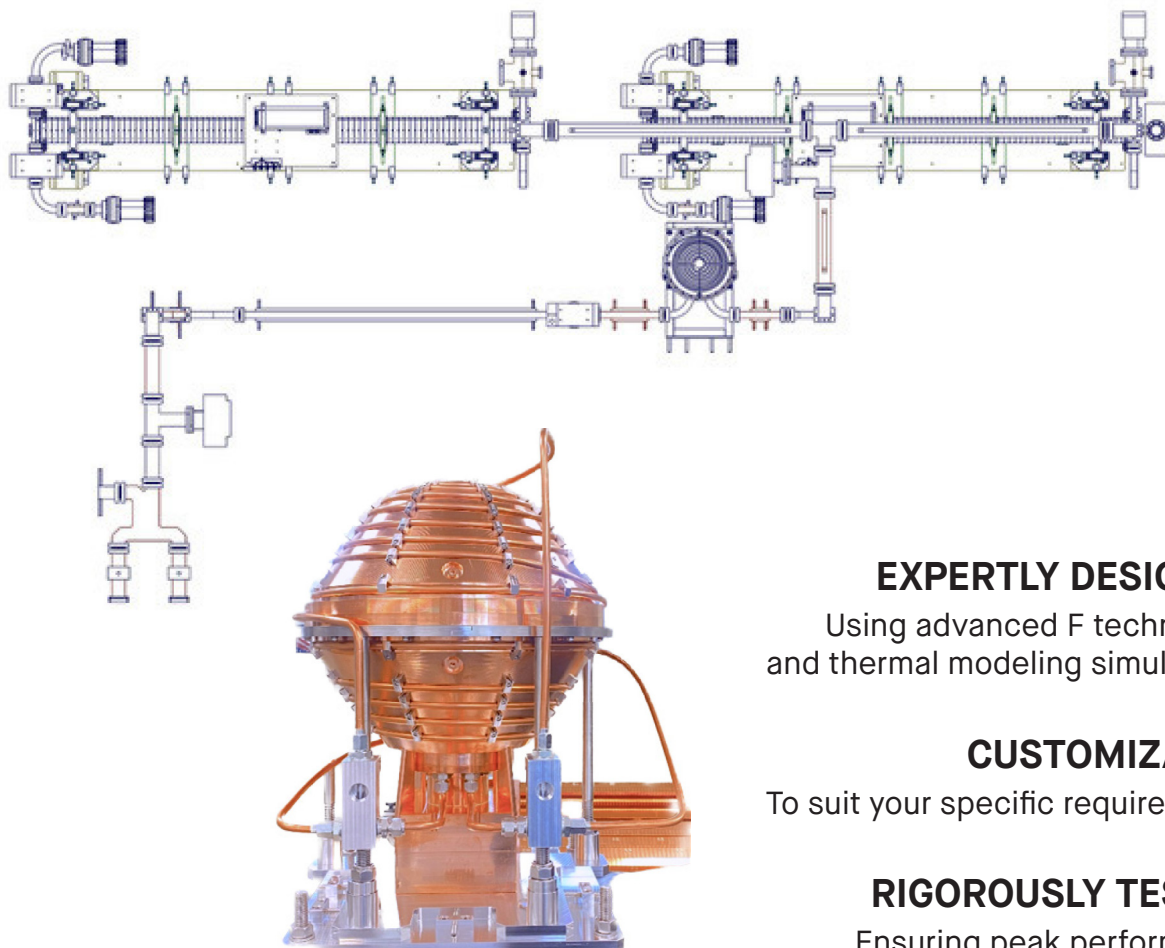
Professor Walker has been directly responsible for many of the achievements of the Elettra source. In addition, he has chaired the Machine Advisory Committee of Elettra Sincrotrone Trieste and over the last years has provided our institution with invaluable advice about our plans for accelerator development in Elettra, FERMI and Elettra 2.0, greatly contributing to the success of our organization.



Elettra Fellows

2023	Peter Kuske Richard P. Walker	2012	Ernst Bauer Helga Nowotny Robert-Jan Smits
2021	Amor Nadji Karsten Horn Maria Novella Piancastelli	2011	Hans Chang Charles S. Fadley Dietrich Menzel
2020	Maya Kiskinova	2010	John Wood
2019	Fulvio Parmigiani	2009	Katepalli R. Sreenivasan
2014	Sergio Tazzari		

High-Power Waveguide Components for Your LINAC!



EXPERTLY DESIGNED

Using advanced F techniques and thermal modeling simulations

CUSTOMIZABLE

To suit your specific requirements

RIGOROUSLY TESTED

Ensuring peak performance

High Gradient Structures, Spherical Pulse Compressors, Compact 3-dB Hybrids, Re-Combiners, Pumping Ports, Power Splitters, Dry Loads, In-Vacuum Variable Power Dividers, In-Vacuum Phase Shifters, Twists and Bends

**Ask for a comprehensive solution:
from design to installation, commissioning and ongoing support!**

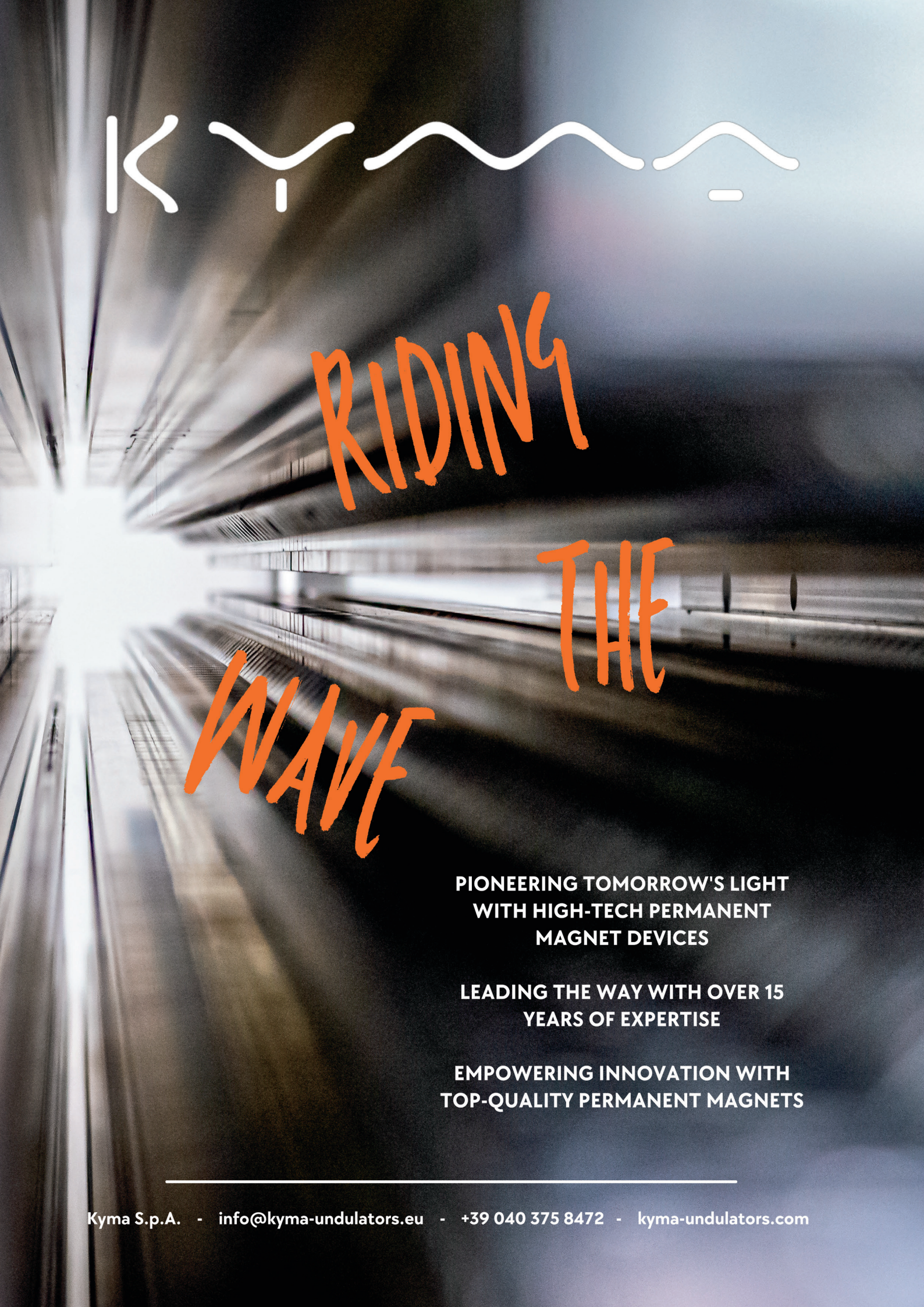
Industrial Liaison Office

Elettra - Sincrotrone Trieste S.C.p.A. S.S.
km 163,5 in Area Science Park 34149
Basovizza - Trieste, Italy
Tel. +39 040 3758056
ilo@elettra.eu - www.elettra.eu/industry



Elettra Sincrotrone Trieste
1993 - 2023 | 30 years of light





KY

RIDING
THE
WAVE

**PIONEERING TOMORROW'S LIGHT
WITH HIGH-TECH PERMANENT
MAGNET DEVICES**

**LEADING THE WAY WITH OVER 15
YEARS OF EXPERTISE**

**EMPOWERING INNOVATION WITH
TOP-QUALITY PERMANENT MAGNETS**

Area Science Park: an ecosystem of research, innovation and enterprise

Supervised by the **Italian Ministry of University and Research**, Area Science Park is a **national research body** headquartered in Trieste.


Established in 1978 to develop scientific and technological research in the region, over the years it has accrued specific skills in conceiving and implementing technology transfer initiatives and **innovative services**. Today, Area Science Park's main focuses include:

- highly specialized research in the fields of **omics sciences, new materials** and **data science**
- innovation models to support industry
- management and development of the **science and technology park**.

With three main laboratories on its premises (**Genomics and Epigenomics Lab, Electron Microscopy Lab, Data Engineering Lab**) operating with cutting edge technology equipment and accessible in an open access mode by researchers from academia and business alike, Area Science Park belongs to **networks of scientific collaboration and international research infrastructures**.



Area Science Park
NATIONAL RESEARCH ORGANISATION

Padriciano, 99, 34149 Trieste - Italy
+39 040 375 5111
urp@areasciencepark.it
 Area Science Park

